# SIMULATING IN VITRO MODELS OF CARDIOVASCULAR FLUID-STRUCTURE INTERACTION: METHODS, MODELS, AND APPLICATIONS

Jae Ho Lee

A dissertation submitted to the faculty at the University of North Carolina at Chapel Hill in partial fulfillment of the requirements for the degree of Doctor of Philosophy in the Department of Mathematics in the College of Arts and Sciences.

Chapel Hill
2020

Approved by:

Boyce E. Griffith

Brent A. Craven

M. Gregory Forest

Laura A. Miller

Simone Rossi

## ABSTRACT

Jae Ho Lee: Simulating In Vitro Models of Cardiovascular Fluid-Structure Interaction: Methods, Models, and Applications
(Under the direction of Boyce E. Griffith)

Computer modeling and simulation (CM&S) in biomedical science is a powerful tool that can offer a cost- and time-efficient complement to traditional clinical diagnosis or medical devices testing. For example, CM&S can be used to study intraventricular fluid dynamics of the left ventricle (LV) of the heart to characterize heart function in health and disease. CM&S can also be used to assess the performance of medical devices such as bioprosthetic heart valves (BHVs). The immersed boundary (IB) method, which can facilitate models such as heart valves with very large structural deformations, was introduced by Peskin to model cardiac fluid-structure interaction (FSI). However, to date, there has been relatively little work on validating IB models of cardiovascular FSI. This thesis describes work that advances the in vitro experimental validation of computational models of blood flow in the LV of the heart and through bioprosthetic heart valves. These models are based on a hyperelastic finite element extension of the the IB method for FSI. For the case of BHVs, we focus on porcine tissue and bovine pericardial BHVs, which are commonly used in surgical valve replacement. We compare our numerical simulations to experimental data from a customized flow circuit for the LV phantom and a commercial ViVitro pulse duplicator for BHVs. We then use this numerical platform to study the role of BHV geometry in leaflet dynamics and possibly leaflet durability. This approach has many potential applications, especially in developing a high-fidelity computational platform for designing and testing cardiovascular devices.

To Judith, Jiah, dad, mom, Jaemo, families, and my Savior Jesus Christ.

## ACKNOWLEDGMENTS

First and foremost, I thank my family for their encouragements. I specifically thank Judith for always being there for me and believing in me even when I didn't believe in myself. Thanks to her, I achieved a much greater goal than getting a Ph.D., which is being a father to our precious daughter Jiah. I also want to thank my parents and Jaemo for their constant support and for their sacrifices that gave me opportunities.

I cannot thank enough for the guidance and support from my thesis advisor Boyce Griffith. Ever since I first reached out to him with a random email that I would love to work with him, he has been nothing but a great mentor not just in research but also in life. I thank him for making research enjoyable and a fun stress to have. He has been a true motivation for me to pursue my career as a researcher.

I am extremely fortunate to have such wonderful postdocs in my life – Simone Rossi, Charles Puelz, Amin Kolahdouz, David Wells, and Amneet Bhalla. They are not only insightful and smart but also very caring. I thank them for always being available to give me advice in research, academic life, and even friendly conversations.

I am grateful for my fellow mathematicians Aaron Barrett, Ben Vadala-Roth, Jason Pearson, Yuan Gao, Nicholas Battista, Manuchehr (Nuch) Aminian, Tim Wessler, Zeliha Kiliç, and Robert Hunt for helping me, guiding me, and suffering with me throughout my time at UNC. I truly enjoyed doing math together and all the conversations over lunch, Oreos, or sodas.

I am thankful for Chris Mack, the director of the Integrative Vascular Biology (IVB) Pre-doctoral Training Program (5T32HL069768-17) at the UNC McAllister Heart Institute that supported my work for the past three years. Chris not only helped me broaden my perspective in cardiovascular research that is outside of my field through the IVB program, but also because of him I got to ride a jet ski for the first time in my life.

One of the most enjoyable part of my experience in graduate school was to have so many mentor figures that I can always talk to for advice. My committee members M. Gregory Forest, Laura

Miller, and Brent Craven have always managed to make time for me whenever I needed to ask them for advice or feedback. They are great role models of what kind of mentor I want to be in the future to younger researchers.

I would also like to specifically thank Laurie Straube, Sara Kross, and Brian Whitling in the Mathematics Student Support Office for always being so motivating, encouraging, and selflessly going above and beyond for all of us students on a daily basis.

My journey would have been difficult without the encouragements from my friends – Daniel Jin, Paul Shin, Daniel Chung, David Lim, Hojoon Chang & Ruth Huh, Josh & Ellie Hall, Eric Kim & Esther Choi, Alex Chang, Daniel & Rachel Kim, Charles & Kimberly Yun, Jake & Sua Stromberg, Doug & Yeon Christie, Daniel & Christine Roh, and Eric & Audrey Chang.

I am indebted to Dan Cristofaro-Gardiner for opening my eyes to how amazing mathematical research can be, Jon Wilkening for patiently listening to my interests and telling me about Boyce's research that led me to come to UNC, and my study buddies in undergraduate Peter Cheng, Ian Pendleton, Sam Braunfeld, and Nielson Weng for always being available to work together and help me understand difficult topics.

Lastly, I give all of my praise to my Savior Jesus Christ.

## TABLE OF CONTENTS

## LIST OF FIGURES

## LIST OF TABLES

CHAPTER 1

# INTRODUCTION

Cardiovascular disease (CVD) remains the leading cause of death both in the U.S. and worldwide [1, 2]. Computer modeling and simulation (CM&S) has become increasingly useful in medical device design for CVDs as a cost- and time-efficient complement to traditional bench testing and clinical trials. CM&S enables assessments of device performance under a broader range of conditions than those listed in the instruction for use, including patient-specific conditions, and a more tightly controlled range of conditions that can be considered on the bench [3]. Simulations may be used in the design phase to optimize device design. Credible simulation data may also be leveraged in regulatory applications to support claims of device safety and effectiveness. Indeed, using modeling and simulation to support regulatory decision-making is a strategic priority area for the U.S. FDA Center for Devices and Radiological Health [4]. CM&S is well-suited for performing root cause analyses to understand impaired device function. For example, CM&S provides information about bioprosthetic heart valve performance that is difficult to acquire on the bench, including assessing the impact of non-circular configurations on transcatheter bioprosthetic heart valves (BHVs) [5].

A fluid–structure interaction (FSI) approach is necessary to model structures such as heart valves across the full cardiac cycle [6]. For example, accounting for coupling between the flexible valve leaflets and the fluid flow is crucial in studying the effect of vortices in the aortic sinuses, predicting fluid-induced shear stress on the leaflets, and assessing valve performance by quantifying the valve orifice area and regurgitation [7]. A widely used approach to simulating cardiovascular FSI is the arbitrary Lagrangian–Eulerian (ALE) method [8,9], which uses body-conforming meshes for the fluid and solid. Though very successful in modeling cardiovascular FSI that involves modest deformations, ALE methods have realized limited success for modeling heart valves to date, however, because of the substantial challenges posed by dynamically generating geometrically conforming discretizations of thin structures, such as heart valves, that undergo substantial motion [8,9]. Non-body conforming discretizations, which avoid the difficulties of body-fitted grids, are now widely used to model heart

valve dynamics. One of the earliest of these types of approaches is the immersed boundary (IB) method [10], which was introduced by Peskin to simulate heart valves [11, 12]. The IB formulation allows the structural discretization to be independent of the fluid grid and thereby facilitates models with very large structural deformations [13]. Extensions to the IB method have also been used to simulate heart valves [14–19]. Methods also have been developed that combine features of ALE and IB-like approaches, including the hybrid fictitious domain/ALE method [20–22] and the immersogeometric (IMGA) method [7, 23–28]. These methods also seek to relax the need to use body-conforming discretizations. The IMGA method is a hybrid ALE-IB approach that uses the IB method in the regions near the valve leaflets and the ALE method elsewhere. Other methods that avoid body-conforming discretizations include smoothed particle hydrodynamics (SPH) [29]. The SPH approach [29], however, cannot fully impose incompressibility, and prescribing boundary conditions is difficult. In addition, several studies have used cut-cell-like methods [30–32] to simulate valve FSI. However, these prior works are lacking validation work to assess the accuracy of their predictions, and to realize its full impact in device regulation, CM&S results must be shown to be credible by performing verification and validation (V&V) [33]. This thesis details work towards in vitro experimental validation of IB models of cardiovascular FSI.

In this thesis work, we simulate cardiovascular FSI using an extension of the IB method described by Griffith and Luo [34]. We first begin with standard FSI benchmark studies to investigate optimal settings to achieve best accuracy for our FSI simulations. These tests are followed by validation studies leveraging two different experimental settings. Chapter 4 works towards validating an FSI model of the intraventricular flow dynamics in an in vitro left ventricle phantom model in a customized pulsatile flow circuit using particle image velocimetry (PIV). Chapters 5 and 6 describe work towards validating the FSI models of bioprosthetic heart valve dynamics in an experimental pulse duplicator system. Chapter 7 uses the platform described in Chapter 5 to investigate the role of bioprosthetic aortic valve geometry in leaflet dynamics and durability. The ultimate goal of this work is to develop a high-fidelity computational platform for designing and testing cardiovascular devices.

CHAPTER 2

# METHODS

## 2.1 Continuum mechanics

In this work, we use the framework of nonlinear continuum mechanics [35, 36] to derive the governing equations of motion and to describe structural deformation of solid bodies. In what follows, capital letters will refer to Lagrangian variables and lower case letters will refer to Eulerian variables.

### 2.1.1 Lagrangian and Eulerian description

In this framework, quantities can be described in terms of Lagrangian (or material) and Eulerian (or spatial) descriptions (Figure 2.1). In the Lagrangian description, quantities are associated with a material particle and its motion, whereas in the Eulerian description, these quantities are associated with a fixed spatial position. Deformation is defined as the change from the reference (initial) configuration, $\Omega_0$, to a deformed configuration, $\Omega_t$, described by the mapping $\boldsymbol{\chi}$ (Figure 2.1). We can then relate a point $\mathbf{X}$ in the reference configuration to its physical location, $\mathbf{x}$, at time $t$ by using the deformation map $\boldsymbol{\chi}$,

$$\mathbf{x} = \boldsymbol{\chi}(\mathbf{X}, t). \tag{2.1}$$

We also define the deformation gradient tensor $\mathbb{F}$,

$$\mathbb{F} = \frac{\partial \mathbf{x}}{\partial \mathbf{X}}, \tag{2.2}$$

whose Jacobian determinant, $J(\mathbf{X}, t) = \det \mathbb{F}$, quantifies the amount of volume change during deformation. This also satisfies the following relation

$$\frac{\partial J(\boldsymbol{\chi}(\mathbf{X}, t), t)}{\partial t} = (\nabla \cdot \mathbf{u}(\boldsymbol{\chi}(\mathbf{X}, t), t)) J(\boldsymbol{\chi}(\mathbf{X}, t)). \tag{2.3}$$

For an incompressible material, $J(\mathbf{X}, t) \equiv 1$, and following Eq (2.3) this implies that $\nabla \cdot \mathbf{u} = 0$ for all $\mathbf{x}$ and $t$.

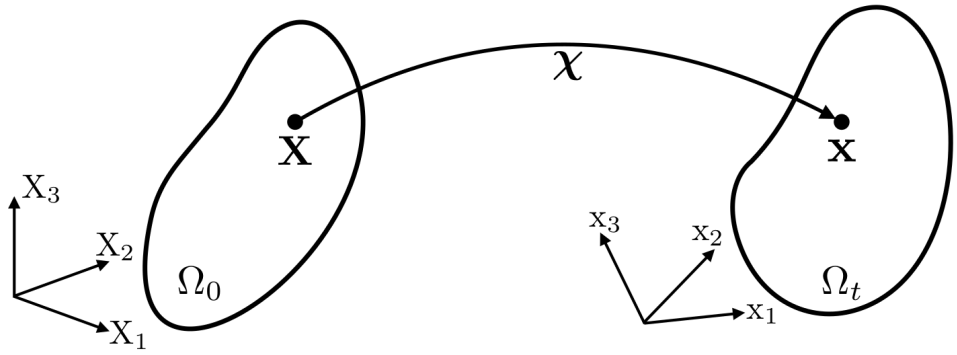


**Figure 2.1:** The deformation mapping of a deformable body.

Now consider a general scalar quantity, $\mathbf{G}$ and $\mathbf{g}$, of the material. In the Lagrangian description, this quantity is assigned to a material particle at the reference coordinate $\mathbf{X}$ on the material,

$$\mathbf{G} = \mathbf{G}(\mathbf{X}, t). \tag{2.4}$$

In the Eulerian description, this quantity is now assigned to a particular position, $\mathbf{x}$,

$$\mathbf{g} = \mathbf{g}(\mathbf{x}, t) = \mathbf{g}(\boldsymbol{\chi}(\mathbf{x}, t), t). \tag{2.5}$$

This also leads to the concept of material time derivative, or convective derivative. Consider the same general scalar or tensor quantity, $\mathbf{G}(\mathbf{X}, t)$, in terms of the reference coordinates $\mathbf{X}$. The material time derivative is defined simply as the time derivative of $\mathbf{G}(\mathbf{X}, t)$,

$$\frac{\mathrm{d}}{\mathrm{d}t}\mathbf{G}(\mathbf{X}, t) = \frac{\partial \mathbf{G}(\mathbf{X}, t)}{\partial t}. \tag{2.6}$$

To calculate the material time derivative in terms of the current physical location $\boldsymbol{\chi}(\mathbf{X}, t)$, then we need to account for the changes in the spatial position of the material particle over time. We can use the chain rule to calculate the material time derivative in this case,

$$\frac{\mathrm{d}}{\mathrm{d}t}\mathbf{g}(\boldsymbol{\chi}(\mathbf{X}, t), t) = \frac{\partial \mathbf{g}(\boldsymbol{\chi}(\mathbf{X}, t), t)}{\partial t} + \frac{\partial \mathbf{g}(\boldsymbol{\chi}(\mathbf{X}, t), t)}{\partial \mathbf{x}} \frac{\partial \boldsymbol{\chi}(\mathbf{X}, t)}{\partial t} \tag{2.7}$$

$$= \left(\frac{\partial}{\partial t} + \mathbf{u} \cdot \nabla\right) \mathbf{g}(\boldsymbol{\chi}(\mathbf{X}, t), t) \equiv \frac{\mathrm{D}\mathbf{g}}{\mathrm{D}t}, \tag{2.8}$$

in which we define $\mathbf{u}(\boldsymbol{\chi}(\mathbf{X}, t)) \equiv \frac{\partial \boldsymbol{\chi}(\mathbf{X}, t), t)}{\partial t}$.

### 2.1.2 Conservation of mass

For some material at $\mathbf{x} \in \Omega_t$, we define its density as $\rho(\mathbf{x}, t)$, which is the mass per volume in the Eulerian description. Consequently, the total mass of material can be found by integrating the density over the material volume, and assuming that the mass is conserved over time,

$$\frac{\mathrm{d}M(t)}{\mathrm{d}t} = \frac{\mathrm{d}}{\mathrm{d}t} \int_{\Omega_t} \rho(\mathbf{x}, t) \, \mathrm{d}\mathbf{x} = 0, \tag{2.9}$$

which we can then rewrite as

$$\begin{aligned}
\frac{\mathrm{d}}{\mathrm{d}t} \int_{\Omega_t} \rho(\mathbf{x}, t) \mathrm{d}\mathbf{x} &= \frac{\mathrm{d}}{\mathrm{d}t} \int_{\Omega_0} \rho(\boldsymbol{\chi}(\mathbf{X}, t), t) J(\mathbf{X}, t) \, \mathrm{d}\mathbf{X} && (2.10)\\
&= \int_{\Omega_0} \frac{\mathrm{d}}{\mathrm{d}t} (\rho(\boldsymbol{\chi}(\mathbf{X}, t), t) J(\mathbf{X}, t)) \, \mathrm{d}\mathbf{X} && (2.11)\\
&= \int_{\Omega_0} \left( \frac{\mathrm{D}\rho(\boldsymbol{\chi}(\mathbf{X}, t), t)}{\mathrm{D}t} + \rho(\boldsymbol{\chi}(\mathbf{X}, t), t) \left( \nabla \cdot \mathbf{u}(\boldsymbol{\chi}(\mathbf{X}, t)) \right) \right) J(\mathbf{X}, t) \, \mathrm{d}\mathbf{X} && (2.12)\\
&= \int_{\Omega_t} \left( \frac{\mathrm{D}\rho(\mathbf{x}, t)}{\mathrm{D}t} + \rho(\mathbf{x}, t) \left( \nabla \cdot \mathbf{u}(\mathbf{x}, t) \right) \right) \mathrm{d}\mathbf{x} && (2.13)\\
&= 0. && (2.14)
\end{aligned}$$

Because this holds for any arbitrary material volume $\Omega_t$, this also holds pointwise, and we obtain

$$\frac{\mathrm{D}\rho(\mathbf{x}, t)}{\mathrm{D}t} + \rho(\mathbf{x}, t) \left( \nabla \cdot \mathbf{u}(\mathbf{x}, t) \right) = 0. \tag{2.15}$$

For an incompressible material, Eq. (2.15) reduces to $\frac{\mathrm{D}\rho(\mathbf{x}, t)}{\mathrm{D}t} = 0$. Therefore, for an incompressible material, we can rewrite conservation of mass as

$$\nabla \cdot \mathbf{u}(\mathbf{x}, t) = 0. \tag{2.16}$$

### 2.1.3 Conservation of momentum

The momentum of the material in $\Omega_t$ is

$$\mathbf{p}(t) = \int_{\Omega_t} \rho(\mathbf{x}, t) \mathbf{u}(\mathbf{x}, t) \, \mathrm{d}\mathbf{x}. \tag{2.17}$$

By Newton's second law, the rate of change in momentum is equal to the total forces acting on the given material region $\Omega_t$,

$$\begin{aligned}
\frac{\mathrm{d}}{\mathrm{d}t}\mathbf{p}(t) &= \frac{\mathrm{d}}{\mathrm{d}t}\int_{\Omega_t}\rho\mathbf{u}(\mathbf{x},t)\,\mathrm{d}\mathbf{x} && (2.18)\\
&= \frac{\mathrm{d}}{\mathrm{d}t}\int_{\Omega_0}\rho\mathbf{u}(\boldsymbol{\chi}(\mathbf{X},t),t)J(\mathbf{X},t)\,\mathrm{d}\mathbf{X} && (2.19)\\
&= \int_{\Omega_0}\left(\frac{\mathrm{D}\rho}{\mathrm{D}t}+\rho\left(\nabla\cdot\mathbf{u}(\boldsymbol{\chi}(\mathbf{X},t))\right)+\rho\frac{\mathrm{D}\mathbf{u}(\boldsymbol{\chi}(\mathbf{X},t),t)}{\mathrm{D}t}\right)J(\mathbf{X},t)\,\mathrm{d}\mathbf{X} && (2.20)\\
&= \int_{\Omega_t}\left(\frac{\mathrm{D}\rho}{\mathrm{D}t}+\rho\left(\nabla\cdot\mathbf{u}(\mathbf{x},t)\right)+\rho\frac{\mathrm{D}\mathbf{u}(\mathbf{x},t)}{\mathrm{D}t}\right)\mathrm{d}\mathbf{x} && (2.21)\\
&= \int_{\Omega_t}\rho\frac{\mathrm{D}\mathbf{u}(\mathbf{x},t)}{\mathrm{D}t}\,\mathrm{d}\mathbf{x} && (2.22)\\
&= \mathbf{f}_{\text{total}}. && (2.23)
\end{aligned}$$

The total force $\mathbf{f}_{\text{total}}$ consists of the external body force densities $\mathbf{f}$ and the surface tractions $\mathbf{t}=\boldsymbol{\varpi}\cdot\mathbf{n}$, in which $\boldsymbol{\varpi}$ is the Cauchy stress tensor and $\mathbf{n}$ is the outward unit normal to the surface $\partial\Omega_t$ at point $\mathbf{x}$. We then write the total force as,

$$\begin{aligned}
\mathbf{f}_{\text{total}} &= \int_{\Omega_t}\mathbf{f}(\mathbf{x},t)\,\mathrm{d}\mathbf{x}+\int_{\partial\Omega_t}\mathbf{t}(\mathbf{x},t)\,\mathrm{d}a && (2.24)\\
&= \int_{\Omega_t}\mathbf{f}(\mathbf{x},t)\,\mathrm{d}\mathbf{x}+\int_{\partial\Omega_t}\boldsymbol{\varpi}\cdot\mathbf{n}\,\mathrm{d}a, && (2.25)\\
&= \int_{\Omega_t}\mathbf{f}(\mathbf{x},t)\,\mathrm{d}\mathbf{x}+\int_{\Omega_t}\nabla\cdot\boldsymbol{\varpi}(\mathbf{x},t)\,\mathrm{d}\mathbf{x}, && (2.26)
\end{aligned}$$

in which the last equality holds from the divergence theorem. Now we can write down the conservation of momentum as,

$$\int_{\Omega_t}\rho\frac{\mathrm{D}\mathbf{u}(\mathbf{x},t)}{\mathrm{D}t}\,\mathrm{d}\mathbf{x}=\int_{\Omega_t}\mathbf{f}(\mathbf{x},t)\,\mathrm{d}\mathbf{x}+\int_{\Omega_t}\nabla\cdot\boldsymbol{\varpi}(\mathbf{x},t)\,\mathrm{d}\mathbf{x}, \tag{2.27}$$

and because this holds for an arbitrary $\Omega_t$, therefore,

$$\rho\frac{\mathrm{D}\mathbf{u}(\mathbf{x},t)}{\mathrm{D}t}=\mathbf{f}(\mathbf{x},t)+\nabla\cdot\boldsymbol{\varpi}(\mathbf{x},t). \tag{2.28}$$

**Fluid model** In this work, we model the fluid as a viscous Newtonian fluid, which is described by the constitutive equation,

$$\boldsymbol{\varpi}^{\mathrm{f}}=-p\mathbb{I}+\mu\left(\nabla\mathbf{u}+\nabla\mathbf{u}^{T}\right), \tag{2.29}$$

in which $\mu$ is the viscosity of the fluid. Using the constitutive law in Eq (2.29) in Eq (2.28) along with Eq (2.16), we obtain the Navier-Stokes equations for an incompressible viscous Newtonian fluid,

$$\rho \frac{\mathrm{D}\mathbf{u}(\mathbf{x},t)}{\mathrm{D}t} = -\nabla p(\mathbf{x},t) + \mu \nabla^2 \mathbf{u}(\mathbf{x},t) + \mathbf{f}(\mathbf{x},t) \tag{2.30}$$

$$\nabla \cdot \mathbf{u}(\mathbf{x},t) = 0. \tag{2.31}$$

**Solid model** As mentioned earlier, we describe the biomechanics of the elastic structures using the framework of nonlinear solid mechanics [35, 36]. The solid model uses the same momentum equation, Eq (2.27), as the fluid model, but with a different stress, $\mathbb{\sigma}^{\mathrm{s}}$, that describes the constitutive model of the solid material. Recall, material deformations are described by the mapping $\boldsymbol{\chi} = \boldsymbol{\chi}(\mathbf{X}, t)$ between reference coordinates $\mathbf{X}$ and current coordinates $\mathbf{x}$ at time $t$. The valve leaflets are treated as anisotropic, incompressible, hyperelastic materials. For hyperelastic materials, we can characterize the material property of the elastic structure in terms of a strain energy functional $\Psi(\mathbb{F})$. The first Piola–Kirchhoff stress $\mathbb{P}^{\mathrm{s}}$ is related to the strain-energy functional $\Psi(\mathbb{F})$ via [18]

$$\mathbb{P}^{\mathrm{s}} = \frac{\partial \Psi}{\partial \mathbb{F}}, \tag{2.32}$$

in which $\mathbb{\sigma}^{\mathrm{s}} = J^{-1}\mathbb{P}^{\mathrm{s}}\mathbb{F}^{T}$.

## 2.2 The immersed boundary method

The immersed boundary (IB) formulation uses an Eulerian description of the momentum, viscosity, and incompressibility of the coupled fluid-structure system, and it uses a Lagrangian description of the deformations, stresses, and resultant forces of the immersed structure. In particular, we model the immersed structure as a viscoelastic solid, in which the viscous stresses in the solid are assumed to be small compared to elastic stresses, as in previous work by us and others [34, 37–41]. The coupling between Eulerian and Lagrangian variables is mediated by integral transforms with delta function kernels. In particular, we use the hyperelastic finite element extension of the IB method by Griffith et al. [13, 34]

### 2.2.1 Continuum equations

In the continuous IB formulation, we consider a fixed three-dimensional Eulerian computational domain $\Omega$ that is divided into the time-dependent solid ($\Omega_t^{\mathrm{s}}$) and fluid ($\Omega_t^{\mathrm{f}}$) subdomains, so that

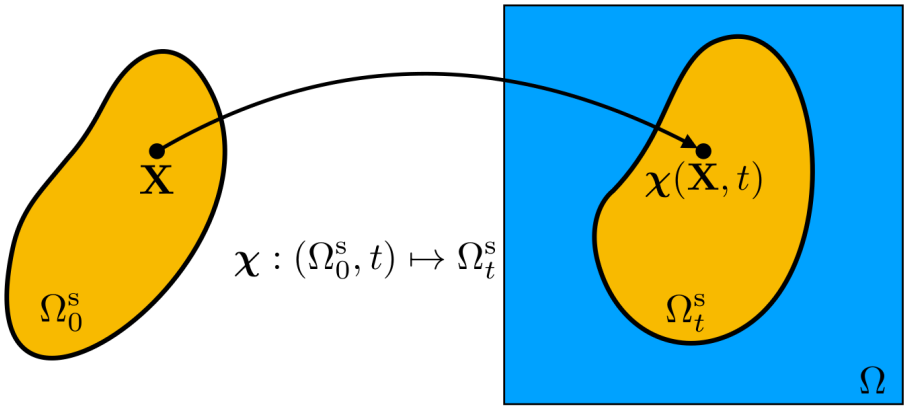


**Figure 2.2:** A schematic of the immersed boundary formulation. In the continuous IB formulation, we consider a fixed three-dimensional Eulerian computational domain $\Omega$ that is divided into the time-dependent solid ($\Omega_t^{\mathrm{s}}$) and fluid ($\Omega_t^{\mathrm{f}}$) subdomains, so that $\Omega = \Omega_t^{\mathrm{s}} \cup \Omega_t^{\mathrm{f}}$. $\boldsymbol{\chi}(\mathbf{X},t) \in \Omega_t^{\mathrm{s}}$ is the physical position of material point $\mathbf{X}$ at time $t$.

$\Omega = \Omega_t^{\mathrm{s}} \cup \Omega_t^{\mathrm{f}}$. Here, $\mathbf{x} = (x_1, x_2, x_3) \in \Omega$ are physical coordinates, $\mathbf{X} = (X_1, X_2, X_3) \in \Omega_0^{\mathrm{s}}$ are reference coordinates attached to the structure, $\mathbf{N}(\mathbf{X}) \in \partial\Omega_0^{\mathrm{s}}$ is the outward unit normal to the reference configuration of the solid region at material point $\mathbf{X}$, and $\boldsymbol{\chi}(\mathbf{X},t) \in \Omega_t^{\mathrm{s}}$ is the physical position of material point $\mathbf{X}$ at time $t$. $\rho$ and $\mu$ are the mass density and viscosity, $\mathbf{u}(\mathbf{x},t)$ and $p(\mathbf{x},t)$ are the Eulerian velocity and pressure fields, $\mathbf{f}(\mathbf{x},t)$ is the Eulerian elastic force density, $\mathbb{P}(\mathbf{X},t)$ is the first Piola-Kirchhoff elastic stress of the immersed structure, and $\delta(\mathbf{x}) = \prod_{i=1}^{3} \delta(x_i)$ is the three-dimensional Dirac delta function. The IB form of the equations of motion for the fluid-structure system is:

$$\rho \frac{\mathrm{D}\mathbf{u}}{\mathrm{D}t}(\mathbf{x},t) = -\nabla p(\mathbf{x},t) + \mu \nabla^2 \mathbf{u}(\mathbf{x},t) + \mathbf{f}(\mathbf{x},t), \tag{2.33}$$

$$\nabla \cdot \mathbf{u}(\mathbf{x},t) = 0, \tag{2.34}$$

$$\begin{aligned} \mathbf{f}(\mathbf{x},t) = &\int_{\Omega_0^s} \nabla_{\mathbf{X}} \cdot \mathbb{P}(\mathbf{X},t)\, \delta(\mathbf{x} - \boldsymbol{\chi}(\mathbf{X},t))\, \mathrm{d}\mathbf{X} \\ &- \int_{\partial\Omega_0^s} \mathbb{P}(\mathbf{X},t)\, \mathbf{N}(\mathbf{X})\, \delta(\mathbf{x} - \boldsymbol{\chi}(\mathbf{X},t))\, \mathrm{d}A, \end{aligned} \tag{2.35}$$

$$\frac{\partial \boldsymbol{\chi}}{\partial t}(\mathbf{X},t) = \int_{\Omega} \mathbf{u}(\mathbf{x},t)\, \delta(\mathbf{x} - \boldsymbol{\chi}(\mathbf{X},t))\, \mathrm{d}\mathbf{x} = \mathbf{u}(\boldsymbol{\chi}(\mathbf{X},t),t). \tag{2.36}$$

Notice that because $\partial\boldsymbol{\chi}/\partial t(\mathbf{X},t) = \mathbf{u}(\boldsymbol{\chi}(\mathbf{X},t),t)$ and $\nabla \cdot \mathbf{u}(\mathbf{x},t) = 0$ everywhere in the domain, the immersed structure is described in the continuous IB framework as an exactly incompressible material. We can further postulate a splitting of the strain energy functional into isochoric and

volumetric parts [42],

$$\Psi(\mathbb{F}) = W(\overline{\mathbb{F}}) + U(J), \tag{2.37}$$

in which $\overline{\mathbb{F}} = J^{-1/3}\mathbb{F}$ and $J = \det \mathbb{F}$. The mathematical framework used in this thesis treats the elastic structures as exactly incompressible. In the numerical studies detailed herein, we choose the volumetric part of the strain energy to be [43]

$$U(J) = \beta(J \ln J - J + 1), \tag{2.38}$$

which can be viewed as a stabilization term. For further details on this stabilization method, see Appendix A for a summary of the work of Vadala-Roth et al. [42].

### 2.2.2 Numerical approximations

The computational domain $\Omega$, which includes both the solid and fluid subregions, is described using a block-structured locally refined Cartesian grid consisting of multiple nested levels of Cartesian grid patches. High spatial resolution is used dynamically near fluid-structure interfaces (Figure 2.3) and near flow features, such as vortices shed from the valve leaflets, that are identified by feature detection criteria that select regions of high vorticity for enhanced spatial resolution. A staggered-grid discretization is used for the incompressible Navier-Stokes that includes a version [44, 45] of the xsPPM7 variant [46] of the piecewise parabolic method (PPM) [47] to approximate the convective term.

### 2.2.3 IBAMR

FSI simulations use the IBAMR software infrastructure, which is a distributed-memory parallel implementation of the IB method with adaptive mesh refinement (AMR) [48, 49]. IBAMR uses SAMRAI [50] for Cartesian grid discretization management, libMesh [51] for finite element discretization management, and PETSc [52] for linear solver infrastructure.

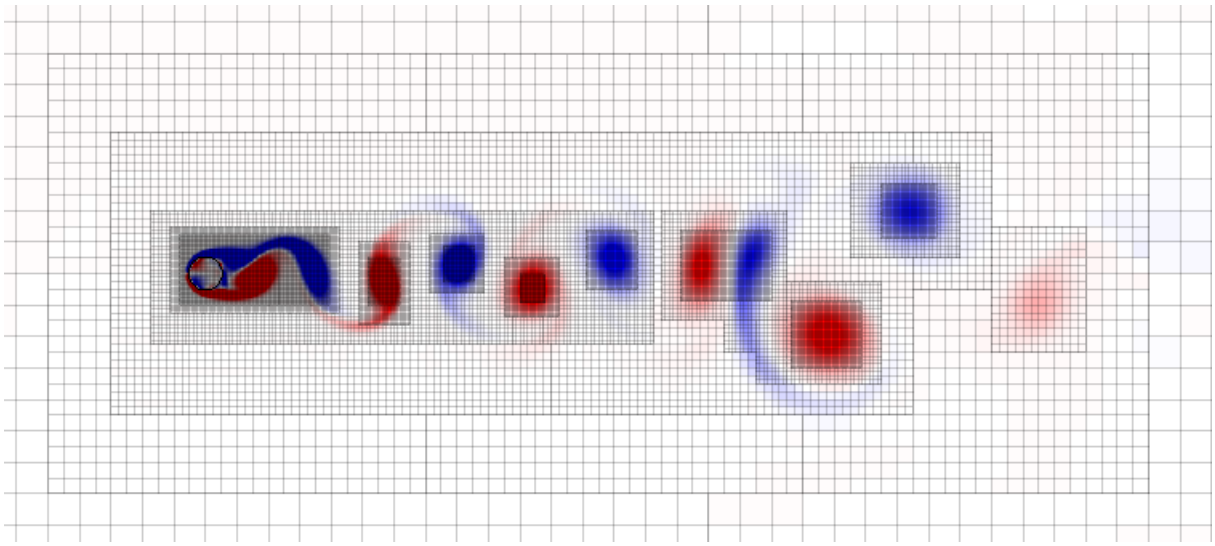

**Figure 2.3:** An example of adaptive mesh refinement in IBAMR in simulating flow past a stationary circular cylinder. The computational domain is described by block-structured adaptively refined Cartesian grid that dynamically tracks vortices shed from the immersed structure.

CHAPTER 3

# FLUID-STRUCTURE INTERACTION BENCHMARKS

## 3.1 Regularized delta functions

As briefly described in Section 2.2.1, in the IB formulation of the equations of motion, coupling between Eulerian and Lagrangian variables is mediated by integral transforms with Dirac delta function kernels [13,34]. In our computations, we use a regularized delta function $\delta_h(\mathbf{x})$ to approximate the integral transforms in Eq. (2.35) and (2.36). We know from previous work that the overall accuracy of the discretization depends on the form of the regularized delta function [10, 34, 53–55]. For example, special forms of delta functions were developed to avoid the "checkerboard" instability that arise from using collocated-grid fluid solver [45, 53–55]. Griffith and Luo [34] show using the standard test case of viscous flow past a circular cylinder that the accuracy of the results obtained by their version of the IB method depends on both the relative structural mesh spacing and the choice regularized kernel function. In this work, we leverage this and other additional FSI benchmarks to investigate the optimal setting to achieve best accuracy for various types of FSI simulations.

The three-dimensional regularized delta function is the tensor product of one-dimensional delta functions, $\delta_h(\mathbf{x}) = \prod_{i=1}^{3} \delta_h(x_i)$, and the one-dimensional delta function is defined in terms of a basic kernel function via $\delta_h(x) = \frac{1}{h}\varphi\left(\frac{x}{h}\right)$. Here, $\varphi(r)$ is continuous for all $r$ and zero outside of the radius of support (see Figure 3.1 for an example). Some kernel functions can be determined by imposing

some or all of the following moment conditions [10],

$$\text{zeroth moment: } \sum_j \varphi(r-j) = 1, \tag{3.1}$$

$$\text{even–odd: } \sum_{j \text{ even}} \varphi(r-j) = \sum_{j \text{ odd}} \varphi(r-j) = \frac{1}{2}, \tag{3.2}$$

$$\text{first moment: } \sum_j (r-j)\varphi(r-j) = 0, \tag{3.3}$$

$$\text{second moment: } \sum_j (r-j)^2\varphi(r-j) = K, \text{ for some constant } K. \tag{3.4}$$

The zeroth moment condition implies total force balance in the Lagrangian and Eulerian grids when $\delta_h$ is used for force spreading. The even–odd condition is to avoid the "checkerboard" instability in a collocated-grid fluid solver and suppresses high-frequency modes. Note that the even-odd condition implies the zeroth moment condition. The first moment condition implies the conservation of total torque. Along with the zeroth moment condition, it guarantees second-order accuracy in smooth function interpolation [10]. If a kernel function satisfies Eq (3.4) with $K = 0$, then the second moment condition implies that the kernel achieves higher order accuracy in interpolating smooth fields. It is also possible to use the higher-order moment condition with $K \neq 0$, which can be used to impose higher continuity order on the kernel function [54]. Peskin also postulated a sum-of-squares condition that $\varphi(r)$ satisfies,

$$\sum_j (\varphi(r-j))^2 = C, \text{ for some constant } C, \tag{3.5}$$

which is a weak version of a grid translational invariance property. We have different choices of delta function kernels with different properties depending on which of the moment conditions are satisfied. Piecewise-constant and piecewise-linear kernels (Figures 3.1a and 3.1b) give sharp resolution at fluid-structure interface, but lower accuracy in lift and drag forces for some cases. At present, the kernel functions most commonly used with the IB method are the IB kernels (Figures 3.1c-3.1f). Three-point and five-point IB kernels are constructed by satisfying the zeroth, first, and second (for the five-point kernel) moment conditions as well as the sum-of-squares condition, but not the even-odd condition. Four-point and six-point IB kernels are constructed by satisfying the even-odd

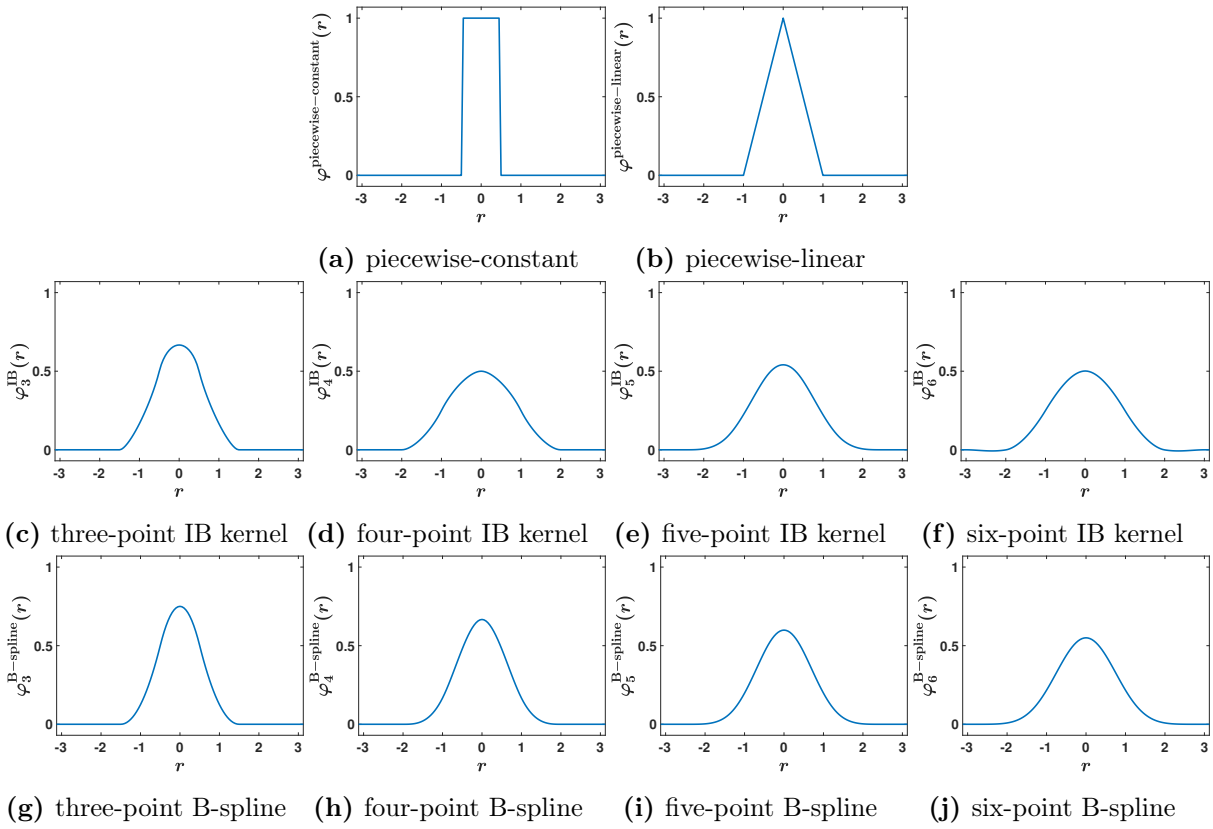


**(a)** piecewise-constant **(b)** piecewise-linear

**(c)** three-point IB kernel **(d)** four-point IB kernel **(e)** five-point IB kernel **(f)** six-point IB kernel

**(g)** three-point B-spline **(h)** four-point B-spline **(i)** five-point B-spline **(j)** six-point B-spline

**Figure 3.1:** Different kinds of regularized delta functions.

condition (which also implies the zeroth moment condition), first, and second (for the five-point kernel) moment conditions as well as the sum-of-squares condition. We can also consider B-spline kernels (Figure 3.1g-3.1j), which are constructed by convolution of piecewise-constant (zeroth-order B-spline) kernels (Figure 3.2 shows examples of these constructions). This means that the $n^{\text{th}}$-order B-spline kernel is constructed by convolving the $(n-1)^{\text{th}}$-order B-spline with the zeroth-order B-spline. B-spline kernels do not satisfy the even-odd condition, and they are shown to have advantages in computation. Both the radius of support and the smoothness of B-splines increase with the order, and the limiting function is a Gaussian [55, 56].

## 3.2 Lagrangian mesh spacing

In addition to the choice of the regularized delta function kernel, we also have to consider the interaction between the Lagrangian mesh and the Eulerian grid. Here, we introduce $M_{\text{fac}}$, which is the ratio of Lagrangian element, or finite element, node spacing to the Eulerian, or Cartesian, grid spacing. See Figure 3.3 for better understanding of the concept of $M_{\text{fac}}$. We investigate through

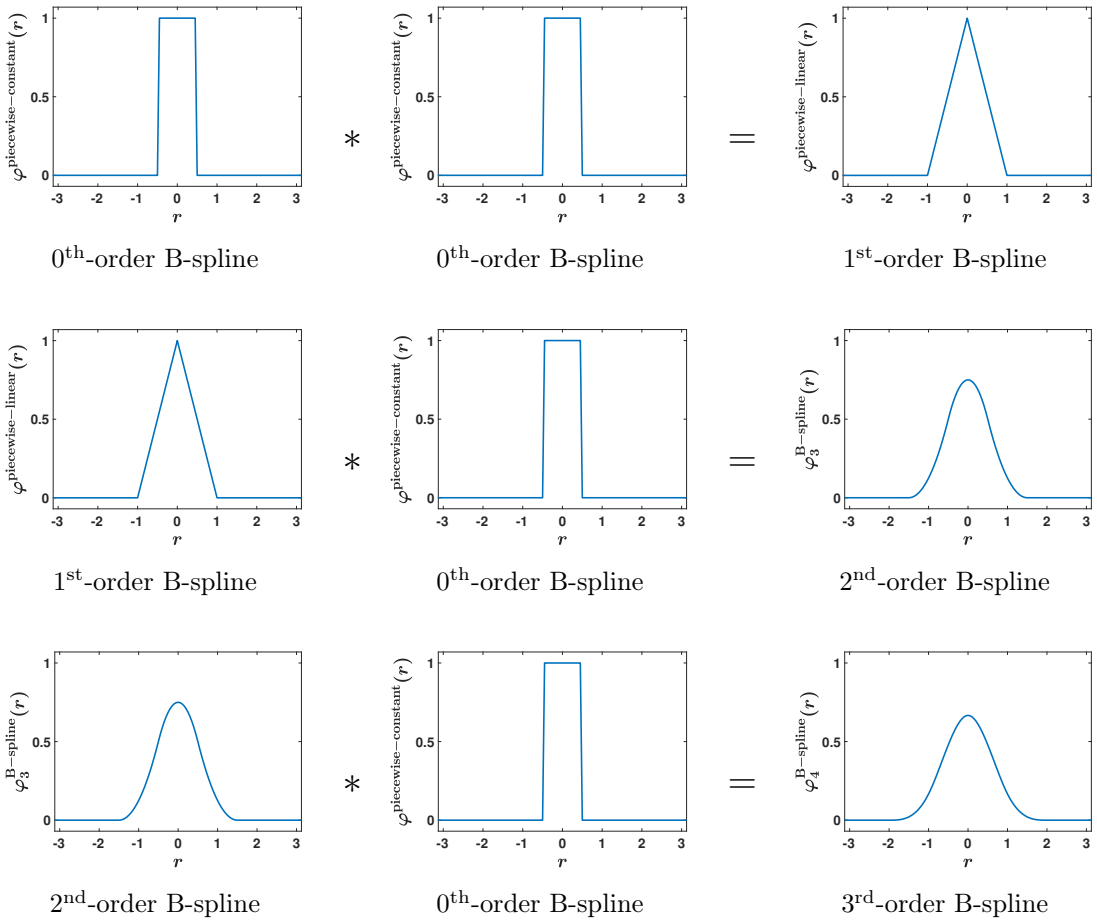


**Figure 3.2:** Construction of B-spline kernels. The $n^{\text{th}}$-order B-spline kernel is constructed by convolving the $(n-1)^{\text{th}}$-order B-spline with the $0^{\text{th}}$-order B-spline (piecewise-constant or a "window" function). B-spline kernels do not satisfy the even-odd condition, and they are shown to have advantages in computation. Both the radius of support and the smoothness of B-splines increase with the order, and the limiting function is a Gaussian function [55, 56].

our FSI benchmarks the effect of the choice of $M_{\text{fac}}$, along with the choice of the regularized delta function kernel, in the accuracy of our solutions.

### 3.3 Two-dimensional flow past cylinder

One of the widely used FSI benchmarks is the flow past a cylinder test, which describes the viscous flow around a stationary geometry [34, 57]. The cylinder has diameter $D = 1$, and is embedded in a computational domain with side lengths of $L = H = 60$. See Figure 3.4 for a schematic of the setup for this benchmark. We use a uniform inflow velocity boundary condition, $\mathbf{u} = (1, 0)$, at the inflow boundary along with zero normal traction and tangential velocity at the outflow boundary. For the

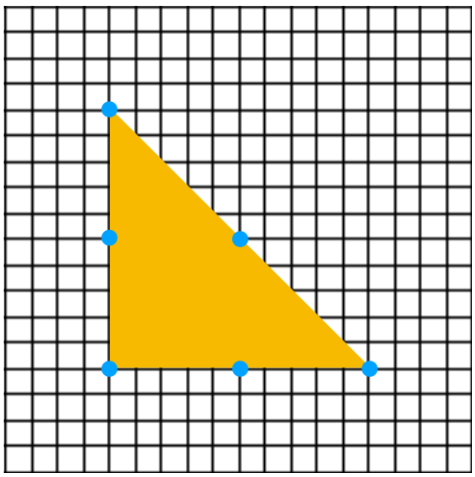

**Figure 3.3:** Description of $M_{\text{fac}}$, which is the ratio between background Cartesian grid spacing and finite element node spacing. In the case shown here, there are about five Cartesian grid cells between two finite element nodes, so we say that $M_{\text{fac}} \approx 5$.

top and bottom boundaries, we use zero normal velocity and tangential traction. We use the fluid with density $\rho = 1$ and viscosity $\mu = 0.005$. We compare the drag ($C_{\text{L}}$) and lift ($C_{\text{D}}$) coefficients to evaluate different regularized delta functions $\delta_h(\mathbf{x})$ and $M_{\text{fac}}$. The drag and lift coefficients are

$$C_{\text{D}} = \frac{F_x}{\rho u_\infty^2 D/2}, \qquad C_{\text{L}} = \frac{F_y}{\rho u_\infty^2 D/2}, \tag{3.6}$$

in which $\mathbf{F} = (F_x, F_y)$ is the net force on the cylinder, $u_\infty$ is the characteristic speed ($x$-component of the inflow velocity), $D$ is the diameter of the cylinder, and the Reynolds number is $Re = \frac{\rho u_\infty D}{\mu} = 200$. Griffith and Luo [34] had conducted an initial benchmark study with three-, four-, and six-point IB delta function kernels. Here, we look at the impact of all of the delta function kernels described earlier except for the piecewise-constant function.

Figures 3.5, 3.7, and 3.9 show the comparison of drag coefficients ($C_{\text{D}}$) as functions of time for different kernels, for $M_{\text{fac}} = 0.5$, 1, 2, and 4, and for $N = 32$, 64, and 128. Figures 3.6, 3.8, and 3.10 show the comparison of lift coefficients ($C_{\text{L}}$) as functions of time for different kernels, for $M_{\text{fac}} = 0.5$, 1, 2, and 4, and for $N = 32$, 64, and 128. We observe that the scheme converges under grid refinement for all choices of kernels and for all values of $M_{\text{fac}}$. We see, however, that cases that use the four- and six-point IB kernels require high grid resolution to obtain convergence for $M_{\text{fac}} = 0.5$ and 1. The three-point IB kernel shows comparable results for $M_{\text{fac}} >= 1$, and $M_{\text{fac}} = 0.5$ converges at the finer grid resolution (Figures 3.9 and 3.10). We can clearly see in the coarsest cases (Figures 3.5

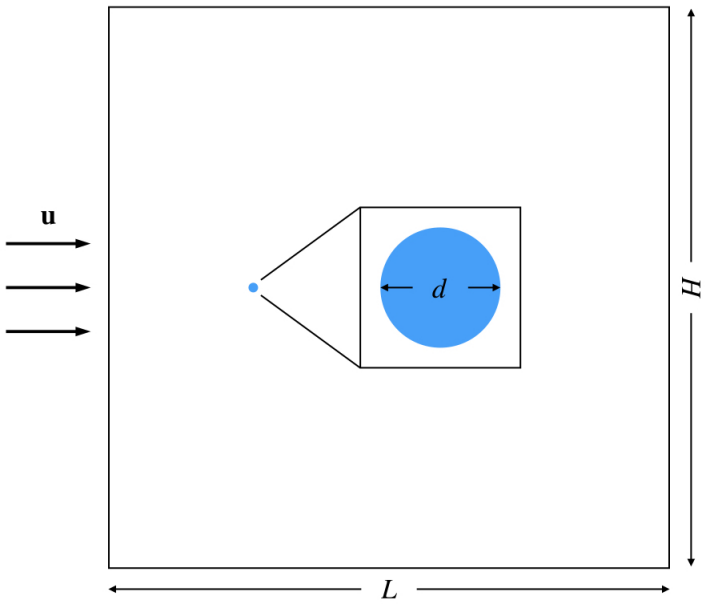


**Figure 3.4:** Schematic of two-dimensional flow past a cylinder. Arrows represent the inflow boundary, where a uniform velocity boundary condition, $\mathbf{u} = (1, 0)$, is applied.

and 3.6) that we want the $M_{\text{fac}}$ value to be larger than 1, indicates that the structural mesh is coarser than the Cartesian grid at the finest level. This result agrees with the results from Griffith and Luo [34]. We further observe that the five-point IB and B-spline kernels yield comparable results for all $M_{\text{fac}} \geq 1$. In particular, the three-point B-spline kernel gives comparable results even for $M_{\text{fac}} = 0.5$ even at $N = 64$. A possible explanation is that the even-odd condition satisfied by the four- and six-point IB kernels over-constrain the solution. Although these results show that refining the Lagrangian mesh while keeping the Eulerian grid resolution fixed generally lowers the accuracy, results obtained using the three-point B-spline kernel indicate that it is less sensitive to the relative structural mesh spacing.

## 3.4 Two-dimensional channel flows

In this section we validate the numerical solution of two-dimensional channel flow, whose exact steady-state solution exists and is given by

$$u_x(y,t) = \frac{\chi}{2\mu} y(H-y), \tag{3.7}$$

in which $u_x(y,t)$ is the steady-state velocity along the flow, $0 \leq y \leq H$ is the coordinate direction across the two channel walls, $H$ and $L$ are the height and length of the computational domain,

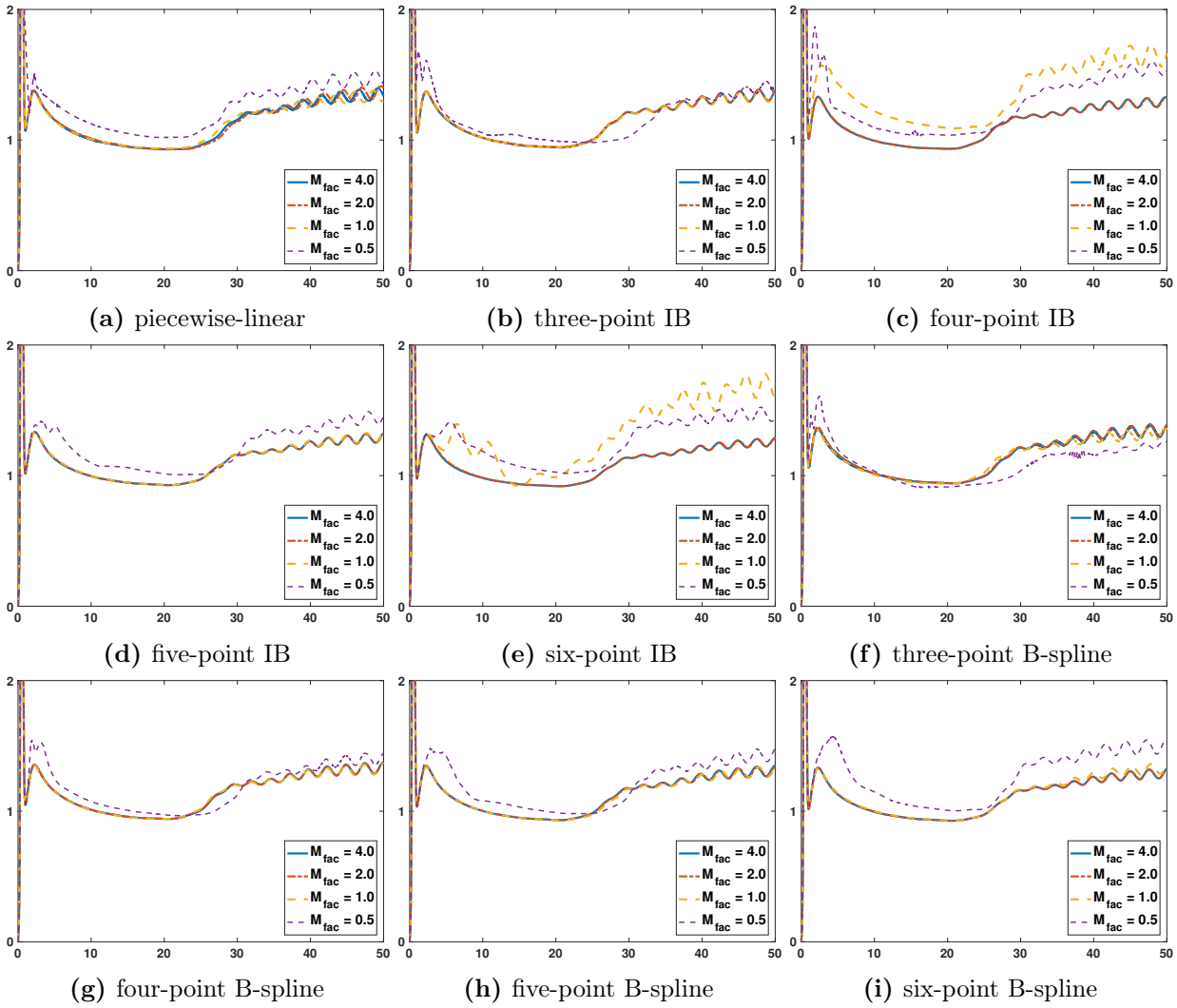


**(a)** piecewise-linear **(b)** three-point IB **(c)** four-point IB

**(d)** five-point IB **(e)** six-point IB **(f)** three-point B-spline

**(g)** four-point B-spline **(h)** five-point B-spline **(i)** six-point B-spline

**Figure 3.5:** Drag coefficients for $N = 32$, which is a very coarse grid, using different regularized delta function kernels.

$\chi = -\frac{\partial p}{\partial x} = \frac{2p_e}{L}$ is the applied pressure gradient, $\mu$ is the dynamic viscosity, $\nu = \mu/\rho$ is the kinematic viscosity, and $\rho$ is the density of the fluid. In our simulation, the domain we use is $L = 6D$ long and $H = 3D$ high, where $D$ is the selected length scale. Two parallel plates, each of which is $w = 0.24D$ thick, are located $D - w$ apart from each other and form a channel. See Figure 3.11a for a schematic of the setup for this benchmark. The two channel ends are prescribed with velocity boundary conditions using the analytic solution of the steady-state velocity (Eq. 3.7), and the remaining parts of the boundary are prescribed with zero-velocity boundary conditions. The channel walls are discretized using second-order triangular (P2) finite elements, where the spacing between the nodes

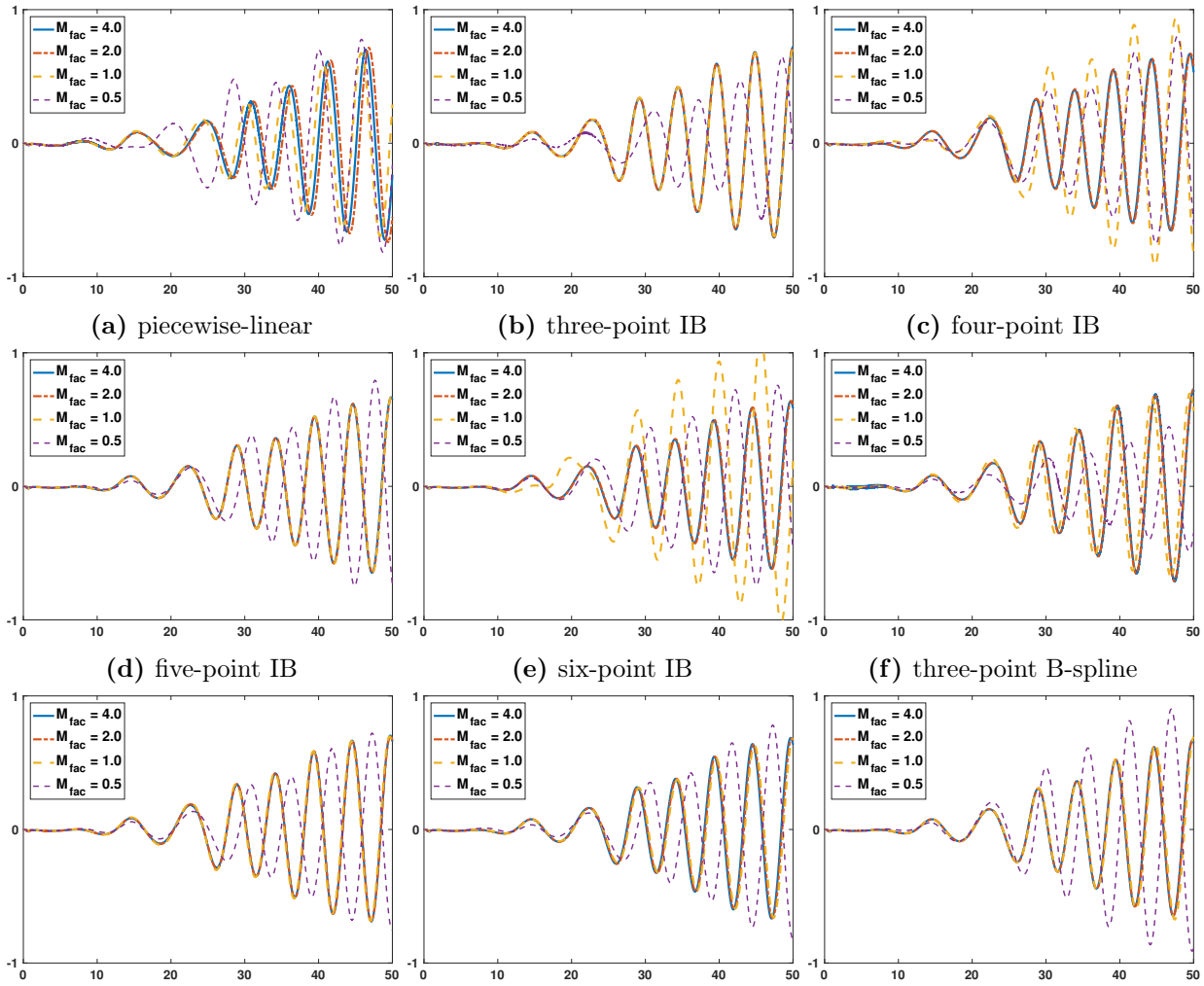


**(a)** piecewise-linear **(b)** three-point IB **(c)** four-point IB

**(d)** five-point IB **(e)** six-point IB **(f)** three-point B-spline

**(g)** four-point B-spline **(h)** five-point B-spline **(i)** six-point B-spline

**Figure 3.6:** Lift coefficients for $N = 32$, which is a very coarse grid, using different regularized delta function kernels.

on each element is set by $M_{\text{fac}} \cdot h$, in which $h$ is the background Eulerian mesh spacing. The goal of this benchmark is to test which kernel and $M_{\text{fac}}$ give the best accuracy for the flow field within a stationary geometry.

The channel walls are modeled as a stiff neo-Hookean material with

$$W_{\text{wall}} = \frac{c_{\text{wall}}}{2}(\bar{I}_1 - 3), \tag{3.8}$$

in which $\bar{I}_1$ is the modified first invariant of the right Cauchy-Green tensor $\bar{\mathbb{C}} = \bar{\mathbb{F}}^T\bar{\mathbb{F}} = J^{-\frac{2}{3}}\mathbb{F}^T\mathbb{F}$. Additional structural forces are included in the model to keep the channel walls tethered in place in

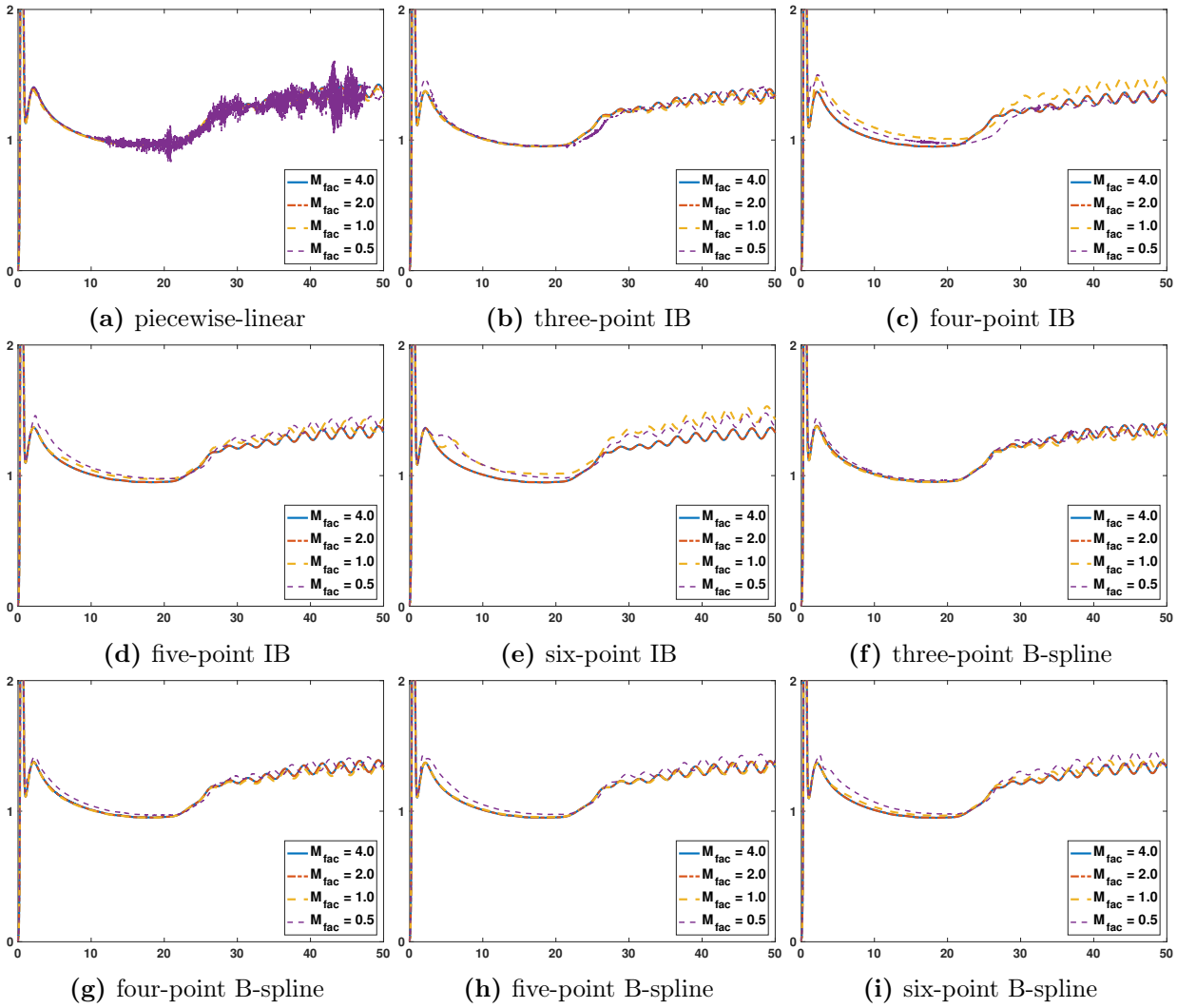


**(a)** piecewise-linear **(b)** three-point IB **(c)** four-point IB

**(d)** five-point IB **(e)** six-point IB **(f)** three-point B-spline

**(g)** four-point B-spline **(h)** five-point B-spline **(i)** six-point B-spline

**Figure 3.7:** Drag coefficients for $N = 64$ using different regularized delta function kernels.

our simulations,

$$\mathbf{F}(\mathbf{X}, t) = \kappa_{\text{wall}}(\mathbf{X} - \boldsymbol{\chi}(\mathbf{X}, t)) - \eta_{\text{wall}}\mathbf{u}(\boldsymbol{\chi}(\mathbf{X}, t), t). \tag{3.9}$$

Here, we use the stiff elasticity ($c_{\text{wall}} \propto h/\Delta t^2$), penalty body spring ($\kappa_{\text{wall}} \propto h/\Delta t^2$), and body damping ($\eta \propto \rho/\Delta t$) forces as well as fixing the edges at the boundary of the computational domain to have zero displacement. In our simulations we use $\mu = 0.01$, $\rho = 1.0$, and $D = 1$, and we define $\Delta t \propto \frac{\text{CFL}_{\max} \cdot h}{u_{\max}}$.

To approach more general case, we consider a slanted channel so that the structural meshes are not aligned background Cartesian mesh (Figure 3.11). This is done by transforming the channel

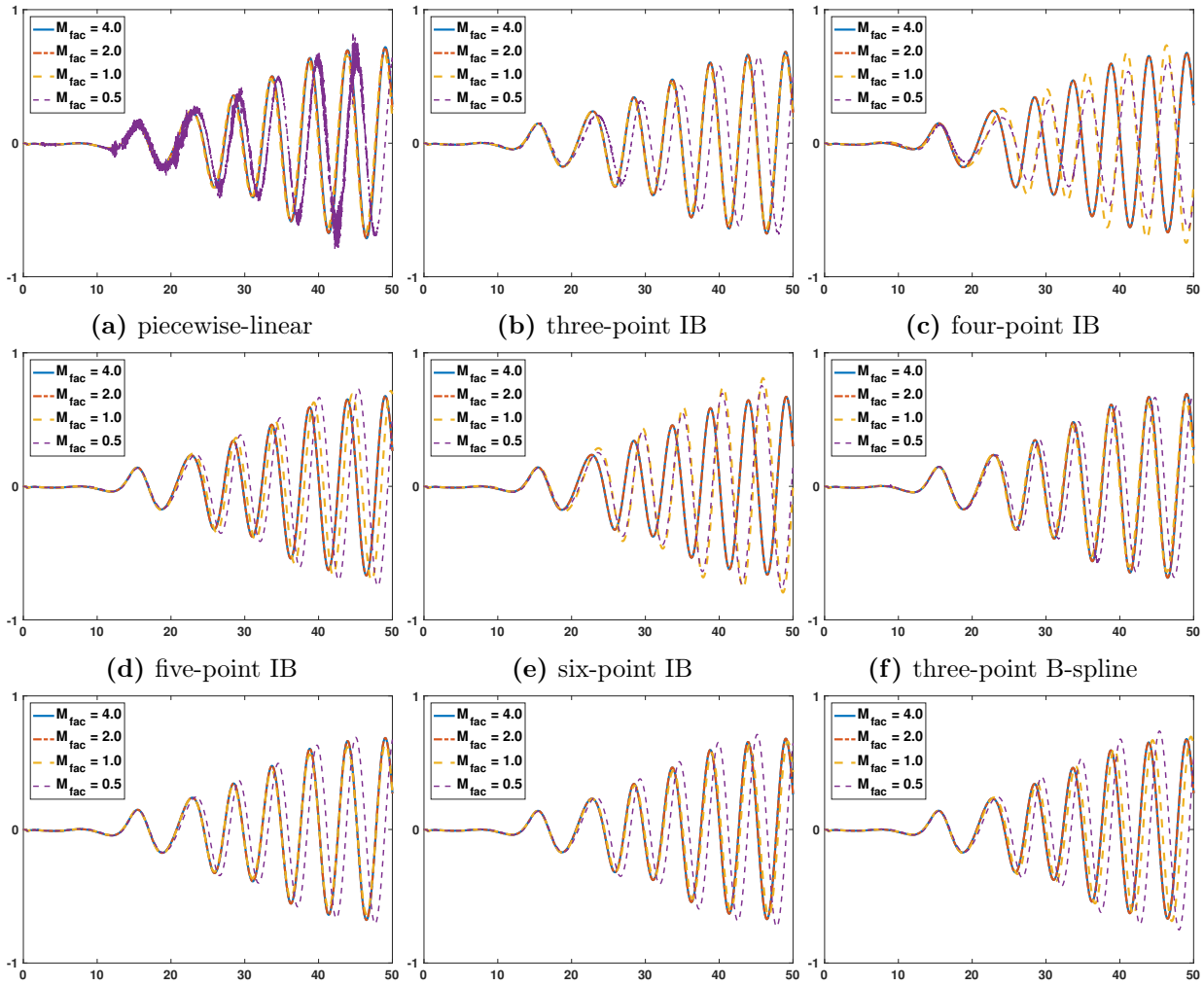


**(a)** piecewise-linear **(b)** three-point IB **(c)** four-point IB

**(d)** five-point IB **(e)** six-point IB **(f)** three-point B-spline

**(g)** four-point B-spline **(h)** five-point B-spline **(i)** six-point B-spline

**Figure 3.8:** Lift coefficients for $N = 64$ using different regularized delta function kernels.

walls so that the walls are rotated by an angle $\theta$, which means for every point on the walls $(x, y)$, we transform the $y$-coordinate to

$$y' = y + \left(x - \frac{L}{2}\right)\tan\theta, \tag{3.10}$$

and let $(x, y')$ be the new points for the walls. The steady-state solution (Figure 3.12) is also transformed to

$$u(\eta, t) = \frac{\chi'}{2\mu}(\eta(H - \eta)), \tag{3.11}$$

in which

$$\eta = -x\sin\theta + (y - y_0)\cos\theta, \tag{3.12}$$

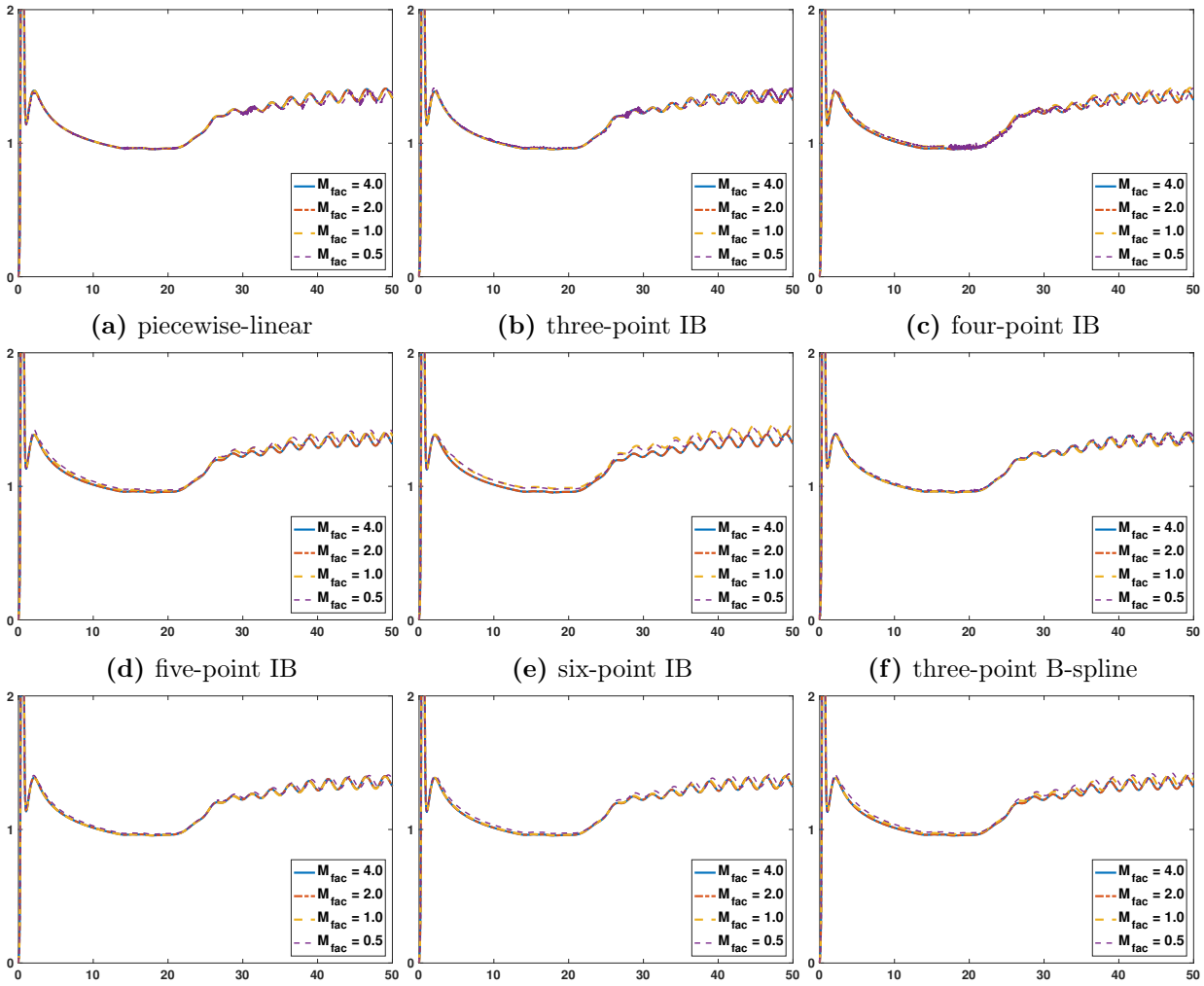


**(a)** piecewise-linear **(b)** three-point IB **(c)** four-point IB

**(d)** five-point IB **(e)** six-point IB **(f)** three-point B-spline

**(g)** four-point B-spline **(h)** five-point B-spline **(i)** six-point B-spline

**Figure 3.9:** Drag coefficients for $N = 128$ using different regularized delta function kernels.

and

$$\chi' = \frac{2p_e}{\frac{L}{\cos\theta} + H\tan\theta}. \tag{3.13}$$

Figure 3.13 shows the log-log plots of grid convergence study using different error norms for three kernels that yield the best accuracy for a fixed $M_{\text{fac}}$ value. This result indicate first-order convergence for velocity, and we can observe that using piecewise-linear kernel leads to smaller errors. Figure 3.14 shows the error plots in velocity for three kernels that yield the best accuracy for $M_{\text{fac}}$ = 1, 2, 3, and 4. In all cases, we observe the general trend that the cases with larger $M_{\text{fac}}$ values result in better accuracy, which means that the structural mesh should be relatively coarser than

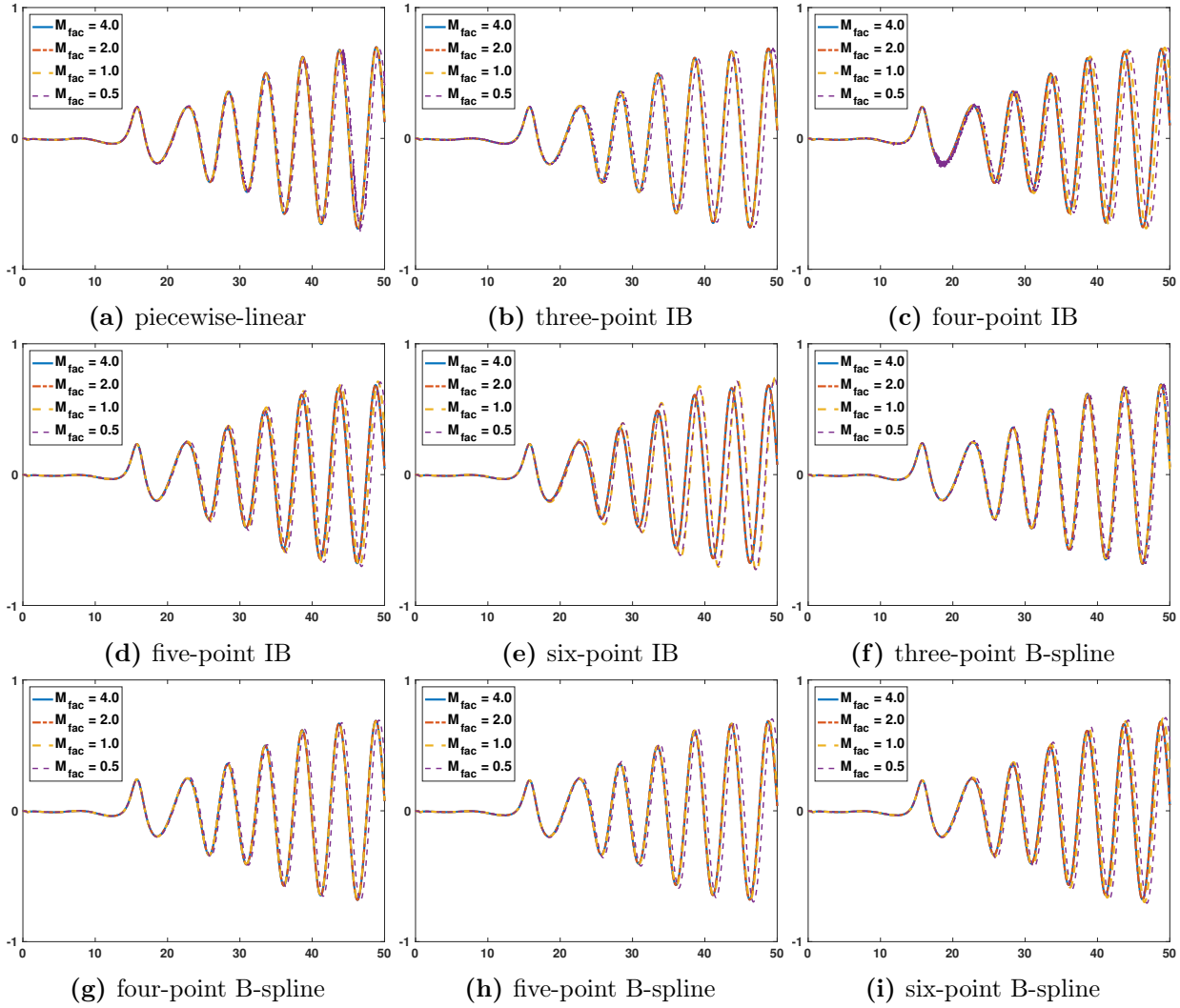


**(a)** piecewise-linear **(b)** three-point IB **(c)** four-point IB

**(d)** five-point IB **(e)** six-point IB **(f)** three-point B-spline

**(g)** four-point B-spline **(h)** five-point B-spline **(i)** six-point B-spline

**Figure 3.10:** Lift coefficients for $N = 128$ using different regularized delta function kernels.

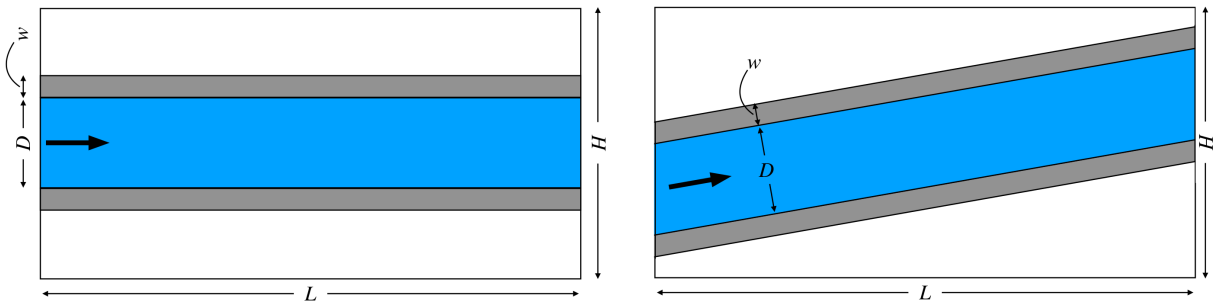


**(a)** **(b)**

**Figure 3.11:** Schematic of two-dimensional flow through a channel.

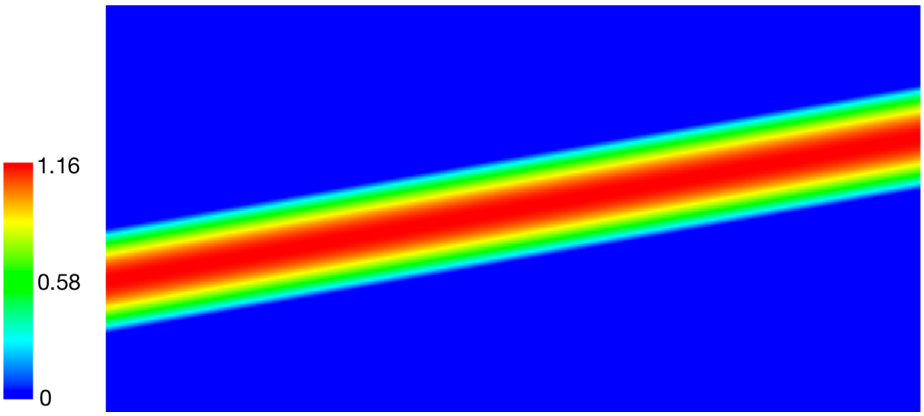


**Figure 3.12:** Representative steady-state velocity solution for the two-dimensional slanted channel flow benchmark. This simulation uses a three-level locally refined grid with a refinement ratio of two between levels and an $N \times N$ coarse grid with $N = 64$. The computation uses a piecewise-linear kernel and $M_{\text{fac}} = 4.0$.

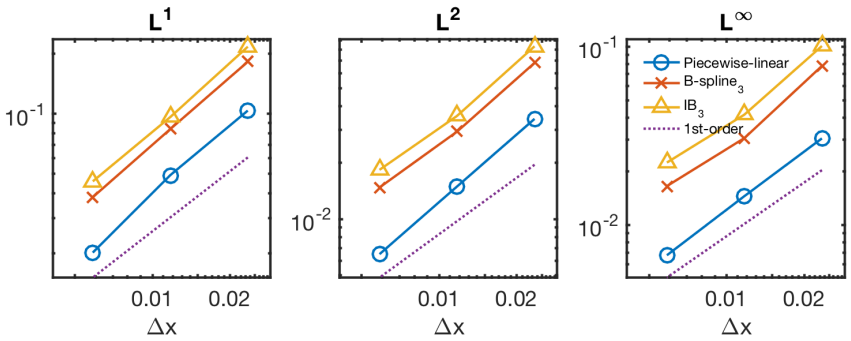


**Figure 3.13:** log-log plot of different error norms in velocity vs. finest Eulerian mesh width $\Delta x$ for the three best kernels with $M_{\text{fac}} = 3.0$. They all show first-order convergence for velocity. The piecewise-linear kernel shows the smallest errors.

the finest background Cartesian grids. We can conclude from these results that using a relatively coarser structural mesh with piecewise-linear kernel yield the best accuracy for simulating internal flow within a stationary geometry.

## 3.5 Turek-Hron benchmark

Next we consider Turek and Hron's FSI benchmark problem that considers the flow around an elastic beam attached to a circular cylinder [58]. Figure 3.15 shows a schematic of the setup for this benchmark, but briefly the domain dimensions are $L = 2.5$ by $H = 0.41$. The circular cylinder is located at $(0.2, 0.2)$ with radius $r = 0.05$. The elastic beam has length $l = 0.35$ and height $h = 0.02$. The left end of the beam is fixed at the cylinder, which is stationary. We look at the position of the control point $A$ as a function of time, whose initial position is at $A(0) = (0.6, 0.2)$. The boundary

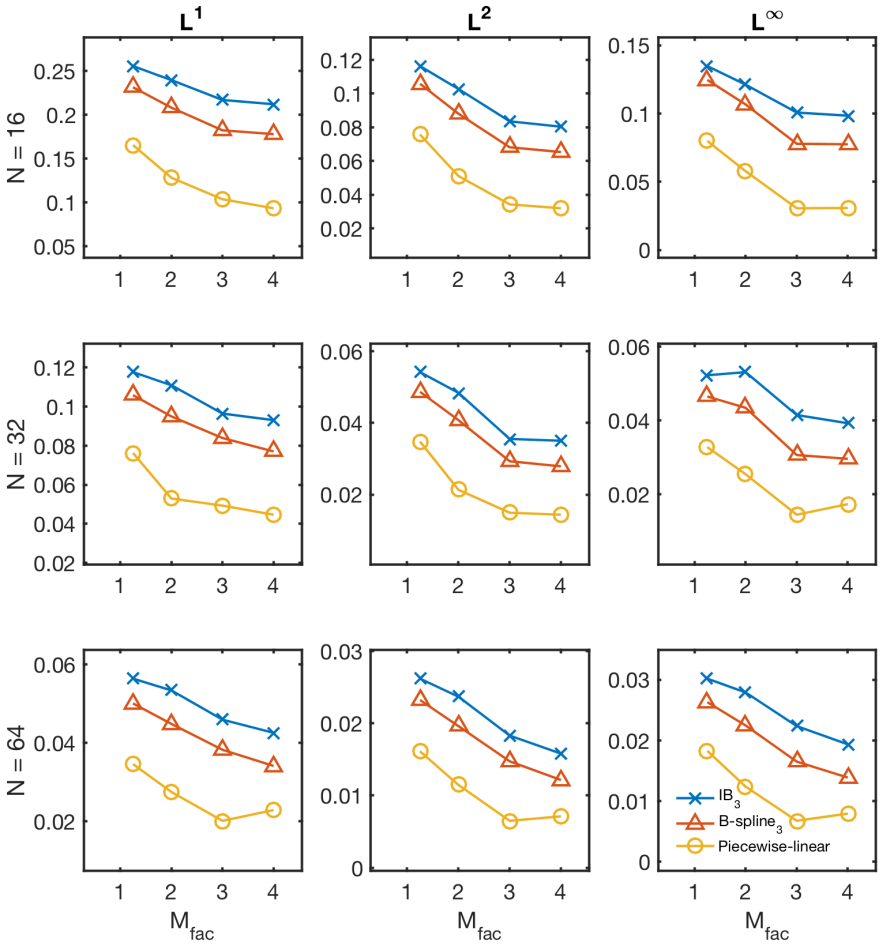


**Figure 3.14:** Plot of the error norms in velocity vs. $M_{\text{fac}}$ for the three best kernels. It shows that the structural mesh should be relatively coarser than the finest background Cartesian grids.

conditions are

$$u(0, y) = 1.5\overline{U}\frac{y(H-y)}{(H/2)^2} \tag{3.14}$$

for $x = 0$, zero normal traction and zero tangential velocity conditions for $x = L$, and zero velocity condition for $y = 0$ and $y = H$. Note that for the actual simulation we use $L = 2.46 = 6.0H$ for the domain to obtain square Cartesian grid cells, but this change is small enough to affect the results. Note that without the elastic beam structure, this problem reduces to a version of the flow past a cylinder problem. We know from the previous study in Section 3.3 that the three-point B-spline kernel with relative coarser mesh for the cylinder gives better accuracy for our staggered-grid discretization [34]. Consequently, here we use the three-point B-spline kernel with $M_{\text{fac}} = 2.0$ for the cylinder mesh. Also note that the immersed body is located slightly asymmetrically in the

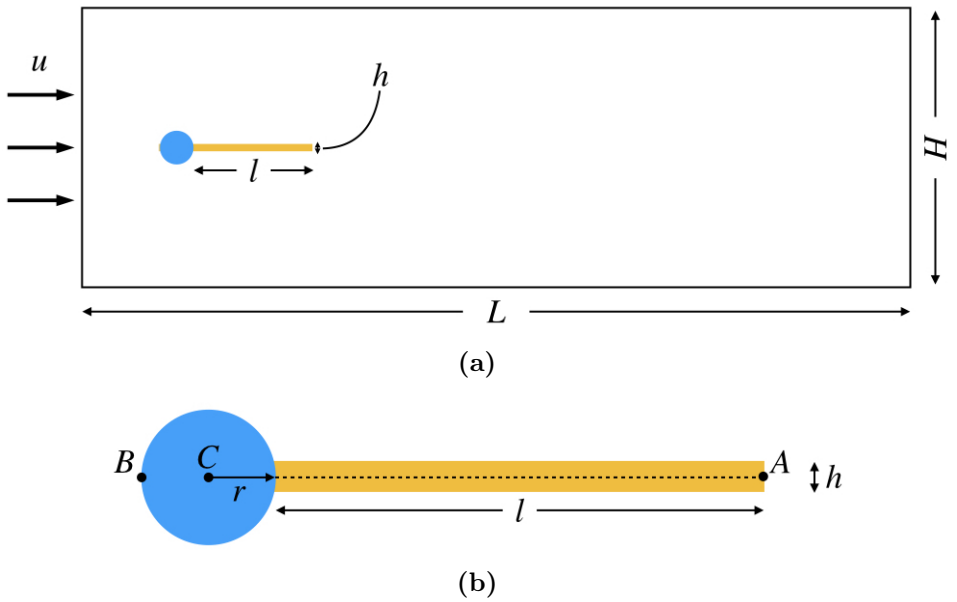


**Figure 3.15:** (a) Schematic of Turek-Hron benchmark [58]. (b) Detail of the immersed cylinder and elastic beam.

$y$-direction to set off motion for the elastic beam.

In Turek and Hron's original paper [58], the compressible St. Venant-Kirchhoff model is used for the elastic beam, which corresponds to the strain energy density functional

$$\Psi_{\mathrm{SVK}} = \frac{1}{2}\lambda_{\mathrm{s}}(\mathrm{tr}\mathbb{E})^2 + \mu_{\mathrm{s}}\mathrm{tr}(\mathbb{E}^2) + \beta(J\ln J - J + 1), \tag{3.15}$$

in which $\mathbb{E} = \frac{1}{2}(\mathbb{F}^T\mathbb{F} - \mathbb{I})$ is the Green-Lagrange strain tensor, and $\lambda_{\mathrm{s}}$ and $\mu_{\mathrm{s}}$ are Lamé parameters. Note that our numerical framework enforces incompressibility on both solid and fluid by formulation, so we cannot model the elastic beam as a compressible material. Previous work by Roy et al. [59] reports results by modeling the elastic beam as compressible material within the immersed finite element framework that show excellent agreement with the original results by Turek and Hron [58]. Therefore, we compare our results from modeling the elastic solid beam as an incompressible St. Venant–Kirchhoff material to the results from Roy et al. to ensure that we obtain reasonable agreements before we proceed to further studies. Figure 3.16 shows the $x$- and $y$-displacements of the control point $A(t)$ as functions of time using the three-point B-spline kernel with an $M_{\mathrm{fac}} = 2.0$. We observe comparable agreement with the results from Turek and Hron [58] and Roy et al. [59],

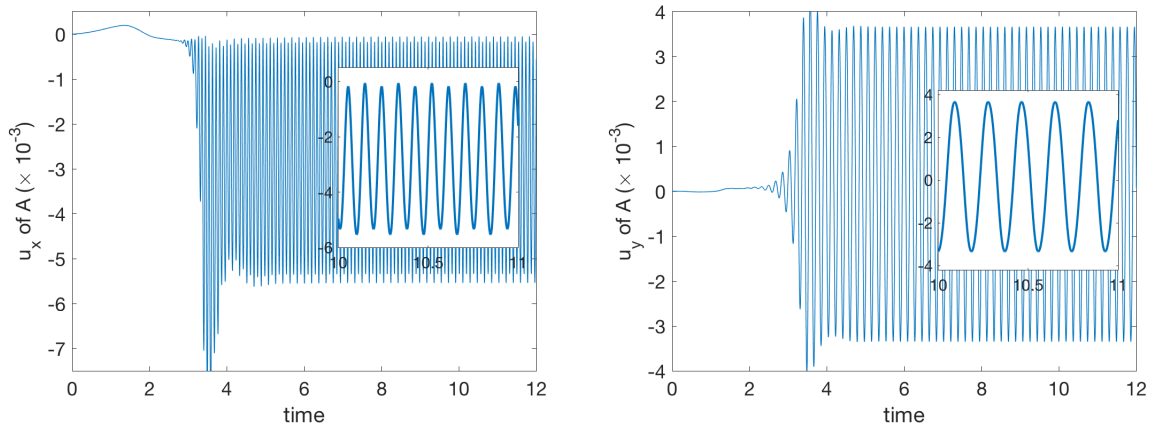


**(a)** $x(t)$ of the control point $A(t)$




**(b)** $y(t)$ of the control point $A(t)$

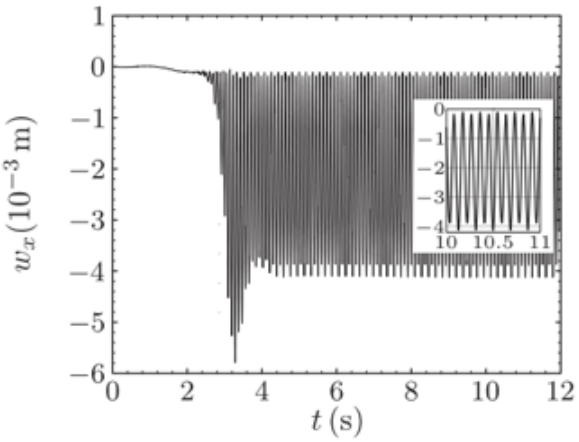


**(c)** $x(t)$ of the control point $A(t)$ (Roy et al.)

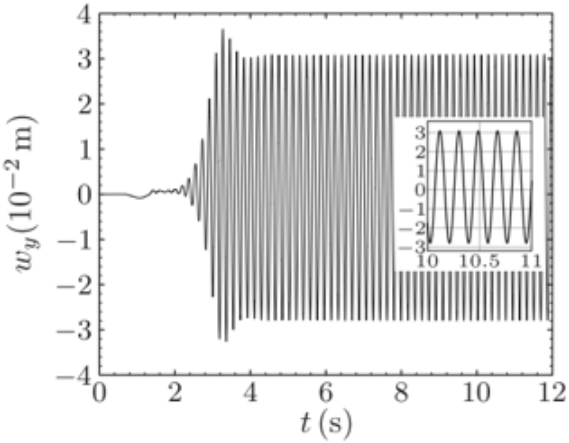


**(d)** $y(t)$ of the control point $A(t)$ (Roy et al.)

**Figure 3.16:** Representative result using St. Venant-Kirchhoff model. This computation uses a three-level locally refined grid with a refinement ratio of two between levels and an $N \times N$ coarse grid with $N = 32$. The three-point B-spline kernel with $M_{\text{fac}} = 2.0$ is used. (a) $x$- and (b) $y$-displacements of the point $A$. (c) and (d) are results from Roy et al. [59] using fully compressible model for the elastic beam.

which suggests that the incompressibility assumption of the flexible beam can be reasonably used to obtain results for the purpose of this study.

In most of our applications, we use incompressible hyperelastic materials, and from herein we consider a neo-Hookean material model to investigate the effect of various choices of $M_{\text{fac}}$ and kernel functions. For an incompressible neo-Hookean material, we define its strain energy functional as

$$W_{\text{NH}} = \frac{1}{2}\mu_{\text{s}}(\bar{I}_1 - 3), \tag{3.16}$$

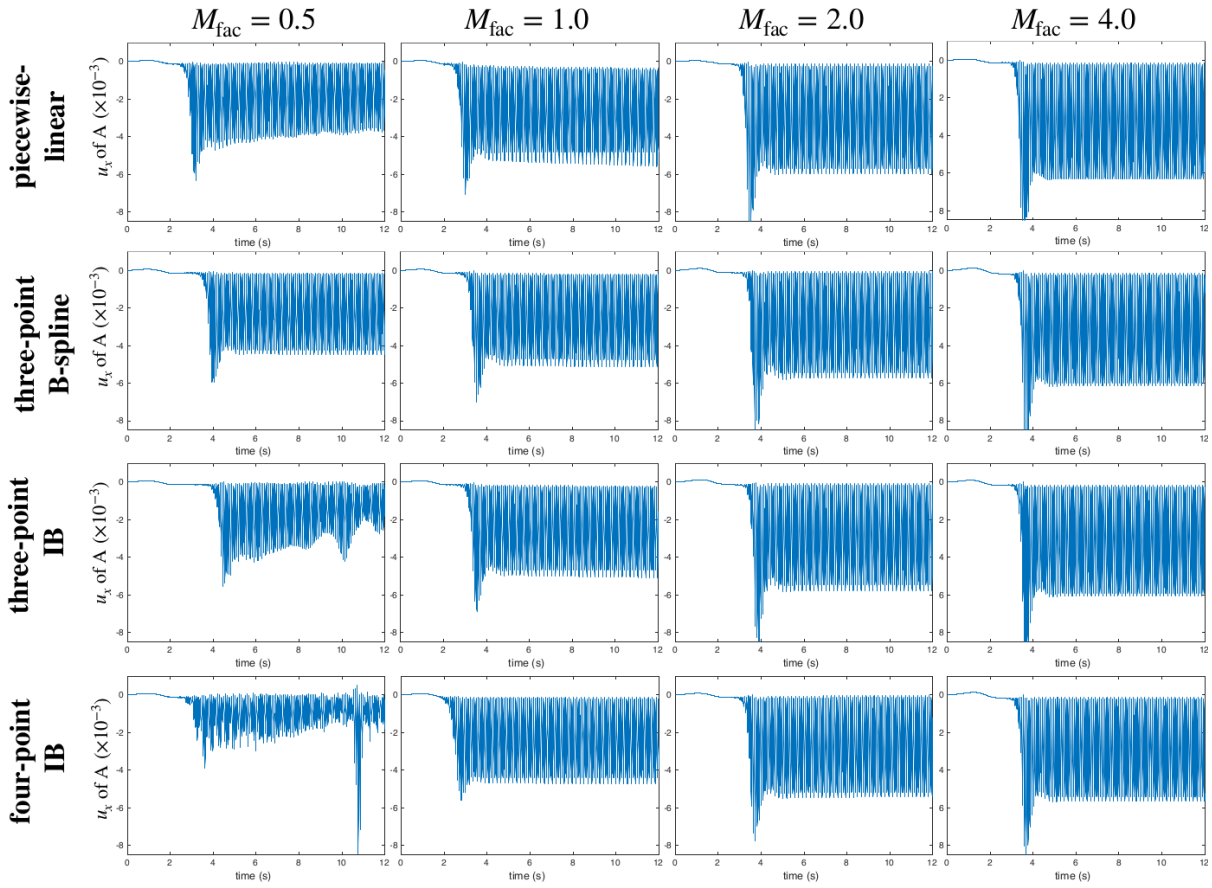


**Figure 3.17:** $x$-displacement ($u_x$) of the point $A$ for different values of $M_{\text{fac}}$ for the neo-Hookean model using different kernels $N = 32$.

in which $\mu_{\text{s}}$ is the shear modulus.

Figures 3.17 and 3.18 show comparisons for some of the representative kernels with $M_{\text{fac}} = 0.5$, 1, 2, and 4 that were used in previous sections. It is clear that the three-point B-spline kernel is less sensitive to changes in $M_{\text{fac}}$, whereas other kernels show clear loss of accuracy with as we refine the Lagrangian mesh for a fixed Eulerian grid. Table 3.1 reports the average and amplitude of the $x$- and $y$-displacements ($u_x(A)$ and $u_y(A)$) of the point $A$, as well as the Strouhal numbers ($St_x$ and $St_y$) to quantify the oscillations of $u_x(A)$ and $u_y(A)$. The three-point B-spline kernel shows the most consistent results for different values of $M_{\text{fac}}$, especially for $M_{\text{fac}} = 0.5$. These results agree with the previous results from Section 3.3, which suggest that the three-point B-spline kernel is relatively less sensitive to the relative mesh spacing with respect to the Eulerian grid spacing. Section B of the Appendix shows results for other IB and B-spline kernels.

Figures 3.19 and 3.20 show comparisons for the three-point B-spline kernel for $M_{\text{fac}} = 0.5, 1, 2,$

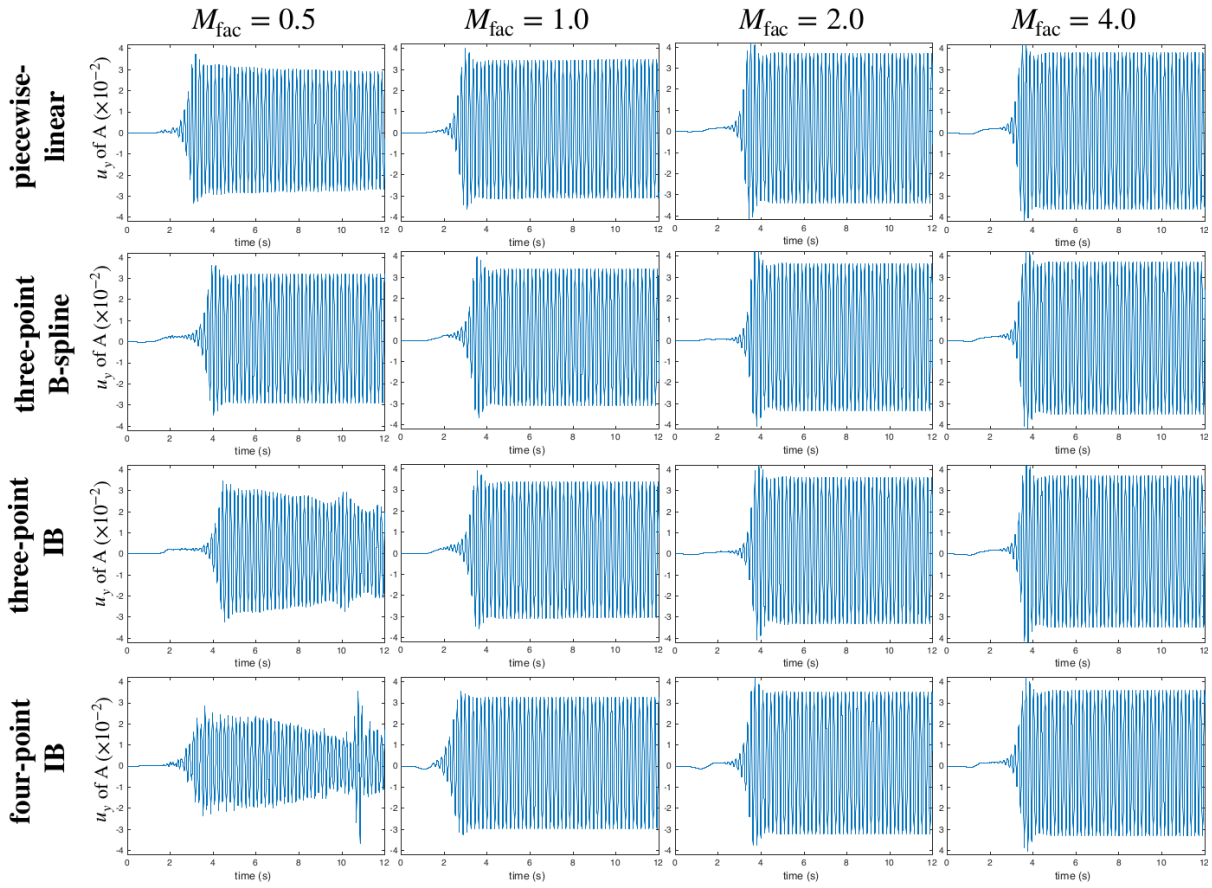


**Figure 3.18:** $y$-displacement ($u_y$) of the point $A$ for different values of $M_{\text{fac}}$ for the neo-Hookean model using different kernels $N = 32$.

and 4 under grid refinement. We observe that $N = 16$ cases are under-resolved, but $N = 32$ and $N = 64$ cases are consistent. Table 3.2 also shows that we obtain comparable results under grid refinement, which are more consistent between different $M_{\text{fac}}$ values as we refined the resolution.

## 3.6 Two-dimensional pressurized channel

So far, Sections 3.3, 3.4, and 3.5 suggest that for any choice of kernels, larger $M_{\text{fac}}$ values generally give higher accuracy without requiring high fluid resolutions. Although this seems to give a rather simple solution to use a structural mesh that is relatively coarser than the Eulerian grid. However, these sections are examples of shear-dominant flows, and it is important to show if the same results hold for pressure-dominant problems that are commonly encountered in biological and biomedical applications. In this section, we look at the pressurized channel (Figure 3.21) to see if this holds for pressure dominant problem, which is relevant in simulating heart valve dynamics [19]. The channel model is adopted from Section 3.4, but here we switch the boundary conditions to pressurize the

| | $M_{\text{fac}}$ | $u_x(A)$ ($\times 10^{-3}$) | $u_y(A)$ ($\times 10^{-3}$) | $St_x$ | $St_y$ |
|---|---|---|---|---|---|
| Piecewise-linear | 0.5 | -2.04 ± 2.01 | 1.20 ± 29.0 | 11.06 | 5.52 |
| | 1.0 | -2.93 ± 2.64 | 1.83 ± 32.9 | 10.99 | 5.50 |
| | 2.0 | -3.05 ± 2.91 | 1.61 ± 35.6 | 10.92 | 5.46 |
| | 4.0 | -3.24 ± 3.08 | 0.97 ± 37.1 | 11.19 | 5.59 |
| B-spline (3-point) | 0.5 | -2.31 ± 2.17 | 1.47 ± 30.6 | 10.93 | 5.46 |
| | 1.0 | -2.65 ± 2.47 | 1.67 ± 32.4 | 10.94 | 5.47 |
| | 2.0 | -2.89 ± 2.84 | 1.56 ± 34.9 | 10.93 | 5.46 |
| | 4.0 | -3.16 ± 3.00 | 1.24 ± 36.1 | 11.25 | 5.52 |
| IB (3-point) | 0.5 | -2.09 ± 2.11 | 1.01 ± 28.4 | 11.18 | 5.57 |
| | 1.0 | -2.64 ± 2.45 | 1.58 ± 32.3 | 10.94 | 5.47 |
| | 2.0 | -2.93 ± 2.84 | 1.56 ± 34.9 | 10.93 | 5.47 |
| | 4.0 | -3.12 ± 2.96 | 1.22 ± 35.9 | 11.25 | 5.63 |
| IB (4-point) | 0.5 | -3.98 ± 4.48 | -0.68 ± 36.2 | 20.27 | 6.15 |
| | 1.0 | -2.42 ± 2.30 | 1.45 ± 31.3 | 10.85 | 5.43 |
| | 2.0 | -2.74 ± 2.70 | 1.52 ± 33.8 | 10.92 | 5.46 |
| | 4.0 | -2.90 ± 2.77 | 1.41 ± 34.4 | 11.31 | 5.65 |
| **Turek and Hron [58]** | | -2.69 ± 2.53 | 1.48 ± 34.4 | 10.9 | 5.3 |

**Table 3.1:** Results for the neo-Hookean model using four representative kernels with various values of $M_{\text{fac}}$. $N = 32$ is the number of grid cells on coarsest grid level, $u_x(A)$ and $u_y(A)$ are $x$-, $y$-displacements of the point $A$, and $St_x$ and $St_y$ are Strouhal numbers for the oscillations of $u_x(A)$ and $u_y(A)$.

channel so that the pressure inside the channel is $p = 10$ and there is no flow. The effective shape of the kernel function changes near the boundary of the computational domain. So we avoid issues that may arise from using a finer structural mesh ($M_{\text{fac}} = 0.5$) at the boundary and $M_{\text{fac}} = 0.5$, 1, 2, and 4 away from the boundary. We observe in Figure 3.22 that if the structural mesh is coarser ($M_{\text{fac}} > 1$) than the finest background Cartesian grids, then the channel leaks.

## 3.7 Discussion

This study is an extension of work by Griffith and Luo [34] to explore various choices of regularized delta functions to approximate the integral transforms (Eq. (2.35) and (2.36)) in the immersed finite element method. We also investigate the effect of relative structural mesh spacing for different kernels on the accuracy using standard FSI benchmark studies. We use standard FSI benchmarks, and the

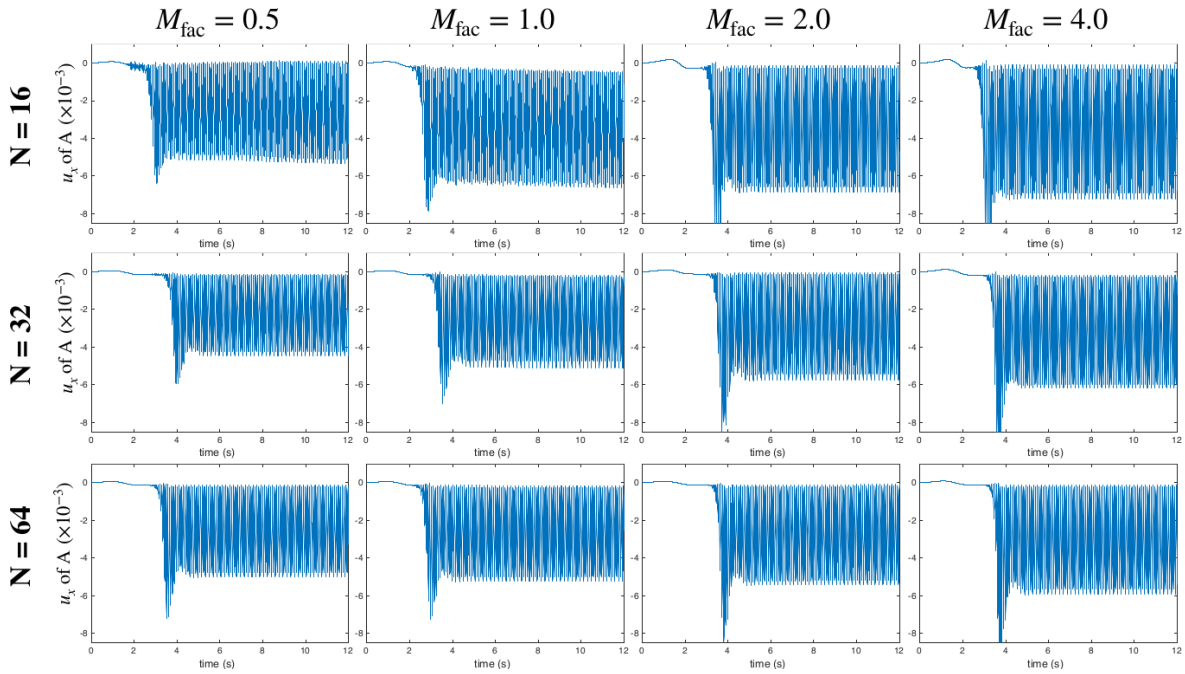


**Figure 3.19:** $x$-displacement ($u_x$) of the point $A$ for different values of $M_{\text{fac}}$ for the neo-Hookean model using three-point B-spline kernel under grid refinement.

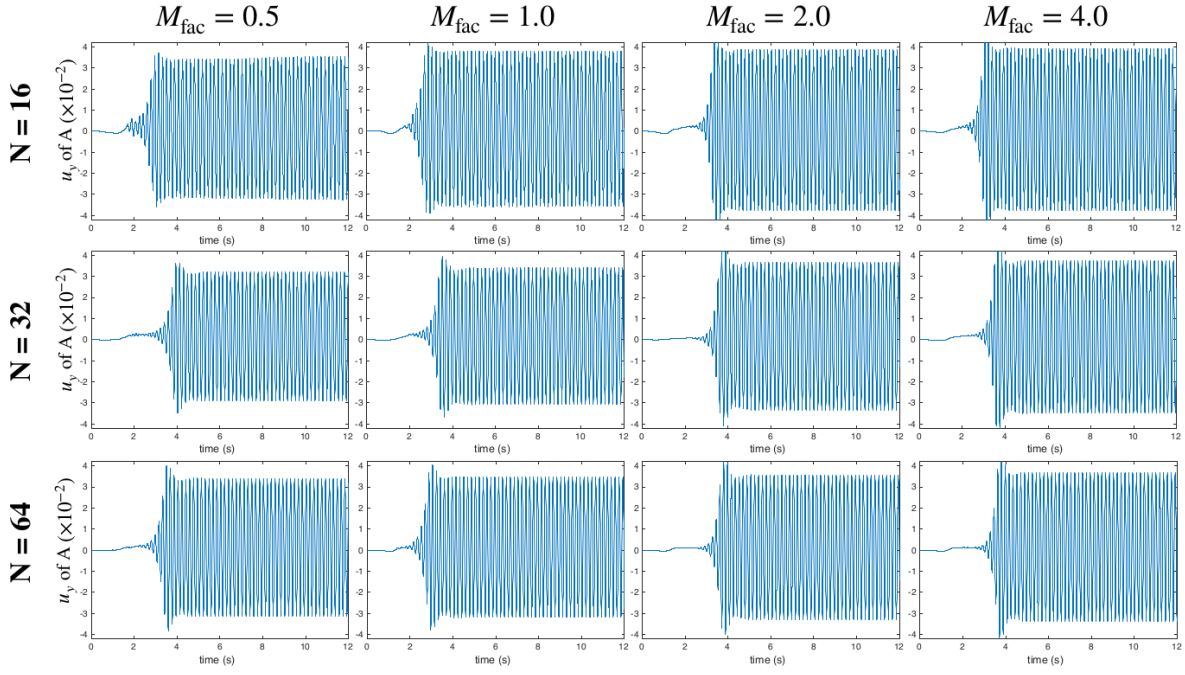


**Figure 3.20:** $y$-displacement ($u_y$) of the point $A$ for different values of $M_{\text{fac}}$ for the neo-Hookean model using three-point B-spline kernel under grid refinement.

results in Sections 3.3, 3.4, and 3.5 show that we obtain better accuracy for these shear-dominant cases by using relatively coarser Lagrangian nodal spacing compared to the background Cartesian

| | $N$ | $M_{\text{fac}}$ | $u_x(A)$ ($\times 10^{-3}$) | $u_y(A)$ ($\times 10^{-3}$) | $St_x$ | $St_y$ |
|---|---|---|---|---|---|---|
| B-spline (3-point) | 16 | 0.5 | -2.61 ± 2.73 | 1.41 ± 33.9 | 10.87 | 5.43 |
| | | 1.0 | -3.48 ± 3.14 | 1.13 ± 36.9 | 10.90 | 5.45 |
| | | 2.0 | -3.49 ± 3.35 | 0.56 ± 38.1 | 11.28 | 5.64 |
| | | 4.0 | -3.66 ± 3.55 | 0.91 ± 38.4 | 11.39 | 5.70 |
| | 32 | 0.5 | -2.31 ± 2.17 | 1.47 ± 30.6 | 10.93 | 5.46 |
| | | 1.0 | -2.65 ± 2.47 | 1.67 ± 32.4 | 10.94 | 5.47 |
| | | 2.0 | -2.89 ± 2.84 | 1.56 ± 34.9 | 10.93 | 5.46 |
| | | 4.0 | -3.16 ± 3.00 | 1.24 ± 36.1 | 11.25 | 5.52 |
| | 64 | 0.5 | -2.57 ± 2.43 | 1.41 ± 32.7 | 11.05 | 5.52 |
| | | 1.0 | -2.70 ± 2.55 | 1.44 ± 33.4 | 11.05 | 5.52 |
| | | 2.0 | -2.75 ± 2.66 | 1.41 ± 34.2 | 11.05 | 5.53 |
| | | 4.0 | -3.03 ± 2.88 | 1.49 ± 35.3 | 11.10 | 5.55 |
| **Turek and Hron [58]** | | | -2.69 ± 2.53 | 1.48 ± 34.4 | 10.9 | 5.3 |

**Table 3.2:** Results for the neo-Hookean model using three-point B-spline kernel with various values of $M_{\text{fac}}$ under different grid resolutions. $N$ is the number of grid cells on coarsest grid level, $u_x(A)$ and $u_y(A)$ are $x$-, $y$-displacements of the point $A$, and $St_x$ and $St_y$ are Strouhal numbers for the oscillations of $u_x(A)$ and $u_y(A)$.

grid spacing ($M_{\text{fac}} > 1$). However, in the pressure-loaded case considered in Section 3.6, we observe that our mesh needs to be similar or relatively finer compared to the Cartesian grids ($M_{\text{fac}} \leq 1$). This is in contrast to the results from all of the previous benchmark studies, which show improved accuracy when the structural mesh is relatively coarser than the Cartesian grids. In fact, it is more common in simulations using complex geometries to have many mesh elements that are similar or even relatively finer compared to the background Cartesian grid. Taken together, our results suggest that the three-point B-spline kernel is the best overall choice considering both shear- and pressure-dominant flows because it is less sensitive to the relative structural mesh spacing.

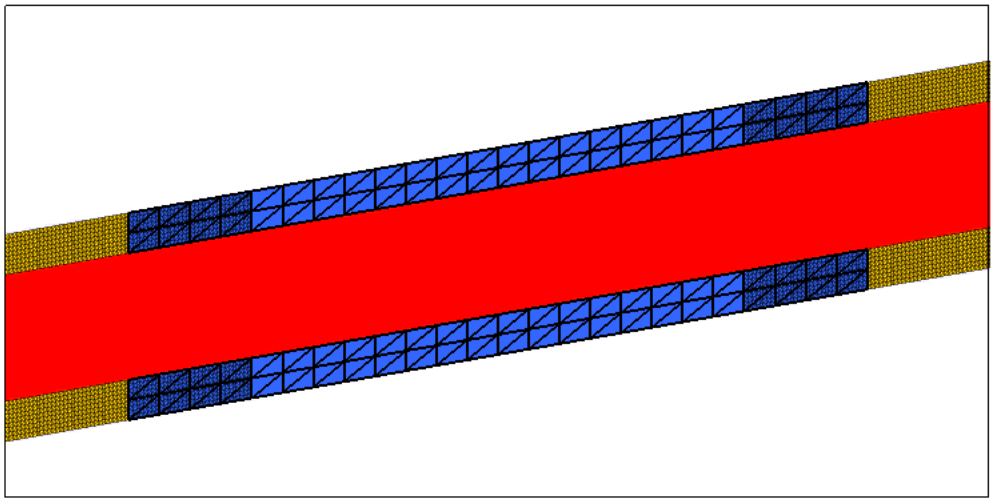

**Figure 3.21:** Schematic of two-dimensional flow through a channel adopted from Section 3.4. We switch the boundary conditions to pressurize the channel so that the pressure inside the channel is $p = 10$ and there is no flow. The effective shape of the kernel function changes near the boundary of the computational domain. So we avoid issues that may arise from using a finer structural mesh ($M_{\text{fac}} = 0.5$) at the boundary and $M_{\text{fac}} = 0.5$, 1, 2, and 4 away from the boundary. In this figure, $M_{\text{fac}} = 4$ away from the boundary.

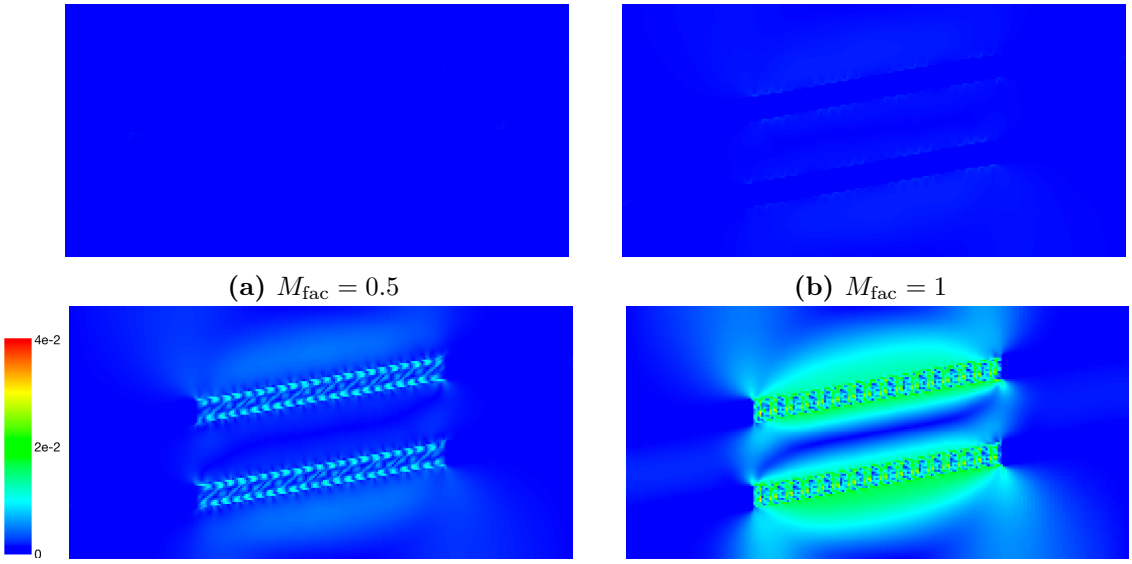


**(a)** $M_{\text{fac}} = 0.5$ **(b)** $M_{\text{fac}} = 1$

**(c)** $M_{\text{fac}} = 2$ **(d)** $M_{\text{fac}} = 4$

**Figure 3.22:** Comparison of velocity fields from the pressurized two-dimensional channel benchmark for $M_{\text{fac}} = 0.5$, 1, 2, and 4. The simulations use a three-level locally refined grid with a refinement ratio of two between levels and an $N \times N$ coarse grid with $N = 32$. The pressure inside the channel is $p = 10$. B-spline kernel is used for this figure, but we observe the similar results with other kernels. If the structural mesh is relatively coarser ($M_{\text{fac}} > 1$) than the finest background Cartesian grids, then we obtain low accuracy for simulating pressurized channel.

CHAPTER 4

# IN VITRO LEFT VENTRICLE MODEL

## 4.1 Background

Left ventricle (LV) function can be characterized in part by intraventricular flow, including its vortical dynamics [60]. Computer modeling and simulation (CM&S) can potentially help understand different intraventricular flow patterns and change the focus from diagnosis to prediction of cardiac diseases such as heart failure. There is also an evidence that fluid shear stress and pressure may play a role in embryonic heart development [61], and CM&S can help quantify and analyze such data that are difficult to acquire on the bench. However, substantial experimental and clinical validation is required before such models can be widely deployed. We leverage an in vitro model of the LV in a flow circuit, which provides physiological pulsatile flow, to validate an FSI model of the intraventricular flow of the LV. A key benefit of using an in vitro model for initial validation is that it provides a known geometry and facilitates quantitative measurements such as flow field quantification using particle image velocimetry (PIV). A high-speed two-dimensional PIV system provides instantaneous and time-averaged flow data that we can use to compare the intraventricular flow patterns generated by the simulation to those from an experiment.

Experimentally validated computational models of cardiac fluid dynamics, mechanics, and FSI are crucial in enhancing patient treatment planning and medical device design because intraventricular fluid dynamics can characterize cardiac health and disease. To accurately capture the intraventricular fluid dynamics, we need to include the valve model to the system. However, three-dimensional FSI simulations of the valves substantially slows down the overall computation. As a first step, we implement a reduced-order lumped-element type description of the valves at the inflow and outflow boundaries as well as the rest of the flow loop system to reduce the computation time while still capturing the intraventricular fluid dynamics of the ventricle model.

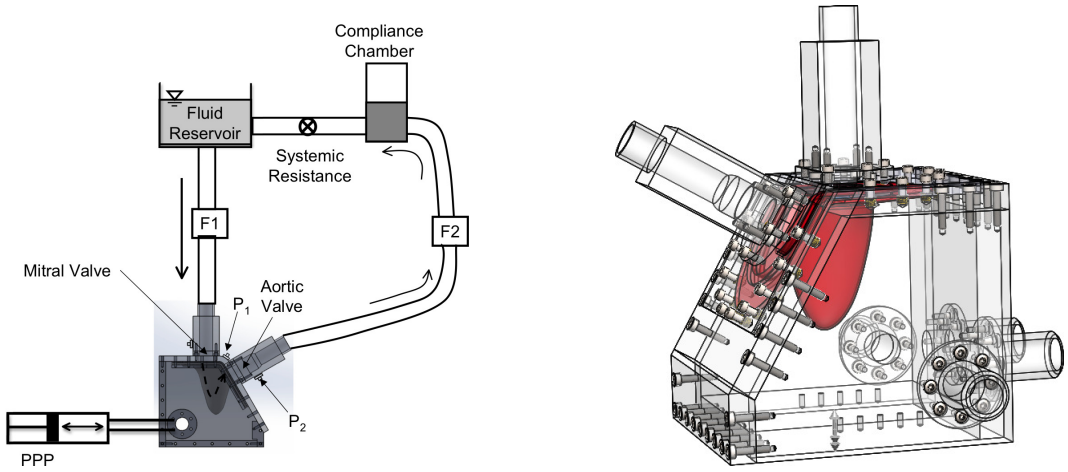


**Figure 4.1:** In vitro experimental flow circuit that provides physiological pulsatile flow through the left ventricle (LV) phantom. (a) Schematic of the flow loop. PPP: programmable piston pump; P1 & P2: pressure transducers; F1 & F2: ultrasonic flow meters. (b) 3D rendering of the LV phantom and the flow circuit system. Images from Dr. Arvind Santhanakrishnan, Oklahoma State University, Stillwater, OK, USA.

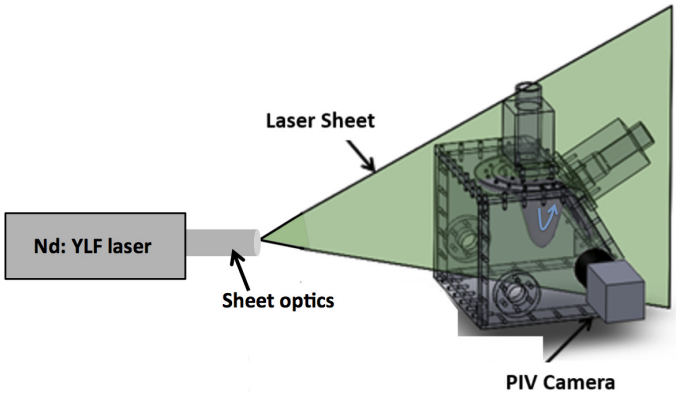


**Figure 4.2:** Particle image velocimetry (PIV) setup for intraventricular flow studies. The flow field along the central left ventricle plane is visualized using a green laser sheet. Image from Dr. Arvind Santhanakrishnan, Oklahoma State University, Stillwater, OK, USA.

## 4.2 Methods

### 4.2.1 Experimental setup

An in vitro flow circuit that is used by Santhanakrishnan group at Oklahoma State University provides physiological pulsatile flow through an optically clear, flexible LV phantom (Figure 4.1). A high-speed two-dimensional PIV system provides instantaneous and time-averaged flow data (Figure 4.2).

### 4.2.2 Constitutive model

In this study, we model the LV phantom as an exponential neo-Hookean material, with the strain-energy density functional,

$$\Psi_{\mathrm{LV}}(\mathbb{F}) = W_{\mathrm{LV}}(\overline{\mathbb{F}}) + U(J), \tag{4.1}$$

with

$$W_{\mathrm{LV}} = \frac{a}{2b} e^{b(\bar{I}_1 - 3)}, \tag{4.2}$$

$$U(J) = \beta(J \ln J - J + 1), \tag{4.3}$$

in which $\overline{\mathbb{F}} = J^{-1/3}\mathbb{F}$, $\bar{I}_1 = \mathrm{tr}(\overline{\mathbb{C}}) = \mathrm{tr}(\overline{\mathbb{F}}^T\overline{\mathbb{F}})$ is the modified first invariant of $\overline{\mathbb{C}}$, the modified right Cauchy-Green strain tensor, and $J = \det \mathbb{F}$. The first Piola-Kirchhoff stress is

$$\mathbb{P} = \frac{\partial \Psi_{\mathrm{LV}}}{\partial \mathbb{F}}. \tag{4.4}$$

We use COMSOL Multiphysics software (COMSOL, Inc., Burlington, MA, USA) to simulate quasi-static deformation of the LV phantom under a systematically incremented pressure load. We measure the internal volume at each pressure value to obtain the compliances of our model and compare with the compliances of the experimental apparatus (Figure 4.3). From this comparison, we empirically determine the coefficients of our constitutive model to be $a = 27.7$ kPa and $b = 1.05$.

### 4.2.3 Housing model

The hosing structure that the LV phantom is mounted on is modeled as a rigid structure. We use a penalty method to model the housing structure as a stiff neo-Hookean material with

$$W_{\mathrm{housing}} = \frac{c_{\mathrm{housing}}}{2}(\bar{I}_1 - 3), \tag{4.5}$$

and keep the housing structure fixed in place with additional penalty forces,

$$\mathbf{F}(\mathbf{X}, t) = \kappa_{\mathrm{housing}}(\mathbf{X} - \boldsymbol{\chi}(\mathbf{X}, t)), \tag{4.6}$$

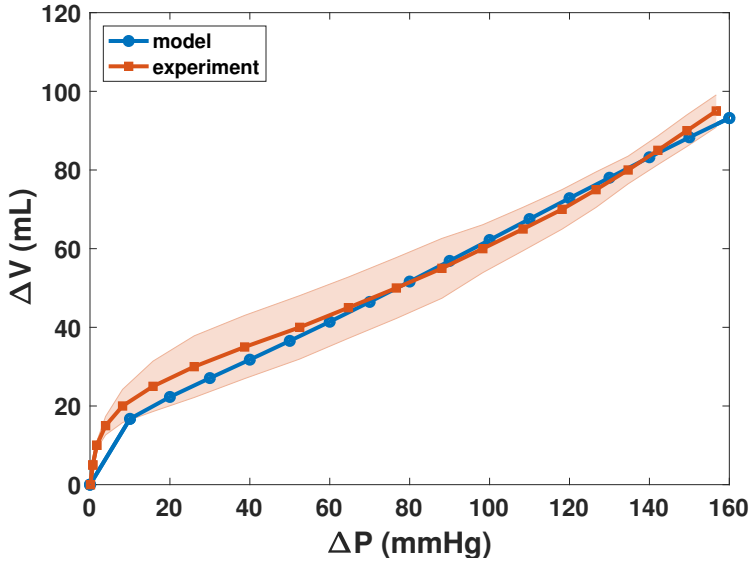


**Figure 4.3:** Comparison of the compliances between the experimental apparatus and the exponential neo-Hookean model with $a = 27.7$ kPa and $b = 1.05$. Shaded region shows where 95% of the experimental data fall.

in which $c_{\text{housing}} = 0.67$ MPa and $\kappa_{\text{housing}} = 8.13$ kPa cm$^{-2}$.

### 4.2.4 Fluid model and boundary conditions

We use the incompressible Navier-Stokes equations to model a the glycerin solution, which is a widely used blood analogue, in the in vitro flow circuit as a viscous incompressible fluid. We model the fluid with a uniform density $\rho = 1.00$ g cm$^{-3}$ and a uniform dynamic viscosity $\mu = 3.5$ cP.

We use reduced-order lumped parameter description in order to establish the driving and loading conditions as well as to model the valves upstream and downstream of the LV phantom model. We impose normal traction and zero tangential velocity boundary conditions at the inlet and outlet to couple of these reduced-order models to the full FSI model of the LV phantom and housing (Figure 4.4).

The upstream driving condition is modeled with a constant pressure reservoir and compliance along with a reduced-order "mitral" valve (MV), which is modeled as a diode. The resistance of the

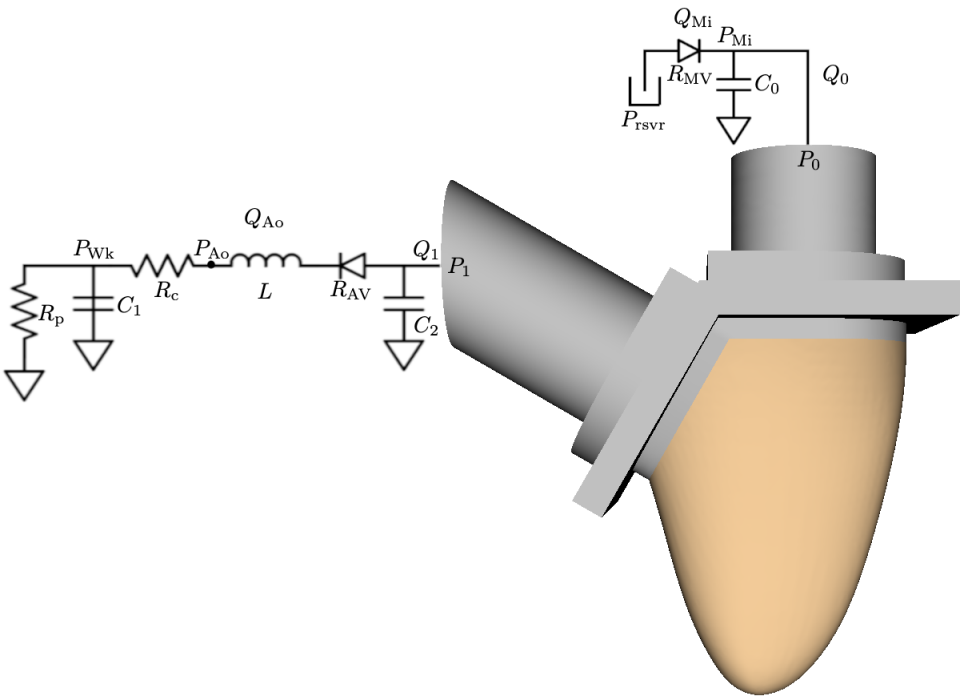


**Figure 4.4:** Reduced-order models that provide driving and loading conditions for the LV phantom and the housing models. The upstream driving condition is modeled with a constant pressure reservoir and compliance along with a reduced-order mitral valve (MV), which is modeled as a diode. The downstream loading condition is modeled with a four-element Windkessel model [62] with a reduced-order aortic valve (AV), also modeled as a diode.

diode varies based on the direction of the pressure gradient. The upstream model can be written as

$$C_0 \frac{\mathrm{d}P_0}{\mathrm{d}t} = Q_{\mathrm{Mi}} - Q_0, \tag{4.7}$$

$$Q_{\mathrm{Mi}} = \frac{P_{\mathrm{rsvr}} - P_0}{R_{\mathrm{MV}}}, \tag{4.8}$$

$$P_{\mathrm{Mi}} = P_0, \tag{4.9}$$

in which $C_0$ characterizes the compliance, $R_{\mathrm{MV}}$ is the variable resistance of the mitral valve, $P_{\mathrm{rsvr}}$ is the reservoir pressure of the flow loop, $Q_{\mathrm{MV}}$ is the volumetric flow rate, $P_{\mathrm{Mi}}$ is the pressure downstream of the mitral valve, and $P_0 = P_{\mathrm{Mi}}$ is the pressure at the inlet of the housing structure that is applied as the upstream boundary condition of the detailed FSI model. The values of the parameters that we use are $C_0 = 0.045$ mmHg ml$^{-1}$, $R_{\mathrm{MV}} = 0.0462$ mmHg ml$^{-1}$ s (MV is open) or 50 mmHg ml$^{-1}$ s (MV is closed), and $P_{\mathrm{rsvr}} = 5$ mmHg, which we choose empirically.

The downstream loading condition is modeled with a four-element Windkessel model [62] with a reduced-order "aortic" valve (AV), which is also modeled as a diode,

$$C_1 \frac{\mathrm{d}P_{\mathrm{Wk}}}{\mathrm{d}t} = Q_{\mathrm{Ao}} - \frac{P_{\mathrm{Wk}}}{R_{\mathrm{p}}}, \tag{4.10}$$

$$C_2 \frac{\mathrm{d}P_1}{\mathrm{d}t} = Q_1 - Q_{\mathrm{Ao}}, \tag{4.11}$$

$$L \frac{\mathrm{d}Q_{\mathrm{Ao}}}{\mathrm{d}t} = P_{\mathrm{Ao}} - P_{\mathrm{Wk}} - Q_{\mathrm{Ao}} R_{\mathrm{c}}, \tag{4.12}$$

$$P_{\mathrm{Ao}} = P_1 - Q_{\mathrm{Ao}} R_{\mathrm{AV}}, \tag{4.13}$$

in which $C_1$ and $C_2$ are the compliances of the apparatus, $R_{\mathrm{c}}$ is the characteristic resistance, $R_{\mathrm{p}}$ is the peripheral resistance, $R_{\mathrm{AV}}$ is the variable resistance of the aortic valve, $L$ is the inertance that accounts for the inertia of the fluid, $P_{\mathrm{Wk}}$ is the Windkessel pressure, $Q_{\mathrm{Ao}}$ and $P_{\mathrm{Ao}}$ are the volumetric flow rate and pressure, respectively, downstream of the aortic valve, $Q_1$ and $P_1$ are the volumetric flow rate and pressure, respectively at the outlet of the housing structure. $Q_1$ is measured from the simulation, and we solve the above equations for $P_1$ to apply as the downstream boundary condition of the detailed FSI model. We use the nonlinear optimization tool `fmincon` in MATLAB to determine the parameters for the downstream model by comparing experimental values of $P_{\mathrm{Ao}}$ to model results obtained by solving Eq (4.10)–(4.13) with measured values of $Q_{\mathrm{Ao}}$ as inputs to the

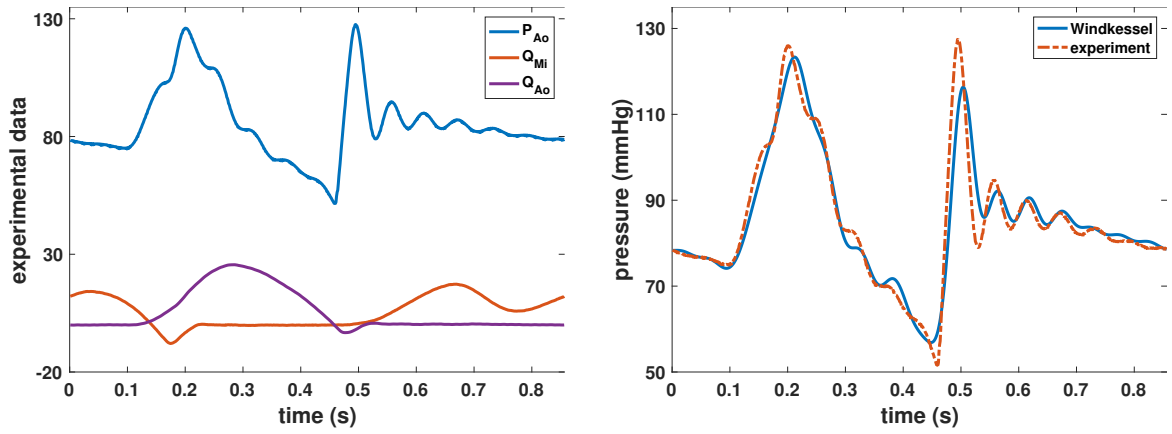


**Figure 4.5:** (a) Both the mitral (upstream) and the aortic (downstream) flow rates (L/min) as well as the downstream pressure waveforms (mmHg) are measured experimentally. Note that there is a lag in the aortic flow data compared to the aortic pressure data, which made it necessary to include an inertance in the reduced-order model to account for this delay. (b) The four-element Windkessel fit of the experimental downstream pressure data. This fit is obtained using a nonlinear optimization tool `fmincon` in MATLAB by comparing experimental values of $P_{\mathrm{Ao}}$ to model results obtained by solving Eq (4.10)–(4.13) with measured values of $Q_{\mathrm{Ao}}$ as inputs to the Windkessel model.

Windkessel model. The values of the parameters that we use are $C_1 = 2.50$ mmHg ml$^{-1}$, $C_2 = 0.03$ mmHg ml$^{-1}$, $R_{\mathrm{c}} = 0.0174$ mmHg ml$^{-1}$ s, $R_{\mathrm{p}} = 0.8701$ mmHg ml$^{-1}$ s, $R_{\mathrm{AV}} = 0.231$ mmHg ml$^{-1}$ s (AV is open) or 50 mmHg ml$^{-1}$ s (AV is closed), $L = 0.01$ mmHg ml$^{-1}$ s$^2$.

A first-order (Godunov) time step splitting is used to decouple the three-dimensional FSI model from the Windkessel model as described by Griffith et al. [14]. At the outlet of the housing structure, the mean flow rate, $Q_1$, through the outlet surface computed by the three-dimensional FSI model is provided as an input to the reduced-order model described above. The pressure, $P_1$, at the outlet surface is determined by solving Eq (4.10)–(4.13), which is used as a boundary condition for the three-dimensional model.

### 4.2.5 Numerical discretization

The LV phantom and the housing structure are embedded in a computational domain with side lengths of 18 cm. The Cartesian grid resolution at the finest level is 0.14 cm. Both the LV phantom and the housing structure meshes use first-order tetrahedral (10-point) elements, which are generated using Trelis (Coreform, LLC, Orem, UT, USA). The average grid-spacings of the meshes are 0.07 cm for the LV phantom and 0.14 cm for the housing. We use a piecewise-linear kernel for

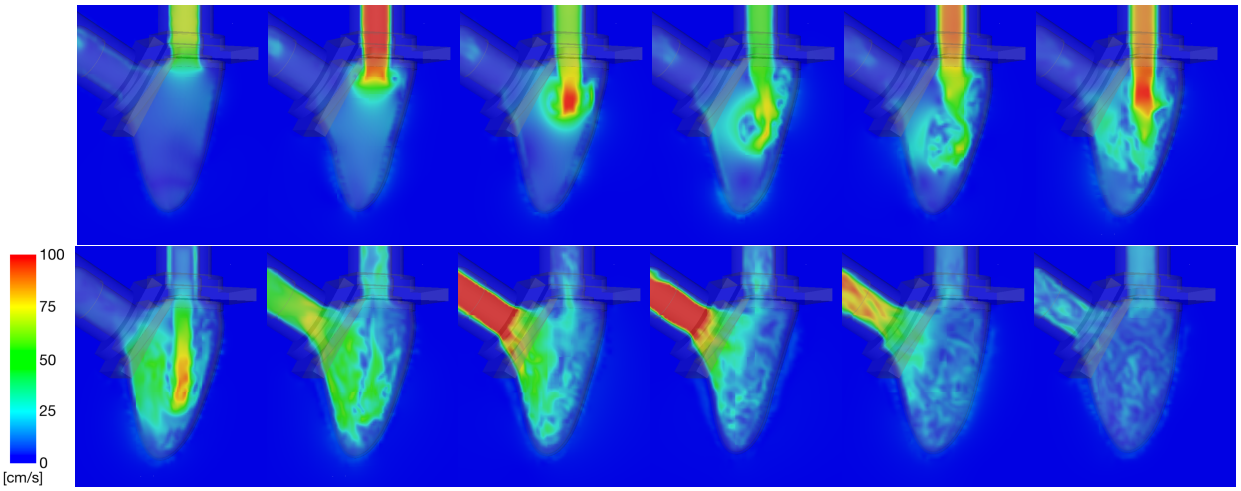


**Figure 4.6:** Cross-section view of simulated flow patterns. The color shows the velocity magnitude in the in vitro left ventricle model at the center plane.

the housing and a three-point B-spline kernel for the LV phantom as regularized delta functions. We use adaptive time stepping scheme to avoid instabilities.

## 4.3 Results

We perform simulations of the corresponding experimental flow circuit model (Figure 4.6) efficiently by using the reduced-order models of the inflow and outflow valves. We compare the computational results to the experimental data, including inflow and outflow flow rates, outflow pressure, and intraventricular flow dynamics.

Figure 4.7 shows comparison between simulated and measured aortic (outflow) pressure downstream of the aortic (outflow) valve, as well as the flow rates at both mitral and aortic flow rates through the mitral (inflow) and aortic valves. They are in reasonable agreement for the most part, but there there is a noticeable discrepancy during systole when the LV phantom ejects fluid out through the aortic valve. In particular, because the valves are modeled as diodes, the simulation results only allow for forward flow, which is reflected in the pressure plot.

Figure 4.8 compares the diastolic intraventricular flow streamlines between simulation and PIV reconstruction. We observe reasonable agreement between the experimental and computational results, in which we see the initial two vortices forming. We also see that in both cases, the vortex closer to the the outflow section develops into a larger vortex, as well as another vortical structure forming closer to the apex of the LV phantom.

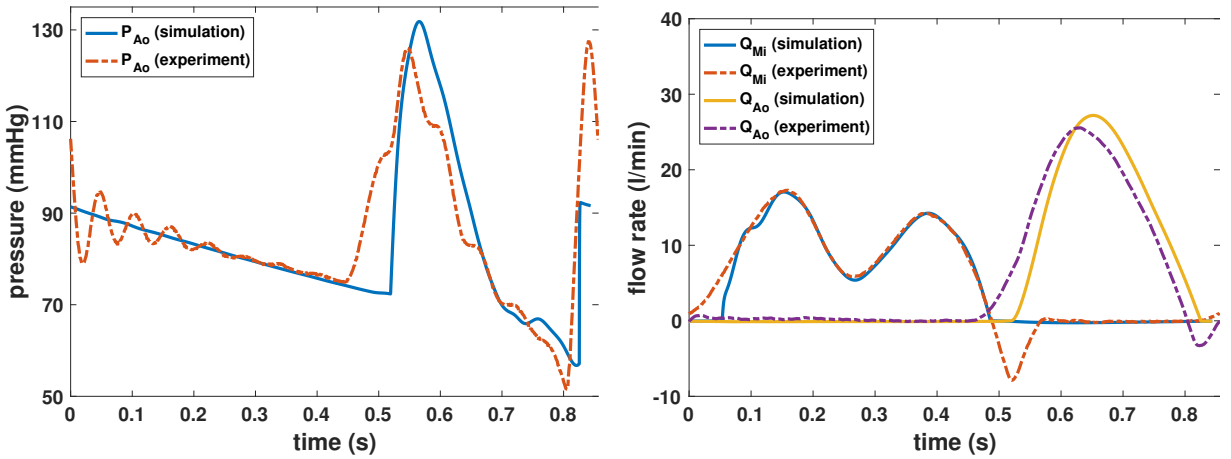


(a) (b)

**Figure 4.7:** (a) Comparison between computed vs. experimental aortic pressure downstream of the aortic valve. (b) Comparison between measured vs. experimental aortic and mitral flow rates through the inflow and outflow valves.

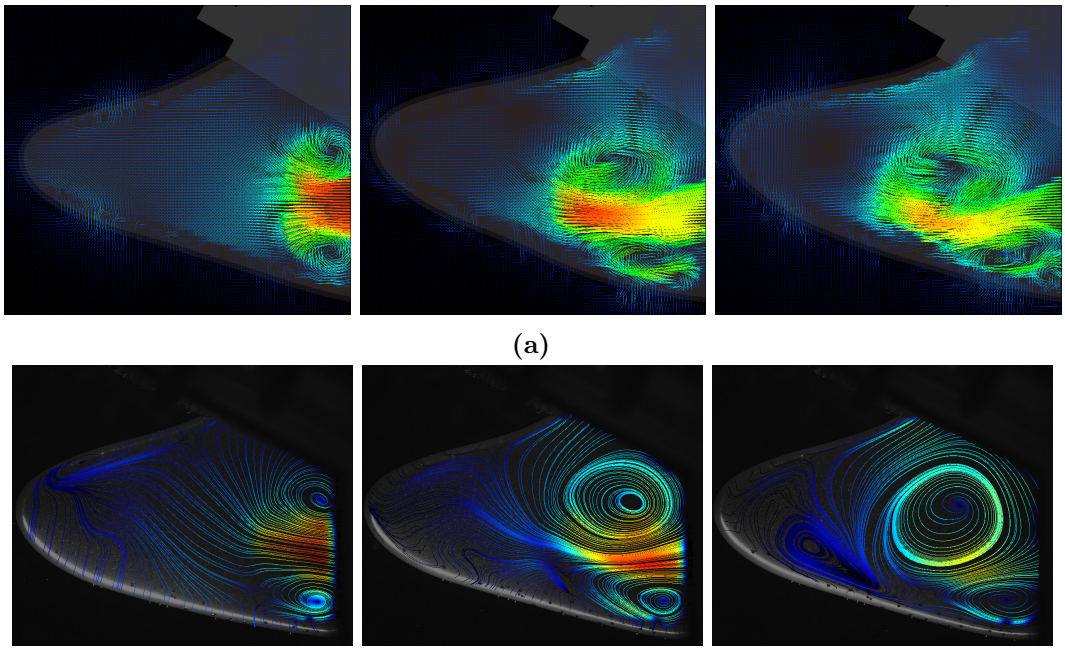

(a)

(b)

**Figure 4.8:** Comparison of diastolic flow fields between (a) experimental particle image velocimetry and (b) simulation for the LV phantom model. We observe reasonable agreement between the experimental and computational results, in which we see the initial two vortices forming. We also see that in both cases, the vortex closer to the the outflow section develops to a larger vortex.

## 4.4 Discussion

This study develops an FSI model of left ventricle (LV) phantom in an in vitro experimental flow circuit as an initial step towards validating our computational platform for intraventricular

flow dynamics. We characterize the material property of the LV phantom based on experimental compliance data. We also use experimental flow rate and pressure waveform to establish driving and loading conditions for the FSI model. In particular, we use reduced-order models, and these boundary models are fit using the experimental data in isolation from the detailed FSI model. The simulated flow rates, pressure, and intraventricular flow dynamics are results of the coupling of the reduced-order models with the detailed FSI model. To make our simulations more computationally more efficient, we model both the mitral (inflow) and aortic (outflow) mechanical heart valves (MHVs) as reduced-order representations as well.

The simulation results in Figure 4.7 show reasonable agreement in both mitral and aortic flow rates as well as the aortic pressure. We observe discrepancies in the simulated results mainly during systole, but the results show excellent agreement during diastole. The discrepancy mainly comes from our reduced-order representations of the mitral and aortic valves, which are described as simple diodes. Diodes are basically variable resistances, which exhibit high resistance with negative pressure gradient (backward flow) and low resistance with positive pressure gradient (forward flow). These diodes behave as a switch that turn on and off, and they cannot capture the detailed intermediate dynamics of real MHVs. As a result, we observe in Figure 4.7 that our valve models are in some sense working too perfectly in that they do not allow for the backward flow that occurs in the experiment. This discrepancy is reflected in the increased aortic flow rate during systole with extra intraventricular fluid with elimination of backward flow out of the LV phantom during LV filling. The discrepancy in the pressure comparison follows naturally from the discrepancies in the flow rates. This suggests that we need to improve our reduced-order models by including more detailed valve dynamics [63] to allow realistic backward flow during valve closure.

Figure 4.8 shows promise that the improved reduced-order models may lead to improvement in the accuracy of the simulated intraventricular flow dynamics. We note that despite the discrepancies in the flow rates and pressure measurements, we observe reasonable agreement in the overall flow features. In particular, we observe similar vortex formations in the LV phantom. It remains as future work to quantify the comparisons between simulation and PIV results.

A limitation of this work is that the compliance data only provides data during expansion and not during compression. We plan to use more complete compliance data to characterize the mechanical response of the LV phantom. Another future work is to incorporate quantification of the uncertainties

that are associated with the cycle-to-cycle variations.

An approach is to incorporate the realistic dynamics of the MHVs is to actually include the MHV models to capture more accurate intraventricular flow dynamics. With recent development in numerical methods, such as the immersed interface approach [64], that improve both the computational cost as well as the resolution of the results, we will be able to capture the complete interplay between the MHVs and LV phantom.

CHAPTER 5

# FLUID-STRUCTURE INTERACTION MODEL OF BIOPROSTHETIC HEART VALVE DYNAMICS IN AN EXPERIMENTAL PULSE DUPLICATOR SYSTEM

**Material in this section is adapted from a paper published in *Annals of Biomedical Engineering* [19].**

## 5.1 Background

Every year, 300,000 heart valve repair/replacement procedures are performed worldwide to treat stenosis or regurgitation, and the rate of heart valve replacement is projected to exceed 850,000/year by 2050 [65]. This number continues to increase as these procedures become less invasive, e.g., via transcatheter aortic valve replacement (TAVR), or through expanded access to cardiac surgery and interventional cardiology. Diseased native heart valves can be replaced by prosthetic valves, but there are still difficulties with current heart valve prostheses. Mechanical heart valves (MHVs) are durable but generate non-physiological flow patterns that induce platelet activation, possibly causing other complications such as stroke, pulmonary embolism, or myocardial infarction. As a result, patients with MHVs require lifelong anticoagulation, which increases bleeding risk. Bioprosthetic heart valves (BHVs) are commonly constructed from fixed porcine heart valves or bovine or porcine pericardial tissues. BHVs are becoming increasingly popular because they generate flow patterns that closely resemble those of the normal human aortic valve and typically allow patients to be managed without chronic anticoagulation [66]. Unfortunately, BHVs have a limited durability, and they typically fail 10–15 years post implantation, primarily from tissue degeneration or calcification [67].

A fluid–structure interaction (FSI) approach is necessary to model heart valves across the full cardiac cycle [6]. Accounting for coupling between the flexible valve leaflets and the fluid flow is crucial in studying the effect of vortices in the aortic sinuses, predicting fluid-induced shear stress on the leaflets, and assessing valve performance by quantifying the valve orifice area and regurgitation [7]. A widely used approach to simulating cardiovascular FSI is the arbitrary Lagrangian–Eulerian (ALE)

method [8, 9], which uses body-conforming meshes for the fluid and solid. ALE methods have realized limited success in simulating the dynamics of heart valves to date, however, because of the substantial challenges posed by dynamically generating geometrically conforming discretizations of thin structures that undergo substantial motion [8, 9].

Non-body conforming discretizations, which avoid the difficulties of body-fitted grids, are now widely used to model heart valve dynamics. One of the earliest of these types of approaches is the immersed boundary (IB) method [10], which was introduced by Peskin to simulate heart valves [11,12]. The IB formulation allows the structural discretization to be independent of the fluid grid and thereby facilitates models with very large structural deformations [13]. Extensions to the IB method have also been used to simulate heart valves [14, 15], but in most cases, these prior simulations were not fully resolved, and the valve leaflets were described using only simple structural models based on linear elasticity. Other studies [16, 68] used anisotropic models of native and bioprosthetic valves but do not address the diastolic phase of the cardiac cycle. Flamini et al. [17] used an IB approach to simulate aortic valve FSI across multiple cardiac cycles, but they used a simplified description of the aortic valve mechanics. Hasan et al. [18] also used an IB approach to simulate FSI in a subject-specific aortic root model, and they used realistic hyperelastic constitutive models to describe the valve leaflets, but their model has not been validated. In addition, neither study used subject-specific driving or loading conditions.

Methods also have been developed that combine features of ALE and IB-like approaches, including the hybrid fictitious domain/ALE method [22] and the immersogeometric (IMGA) method [7, 24, 25, 27, 28]. These methods also seek to relax the need to use body-conforming discretizations. Prior models of aortic valves using a fictitious domain/ALE method [22] showed instabilities when simulated under physiological Reynolds numbers and transvalvular pressures. The IMGA method has been used in several studies on pericardial BHVs that include experimentally derived constitutive models of the valve leaflets. Hsu et al. [24] validated the leaflet kinematics of their model by comparing the cross-sectional profiles of the leaflets to those from dynamic in vitro experimental measurements [69]. Xu et al. [27] used in vivo imaging data to drive their simulations and compared the fluid flow patterns with those from magnetic resonance imaging. These models both employed isotropic descriptions of the pericardial BHV leaflets. Wu et al. [28] used an anisotropic model that incorporated the fiber structure of a bovine pericardial valve that was developed and validated with

experimental data from Sun and Sacks [70]. These prior studies did not use boundary condition models that established flow conditions directly comparable to available experimental or clinical data.

Other methods that avoid body-conforming discretizations include smoothed particle hydrodynamics (SPH) [29]. The SPH approach [29], however, cannot fully impose incompressibility, and prescribing boundary conditions is difficult. In addition, several studies have used cut-cell-like methods [30–32] to simulate valve FSI, but these studies also used linearly elastic leaflet models and have not yet been validated.

To date, there have been relatively few experimental validation studies of FSI models of native or bioprosthetic aortic valves [71, 72]. The two studies by Tang et al. [71] and Sigüenza et al. [72] use idealized isotropic leaflet models that do not account for leaflet anisotropy and, as a result, their simulations show discrepancies in the dynamics of the valve compared with experimental data. These studies also do not use flow domains that are long enough to allow the complex flow patterns downstream of the valve to fully develop. The model of Sigüenza et al. exhibits incomplete closure and experiences substantial regurgitation during diastole, leading to an underestimation of the transvalvular pressure gradient. The study of Sigüenza et al. also uses flow rate boundary conditions throughout the cycle, which introduces bias in the valve dynamics.

This study develops a computational FSI model based on the IB method of an experimental pulse-duplicator platform for simulating BHV dynamics. The model is calibrated using relatively limited experimental data, and this study describes initial work towards the V&V of this model for porcine tissue and bovine pericardial BHVs. Our models of the leaflet mechanics are based on experimental tensile test data [73–75] of fixed tissues that are similar to the biomaterials used to construct porcine aortic and bovine pericardial BHVs. To provide realistic driving and loading conditions across the full cardiac cycle, we use reduced-order models that are calibrated using pressure and flow data acquired from the pulse-duplicator systems. Simulation results are compared to experimental data obtained from a commercial ViVitro pulse duplicator and a customized experimental apparatus based on the ViVitro pulse duplicator.

## 5.2 Methods

In vitro experiments are performed using two different experimental platforms, including a ViVitro Pulse Duplicator (ViVitro Labs, Inc., Victoria, BC, Canada) available through the FDA

Cardiac Device Flow Lab and a customized pulse duplicator developed by Scotten that is similar to the commercial ViVitro system. Figure 5.1a details Scotten's customized system. It includes a prototype *Leonardo* electro-optical sub-system [76] to assess projected dynamic valve area (PDVA). The commercial ViVitro system is similar but uses high-speed videography to assess valve kinematics, from which we reconstruct PDVA data via automatic image analysis in DataTank (Visual Data Tools, Inc., Chapel Hill, NC, USA). We also measure flow rates and pressures, as indicated in Figure 5.1b. Experiments by Scotten in the customized pulse duplicator use a 25 mm Labcor TLBP A Supra (Labcor Laboratórios Ltd., Belo Horizonte, Brazil) porcine aortic valve. Flow and pressure signals are filtered at 100 Hz, and PDVA signals are not filtered. Experiments by the FDA Heart Valve Laboratory use a Model 2800 25 mm Carpentier–Edwards PERIMOUNT RSR (Edwards Lifesciences, Irvine, CA, USA) bovine pericardial aortic valve. Flow signals are filtered at 100 Hz, and pressure signals are not filtered. Both experiments use saline as the test fluid for this initial study because the viscosities of common blood analogues are more sensitive to temperature than saline. In addition, saline is widely used for hydrodynamic assessments of heart valves [77]. For instance, the ISO 5840-3 standard allows saline to be used as a test fluid [78], and the most recent inter-laboratory study by Wu et al. [79] also used saline as the test fluid. Results presented in Section 5.3.2 examine the effect of using a Newtonian blood analogue instead of saline in the computational model.

### 5.2.1 BHV geometries

The geometry of the Labcor TLBP A Supra porcine aortic valve is constructed based on literature values [80]. The pericardial valve geometry was reconstructed from micro-CT images of a Carpentier-Edwards PERIMOUNT RSR Model 2800 surgical aortic heart valve. The DICOM files, consisting of approximately 500 slices of the 25 mm valve after micro-CT scanning (Scanco Medical; scan parameters: 90 kV; 88 $\mu$A; voxel size 24.6 $\mu$m), were imported into Mimics (Materialise Inc., Leuven, Belgium) for further segmentation and reconstruction. Segmentation and reconstruction operations in Mimics involved first thresholding to remove the dense metal and its artifacts from all the slices, and then cavity filling and region growing to reconstruct the continuity in the leaflet material. These operations helped reconstruct the three-dimensional shape of the leaflets. Other segmentation morphology operations were used to ensure that the leaflet thickness was consistent with the measured thickness of the leaflet. After these operations, the leaflet masks were smoothed, wrapped, and smoothed again prior to importing into Materialise 3-matic (Materialise Inc., Leuven, Belgium).

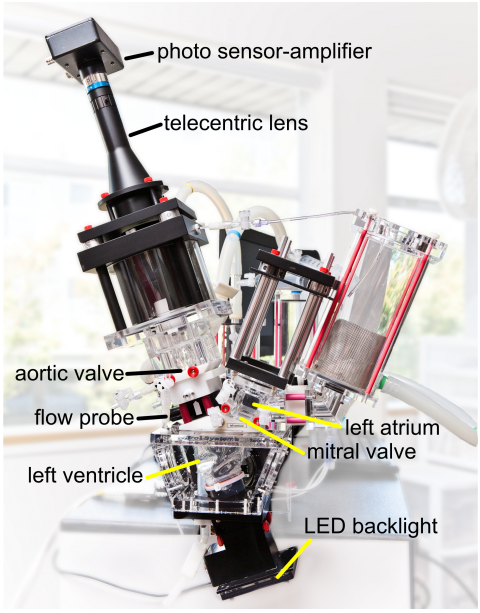


(a)

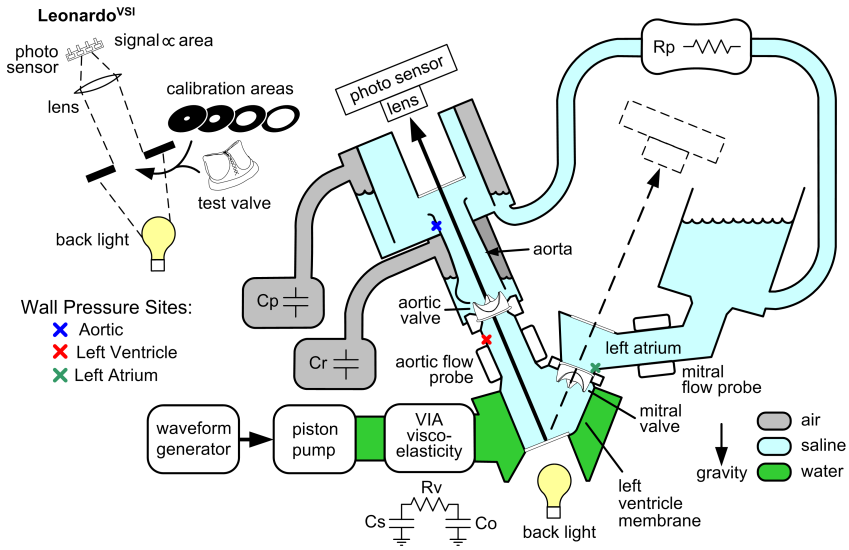


(b)

**Figure 5.1:** (a) A customized pulse duplicator based on the commercial ViVitro pulse-duplicator system adapted with prototype electro-optical subsystem for measuring aortic valve projected dynamic valve area (PDVA), or alternate configuration for measuring mitral valve PDVA. (b) A schematic diagram of the custom pulse duplicator based on the commercial ViVitro pulse-duplicator system adapted with prototype electro-optical subsystem for measuring aortic valve PDVA, or alternate configuration for measuring mitral valve PDVA. The commercial ViVitro system is similar but lacks the back light and the photo sensor for acquiring PDVA.

Further processing using design tools in Materialise 3-matic was necessary to sketch and sweep edges of the leaflet to create a smooth outline of the entire leaflet.

### 5.2.2 Constitutive model

We use a modified version of the Holzapfel–Gasser–Ogden model from Murdock et al. [81] with the addition of angle dispersion [82]. The isochoric part of the model, $W(\overline{\mathbb{F}})$, includes an isotropic contribution from the extracellular matrix and an anisotropic contribution from the collagen fibers embedded in the leaflets,

$$W(\overline{\mathbb{F}}) = W_{\text{iso}}(\overline{\mathbb{F}}) + W_{\text{aniso}}(\overline{\mathbb{F}}). \tag{5.1}$$

This model describes the extracellular matrix as an exponential neo-Hookean material along with a collagen fiber reinforcement model accounting for angle dispersion,

$$W_{\text{iso}}(\overline{\mathbb{F}}) = C_{10}\{\exp\left[C_{01}(\bar{I}_1 - 3)\right] - 1\}, \tag{5.2}$$

$$W_{\text{aniso}}(\overline{\mathbb{F}}) = \frac{k_1}{2k_2}\{\exp\left[k_2(\kappa\bar{I}_1 + (1-3\kappa)\bar{I}_4^{\star} - 1)^2\right] - 1\}, \tag{5.3}$$

in which $\bar{I}_1 = \text{tr}(\overline{\mathbb{C}})$ is the first invariant of the modified right Cauchy–Green strain tensor $\overline{\mathbb{C}} = \overline{\mathbb{F}}^T\overline{\mathbb{F}}$, $\bar{I}_4^{\star} = \max(\bar{I}_4, 1) = \max(\mathbf{e}_0^T\overline{\mathbb{C}}\mathbf{e}_0, 1)$, and $\mathbf{e}_0$ is a unit vector aligned with the mean fiber direction in the reference configuration. By construction, $\bar{I}_4^{\star}$ is nonzero in extension but not in compression. The parameter $\kappa \in [0, \frac{1}{3}]$ describes collagen fiber angle dispersion. If $\kappa = 0$, the fibers are perfectly aligned and the constitutive model becomes the same as that of Murdock et al. [81]. By contrast, if $\kappa = \frac{1}{3}$, then the model describes an isotropic distribution of fibers, and we obtain an isotropic model with no preferred direction of fiber reinforcement. The parameters for the porcine aortic valve are fit to experimental tensile test data from Billiar and Sacks [73, 74] for glutaraldehyde-fixed porcine aortic valves (Figure 5.2a). We obtain $C_{10} = 0.302$ kPa, $C_{01} = 3.25$, $k_1 = 0.197$ MPa, $k_2 = 0.001$, and $\kappa = 0.0$. The parameters for the bovine pericardial valve are fit to biaxial data from Kim et al. [75], and we obtain $C_{10} = 0.119$ kPa, $C_{01} = 22.59$, $k_1 = 2.38$ MPa, $k_2 = 149.8$, and $\kappa = 0.292$. For further details on parameter fitting, see Appendix C. The mathematical framework used in this study treats the leaflets as exactly incompressible. Thus, within our numerical framework, the volumetric part of the strain energy,

$$U(J) = \beta(J\ln J - J + 1). \tag{5.4}$$

A model collagen fiber architecture for the porcine valve is created using Poisson interpolation [83]

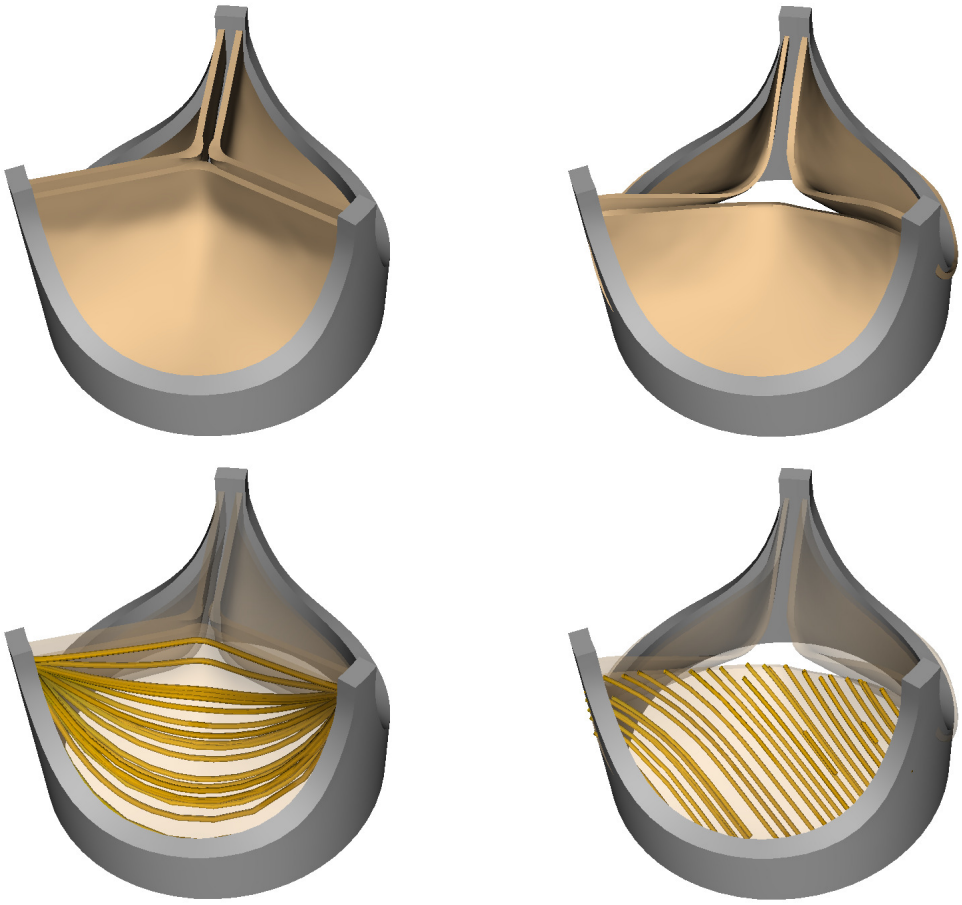

**(a)** **(b)**

**Figure 5.2:** (a) Model porcine bioprosthetic valve geometry and fiber architecture. The idealized geometry of the Labcor TLBP A Supra porcine aortic valve is reconstructed based on literature values [80]. The model fiber structure is generated using Poisson interpolation [83]. (b) Model bovine pericardial bioprosthetic valve geometry and fiber architecture. This valve geometry is obtained from micro-CT imaging of a Carpentier-Edwards PERIMOUNT RSR Model 2800 surgical aortic heart valve. The model fiber structure is generated based on the small angle light scattering (SALS) data of Sun et al. [70] The SALS data show that the mean fiber orientation of a bovine pericardial valve leaflet is 45°.

(Figure 5.2a). The mean fiber orientation for the pericardial valve is chosen to be 45° (Figure 5.2b), following the small angle light scattering data of Sun et al. [70]

### 5.2.3 Aortic test section model

The wall of the aortic test section is glass. To avoid the expensive linear solvers required by exactly imposing the rigidity constraint within the present computational framework [84], we instead

use a penalty method that models the test section as a stiff neo-Hookean material with [18]

$$W_{\text{wall}} = \frac{c_{\text{wall}}}{2}(\bar{I}_1 - 3). \tag{5.5}$$

Additional structural forces are included in the rigid test section model,

$$\mathbf{F}(\mathbf{X}, t) = \kappa_{\text{wall}}(\mathbf{X} - \boldsymbol{\chi}(\mathbf{X}, t)). \tag{5.6}$$

In the limit as $c_{\text{wall}}$ and $\kappa_{\text{wall}}$ become large, the test section becomes effectively rigid and stationary. We use $c_{\text{wall}} = 33.1$ kPa and $\kappa_{\text{wall}} = 8.52 \times 10^5$ kPa cm$^{-2}$.

### 5.2.4 Fluid model and boundary conditions

We use the incompressible Navier–Stokes equations to model the test fluid in the aortic test section of the pulse duplicator as a viscous incompressible fluid. We model the saline solution with a uniform density $\rho = 1.0$ g cm$^{-3}$ and a uniform dynamic viscosity $\mu = 1.0$ cP (saline at 25 °C) for both cases. Results from additional simulations using a blood analogue fluid with density 1.0 g cm$^{-3}$ and viscosity 3.5 cP are provided in Section 5.3.2. These simulations indicate that the large-scale flow structures and leaflet kinematics are similar between saline and the blood analogue.

Three-element Windkessel (R–C–R) models establish downstream loading conditions for the aortic test section for both cases (Figure 5.3). A three-element Windkessel model is also used for the porcine BHV simulations to capture the upstream driving conditions for the aortic test section (Figure 5.3a). Additional data are available for the bovine pericardial case, including the experimental pump flow and atrial pressure waveforms, which allow for a more complete description of the upstream components of the system (Figure 5.3b). In both cases, we impose a combination of normal traction and zero tangential velocity boundary conditions at the inlet and outlet of the FSI model to couple the reduced-order models to the detailed description of the flow within the aortic test section.

Pulse-duplicator system components upstream of the aortic test section, including the resistance and compliance of the pump, the viscoelastic impedance adapter (VIA) subsystem, and the left ventricular chamber of the pulse duplicator, are described by a three-element Windkessel (R-C-R) model for the porcine aortic valve, whereas a more detailed model is used for the bovine pericardial

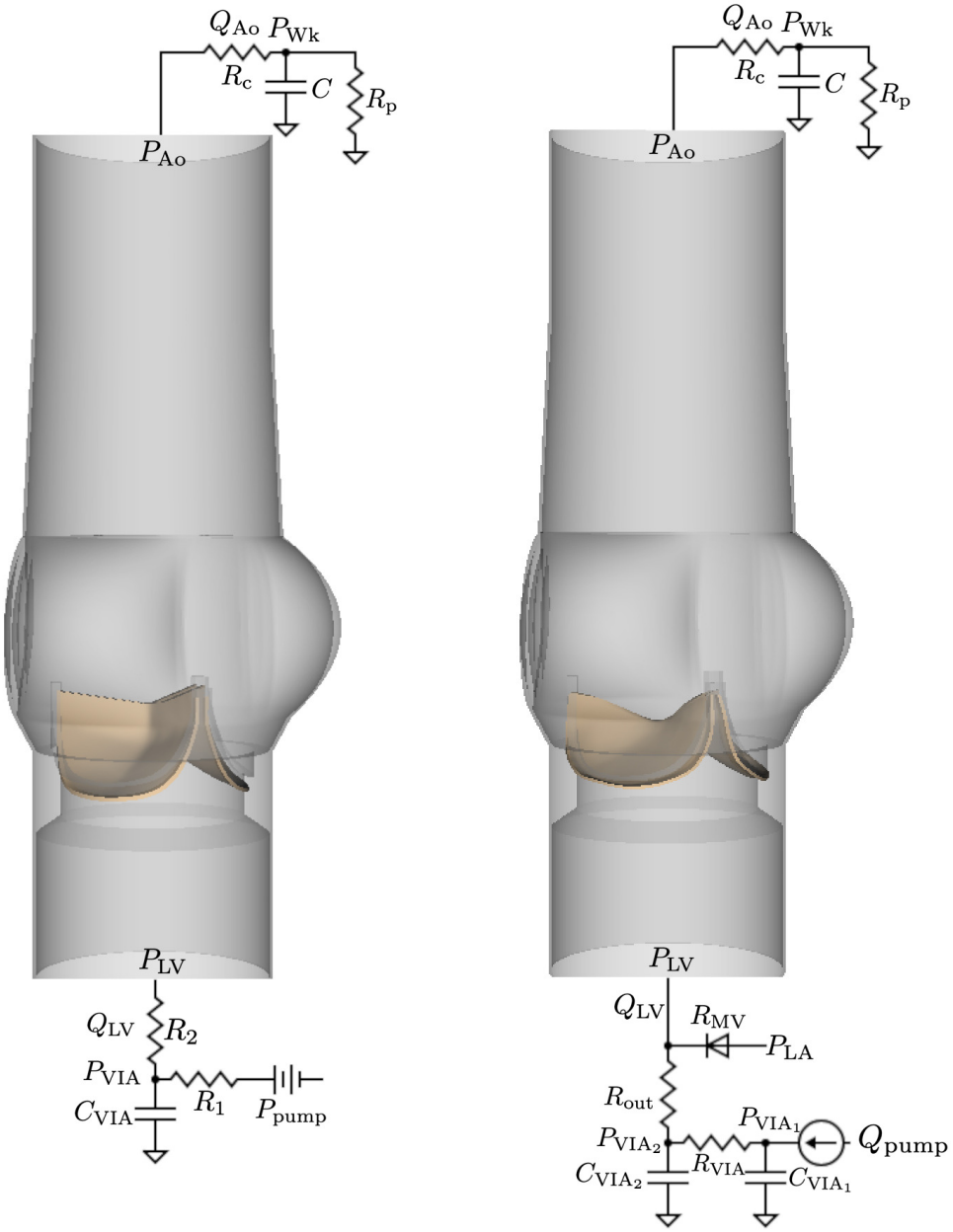


**Figure 5.3:** Three-dimensional aortic test section models for the porcine (a) and bovine pericardial (b) BHV simulations along with the reduced-order models that provide driving and loading conditions. Three-element Windkessel models are used at the downstream (outlet) for both cases. (a) A three-element Windkessel model is used at the upstream (inlet) for the porcine aortic valve simulations. The pump pressure is derived from pressure and flow data from the ventricular outflow tract of the pulse duplicator. (b) Because the pump flow waveform and atrial pressure data are available for the bovine pericardial valve experiments, a more detailed pump model is used upstream for the bovine pericardial valve simulations.

valve because additional experimental data are available for the bovine pericardial BHV cases. See Figure 5.3. We remark that the VIA subsystem includes tunable compliance chambers (see Figure 5.1b) that help to ameliorate unphysiological pressure oscillations in the left ventricular pressure [76]. The upstream model used in the porcine aortic valve simulations is

$$C_{\mathrm{VIA}}\frac{\mathrm{d}P_{\mathrm{VIA}}}{\mathrm{d}t} = \frac{P_{\mathrm{pump}} - P_{\mathrm{VIA}}}{R_1} + Q_{\mathrm{LV}}, \tag{5.7}$$

$$\frac{P_{\mathrm{LV}}}{R_2} = \frac{P_{\mathrm{VIA}}}{R_2} + Q_{\mathrm{LV}}, \tag{5.8}$$

in which $C_{\mathrm{VIA}}$, $R_1$, and $R_2$ characterize the VIA system, and $Q_{\mathrm{LV}}$ and $P_{\mathrm{LV}}$ are the volumetric flow rate and pressure, respectively, at the inlet of the aortic test section model. $P_{\mathrm{pump}}$ is derived from Eq (5.7) and (5.8) using experimental measurements of $Q_{\mathrm{LV}}$ and $P_{\mathrm{LV}}$. The upstream model used in the bovine pericardial valve simulations is

$$C_{\mathrm{VIA}_1}\frac{\mathrm{d}P_{\mathrm{VIA}_1}}{\mathrm{d}t} = Q_{\mathrm{pump}} - \frac{P_{\mathrm{VIA}_1} - P_{\mathrm{VIA}_2}}{R_{\mathrm{VIA}}}, \tag{5.9}$$

$$C_{\mathrm{VIA}_2}\frac{\mathrm{d}P_{\mathrm{VIA}_2}}{\mathrm{d}t} = \frac{P_{\mathrm{VIA}_1} - P_{\mathrm{VIA}_2}}{R_{\mathrm{VIA}}} - \frac{P_{\mathrm{VIA}_2} - P_{\mathrm{LA}} + Q_{\mathrm{LV}}R_{\mathrm{MV}}}{R_{\mathrm{out}} + R_{\mathrm{MV}}}, \tag{5.10}$$

$$P_{\mathrm{LV}} = \frac{P_{\mathrm{VIA}_2}R_{\mathrm{MV}} + P_{\mathrm{LA}}R_{\mathrm{out}} - Q_{\mathrm{LV}}R_{\mathrm{out}}R_{\mathrm{MV}}}{R_{\mathrm{out}} + R_{\mathrm{MV}}}, \tag{5.11}$$

in which $C_{\mathrm{VIA}_1}$, $C_{\mathrm{VIA}_2}$, $R_{\mathrm{VIA}}$, and $R_{\mathrm{out}}$ characterize the VIA system, $R_{\mathrm{MV}}$ characterizes the resistance at the mitral position, $P_{\mathrm{LA}}$ is the left atrial pressure, $Q_{\mathrm{pump}}$ is the prescribed volumetric flow rate of the pump, and $Q_{\mathrm{LV}}$ and $P_{\mathrm{LV}}$ are the volumetric flow rate and pressure, respectively, at the inlet of the aortic test section model.

The downstream loading conditions of the pulse duplicator are also described by a three-element Windkessel model,

$$C\frac{\mathrm{d}P_{\mathrm{Wk}}}{\mathrm{d}t} = Q_{\mathrm{Ao}} - \frac{P_{\mathrm{Wk}}}{R_{\mathrm{p}}}, \tag{5.12}$$

$$P_{\mathrm{Ao}} = P_{\mathrm{Wk}} + Q_{\mathrm{Ao}}R_{\mathrm{c}}, \tag{5.13}$$

in which $C$ is the compliance, $R_{\mathrm{c}}$ is the characteristic resistance, $R_{\mathrm{p}}$ is the peripheral resistance, $P_{\mathrm{Wk}}$ is the Windkessel pressure, and $Q_{\mathrm{Ao}}$ and $P_{\mathrm{Ao}}$ are the volumetric flow rate and pressure, respectively,

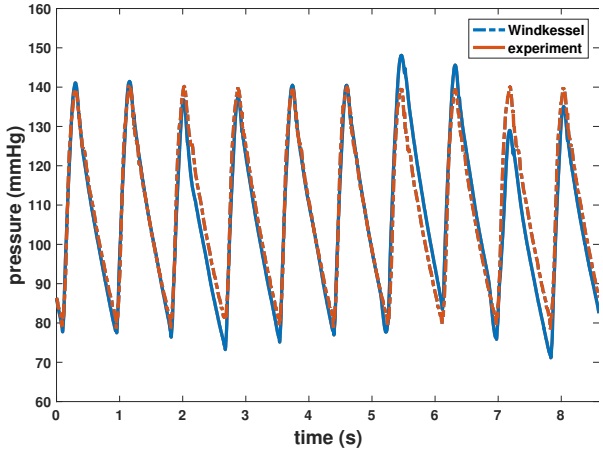


**(a)** Porcine aortic valve (downstream)

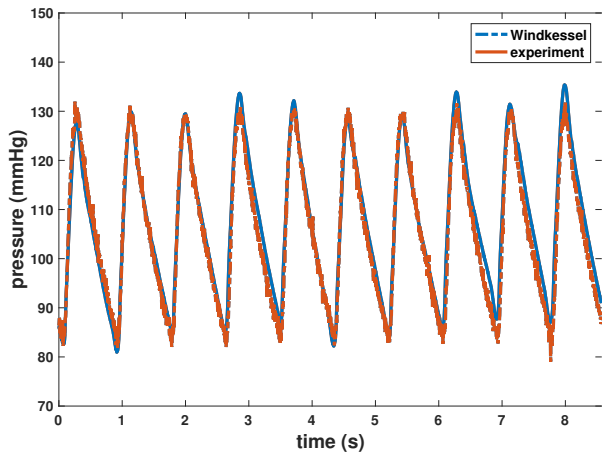


**(b)** Bovine pericardial valve (downstream)

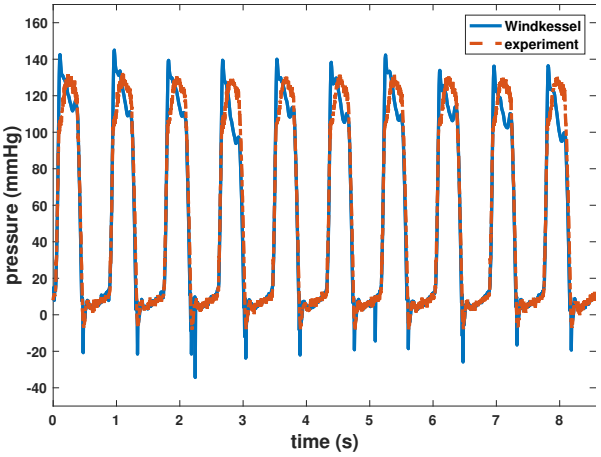


**(c)** Bovine pericardial valve (upstream)

**Figure 5.4:** (a)-(b) The three-element Windkessel model fits of the experimental downstream pressure (pressure at the outlet) data for both porcine aortic valve and bovine pericardial valve models (Figure 5.3). These fits are obtained using a nonlinear optimization tool fmincon in MATLAB by comparing experimental values of $P_{\mathrm{Ao}}$ to model results obtained by solving Eq (5.12) and (5.13) with measured values of $Q_{\mathrm{Ao}}$ as inputs to the Windkessel models. (c) Model fit of the experimental upstream pressure (pressure at the inlet) data for the bovine pericardial valve model using a detailed upstream model shown in Figure 5.3b. These fits are obtained by comparing experimental values of $P_{\mathrm{LV}}$ to model results obtained by solving Eq (5.9), (5.10), and (5.11) with measured values of $Q_{\mathrm{pump}}$, $Q_{\mathrm{LV}}$, and $P_{\mathrm{LA}}$.

at the outlet of the test section. The Windkessel parameters $R_{\mathrm{c}}$, $R_{\mathrm{p}}$, and $C$ are calibrated using experimental measurements of $Q_{\mathrm{Ao}}$ and $P_{\mathrm{Ao}}$. We use the nonlinear optimization tool fmincon in MATLAB to determine the model parameters by comparing $P_{\mathrm{Ao}}$ from Eq (5.12) and (5.13) with that of experimental system (Figure 5.4). When calibrating the reduced-order models, the experimental measurements of $Q_{\mathrm{Ao}}$ are used as inputs to the Windkessel models.

The values of the resistances and compliance for the upstream model are $C_{\mathrm{VIA}} = 0.1$ mmHg mL$^{-1}$, $R_1 = 0.15$ mmHg mL$^{-1}$ s, and $R_2 = 0.15$ mmHg mL$^{-1}$ s for the porcine aortic valve case, which characterize compliance and resistance of the VIA system. The values for the bovine pericardial valve case are $C_{\mathrm{VIA}_1} = 0.0275$ mmHg mL$^{-1}$, $C_{\mathrm{VIA}_2} = 0.0347$ mmHg mL$^{-1}$, $R_{\mathrm{VIA}} = 0.15$ mmHg mL$^{-1}$ s, and $R_{\mathrm{out}} = 0.0898$ mmHg mL$^{-1}$ s. The mitral valve is modeled as a diode, with a resistance of $R_{\mathrm{MV}} = 0.0280$ mmHg mL$^{-1}$ s when the valve is open. The values for the downstream model are $R_{\mathrm{c}} = 0.0218$ mmHg mL$^{-1}$ s, $R_{\mathrm{p}} = 1.31$ mmHg mL$^{-1}$ s, and $C = 0.915$ mmHg mL$^{-1}$ for the porcine BHV, and $R_{\mathrm{c}} = 0.0282$ mmHg mL$^{-1}$ s, $R_{\mathrm{p}} = 1.22$ mmHg mL$^{-1}$ s, and $C = 1.27$ mmHg mL$^{-1}$ for the bovine pericardial BHV. We use both zero normal and zero tangential velocity boundary conditions everywhere else at the boundaries in the computational domain of the FSI model.

A first-order (Godunov) time step splitting is used to decouple the three-dimensional FSI model from the Windkessel model as described by Griffith et al. [14]. At the outlet of the aortic test section, for example, the mean flow rate through the outlet surface computed by the three-dimensional FSI model is provided as an input to the Windkessel model. The pressure generated in the Windkessel model is used, along with the flow rate, to determine the pressure along the outlet surface, which is used as a boundary condition for the three-dimensional model.

### 5.2.5 Numerical discretizations

Simulations are performed using a geometrically realistic model of the aortic test section of the pulse duplicator with length 10.1 cm and diameter 28 mm (see Figure 5.3). The aortic test section is embedded in a square computational domain with side lengths of 10.1 cm. In our IB formulation, Eulerian variables are approximated using a block-structured adaptively refined Cartesian grid, and Lagrangian variables are approximated using an unstructured FE mesh that conforms to the geometry of the structure [34]. The effective fine-grid resolution of the Cartesian grid is approximately 0.39 mm. The structural meshes use second-order hexahedral (27-node) elements for the BHV leaflets and first-order tetrahedral (four-node) elements for the aortic test section. The aortic test section and porcine BHV meshes were generated using Trelis (Coreform, LLC, Orem, UT, USA), and the bovine pericardial BHV mesh was generated using Pointwise (Pointwise, Inc., Ft. Worth, TX, USA). The average grid-spacings of the meshes are 0.4 mm for the aortic test section, 0.59 mm for the porcine aortic valve, and 0.75 mm for the bovine pericardial valve. The time step size starts at $\Delta t = 7.5 \times 10^{-6}$ s, and it is systematically reduced if needed to avoid instabilities related to our

time stepping scheme. The penalty parameters $c_{\text{wall}}$ and $\kappa_{\text{wall}}$ in Eqs. (5.5) and (5.6) detailed in Section 5.2.3 are empirically determined as approximately the largest values allowed by our explicit time stepping algorithm at the time step sizes used in the simulations. Section 5.3.1 shows results from a grid convergence study to quantify the level of consistency in our numerical results and to justify the chosen level of grid resolution for the final results reported here.

In our computations, different regularized delta functions are used for the rigid aortic test section and flexible valve leaflets. These choices are based on preliminary tests in Chapter 3. For the aortic test section, we use a simple piecewise-linear (PWL) kernel that takes the form,

$$\varphi^{\text{PWL}}(r) = \begin{cases} 1 - r, & 0 \leq r < 1, \\ 0, & 1 \leq r, \end{cases} \tag{5.14}$$

whereas we use a three-point B-spline (BS3) kernel for the valve leaflets,

$$\varphi^{\text{BS3}}(r) = \begin{cases} \frac{3}{4} - r^2, & 0 \leq r < 0.5, \\ \frac{9}{8} - \frac{3}{2}r + \frac{1}{2}r^2, & 0.5 \leq r \leq 1.5, \\ 0, & 1.5 \leq r. \end{cases} \tag{5.15}$$

## 5.3 Results

We perform corresponding experiments and simulations using a pulse rate of 70 beats per minute in all cases. We use 10 consecutive cycles of experimental pressure and flow rate waveforms for both valves to characterize the reduced-order models that provide driving and loading conditions for the three-dimensional FSI models. The stroke volumes of the average flow waveforms are $69.4 \pm 0.4$ mL and $71.6 \pm 0.7$ mL for the porcine and bovine pericardial BHVs, respectively. We assess the computational results by comparisons to available experimental data, including flow rates, upstream and downstream pressures, and leaflet kinematics. The computational models also provide detailed flow patterns and leaflet stress distributions, which are not readily available in the present experimental models.

Figure 5.5 shows comparisons between simulated and experimental pressures and flow rates for both valves, which are in good agreement. To quantify this, we calculate the discrepancy between

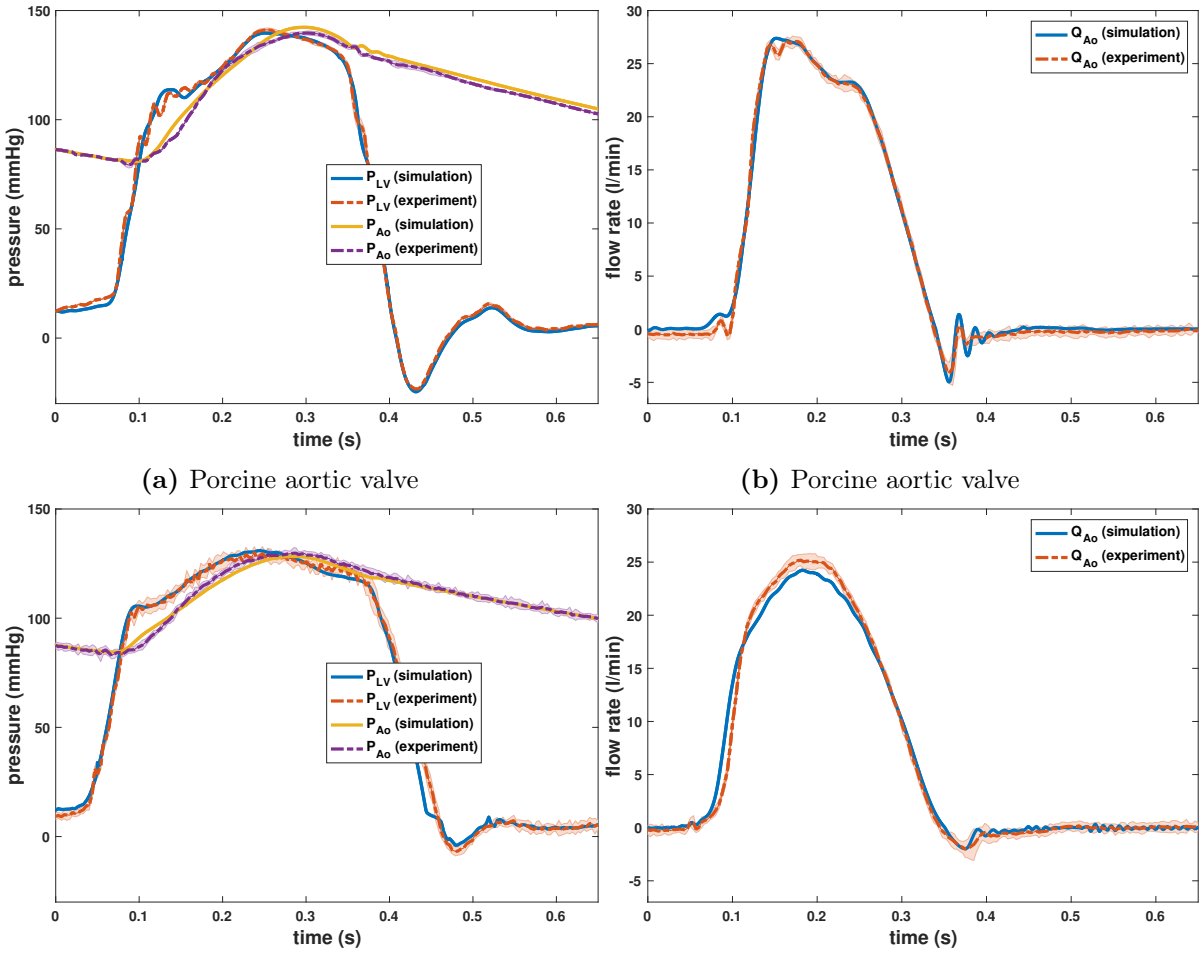


**(a)** Porcine aortic valve

**(b)** Porcine aortic valve

**(c)** Bovine pericardial valve

**(d)** Bovine pericardial valve

**Figure 5.5:** Comparisons between simulated and experimental pressure and flow rate waveforms for the porcine aortic valve (a)-(b) and bovine pericardial valve (c)-(d). The experimental waveforms shown are the average waveforms over 10 consecutive cycles of data, with shaded regions showing where 95% of the data fall. The experimental and computational stroke volumes for the porcine aortic valve are $69.4 \pm 0.4$ mL and 72.7 mL, respectively, and $71.6 \pm 0.7$ mL and 72.1 mL for the bovine pericardial valve. The maximum experimental pressure differences during forward flow for the porcine aortic and bovine pericardial valve are $22.8 \pm 0.2$ mmHg and $19.7 \pm 0.5$ mmHg, respectively. The maximum computational pressure differences during forward flow are 22.4 mmHg and 16.4 mmHg, respectively.

the simulation data and the mean experimental data by

$$\Delta M_q = \frac{\left\| M^{\text{simulation}} - M^{\text{experiment}} \right\|_{L^q(0,T)}}{\left\| M^{\text{experiment}} \right\|_{L^q(0,T)}}, \qquad q = 2, \infty, \tag{5.16}$$

in which $(0, T)$ indicates an integral over time and $M^{\text{experiment}}$ is the experimental data averaged

**Table 5.1:** Comparisons of normalized $L^2$- and $L^\infty$-norms of discrepancies in the bulk measurements between simulation and experiment*

| | porcine ($L^2$) | pericardial ($L^2$) | porcine ($L^\infty$) | pericardial ($L^\infty$) |
|---|---|---|---|---|
| $P_{\text{LV}}$ | 3.4% | 4.6% | 8.6% | 14.4% |
| $P_{\text{Ao}}$ | 1.9% | 1.4% | 4.5% | 3.6% |
| $Q_{\text{Ao}}$ | 4.7% | 8.6% | 9.5% | 20.2% |

* Comparisons of $L^2$- and $L^\infty$-norms of the discrepancies in the bulk measurements from simulation and experiment shown in Figure 5.5, normalized by the $L^2$- and $L^\infty$-norms of the measurements from the experiment.

over 10 consecutive cycles. Comparisons are shown in Table 5.1.

The computational stroke volumes are 72.7 mL and 72.1 mL for the porcine and bovine pericardial BHVs, which are 4.68% and 0.71% larger than the mean experimental stroke volumes, respectively. The maximum experimental pressure differences during forward flow for the porcine aortic and bovine pericardial valves are $22.8 \pm 0.2$ mmHg and $19.7 \pm 0.5$ mmHg, respectively. The maximum computational pressure differences during forward flow are 22.4 mmHg and 16.4 mmHg, which correspond to differences of 2.0% and 16.5% compared to the experimental pressure difference in the mean pressure waveforms.

Figure 5.6 uses PDVA to compare the leaflet kinematics in the experimental and computational models. The experimental data are systematically shifted in time to align with the simulation data at the beginning of valve opening. The timing of opening and closing are in excellent agreement, and the open area is also in excellent agreement. There are some differences in the fluttering frequency, and we discuss potential sources of these discrepancies in Section 5.4.

Figure 5.7 compares the leaflet kinematics of the bovine pericardial valve during closure in our simulation to images acquired via high-speed videography. We observe that each of the leaflets close one at a time in the experiment as well as in the simulation.

Figure 5.8 provides detailed flow patterns generated in the FSI simulations of the porcine aortic (Figure 5.8a) and bovine pericardial (Figure 5.8b) BHVs. We observe that the large-scale flow features are similar in both cases. We classify the flow regime of our simulations by computing the peak Reynolds number $Re_{\text{peak}}$,

$$Re_{\text{peak}} = \frac{\rho Q_{\text{peak}} D}{\mu A}, \tag{5.17}$$

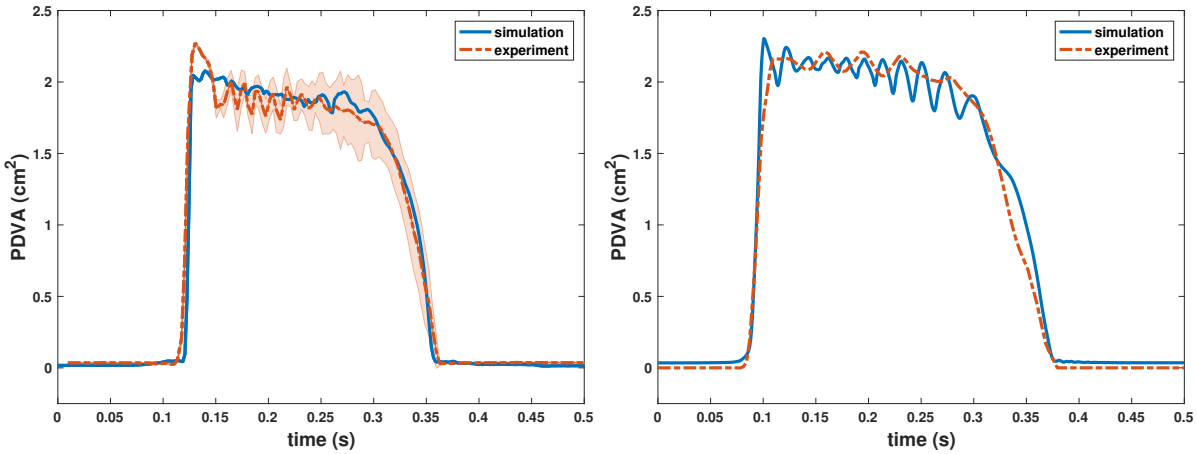


**(a)** Porcine aortic valve **(b)** Bovine pericardial valve

**Figure 5.6:** Comparisons between simulated and experimental projected dynamic valve area (PDVA) for the porcine aortic (a) and bovine pericardial (b) valves. (a) The experimental data (acquired using custom apparatus depicted in Figure 5.1b) are manually aligned with the beginning of the valve opening with the simulation data. The experimental PDVA measurement shown is the average PDVA over 10 consecutive cycles of data with shaded region showing where 95% of the data fall. (b) The experimental data are acquired using a high-speed videographic method, from which we reconstruct PDVA data via automatic image analysis via DataTank. Videographic data are available for only a single cycle for the pericardial BHV.

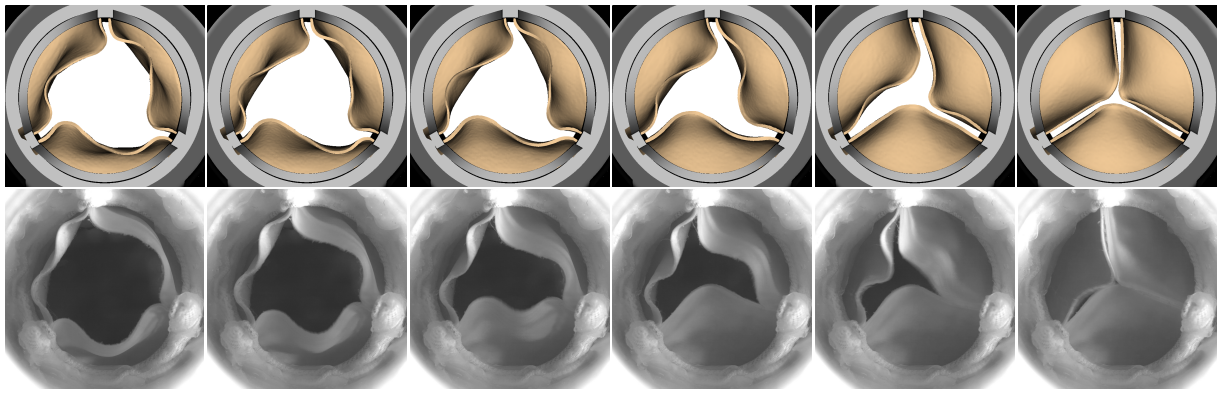

**Figure 5.7:** Detailed comparison of the bovine pericardial valve leaflet kinematics during closure from simulation (top) and experiment (bottom). The simulation captures the behavior of each of the leaflets closing one at a time (order: bottom → right → left leaflet) as observed in the experiment. The time increment between frames for simulation is 9.6 ms.

in which $\rho$ is the density, $Q_{\text{peak}}$ is the peak flow rate, $D$ is the diameter of the aortic test section, $\mu$ is the dynamic viscosity of the fluid, and $A$ is the cross-sectional area of the aortic test section. $Re_{\text{peak}}$ is 20,576 and 19,330 for the porcine tissue and bovine pericardial BHV, respectively.

We also compare the leaflet kinematics of the porcine tissue (Figures 5.9a and 5.10a) and bovine

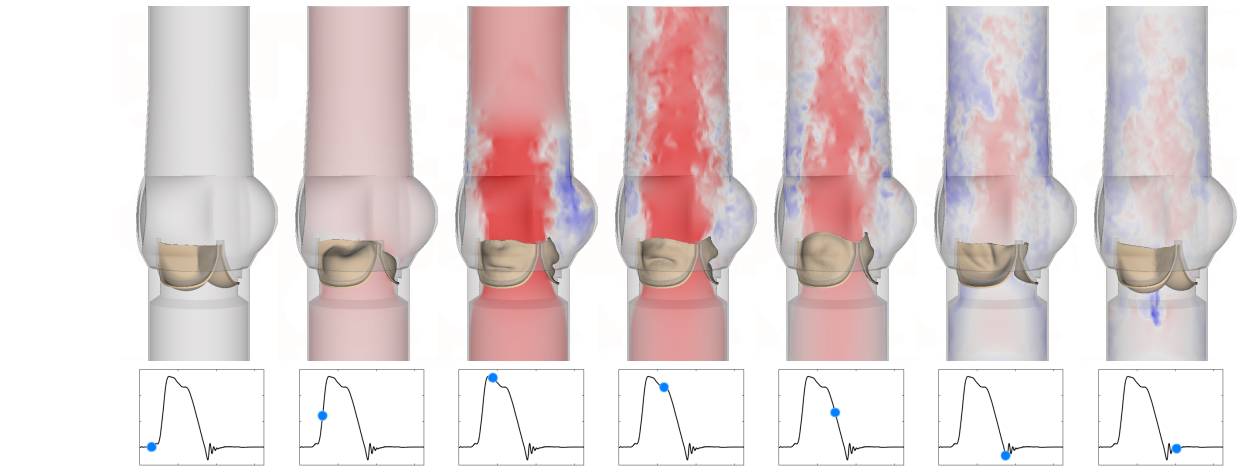

**(a)** Porcine aortic valve

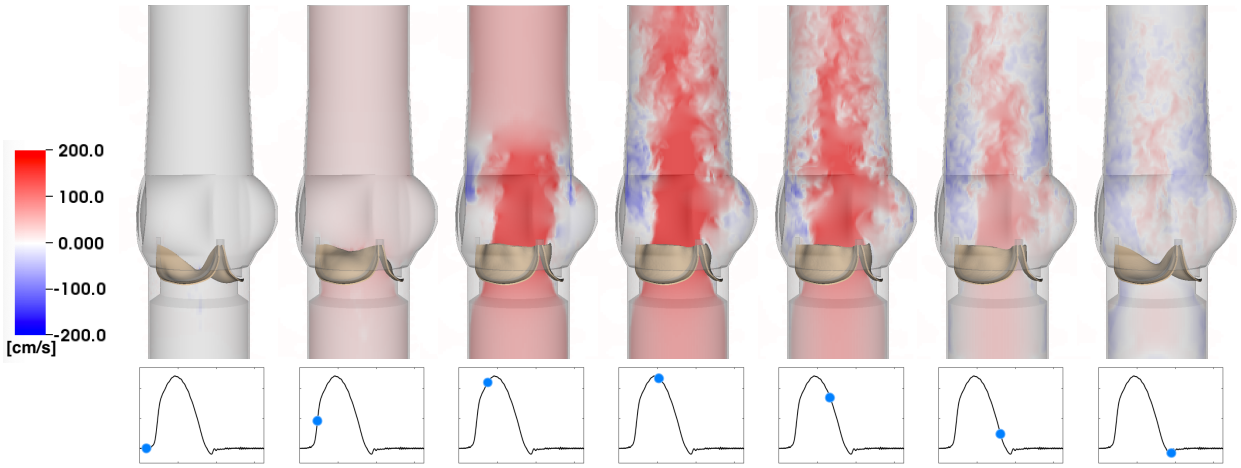


**(b)** Bovine pericardial valve

**Figure 5.8:** Cross-section view of simulated flow patterns using the porcine aortic (a) and bovine pericardial (b) valve models. The color shows the axial velocity through the aortic test section at the center plane, with red indicating forward flow and blue indicating reverse flow. (a) $Re_{\text{peak}} =$ 20,576. (b) $Re_{\text{peak}} =$ 19,330. The time increment between frames is 57.6 ms.

pericardial (Figures 5.9b and 5.10b) valves. One important difference between the two valves is the symmetry breaking in the pericardial leaflets, especially during closure. Because of the asymmetric fiber architecture in each of its leaflets, the bovine pericardial valve shows a swirling motion during closure, as also observed in real pericardial BHVs [85].

Differences between the porcine valve and bovine pericardial valve resulting from different fiber architectures are also clear in the stress distributions (Figure 5.11). The von Mises stresses on the valves are distributed according to the anisotropic material responses. The porcine valve shows

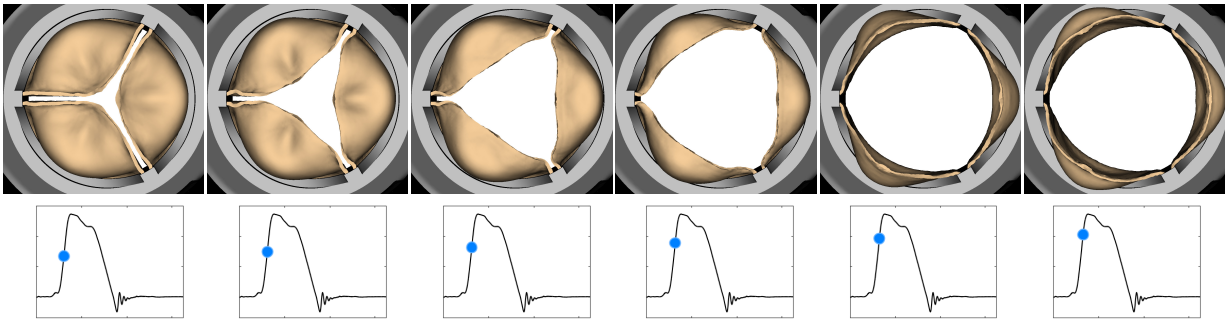

**(a)** Porcine aortic valve

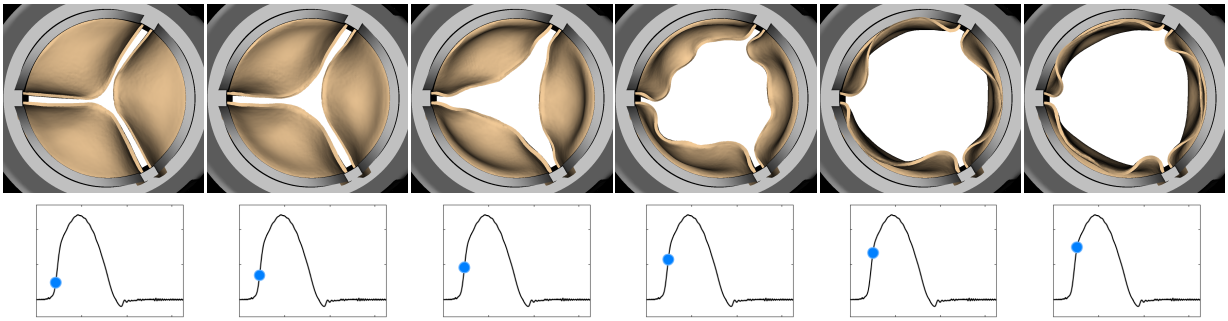

**(b)** Bovine pericardial valve

**Figure 5.9:** Leaflet kinematics of the porcine aortic (a) and bovine pericardial (b) valves during opening. (a) The time increment between frames is 1.92 ms. (b) The time increment between frames is 3.84 ms.

a stress distribution that is aligned from commissure to commissure when the valve is loaded in diastole (Figure 5.11a). The stress is also distributed symmetrically on each porcine leaflet during valve opening (Figure 5.11c), which is again concentrated around the commissures. In contrast, the bovine pericardial valve shows an asymmetric stress distribution, and the von Mises stresses are concentrated at one of each leaflet's commissures. The locations where stress is largest on the leaflet occur where the fibers collect at the commissures (Figure 5.11b). The opposite is true during valve opening, when the highest leaflet stresses occur near the free edges of the leaflets (Figure 5.11d). These patterns appear because the parts of the leaflets with less commissural support experience larger deformations.

### 5.3.1 Solution verification

We perform grid convergence studies to verify the level of consistency in our numerical results. We consider both dynamic and steady flow conditions at three different spatial resolutions. For the dynamic cases, we consider the consistency under grid refinement of all of the measurements

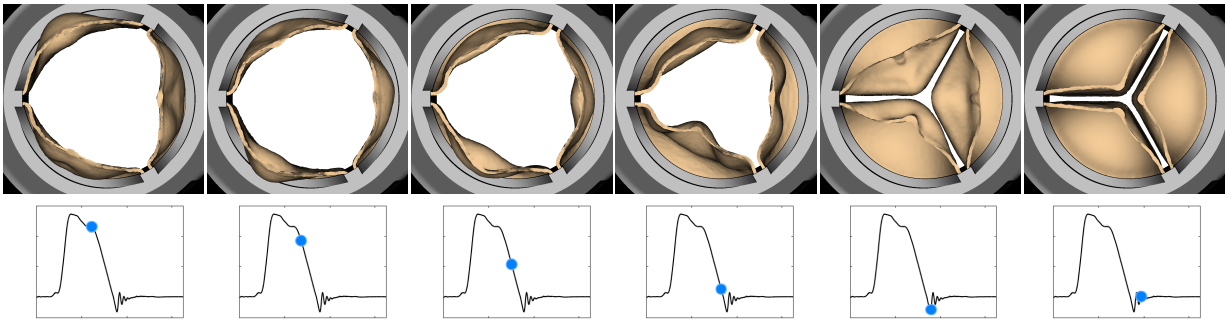

**(a)** Porcine aortic valve

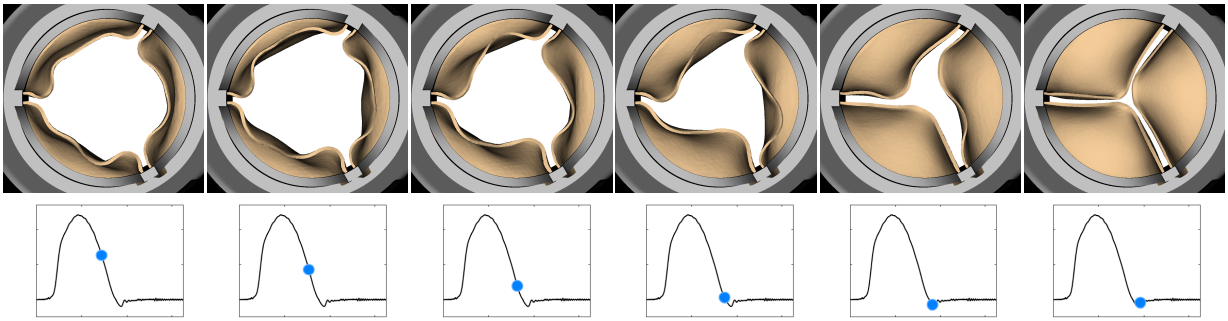

**(b)** Bovine pericardial valve

**Figure 5.10:** Leaflet kinematics of the porcine aortic (a) and bovine pericardial (b) valves during closure. (a) The time increment between frames is 9.6 ms. (b) The time increment between frames is 19.2 ms.

reported previously. For the steady flow conditions, we compute the time-averaged flow rates and the turbulence kinetic energy (TKE) between different resolutions, in addition to bulk measurements.

We use locally refined Cartesian grids with an effective fine-grid resolution that corresponds to a uniform $N \times N \times N$ grid, and we compare results obtained for $N = 192$, 256, and 320. The effective fine-grid Cartesian resolutions are approximately 0.53 mm ($N = 192$), 0.39 mm ($N = 256$), and 0.32 mm ($N = 320$). The average grid-spacings of meshes are 0.5 mm ($N = 192$), 0.4 mm ($N = 256$), and 0.3 mm ($N = 320$) for the aortic test section, 0.75 mm ($N = 192$), 0.59 mm ($N = 256$), and 0.45 mm ($N = 320$) for the porcine aortic valve, and 0.75 mm ($N = 192$, 256, and 320) with a wider range of grid-spacings for the bovine pericardial valve.

Figure 5.12 compares the bulk flow properties under grid refinement, indicating that our simulations are consistent under grid refinement. This suggests that the results reported are sufficiently resolved for these measurements by the resolutions considered therein. Tables 5.2, 5.3, 5.4, and 5.5 quantify the discrepancies relative to the experimental data under grid refinement, as well as the

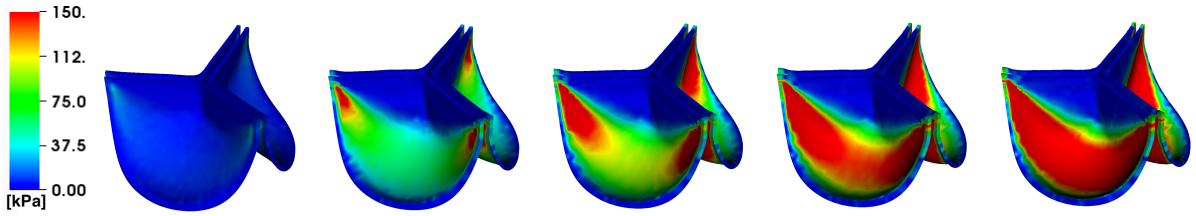


**(a)** Porcine aortic valve (diastole)

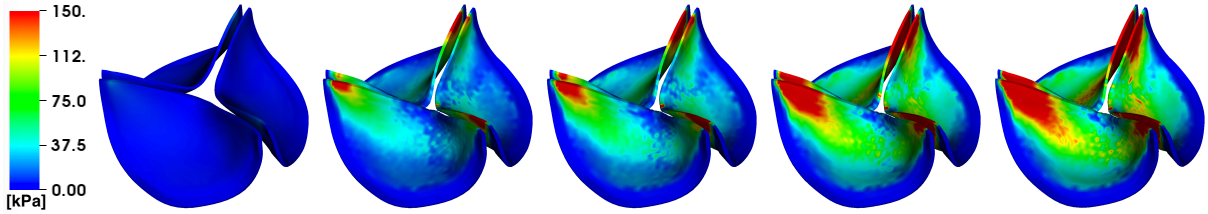


**(b)** Bovine pericardial valve (diastole)

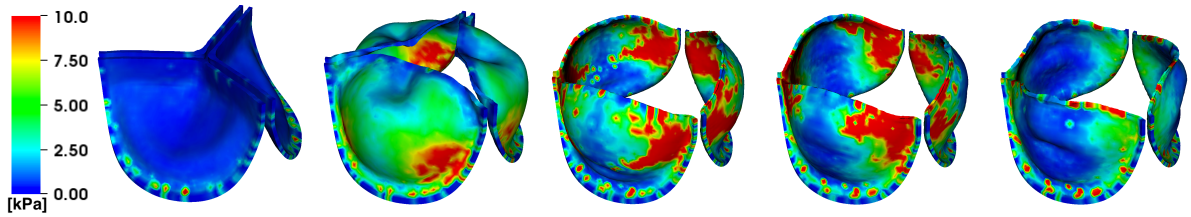


**(c)** Porcine aortic valve (systole)

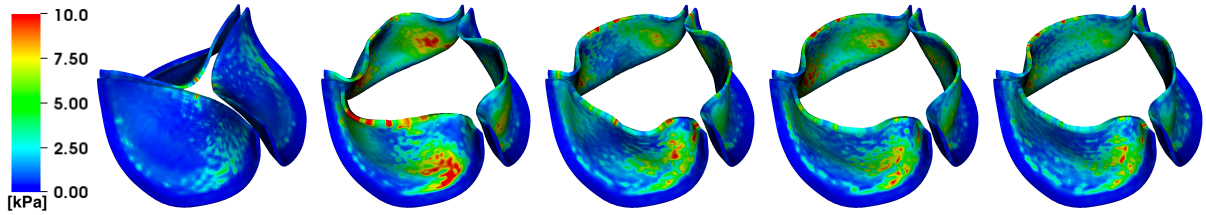


**(d)** Bovine pericardial valve (systole)

**Figure 5.11:** von Mises stress (kPa) on the porcine aortic (a), (c) and bovine pericardial (b), (d) valves during diastole (a)-(b) and systole (c)-(d). The time increment between frames in panels (a)-(b) is 30.72 ms, and the time increment between frames in panels (c)-(d) is 11.52 ms.

relative difference between resolutions ($N = 192$, $N = 256$, and $N = 320$). The relative differences are calculated by

$$\text{Normalized difference of } M^{N=192} \text{ and } M^{N=256} = \frac{\left\| M^{N=192} - M^{N=256} \right\|_{L^q(0,T)}}{\| M^{N=256} \|_{L^q(0,T)}}, \tag{5.18}$$

$$\text{Normalized difference of } M^{N=256} \text{ and } M^{N=320} = \frac{\left\| M^{N=256} - M^{N=320} \right\|_{L^q(0,T)}}{\| M^{N=320} \|_{L^q(0,T)}}, \tag{5.19}$$

in which $(0, T)$ indicates an integral over time, and $q = 2$ or $\infty$ for the $L^2$- and $L^\infty$-norms, respectively. This shows that the discrepancies in bulk flow measurements compared to the experimental data are

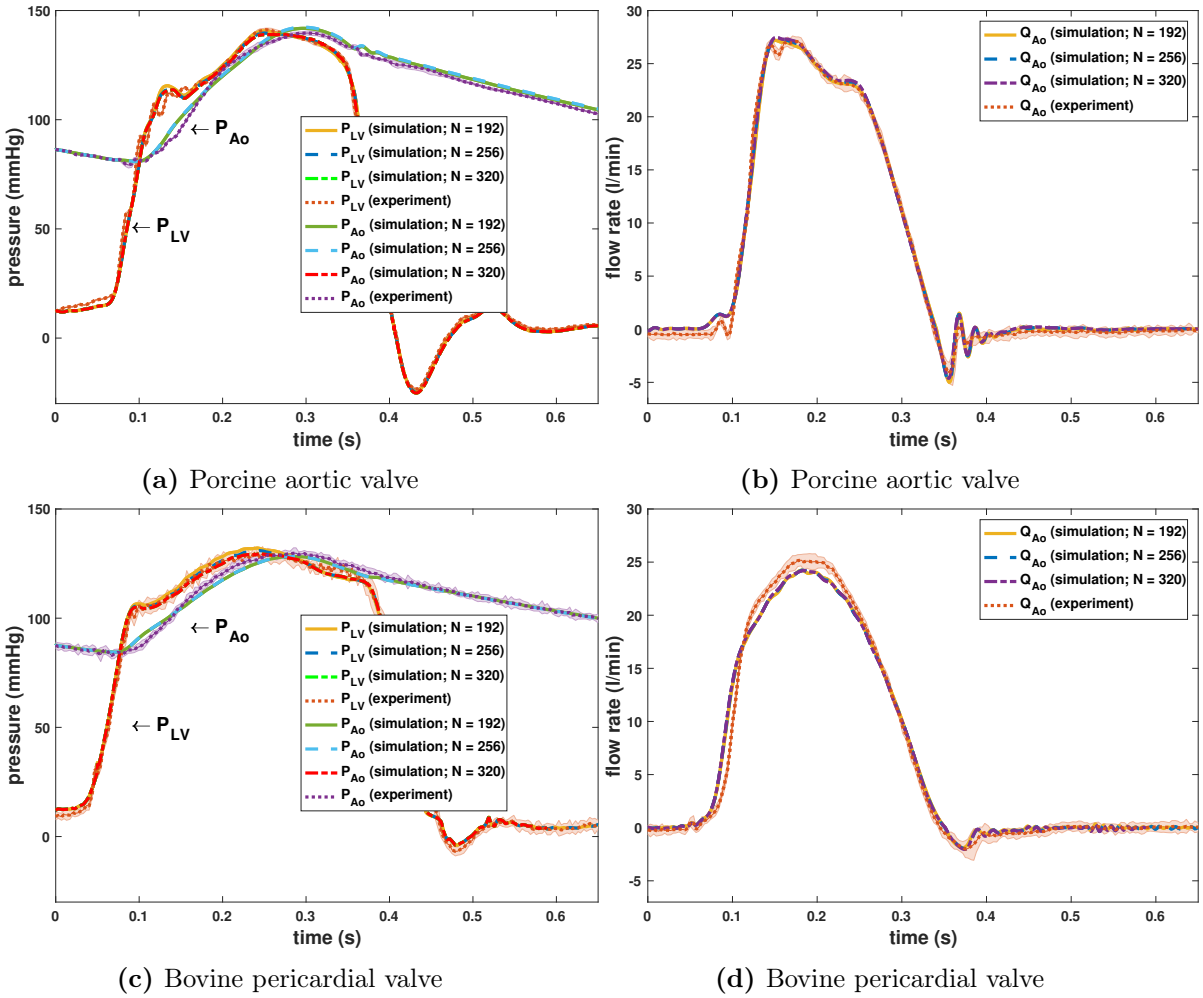


**(a)** Porcine aortic valve

**(b)** Porcine aortic valve

**(c)** Bovine pericardial valve

**(d)** Bovine pericardial valve

**Figure 5.12:** Grid refinement test corresponding to Figure 5.5. The bulk flow waveforms are consistent under grid refinement.

within 8.7% at all resolutions. The relative differences between successive resolutions are within 1.6%, indicating consistency under grid refinement. This suggests that the bulk properties are reasonably resolved by our FSI model of the BHVs at the higher spatial resolutions ($N = 256$ and $N = 320$).

The comparison of PDVA results is similar to that of other bulk measurements under grid refinement, as observed in Figure 5.12.

Figures 5.14 and 5.15 also give a qualitative sense of model consistency under grid refinement. Although Figures 5.14 and 5.15 indicate that additional small-scale flow features are generated by the model at higher spatial resolutions, the large scale flow features are consistent between grid resolutions.

We also observe that the time-averaged flow fields (Eq. (5.20)) as well as the flow profiles

**Table 5.2:** Comparisons of normalized $L^2$-norms of discrepancies in the bulk measurements between simulation and experiment*

| | Porcine aortic | | | Bovine pericardial | | |
|---|---|---|---|---|---|---|
| | $N = 192$ | $N = 256$ | Relative | $N = 192$ | $N = 256$ | Relative |
| $P_{\mathrm{LV}}$ | 3.6% | 3.4% | 0.73% | 5.2% | 4.6% | 1.1% |
| $P_{\mathrm{Ao}}$ | 1.7% | 1.9% | 0.33% | 1.4% | 1.4% | 0.09% |
| $Q_{\mathrm{Ao}}$ | 5.0% | 4.7% | 1.6% | 8.4% | 8.6% | 0.71% |

* Comparisons of $L^2$-norms of the discrepancies in the bulk measurements from the simulation and experiment shown in Figure 5.12 under the coarser ($N = 192$) and finer ($N = 256$) resolutions, normalized by the $L^2$-norms of the measurements from the experiment. Relative indicates the $L^2$-norms of the differences between the measurements from the two resolutions, normalized by the $L^2$-norms of the measurements from the finer ($N = 256$) case.

**Table 5.3:** Comparisons of normalized $L^2$-norms of discrepancies in the bulk measurements between simulation and experiment*

| | Porcine aortic | | | Bovine pericardial | | |
|---|---|---|---|---|---|---|
| | $N = 256$ | $N = 320$ | Relative | $N = 256$ | $N = 320$ | Relative |
| $P_{\mathrm{LV}}$ | 3.4% | 3.4% | 0.45% | 4.6% | 4.5% | 0.67% |
| $P_{\mathrm{Ao}}$ | 1.9% | 1.9% | 0.21% | 1.4% | 1.4% | 0.004% |
| $Q_{\mathrm{Ao}}$ | 4.7% | 4.8% | 0.74% | 8.6% | 8.7% | 0.43% |

* Comparisons of $L^2$-norms of the discrepancies in the bulk measurements from the simulation and experiment shown in Figure 5.12 under the finer ($N = 256$) and finest ($N = 320$) resolutions, normalized by the $L^2$-norms of the measurements from the experiment. Relative indicates the $L^2$-norms of the differences between the measurements from the two resolutions, normalized by the $L^2$-norms of the measurements from the finer ($N = 320$) case.

**Table 5.4:** Comparisons of normalized $L^\infty$-norms of discrepancies in the bulk measurements between simulation and experiment*

| | Porcine aortic | | | Bovine pericardial | | |
|---|---|---|---|---|---|---|
| | $N = 192$ | $N = 256$ | Relative | $N = 192$ | $N = 256$ | Relative |
| $P_{\mathrm{LV}}$ | 8.5% | 8.6% | 1.6% | 15.6% | 14.4% | 1.7% |
| $P_{\mathrm{Ao}}$ | 4.3% | 4.5% | 0.42% | 3.5% | 3.6% | 0.17% |
| $Q_{\mathrm{Ao}}$ | 11.6% | 9.5% | 2.4% | 19.2% | 20.2% | 1.4% |

* Comparisons of $L^\infty$-norms of the discrepancies in the bulk measurements from the simulation and experiment shown in Figure 5.12 between the coarser ($N = 192$) and finer ($N = 256$) resolutions, normalized by the $L^\infty$-norms of the measurements from the experiment. Relative indicates the $L^\infty$-norms of the differences between the measurements from the two resolutions, normalized by the $L^\infty$-norms of the measurements from the finer ($N = 256$) case.

(Figures 5.16 and 5.17) are in reasonable agreement between different spatial resolutions. The mean

**Table 5.5:** Comparisons of normalized $L^\infty$-norms of discrepancies in the bulk measurements between simulation and experiment*

| | Porcine aortic | | | Bovine pericardial | | |
|---|---|---|---|---|---|---|
| | $N = 256$ | $N = 320$ | Relative | $N = 256$ | $N = 320$ | Relative |
| $P_{\mathrm{LV}}$ | 8.6% | 8.6% | 1.5% | 14.4% | 14.1% | 1.1% |
| $P_{\mathrm{Ao}}$ | 4.5% | 4.5% | 0.31% | 3.6% | 3.6% | 0.001% |
| $Q_{\mathrm{Ao}}$ | 9.5% | 9.2% | 2.2% | 20.2% | 20.8% | 0.6% |

* Comparisons of $L^\infty$-norms of the discrepancies in the bulk measurements from the simulation and experiment shown in Figure 5.12 between the finer ($N = 256$) and finest ($N = 320$) resolutions, normalized by the $L^\infty$-norms of the measurements from the experiment. Relative indicates the $L^\infty$-norms of the differences between the measurements from the two resolutions, normalized by the $L^\infty$-norms of the measurements from the finer ($N = 320$) case.

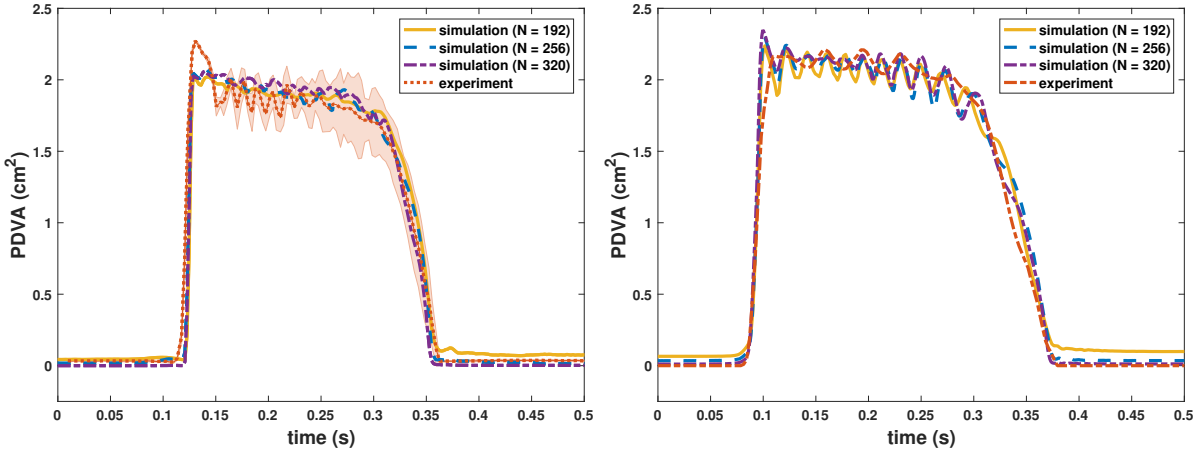


**(a)** Porcine aortic valve **(b)** Bovine pericardial valve

**Figure 5.13:** Grid refinement test corresponding to Figure 5.6. The PDVA results are consistent under grid refinement. This result is in agreement with the consistency under grid refinement demonstrated in Figure 5.12d.

flow is determined via

$$\overline{u}_i = \frac{1}{T_2 - T_1} \int_{T_1}^{T_2} u_i(\mathbf{x}, t)\, \mathrm{d}t, \quad i = 1, 2, 3, \tag{5.20}$$

We consider steady inflow conditions at two different flow rates: 100% and 50% of the maximum flow rate from the fully dynamic simulations. In particular, we find that the difference between $N = 256$ and $N = 320$ cases are small, and we conclude that $N = 256$ results are reasonably well resolved for large-scale flow measures.

We observe that the turbulence kinetic energy (Eq. (5.21)) as well as its profiles for each bovine

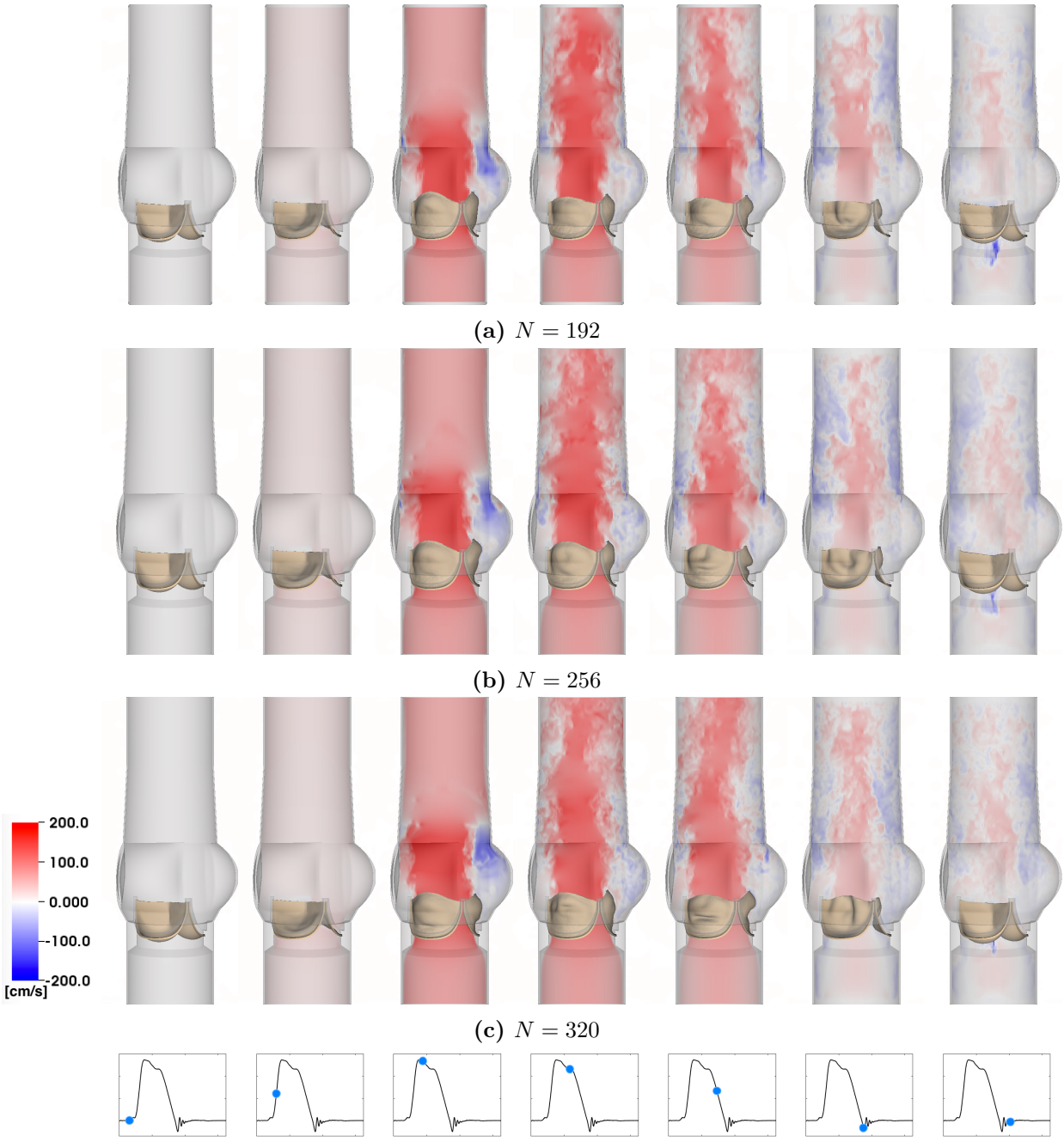


**(a)** $N = 192$

**(b)** $N = 256$

**(c)** $N = 320$

**Figure 5.14:** Grid refinement test corresponding to Figure 5.8a. Although additional small-scale flow features are generated by the model at higher spatial resolutions, the large scale flow features are consistent between grid resolutions.

pericardial valve case (Figures 5.18 and 5.19) still show some differences between different spatial

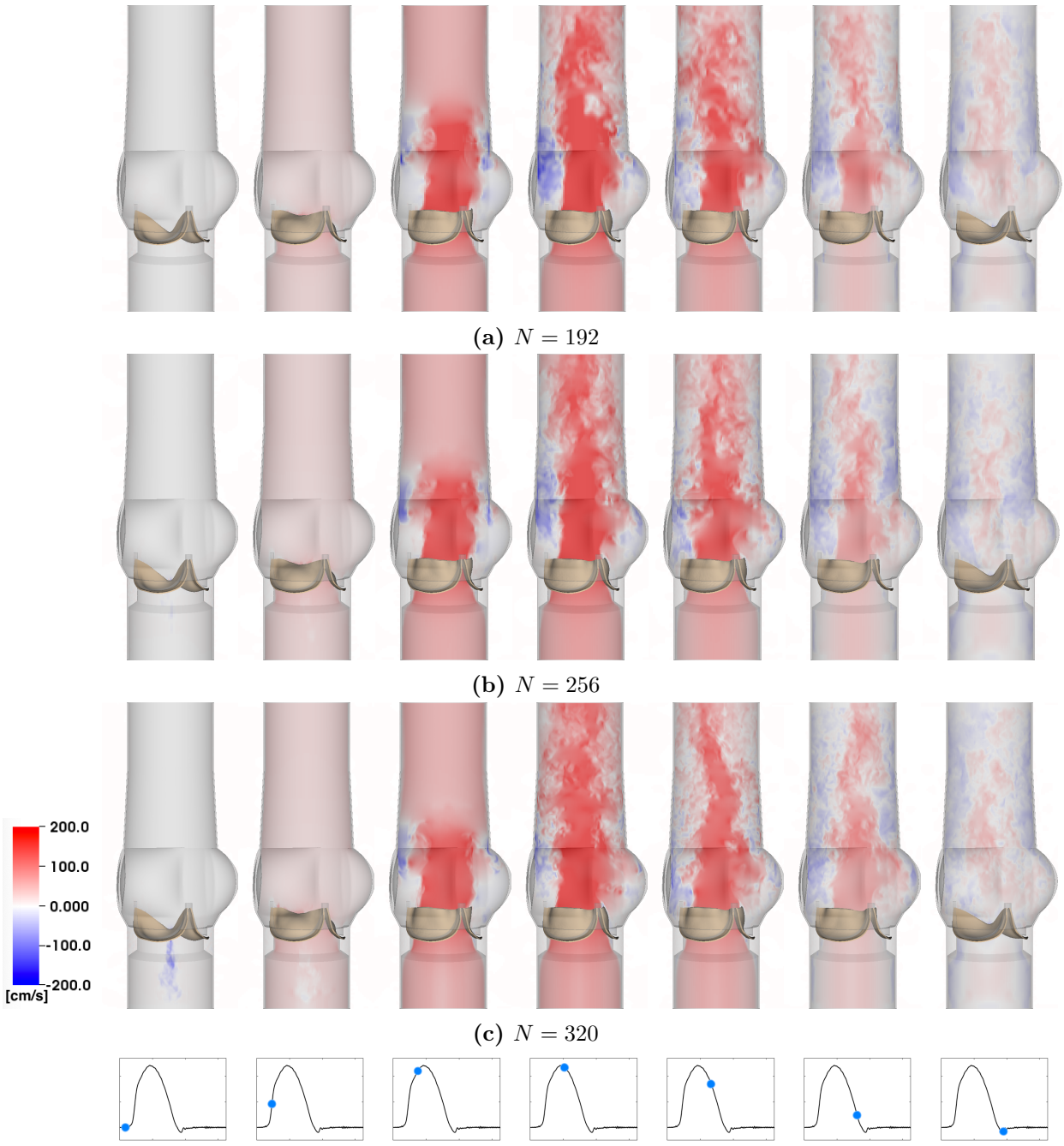


**(a)** $N = 192$

**(b)** $N = 256$

**(c)** $N = 320$

**Figure 5.15:** Grid refinement test corresponding to Figure 5.8b. Although additional small-scale flow features are generated by the model at higher spatial resolutions, the large scale flow features are consistent between grid resolutions.

resolutions. Turbulence kinetic energy is defined by

$$TKE \equiv \frac{1}{2}\overline{u_i' u_i'}, \tag{5.21}$$

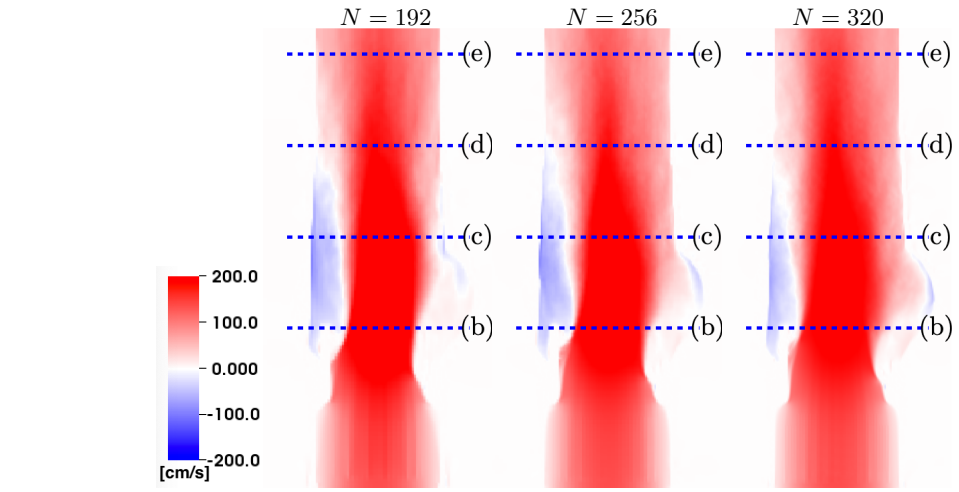


**(a)** Axial velocity ($u_y$) fields

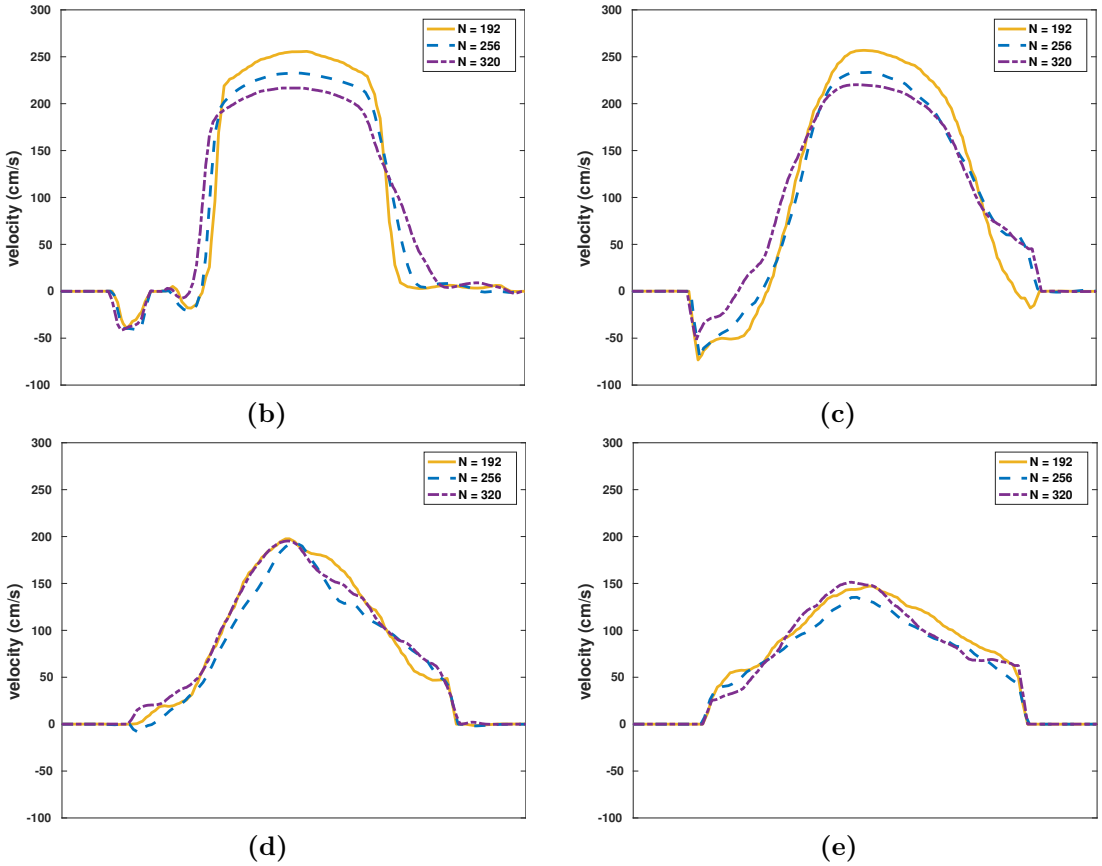


**Figure 5.16:** (a) Cross-section view of time-averaged flow fields and (b)-(e) flow profiles at different locations downstream of the valve for the bovine pericardial valve model. We use steady flow at the maximum flow rate. In panel (a), the color shows the time-averaged axial velocity through the aortic test section at the center plane, with red indicating forward flow and blue indicating reverse flow. Blue dashed lines show where the profiles shown in panels (b)-(e) are obtained. The axial flow fields agree to approximately 1.6% in the $L^2$ norm for $N = 256$ and $N = 320$, with peak velocities differing by approximately 7%.

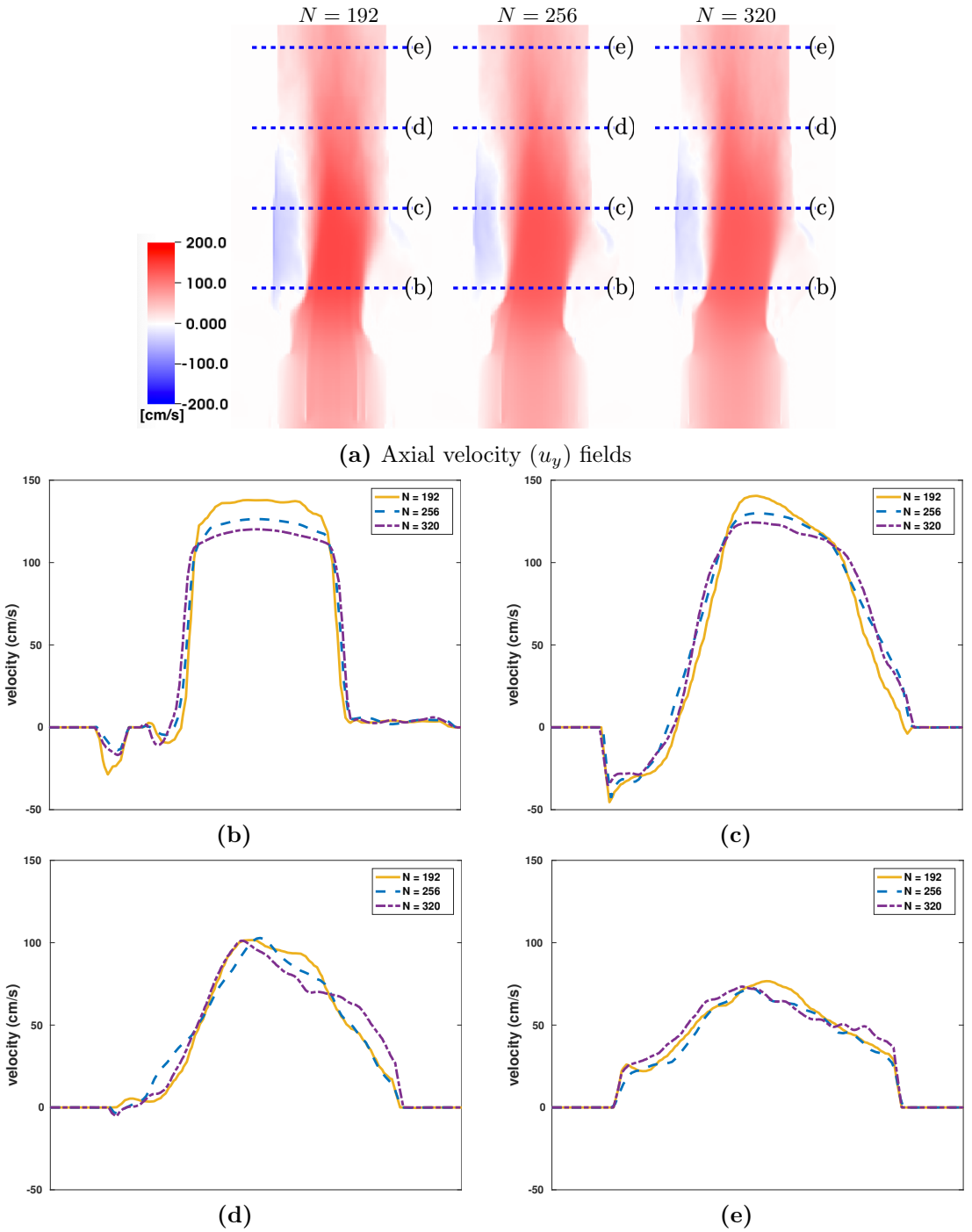


**(a)** Axial velocity ($u_y$) fields

**Figure 5.17:** (a) Cross-section view of time-averaged flow fields and (b)-(e) flow profiles at different locations downstream of the valve for the bovine pericardial valve model. We use steady flow at 50% of the maximum flow rate. In panel (a), the color shows the time-averaged axial velocity through the aortic test section at the center plane, with red indicating forward flow and blue indicating reverse flow. Blue dashed lines show where the profiles shown in panels (b)-(e) are obtained. The flow fields agree to within approximately 1.1% in the $L^2$ norm, with peak velocities agreeing to within approximately 4%.

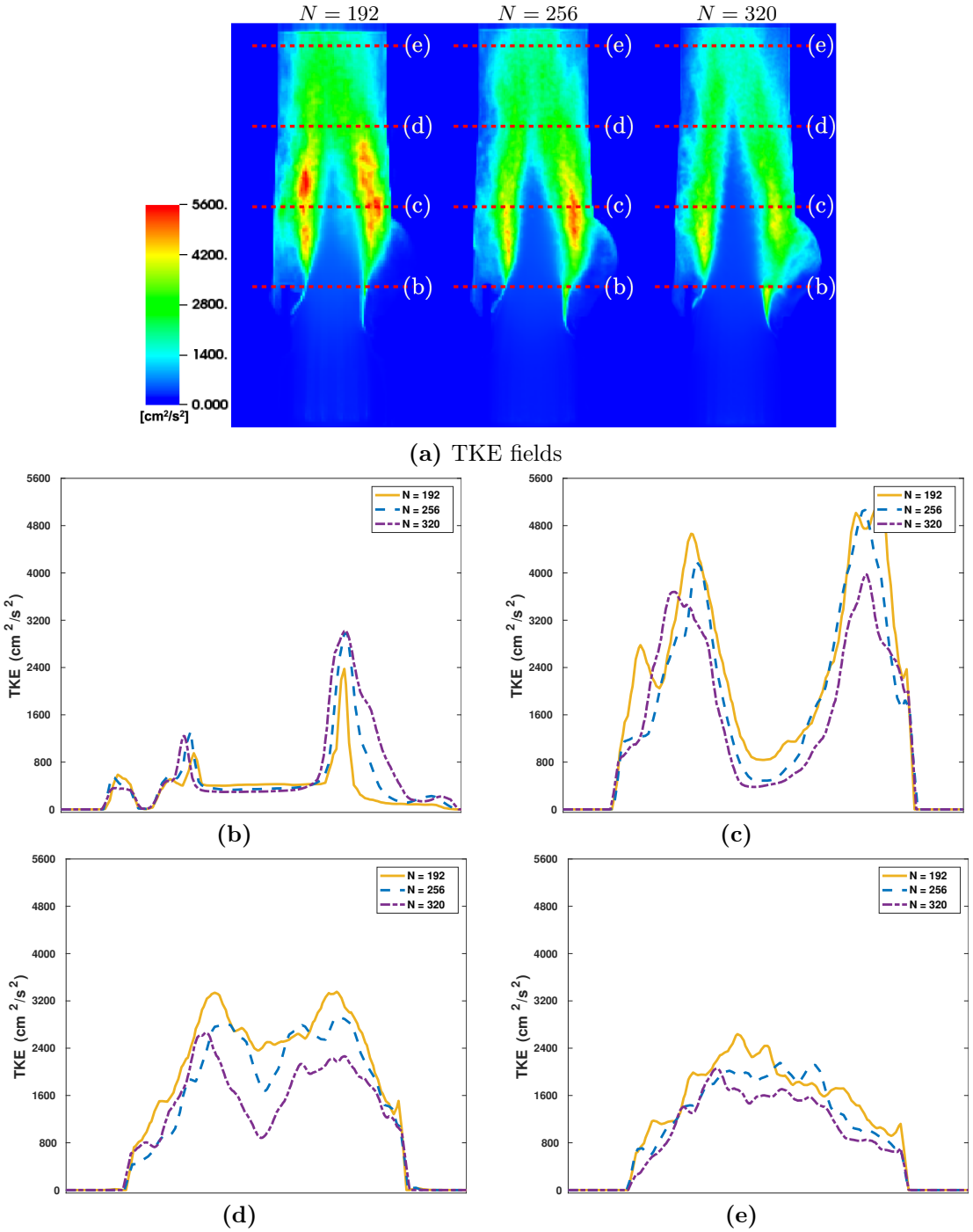


**Figure 5.18:** (a) Cross-section view of turbulence kinetic energy (TKE) fields and (b)-(e) TKE profiles at different locations downstream of the valve for the bovine pericardial valve model. We use steady flow at the maximum flow rate. In panel (a), the color shows the magnitude of TKE through the aortic test section at the center plane. Red dashed lines show where the profiles shown in panels (b)-(e) are obtained. The $L^2$ differences are on the order of 10% between $N = 256$ and $N = 320$, with peak values of TKE differing by approximately 17.5%.

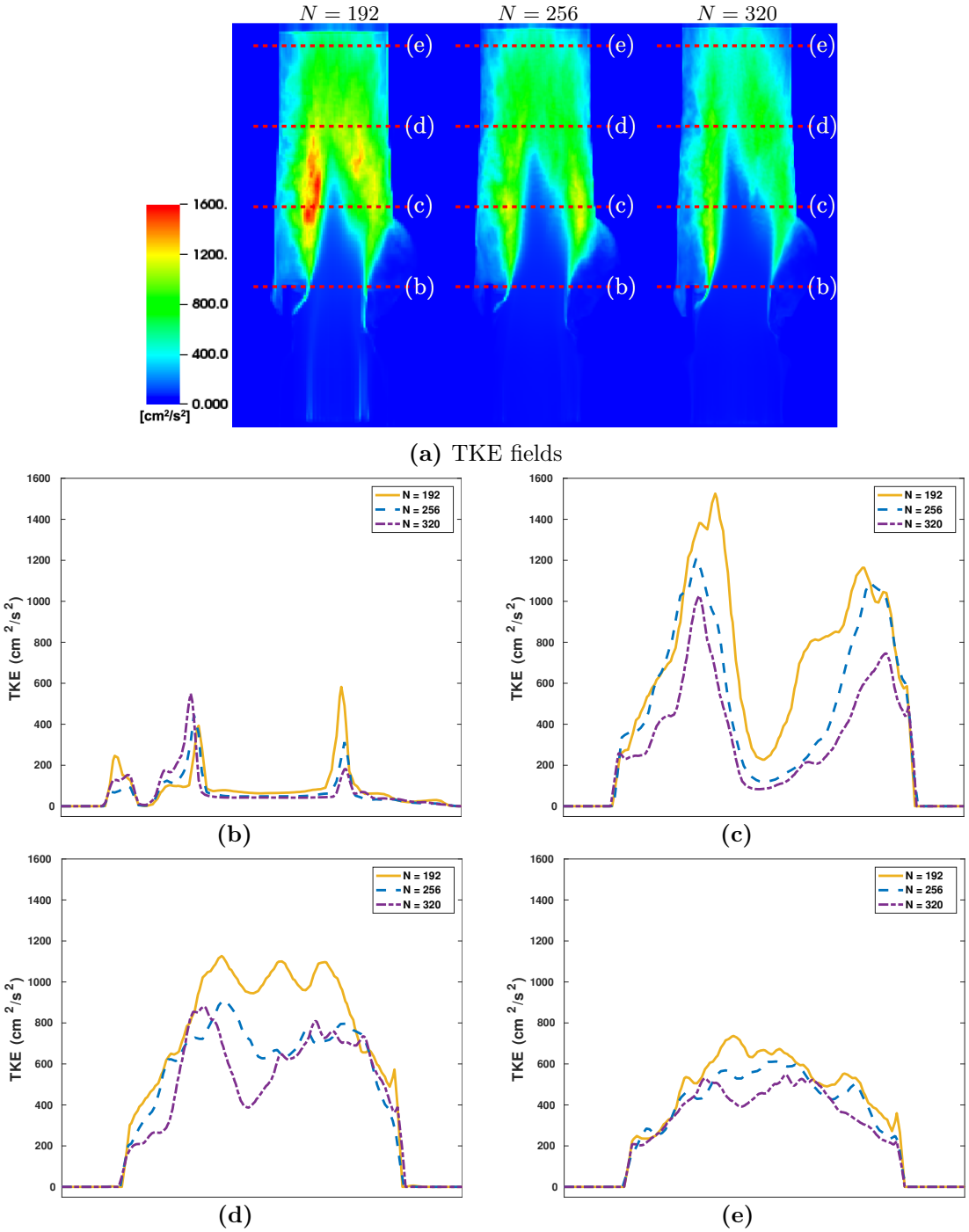


**Figure 5.19:** (a) Cross-section view of turbulence kinetic energy (TKE) fields and (b)-(e) TKE profiles at different locations downstream of the valve for the bovine pericardial valve model. We use steady flow at 50% of the maximum flow rate. In panel (a), the color shows the magnitude of TKE through the aortic test section at the center plane. Red dashed lines show where the profiles shown in panels (b)-(e) are obtained. The $L^2$ differences are on the order of 10% between $N = 256$ and $N = 320$, with peak values of TKE differing by approximately 1.5%.

in which $u_i' = u_i - \overline{u}_i$ is the fluctuating velocity. We again consider steady inflow conditions at two different flow rates: 100% and 50% of the maximum flow rate. At the maximum flow rate, the axial flow fields agree to approximately 1.6% in the $L^2$ norm for $N = 256$ and $N = 320$, with peak velocities differing by approximately 7%. At 50% of maximum flow, the flow fields agree to within approximately 1.1% in the $L^2$ norm, with peak velocities agreeing to within approximately 4%. The differences are larger for the TKE, with $L^2$ differences on the order of 10% and maximum TKE values differing by 17.5% at the maximum flow rate but to within approximately 1.5% at 50% of the maximum flow rate. The mean flow and TKE profiles are in reasonable agreement and appear to be converging under grid refinement. Although we find that the differences between $N = 256$ and $N = 320$ are not large, these results suggest that we are able to resolve the large-scale flow features, but higher spatial resolution is clearly needed to fully resolve the flow fields.

It is apparent, however, that the peak flow velocities for the coarser cases are larger than those of the finer cases. The observed differences in the peak flow velocities are a consequence of the numerical scheme that is used to couple the Lagrangian and Eulerian variables in the present IB method. Specifically, the use of regularized delta functions in the Lagrangian-Eulerian coupling operators causes the "effective" numerical sizes of the Lagrangian structures to be larger than their "actual" sizes, with a length scale that is related to the regularization width of the delta function. In practice, the width of the regularized delta function is tied to the Cartesian grid spacing. This results in an effective narrowing of the flow path that is on the order of a few Cartesian grid cell widths, which is more pronounced on coarser grids. The effect of this narrowing is apparent in Figures 5.16 and 5.17 and results in higher flow velocities at the same volumetric flow rates. This effect also diminishes under grid refinement, as observed in the grid convergence study.

Figures 5.20 and 5.21 qualitatively compare the leaflet kinematics for $N = 192$, $N = 256$, and $N = 320$ during valve opening and closure for the porcine aortic valve and bovine pericardial valve, respectively. These results indicate that the computed structural deformations are consistent under grid refinement.

Comparing the stress distributions of the leaflets in two grid resolutions (Figures 5.22 and 5.23) also confirms that the stress distributions are consistent under grid refinement.

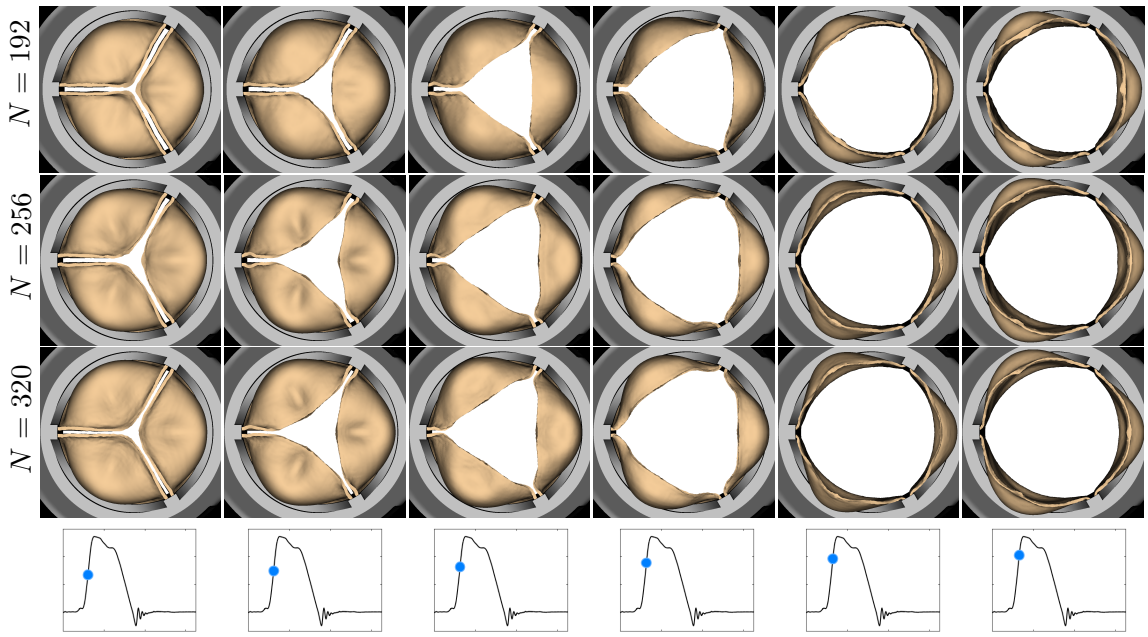


**(a)**

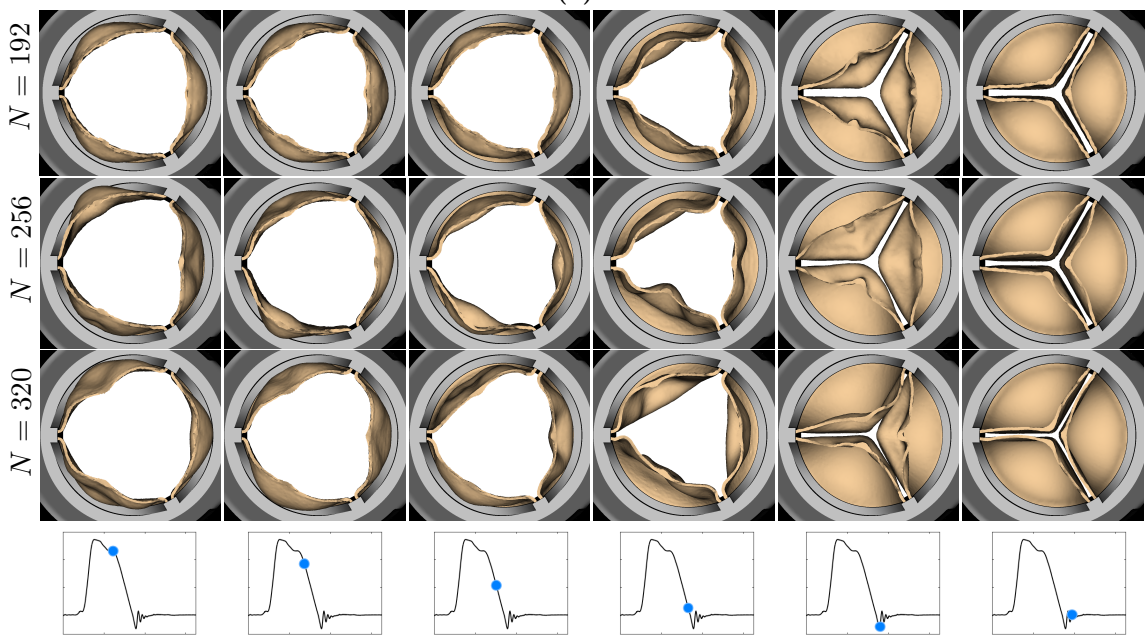


**(b)**

**Figure 5.20:** Leaflet kinematics of the porcine aortic valve during (a) valve opening and (b) valve closure under grid refinement. *Top panels*: $N = 192$, *middle panels*: $N = 256$, and *bottom panels*: $N = 320$. The time increment between frames in panel (a) is 1.92 ms, and the time increment between frames in panel (b) is 9.6 ms.

### 5.3.2 Comparison between saline and newtonian blood analogue test fluids

The goal of this study is to present our FSI models of bioprosthetic heart valves in the in vitro pulse duplicator system in the same setting as the completed experiments, which use saline as the

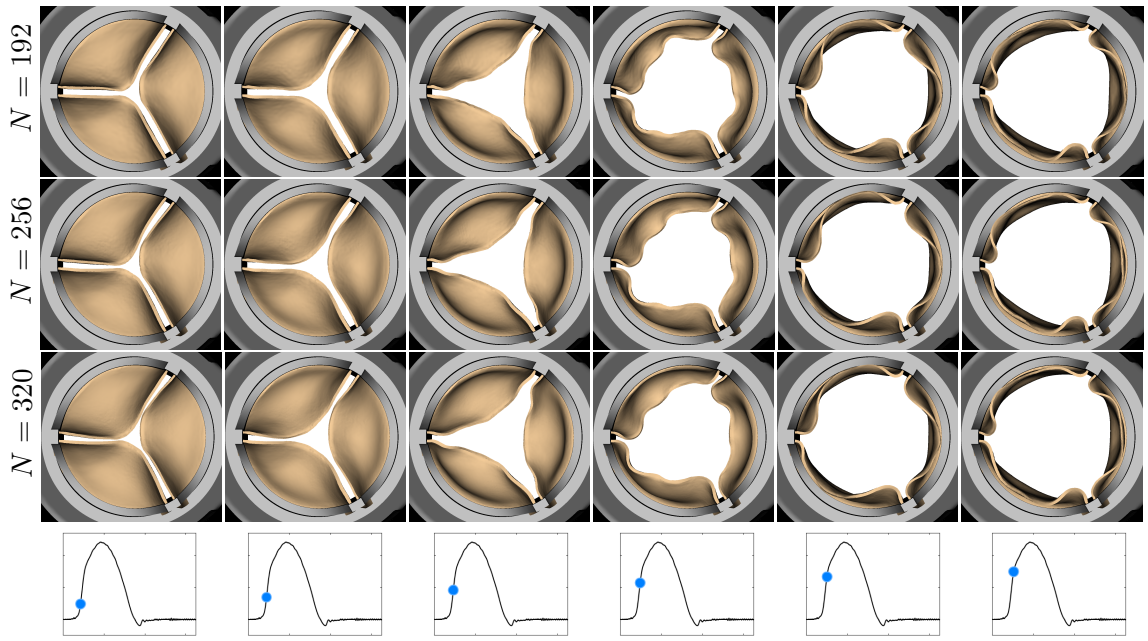


**(a)**

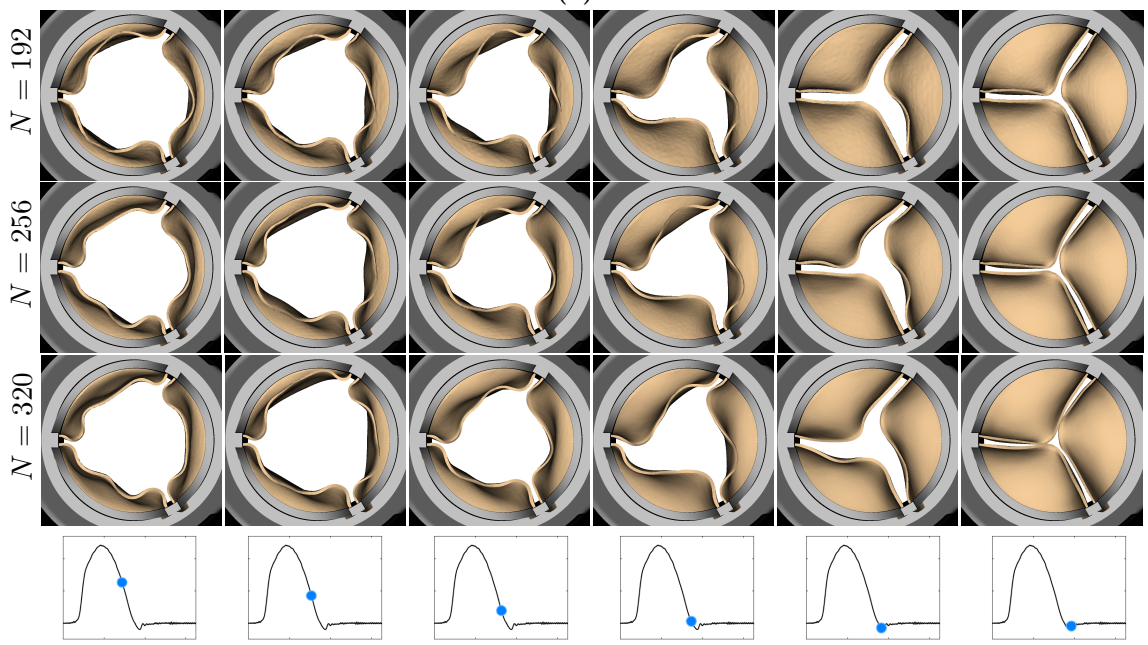


**(b)**

**Figure 5.21:** Leaflet kinematics of the bovine pericardial valve during (a) valve opening and (b) valve closure under grid refinement. *Top panels*: $N = 192$, *middle panels*: $N = 256$, and *bottom panels*: $N = 320$. The time increment between frames in panel (a) is 3.84 ms, and the time increment between frames in panel (b) is 19.2 ms.

test fluid. Even so, we performed additional simulations with a Newtonian blood analogue fluid with density 1.0 g cm$^{-3}$ and viscosity 3.5 cP to show that our FSI models can be used in such flow regime

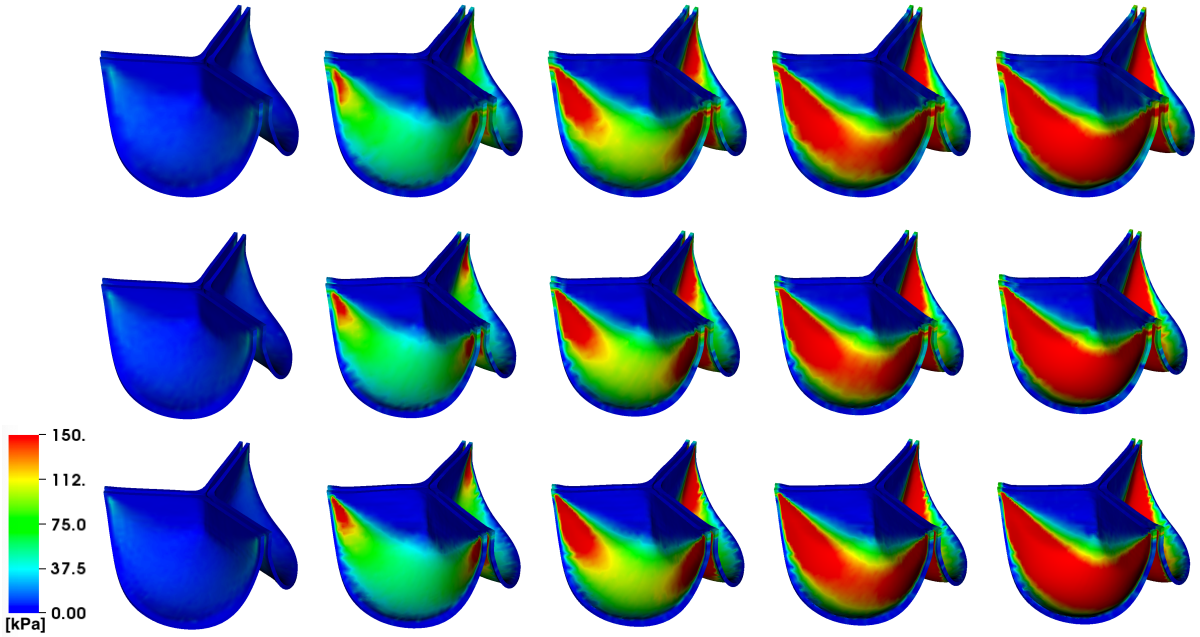


(a)

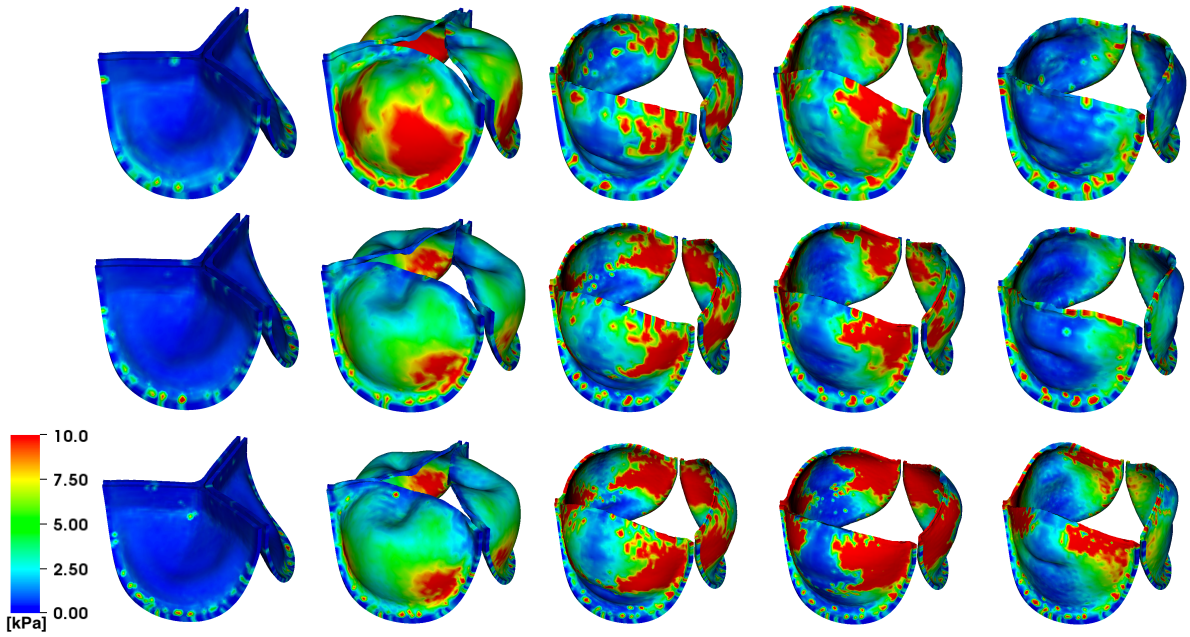


(b)

**Figure 5.22:** von Mises stress (kPa) on the porcine aortic valve during (a) valve closure and (b) valve opening under grid refinement. *Top panels*: $N = 192$, *middle panels*: $N = 256$, and *bottom panels*: $N = 320$ for both cases. The time increment between frames in panel (a) is 30.72 ms, and the time increment between frames in panel (b) is 11.52 ms.

without numerical instabilities (Figures 5.24 and 5.25). We are also interested in understanding the influence of using saline as compared to a more realistic blood analogue fluid in in vitro testing. To

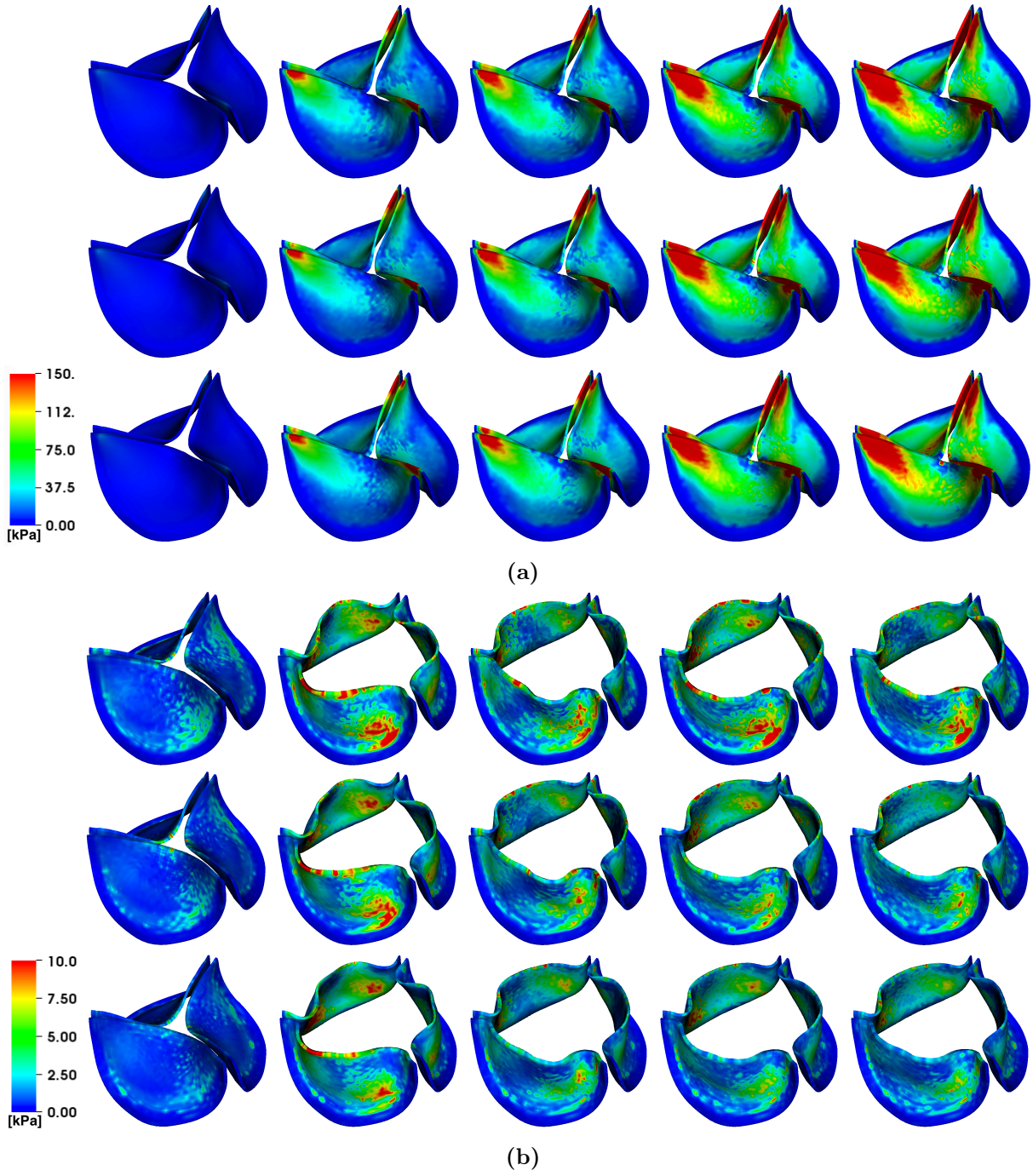


**Figure 5.23:** von Mises stress (kPa) on the porcine aortic valve during (a) valve closure and (b) valve opening under grid refinement. *Top panels*: $N = 192$, *middle panels*: $N = 256$, and *bottom panels*: $N = 320$ for both cases. The time increment between frames in panel (a) is 30.72 ms, and the time increment between frames in panel (b) is 11.52 ms.

compare the predictions of the model for different test fluids, we perform simulations at the finer resolution ($N = 256$) for both pulsatile and steady mean simulations. For the comparison of the

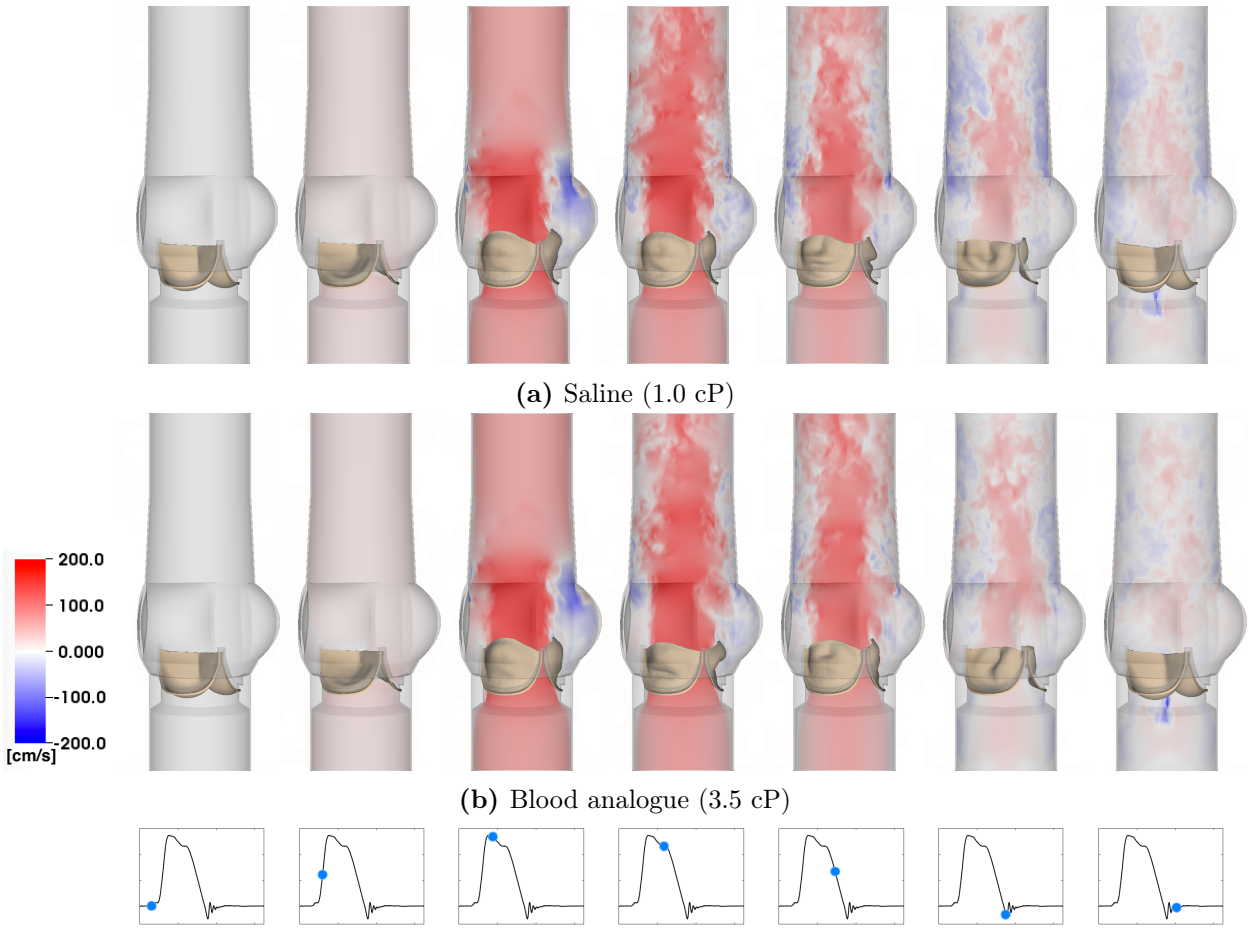


**(a)** Saline (1.0 cP)

**(b)** Blood analogue (3.5 cP)

**Figure 5.24:** Cross-section view of simulated flow patterns for the porcine aortic valve model using (a) saline with density 1.0 g cm$^{-3}$ and viscosity 1.0 cP versus (b) Newtonian blood analogue with density 1.0 g cm$^{-3}$ and viscosity 3.5 cP. The color shows the axial velocity through the aortic test section at the center plane, with red indicating forward flow and blue indicating reverse flow. (a) $Re_{\text{peak}} = 20{,}576$. (b) $Re_{\text{peak}} = 5{,}879$. The time increment between frames is 57.6 ms.

steady mean simulation, we only show the results for the bovine pericardial valve case. The porcine aortic valve model yields similar results and is not shown.

Our simulations indicate that the large scale flow structures are very similar between saline and the blood analogue fluid (Figures 5.24, 5.25, and 5.26). However, we observed differences in the small-scale turbulent flow structures present between saline and blood analogue fluid case (Figure 5.27), especially in the maximum steady flow case (Figure 5.27a). This is expected because of the larger Reynolds number associated with saline compared to the blood analogue.

Figures 5.28 and 5.29 show that the leaflet kinematics for saline versus the blood analogue fluid are similar because the leaflet kinematics are driven mostly by large-scale flow features.

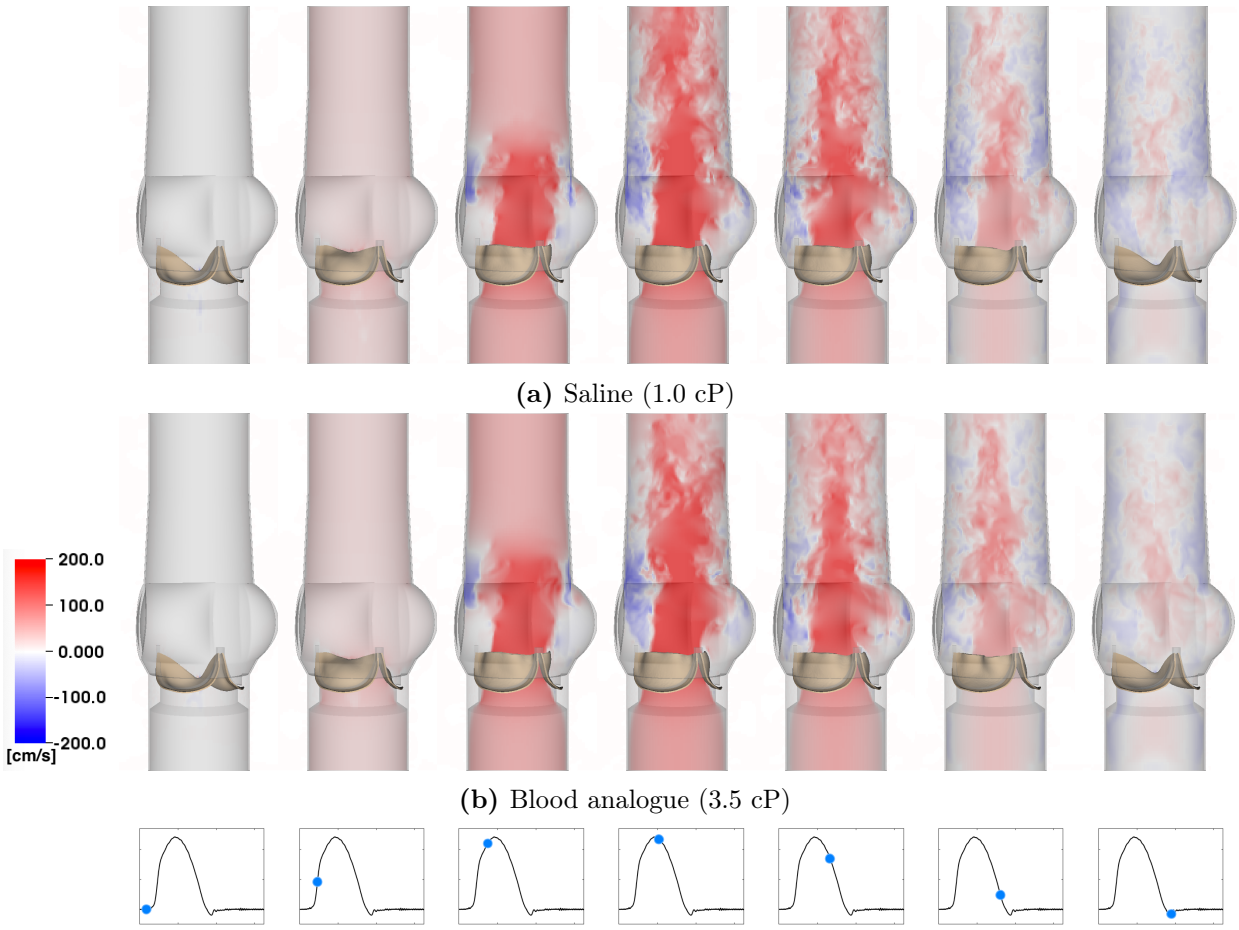


**(a)** Saline (1.0 cP)

**(b)** Blood analogue (3.5 cP)

**Figure 5.25:** Cross-section view of simulated flow patterns for the bovine pericardial valve model using (a) saline with density 1.0 g cm$^{-3}$ and viscosity 1.0 cP versus (b) Newtonian blood analogue with density 1.0 g cm$^{-3}$ and viscosity 3.5 cP. The color shows the axial velocity through the aortic test section at the center plane, with red indicating forward flow and blue indicating reverse flow. (a) $Re_{\text{peak}} = 19{,}330$. (b) $Re_{\text{peak}} = 5{,}523$. The time increment between frames is 57.6 ms.

## 5.4 Discussion

This study has developed FSI models of BHVs in an experimental pulse-duplicator platform. Our leaflet models include anisotropic descriptions of the leaflet biomechanics that are based on experimental tensile test data. In addition, we use experimental pressure and flow data obtained from the pulse-duplicator systems to establish realistic boundary models for the detailed FSI models. These boundary models are calibrated in isolation from the rest of the system, independent of the FSI model of the valves. The simulated pressures, flow rates, and leaflet kinematics all emerge from integrating these three model components, and the motion of the leaflets, including the timing of valve opening and closing, is not prescribed. Further, because the flow rate is not imposed in the

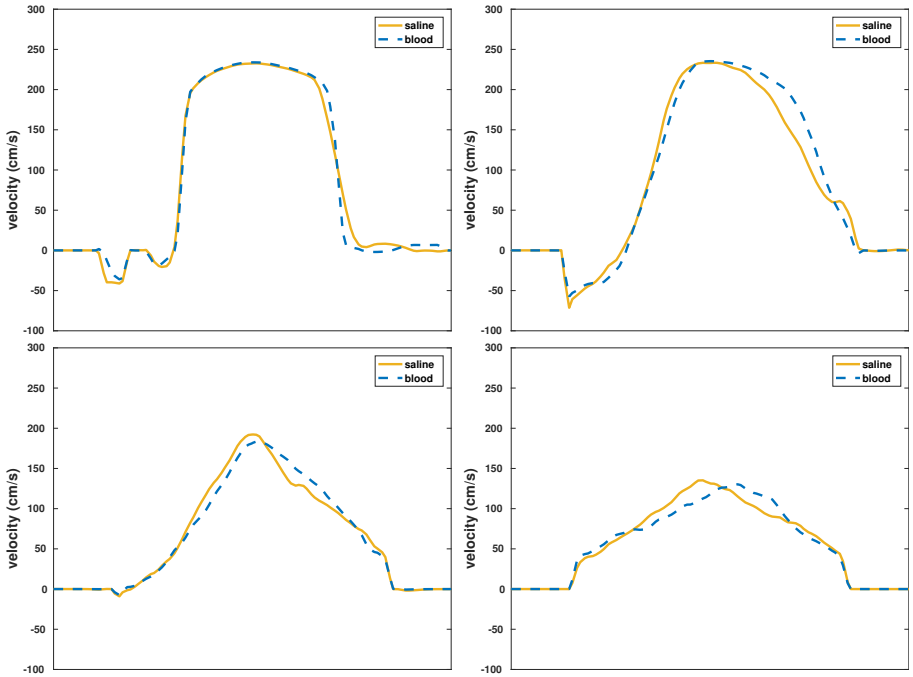


**(a)** Maximum steady flow rate

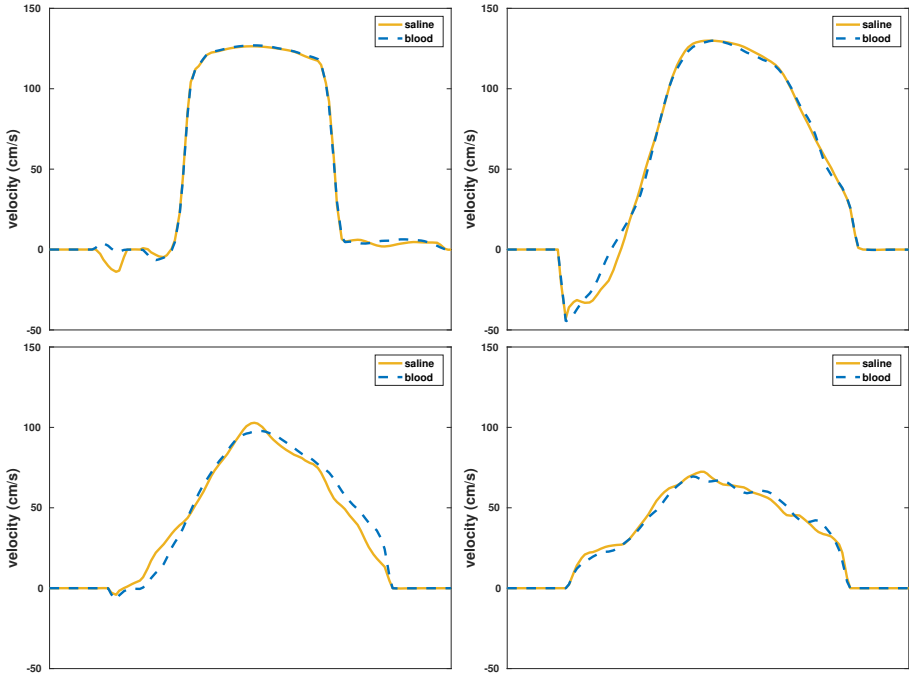


**(b)** 50% maximum steady flow rate

**Figure 5.26:** (a) Cross-section view of time-averaged axial velocity profiles at different locations downstream of the valve for the bovine pericardial valve model. We use steady flow at (a) the maximum and (b) 50% of the maximum flow rate. Flow profiles are show at the same locations as indicated in Figures 5.16 and 5.17.

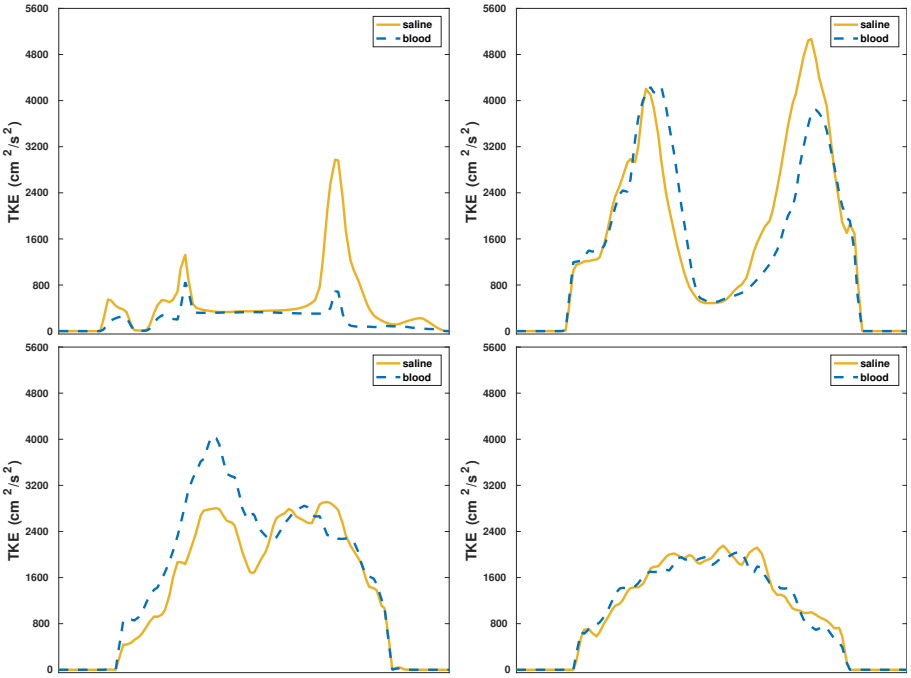


**(a)** Maximum steady flow rate

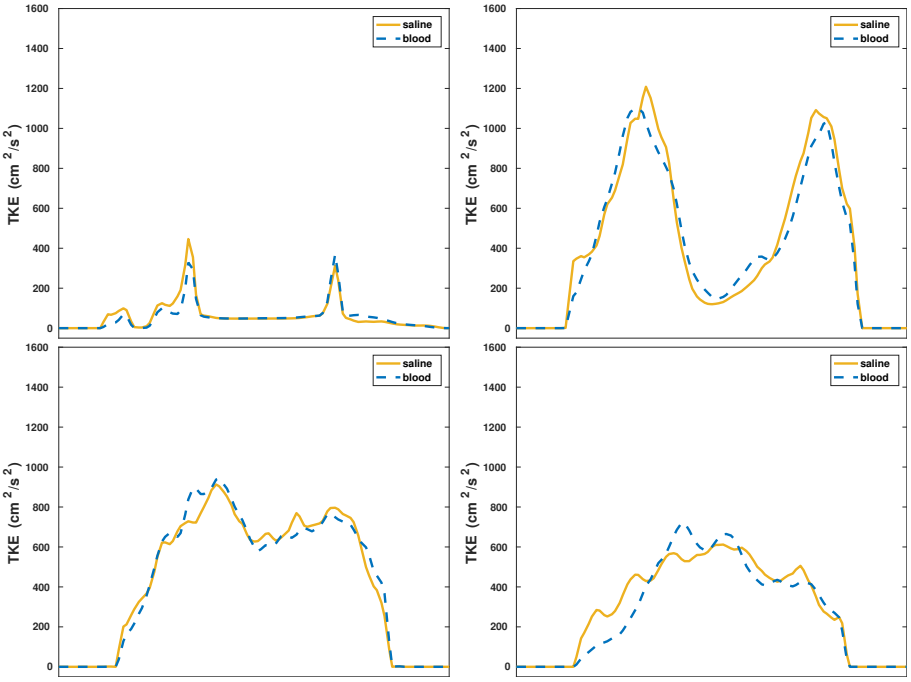


**(b)** 50% maximum steady flow rate

**Figure 5.27:** (a) Cross-section view of time-averaged turbulence kinetic energy (TKE) profiles at different locations downstream of the valve for the bovine pericardial valve model. We use steady flow at (a) the maximum and (b) 50% of the maximum flow rate. TKE profiles are show at the same locations as indicated in Figures 5.18 and 5.19.

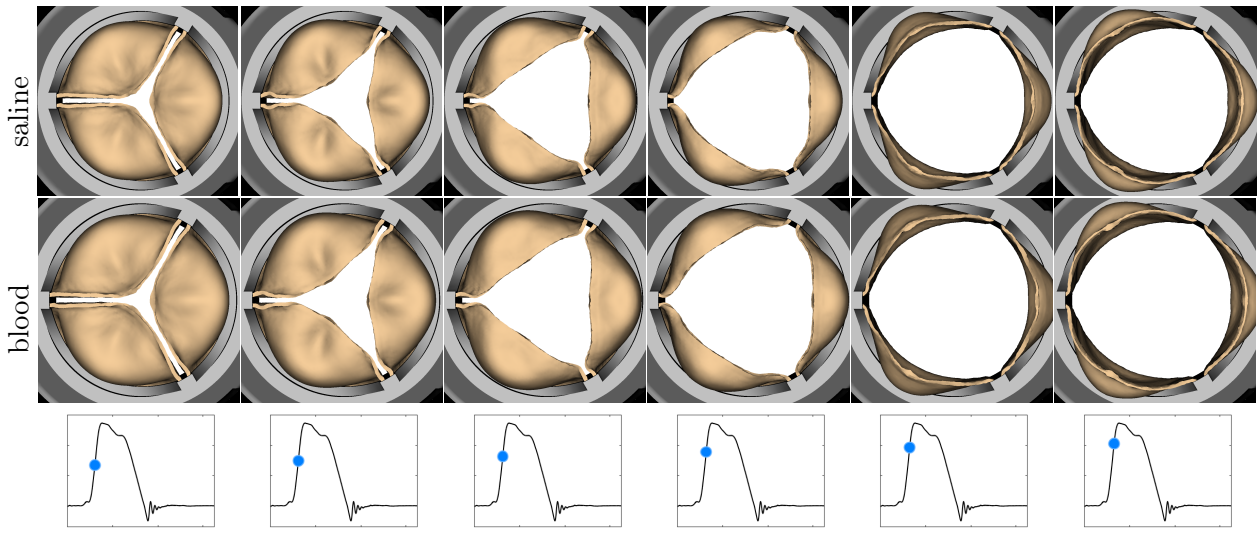


**(a)**

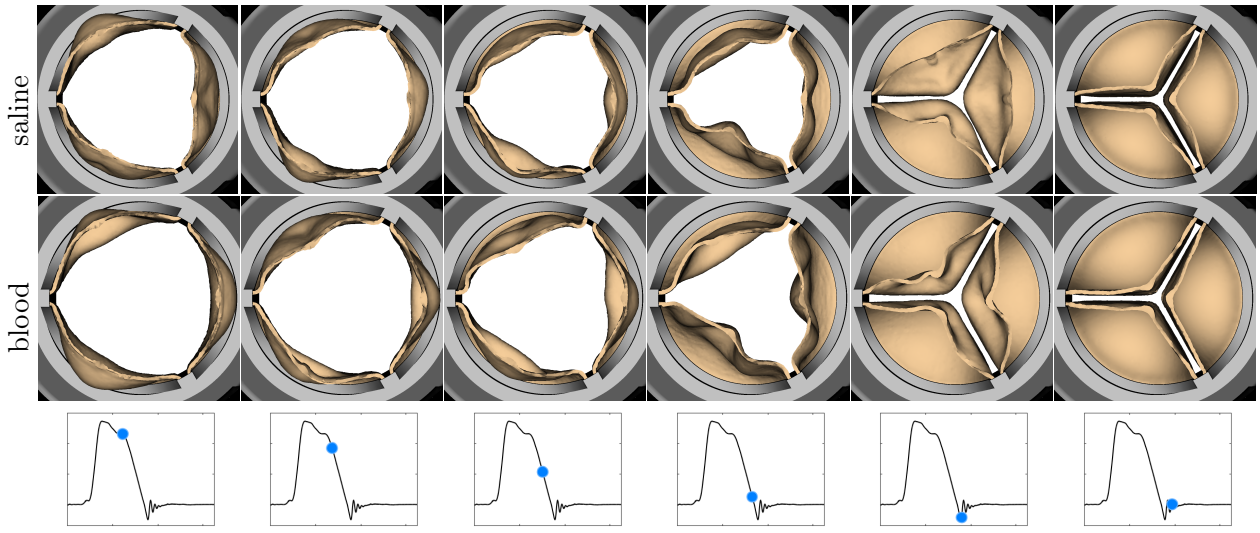


**(b)**

**Figure 5.28:** Comparison of leaflet kinematics of the porcine aortic valve during (a) valve opening and (b) valve closure between saline and blood analogue. The time increment between frames in panel (a) is 1.92 ms, and the time increment between frames in panel (b) is 9.6 ms.

model, and because the time-dependent configuration of the valve determines the resistance of the aortic test section, achieving both pressures and flow rates that are in good agreement with the experimental data represents a nontrivial test of the model.

The numerical results detailed in Figure 5.5 show excellent agreement in flow rates, pressures, valve open areas, and the timing of valve opening and closure between the simulations and experiments. For instance, the experimental flow rate oscillations that are present during valve closure in the

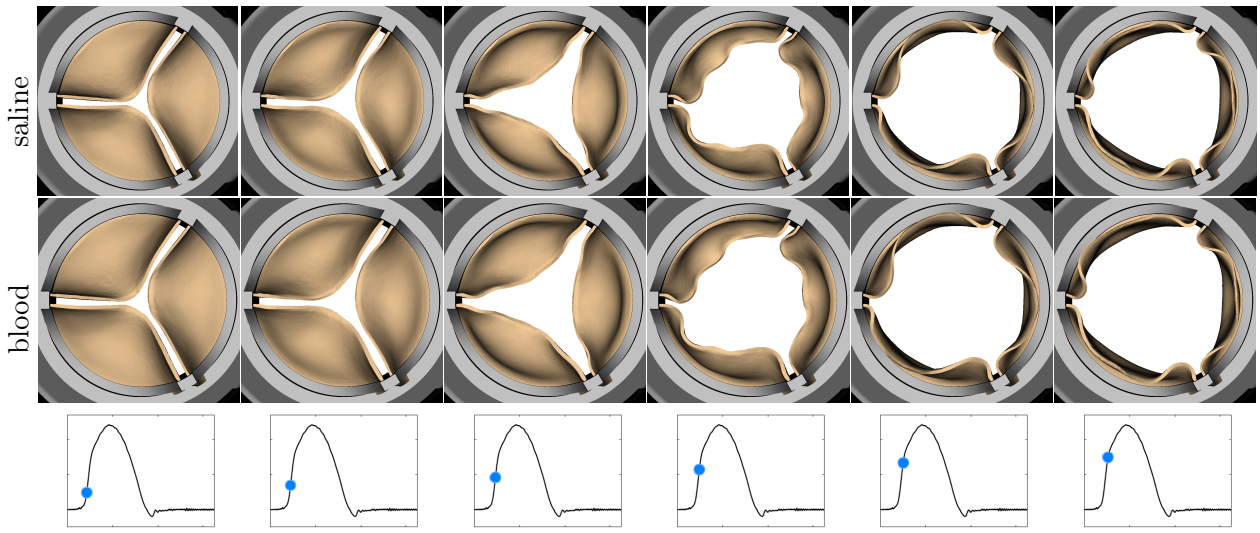


**(a)**

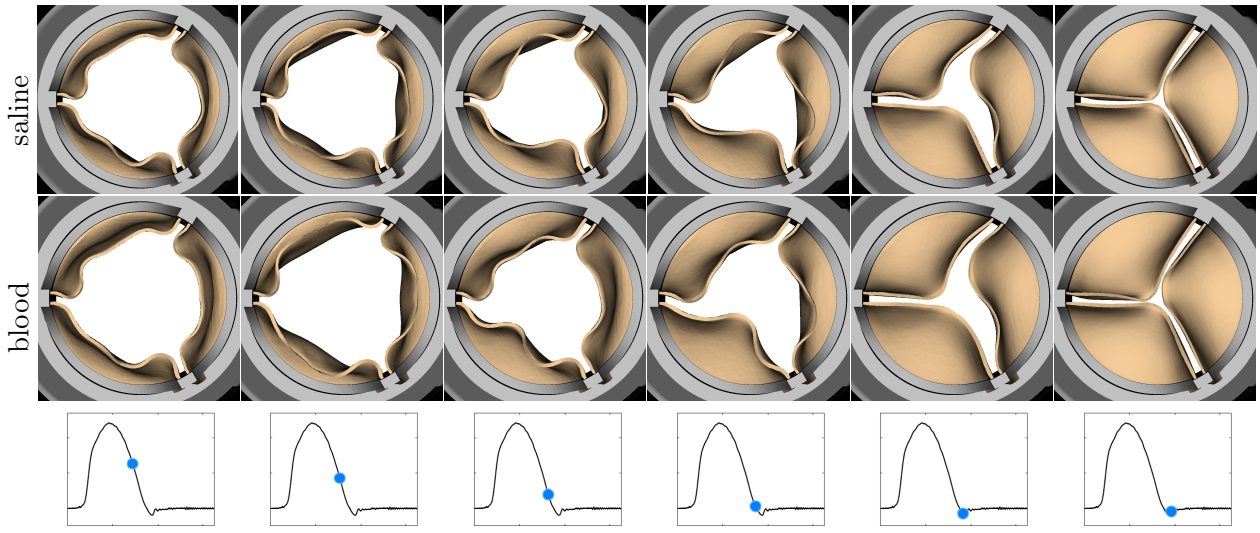


**(b)**

**Figure 5.29:** Comparison of leaflet kinematics of the bovine pericardial valve during (a) valve opening and (b) valve closure between saline and blood analogue. The time increment between frames in panel (a) is 3.84 ms, and the time increment between frames in panel (b) is 19.2 ms.

porcine aortic valve (Figure 5.5b) are physical because they come from the interaction between the momentum of the fluid and the compliance of the system, and these oscillations are captured by the computational model. We observe from the bovine pericardial BHV case that a more comprehensive reduced-order model of the upstream components of the pulse-duplicator system, including the pump, VIA, left ventricle, left atrium, and mitral valve, allows us to capture system dynamics, including closure (Figure 5.5d), more completely. Table 5.1 shows the $L^2$- and $L^\infty$-norms of the discrepancies

in the simulation results relative to the experimental measurements. In particular, the $L^2$-differences demonstrate good quantitative agreement, in which the relative discrepancies are within 4.7% for the porcine aortic valve and 8.6% for the bovine pericardial valve. These results show that our valve models generate leaflet kinematics that yield realistic pressures and flow rates in the fully coupled FSI models.

The experimental and computational leaflet kinematics are assessed using PDVA (Figures 5.6a and 5.6b). The PDVA measurements for the porcine aortic valve indicate reasonable agreement between simulations and experiments. There is a key difference in the techniques used to acquire these data. An electro-optical system (Figure 5.1b) was used to measure PDVA directly for the porcine aortic valve. For the bovine pericardial valve, PDVA was calculated indirectly using automatic image analysis via DataTank from videographic images. An advantage of the electro-optical subsystem is that it is calibrated with a reference area at the same location as the valve in the test section, but high-speed video is not available for this system. In contrast, although high-speed video is available for the pericardial BHV as shown in Figure 5.7, the image analysis method uses an estimated area-to-pixel scaling. In addition, the frame rate (400 fps) of the high-speed video of bovine pericardial valve is not sufficient to capture the full dynamic response. Consequently, we are missing data needed to resolve the full dynamic waveform. We plan to use higher speed ($\geq$5000 fps) videography in future work to quantify leaflet motion more completely. An important limitation of the present model is that we do observe discrepancies between the computational and experimental leaflet fluttering frequencies and amplitudes. BHVs are known to be viscoelastic [86], and fully viscoelastic models may be needed to achieve better agreement between simulation and experiment. At present, however, experimentally constrained viscoelastic models of BHV biomaterials suitable for three-dimensional mechanical analyses appear to be lacking. The structural models could be improved by incorporating additional experimental data that characterize the flexural properties of the valve leaflets.

Detailed comparisons of the leaflet kinematics for the bovine pericardial BHV showed that the leaflets closed one at a time both in the experiment and simulation (Figure 5.7). This result indicates that the overall kinematics are in reasonable agreement between the experiment and our model. We speculate that this may be because each of the leaflets has slightly different size and geometric features, along with the contribution from its fiber structure. Alternatively, flow instabilities may induce the sequential closure of the valve leaflets.

The large-scale flow features for the porcine aortic and bovine pericardial valves are similar (Figure 5.8). We also observe additional small-scale turbulent flow features at current spatial resolutions, which are also present in physiological flow regimes [87]. $Re_{\text{peak}}$ for both cases is approximately 20,000, which clearly motivates the need for further studies on the treatment of turbulence in these types of models. In the present study, we perform implicit large-eddy simulation (ILES) using high-resolution slope limiters, based on the piecewise parabolic method (PPM) [46, 47, 88, 89], to model the flow field. Explicit LES methods have not yet been completely developed for the present IB approach to FSI. We plan to compare ILES [46, 47, 88, 89] and explicit LES [90, 91] models for cardiovascular flows in future work. The similarity in the large-scale flow features for the two BHVs suggests that it is important to consider the leaflet kinematics in addition to the flow patterns in comparing different BHVs. Studying leaflet kinematics could also be important in identifying the factors that affect the durability of different BHVs.

Differences in the porcine and bovine pericardial leaflet kinematics are particularly prominent during leaflet closure (Figures 5.9 and 5.10). Specifically, the twisting motion during closure that we see in the bovine pericardial valve results from the asymmetric alignment of its fibers. This is also evident in stress analyses of the leaflets. Differences in stress distributions (Figure 5.11) are caused by the reduced strain at one of two commissure points of each of the bovine pericardial leaflets, whereas the stress distributions in the porcine BHV model reflects the symmetric fiber architecture of the porcine valve cusps. Also, unlike the porcine aortic valve, the pericardial valve lacks nodes of Arantius, which are intrinsic anatomic structures in native aortic valve leaflets. It has been hypothesized that the nodes may play a role in distributing and equalizing leaflet closing stresses [92]. We also observe that the porcine BHV leaflets experience higher stresses, which may also explain why porcine BHVs have a greater tendency to develop leaflet tears with regurgitation compared to bovine pericardial BHV [93, 94]. The stress concentrations at the commissures of the bovine pericardial BHV also agrees with the known failure regions for bovine pericardial BHVs [95, 96].

The present study has several limitations. Although we report 10 consecutive cycles of experimental data, one future aim is to better quantify the uncertainty associated with cycle-to-cycle variability in the experiments, and to integrate this uncertainty into our computational models. We shall also quantify variability in the leaflet kinematics along with variability in the pressure and flow rate measurements by collecting high-speed video and data over multiple cycles. We also have

not yet systematically performed sensitivity analysis or uncertainty quantification of the model. Performing such analyses is crucial for establishing the credibility of the model but is challenging because of the substantial computational requirements of such analyses. We also plan to validate the flow fields by particle image velocimetry (PIV) under different conditions, as well as using a blood analogue (dynamic viscosity of 3–4 cP) as our test fluid. With PIV, we also plan to perform direct comparison between computational and experimental flows in steady state cases in which we expect to obtain converged mean flows. This will help us quantify the accuracy our model by comparing time-averaged flows as well as turbulence kinetic energies to compare both large- and small-scale flow features to those of the experiments. In this study, we also use homogeneous structural models that omit descriptions of the discrete layers of the valve leaflets, which will affect how the leaflets deform [97, 98]. Therefore we shall also further validate specifically the leaflet kinematics by focusing on quasi-static BHV deformations, as done by Sun et al. [70], or by comparing the leaflet kinematics with reconstructions of leaflet deformations from in vitro experiments, as done by Iyengar et al. [69] or Sugimoto et al. [99] Other potential validation tests include assessing BHV performance using additional hydrodynamics performance measures (pressure drop, effective orifice area, etc.) [100–102].

In summary, this study describes work to model BHVs in an experimental pulse-duplicator platform that is used in various settings to assess their performance. Ultimately, fully validated FSI models of BHVs may be used to develop a high-fidelity model for predicting dynamic performance amongst different valve designs and addressing persistent challenges posed by current BHV designs. They could also facilitate matching patient requirements with valve performance specifics and the development of regulatory guidelines for evaluation of novel designs. This methodology may also be extended and further validated to be applicable to study the effectiveness of TAVR devices with varying degrees of intra- and paravalvular leak, reduced leaflet mobility, subclinical valve thrombosis, and potential pannus formation [103].

CHAPTER 6

# PROGRESS TOWARDS VALIDATING A FLUID-STRUCTURE INTERACTION MODEL OF BIOPROSTHETIC HEART VALVE DYNAMICS USING PARTICLE IMAGE VELOCIMETRY

## 6.1 Background

An in vitro approach, such as pulse duplicator, is often taken to study the interplay between leaflet kinematics and fluid dynamics experimentally. Particle image velocimetry (PIV) [104] is a popular means to analyze fluid dynamics because it is capable of providing detailed flow velocity field and flow stress such as Reynolds stresses and turbulence kinetic energy (TKE). There have been many previous efforts to study the role of fluid dynamics in valve performance experimentally with PIV [104–115] for both BHVs and mechanical heart valves (MHVs). Despite its advantages, PIV has disadvantages such as the need for careful calibration and index of refraction matching. There are also variations both from cycle to cycle within a given experiment, and between different experiments. Additionally, the information from PIV is limited to the areas where the view is not blocked, for example, by the valve leaflets or stent. Computational modeling and simulation (CM&S) has several advantages that can complement the experimental work. First, CM&S allows us to obtain full flow information without being obstructed by the valve leaflets. The operating conditions are trivially reproducible. We can also test different cases under various operating conditions in parallel. CM&S also provide access to data obtained at much higher spatial and temporal resolutions, which enables observations of small scale features that are difficult to see in experiments. However, leveraging these benefits requires that CM&S results must be validated with experimental results to ensure that the results are credible [116].

Although many have worked on validating computational models heart valves using PIV [109, 117–120], these were limited to studying mechanical heart valves. There have been only a few validation studies of fluid-structure interaction (FSI) models of bioprosthetic heart valves using PIV [71, 72], mainly because of the challenges involving complex leaflet kinematics generated by

elastic tissues. Even then, these studies do not account for the anisotropic tissue mechanics of the valve, leading to discrepancies in the dynamics of the valve compared to the experimental results. These studies use limited flow domains that prevent complex flow patterns downstream of the valve to fully develop. For instance, the prior study of Sigüenza et al. [72] compares the fluid dynamics between FSI simulations and experiment for validation of their computational model. Their model, however, exhibits substantial regurgitation during diastole, which leads an underestimation of the transvalvular pressure gradient, and uses flow rate boundary conditions that introduce bias in the valve dynamics. The study of Tango et al. [71] compares the detailed velocity profiles between PIV and simulation, but the differences are large.

We have previously presented work to create FSI models of an experimental pulse duplicator for simulating surgical BHV dynamics [19]. The previous study demonstrates that our FSI models yield excellent agreements with experimental measurements, including bulk flow rates, pressure waveforms, and valve open area waveforms, as well as reasonable agreements in valve leaflet kinematics. We also show that the large-scale flow features are reasonably resolved at practical computational grid resolutions. This study builds upon our previous work towards validating our FSI model by comparing flow patterns from numerical simulations to experimental PIV data. We also perform verification studies by looking at the system under different flow conditions. Excellent agreement is demonstrated between the numerical and experimental results again for bulk flow rates and pressure waveforms across different flow conditions. This work presents a progress towards the experimental validation of our FSI models of BHVs.

## 6.2 Methods

### 6.2.1 Experimental setup

Experimental studies use a ViVitro Pulse Duplicator (ViVitro Labs, Inc., Victoria, BC, Canada) (Figure 6.1a). We use a 27 mm bovine pericardial valve (Carpentier-Edwards PERIMOUNT surgical aortic heart valve) in our experiments. Flow and pressure signals are acquired by the pulse duplicator and are filtered at 100 Hz. We use glycerin with a viscosity of about 3.6 cP as a Newtonian blood analogue test fluid. The ViVitro system can also use high-speed videography to assess valve kinematics or particle image velocimetry (PIV) to provide instantaneous and time-averaged flow data.

In this study, a high-speed PIV system (LaVision, Inc.) is used to obtain flow data. This system uses two Vision Research Phantom v9.1 CMOS cameras which can operate at 1000 frames per second (fps) at full resolution (1632x1200px, 2 megapixels), or up to 153,846 fps with reduced resolution (96x8px), along with a Litron Nano L 50-100 system which includes two Nd:Yag lasers, each capable of running at 100 Hz with 50 mJ of power at a wavelength of 532nm. Figure 6.1b shows a schematic diagram of PIV setup. Consecutive image pairs are captured every 10 ms over 37 seconds.

A solution of 35% glycerin and 65% water by volume is used to match physiological viscosity. Our solution also contains 0.9% NaCl by volume to allow for the bulk flow measurement using the Carolina Medical flowmeter (Carolina Medical Electronics, Inc., East Band, NC, USA). To correct for the distortion induced in the images by the jump in the index of refraction between the acrylic aortic test section and the test fluid, a custom calibration plate (Figure 6.1c) is manufactured using a Formlabs Form 2 3D printer (Formlabs, Somerville, MA, USA). The calibration target utilizes cylindrical posts 1 mm in diameter, spaced on a 3 mm grid center to center, with one grid on each plane, with a 1 mm distance between planes. Because of the complex geometry of the test section, a custom image calibration code is implemented in MATLAB (MathWorks, Inc., Natick, MA, USA) to segment the calibration images between relatively smooth regions, identify displacement fields, and calculate least-squares fit image corrections.

Three pressure transducers located in the aortic, ventricular, and atrial positions are used, and the recirculation resistance and compliance volume in the outflow region are adjusted to provide physiological flow conditions.

To choose the optimal duration between image pairs, an empirical study is performed. Velocity data is rejected when its correlation signal-to-noise ration (SNR) is below a given tolerance, and the time interval is chosen based on giving valid velocity measurements over the largest set in the interrogation domain.

Because of the index of refraction mismatch, the incident laser sheet orientation is chosen to enter the acrylic section normally and to vertically bisect a sinus so that the distortion is constrained to the vertical direction, thus preserving the planar interrogation surface. Given this restriction, the angle between cameras is chosen to be relatively small ($\sim 45^\circ$) to allow for the laser sheet to be viewed through one exterior plane of the square prism test section, avoiding distortion from the exterior edge. The laser sheet thickness is increased to  2 mm to allow for an optimal time interval

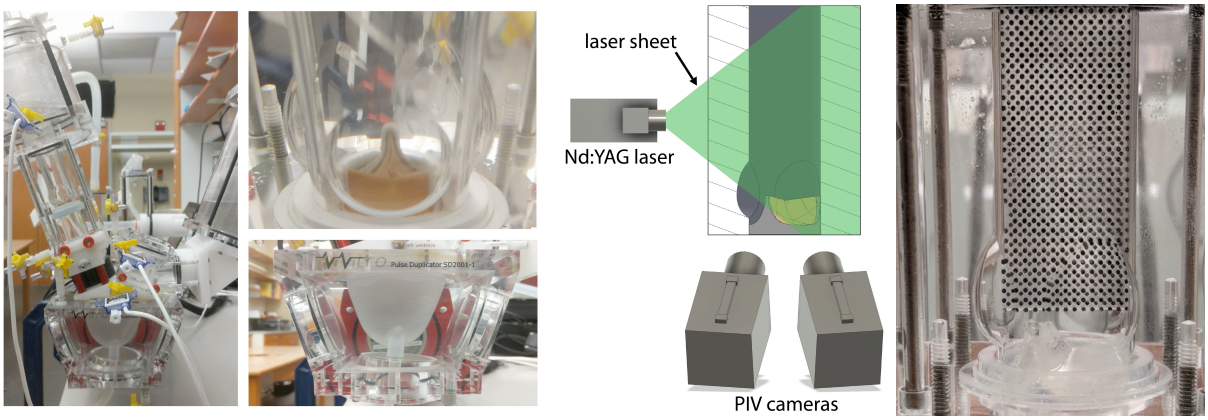


(a) (b) (c)

**Figure 6.1:** (a) A commercial ViVitro pulse-duplicator system in Cardiovascular Modeling and Simulation Laboratory at UNC Chapel Hill. (b) A schematic diagram of particle image velocimetry (PIV) setup for the aortic test section. The flow field along the central plane is visualized using a green laser sheet. (c) a custom calibration plate is manufactured using a Formlabs Form 2 3D printer (Formlabs, Somerville, MA, USA) to correct for the distortion induced in the images by the jump in the index of refraction between the acrylic aortic test section and the test fluid.

between consecutive images. This time is bounded from above by the transit time through the laser sheet of a tracer particle in the out-of-plane direction and bounded from below by the minimal number of pixels traveled in the planar direction between images to achieve appropriate fidelity in displacement measurements.

The detailed flow field comparison is performed using constant flow test. A recirculating pump system is constructed to create constant flow conditions. This setup uses the same PIV interrogation section and bulk flowmeter included with the ViVitro system as used in the dynamic case, but includes a custom-designed 3D-printed flow straightener and mount. A study is performed to assess the convergence of the average flow in time in terms of $L^2$-norm taken over the entire interrogation region. This result is compared directly with the simulation under constant flow conditions, which avoids the constrain of computation time for obtaining average flow statistics in the dynamic case.

### 6.2.2 Computational model

**Bovine pericardial BHV geometry** For our simulations, an idealized pericardial valve geometry, which is based on the geometric measurements of the valve used in our experiments, is created using combination of MATLAB and SOLIDWORKS (Dassault Systèmes SE, Vélizy-Villacoublay, France). Here, we assume that all three valve leaflets have the same geometry. First, we generate

the free edge and seam curves of a pericardial valve leaflet based on the geometric measurements such as diameter, commissure heights, and heights of the center of the free edges of the real valve (Figures 6.2a and 6.2b). A parameterized description of the free edge curve is defined by

$$y_1 = \sqrt{\delta^2 + (x \tan\theta)^2}, \tag{6.1}$$

$$z_1 = c_1|x|^3 + c_2 x^2 + h_\mathrm{e}, \;\; -R\cos\theta \le x \le R\cos\theta, \tag{6.2}$$

in which $z_1$ is a natural spline with $z_1' = 0$ at the end points. The parameters are determined by solving a system of equations, and we obtain $c_1 = -0.4937$ cm$^{-2}$ and $c_2 = 0.8980$ cm$^{-1}$. The seam curve, which is in contact with the stent, is defined as

$$y_2 = \sqrt{R^2 - x^2}, \tag{6.3}$$

$$z_2 = h_\mathrm{c} - h_\mathrm{c}\sqrt{1 - \left(\frac{x}{R\cos\theta}\right)^4}, \;\; -R\cos\theta \le x \le R\cos\theta. \tag{6.4}$$

A spanning surface representation of the idealized valve leaflet is created by sweeping between the two curves with a family of parametric curves (Figure 6.2c) that are defined via

$$y = ty_1 + (1-t)y_2, \tag{6.5}$$

$$z_1 = \left(\frac{y - y_2}{y_1 - y_2}\right)^3 (z_1 - z_2) + z_2, \; 0 \le t \le 1. \tag{6.6}$$

A surface mesh is generated from this parametric representation using a custom MATLAB script. A volumetric leaflet model is generated by thickening the surface model using SOLIDWORKS. This thickness is assumed to be uniform and is determined to be the average thickness of a real bovine pericardial valve that is reconstructed by micro-CT in Lee et al. [19]. The geometric parameters used in creating the our valve leaflet model are listed in Table 6.1

**Leaflet biomechanics** We use a modified version [19] of Holzapfel–Gasser–Ogden (HGO) model [82] that is described earlier in Section 5.2.2. We also use the same material parameters that are fit to biaxial data (see Appendix C for details). We also follow the previously described fiber architecture for bovine pericardial BHV, which is based on experimental measurements of small

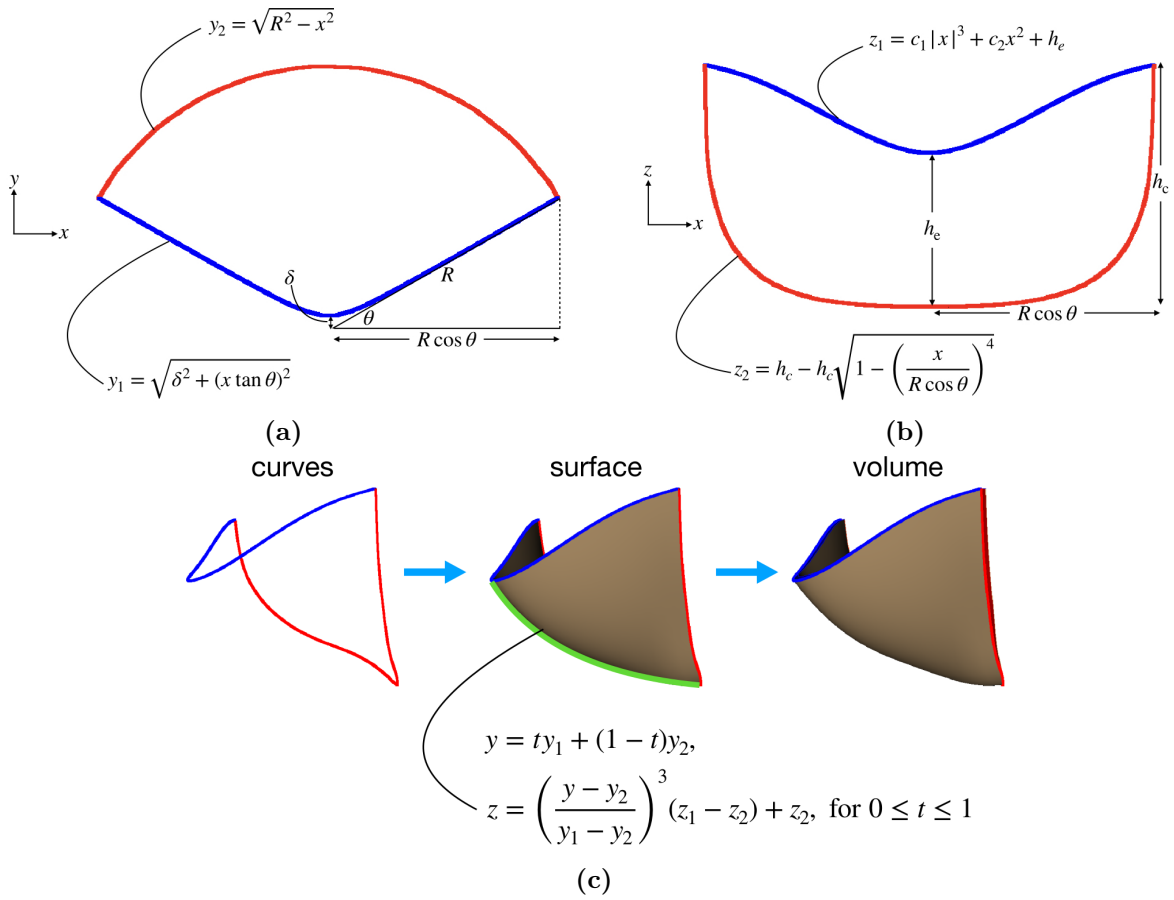


**Figure 6.2:** Parametric model of a BHV leaflet. Top (a) and front (b) views of the model free edge (blue) and the seam (red) curves of a pericardial valve leaflet. (a) A parameterized description of the free edge curve. (b) A parameterized description of the seam curve, which is in contact with the stent. A natural spline is used to represent $z_1(x)$ of the free edge curve with $c_1 = -0.4937$ cm$^{-2}$ and $c_2 = 0.8980$ cm$^{-1}$, which ensure that $z_1' = 0$ at the end points. (c) The leaflet surface model is generated by sweeping between the free edge and the seam curves with a family of parametric curves along the green line.

**Table 6.1:** Geometric parameters used for construction of bovine pericardial valve leaflet*

| parameters | $R$ | $h_c$ | $h_e$ | $\theta$ | $\delta$ | $h_t$ |
|---|---|---|---|---|---|---|
| | 13.5 mm | 1.1 cm | 6.6 mm | 30° | 0.8 mm | 0.4 mm |

* The radius ($R$), commissural height ($h_c$), and the height of the center of the free edge ($h_e$) are the actual measurements of the bovine pericardial valve that is used in our experiment. The size of gap in the middle of the valve ($\delta$) is determined empirically, and $\theta$ is determined by assuming that the valve leaflets have the identical geometry. Leaflet thickness ($h_t$) is assumed to be uniform and is determined to be the average thickness of a real bovine pericardial valve that is reconstructed by micro-CT in Lee et al. [19].

angle light scattering data [70] (Figure 6.3a).

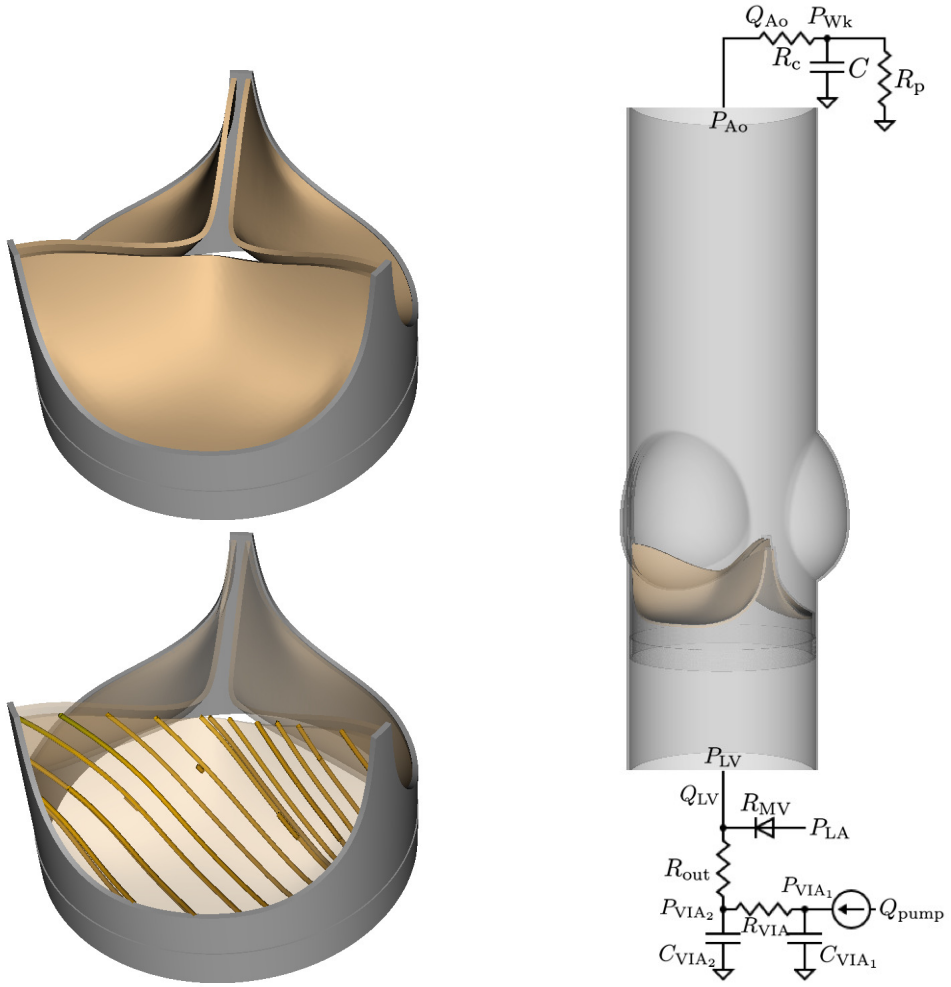


**(a)** **(b)**

**Figure 6.3:** (a) Model bovine pericardial bioprosthetic valve geometry and fiber architecture. The valve geometry is constructed parametrically, in which we can control the diameter, commissure and center heights, and the size of the central gap. The model fiber structure is generated based on the small angle light scattering (SALS) data of Sun et al. [70].

**Aortic test section model** To reconstruct the geometry of the ViVitro Labs, Inc. PIV test section, a mold of the interior is made using plaster of Paris. The surface of this mold is scanned using the NextEngine 3D scanner (NextEngine, Inc., Santa Monica, CA, USA). The geometry of the outflow section is assumed to exhibit tri-fold symmetry, with the section downstream of the sinuses approximately cylindrical and the sinuses approximately bodies of revolution. Best-fit surfaces are found using MATLAB, with the resulting 3D model constructed in SOLIDWORKS. We use a penalty

method to model the PIV mount as an essentially rigid material model via

$$W_{\text{wall}} = \frac{c_{\text{wall}}}{2}(\bar{I}_1 - 3), \text{ and} \tag{6.7}$$

$$\mathbf{F}(\mathbf{X}, t) = \kappa_{\text{wall}}(\mathbf{X} - \boldsymbol{\chi}(\mathbf{X}, t)), \tag{6.8}$$

in which $c_{\text{wall}} = 33.1$ kPa and $\kappa_{\text{wall}} = 8.52 \times 10^5$ kPa cm$^{-2}$.

**Fluid model and boundary conditions** We use the incompressible Navier–Stokes equations to model the fluid in the PIV mount as a viscous incompressible fluid. We use a Newtonian blood analogue as the test fluid with a uniform density $\rho = 1.12$ g cm$^{-3}$ and a uniform viscosity $\mu = 3.60$ cP.

Both upstream driving and downstream loading conditions follow from the boundary models of the bovine pericardial BHV in Section 5.2.4. Briefly, the upstream model used in the bovine pericardial valve simulations is

$$C_{\text{VIA}_1}\frac{\mathrm{d}P_{\text{VIA}_1}}{\mathrm{d}t} = Q_{\text{pump}} - \frac{P_{\text{VIA}_1} - P_{\text{VIA}_2}}{R_{\text{VIA}}}, \tag{6.9}$$

$$C_{\text{VIA}_2}\frac{\mathrm{d}P_{\text{VIA}_2}}{\mathrm{d}t} = \frac{P_{\text{VIA}_1} - P_{\text{VIA}_2}}{R_{\text{VIA}}} - \frac{P_{\text{VIA}_2} - P_{\text{LA}} + Q_{\text{LV}}R_{\text{MV}}}{R_{\text{out}} + R_{\text{MV}}}, \tag{6.10}$$

$$P_{\text{LV}} = \frac{P_{\text{VIA}_2}R_{\text{MV}} + P_{\text{LA}}R_{\text{out}} - Q_{\text{LV}}R_{\text{out}}R_{\text{MV}}}{R_{\text{out}} + R_{\text{MV}}}, \tag{6.11}$$

in which $C_{\text{VIA}_1}$, $C_{\text{VIA}_2}$, $R_{\text{VIA}}$, and $R_{\text{out}}$ characterize the VIA system, $R_{\text{MV}}$ characterizes the resistance at the mitral position, $P_{\text{LA}}$ is the left atrial pressure, $Q_{\text{pump}}$ is the prescribed volumetric flow rate of the pump, and $Q_{\text{LV}}$ and $P_{\text{LV}}$ are the volumetric flow rate and pressure, respectively, at the inlet of the aortic test section model. We use the nonlinear optimization tool fmincon in MATLAB to determine the model parameters by comparing $P_{\text{LV}}$ from Eq (6.9)–(6.11) with that of experimental system (Figure 6.4). When calibrating the reduced-order models, the experimental measurements of $Q_{\text{pump}}$ and $P_{\text{LA}}$ are used as inputs to the upstream model.

The downstream loading conditions of the pulse duplicator are also described by a three-element

Windkessel model,

$$C\frac{\mathrm{d}P_{\mathrm{Wk}}}{\mathrm{d}t} = Q_{\mathrm{Ao}} - \frac{P_{\mathrm{Wk}}}{R_{\mathrm{p}}}, \tag{6.12}$$

$$P_{\mathrm{Ao}} = P_{\mathrm{Wk}} + Q_{\mathrm{Ao}}R_{\mathrm{c}}, \tag{6.13}$$

in which $C$ is the compliance, $R_{\mathrm{c}}$ is the characteristic resistance, $R_{\mathrm{p}}$ is the peripheral resistance, $P_{\mathrm{Wk}}$ is the Windkessel pressure, and $Q_{\mathrm{Ao}}$ and $P_{\mathrm{Ao}}$ are the volumetric flow rate and pressure, respectively, at the outlet of the test section. The Windkessel parameters $R_{\mathrm{c}}$, $R_{\mathrm{p}}$, and $C$ are calibrated using experimental measurements of $Q_{\mathrm{Ao}}$ and $P_{\mathrm{Ao}}$. We determine the model parameters by comparing $P_{\mathrm{Ao}}$ from Eq (6.12) and (6.13) with that of experimental system (Figure 6.5). When calibrating the downstream model, the experimental measurements of $Q_{\mathrm{Ao}}$ are used as inputs to the Windkessel model.

**Numerical discretizations** Simulations are performed using the reconstructed geometry of the ViVitro PIV mount embedded in a computational domain with dimensions 10.1 cm $\times$ 5.05 cm $\times$ 5.05 cm. We use an adaptively refined Cartesian grid to solve the Navier–Stokes equations, and we use an unstructured finite element (FE) mesh that conforms to the geometry of the structure [34]. The effective fine-grid resolution of the Cartesian grid is approximately 0.4 mm. Structural models use second-order tetraahedral (10-node) elements for the BHV leaflets and first-order tetrahedral (four-node) elements for the PIV mount, which are generated using Trelis (Coreform, LLC, Orem, UT, USA). The average grid-spacings of the structural meshes are 0.4 mm. We use a piecewise-linear kernel for the aortic test section and a three-point B-spline kernel for the valve leaflets as regularized delta functions. The time step size starts at $\Delta t = 7.5 \times 10^{-6}$ s, and it is systematically reduced if needed to avoid instabilities related to our time stepping scheme.

## 6.3 Results

We perform corresponding experiments and simulations using pulse rates of 60, 80, 100, and 120 beats per minute. We use 10 consecutive cycles of experimental measurements to characterize the reduced-order models that provide driving and loading conditions for the detailed FSI model. We compare both bulk measurements (flow rates and pressure waveforms) and detailed flow fields inside the PIV mount.

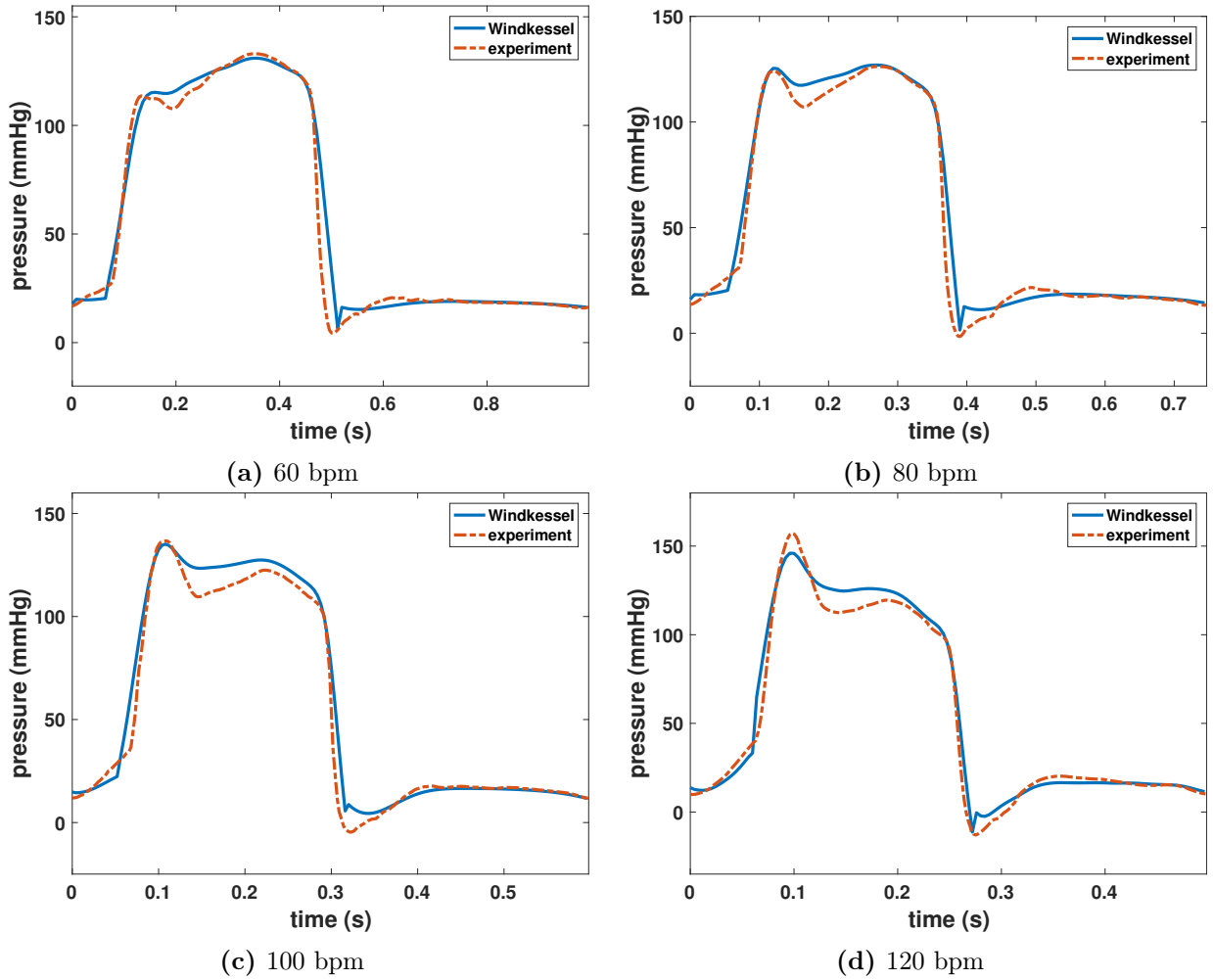


**(a)** 60 bpm **(b)** 80 bpm

**(c)** 100 bpm **(d)** 120 bpm

**Figure 6.4:** Fit of the experimental upstream pressure data at (a) 60, (b) 80, (c) 100, and (d) 120 beats per minute (bpm) (showing all 10 cycles) of the detailed upstream model shown in Figure 6.3b. These fits are obtained using fmincon in MATLAB by comparing experimental values of $P_{\mathrm{LV}}$ to model results obtained by solving Eq (5.9), (5.10), and (5.11) with measured values of $Q_{\mathrm{pump}}$, $Q_{\mathrm{LV}}$, and $P_{\mathrm{LA}}$.

Figures 6.6a, 6.7a, 6.8a, and 6.9a show comparison of flow rates and pressure waveforms between simulated and experimental results for pulse rates of 60, 80, 100, and 120 beats per minute (bpm). Although we observe discrepancies during valve closure, the simulation results show excellent agreement in flow rates for all cases and in pressure waveforms for 60 and 80 bpm cases.

Figures 6.6b, 6.7b, 6.8b, and 6.9b provide detailed flow patterns generated in the FSI simulations as well as the PIV reconstructions. We note that the white obstructions in the PIV reconstructions are one of the aortic sinuses of the PIV mount, which limits the available flow data. We compute the peak Reynolds number using Eq. (7.1) from Section 5.3, which yields $Re_{\mathrm{peak}} = 6{,}167$. The

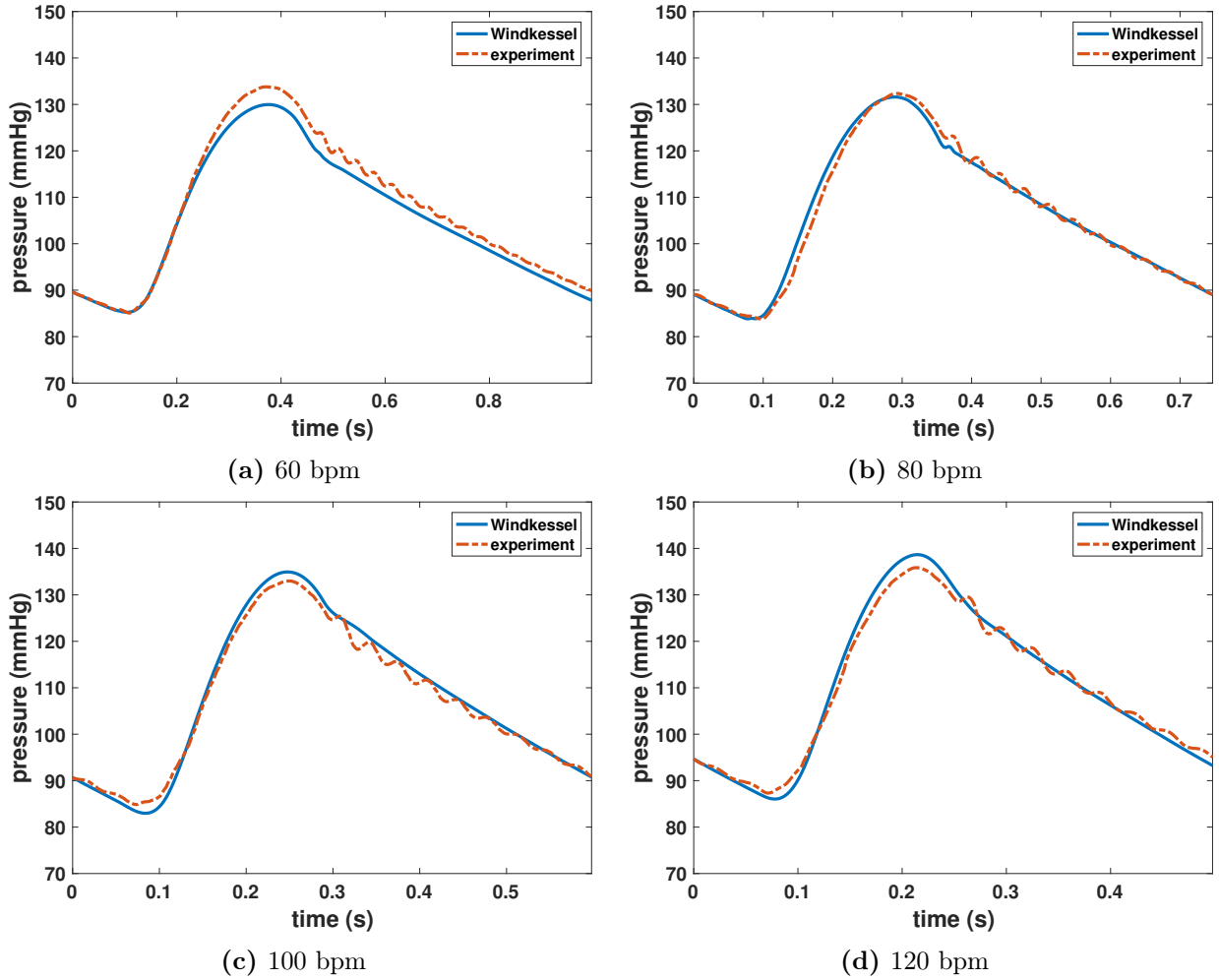


**(a)** 60 bpm **(b)** 80 bpm

**(c)** 100 bpm **(d)** 120 bpm

**Figure 6.5:** The three-element Windkessel fit of the experimental downstream pressure data at (a) 60, (b) 80, (c) 100, and (d) 120 beats per minute (bpm) (showing all 10 cycles). These fits are obtained using fmincon in MATLAB by comparing experimental values of $P_{\mathrm{Ao}}$ to model results obtained by solving Eq (5.12) and (5.13) with measured values of $Q_{\mathrm{Ao}}$ as inputs to the Windkessel models.

detailed flow patterns show reasonable overall agreement, including the recirculation regions that are observed in the right side of the PIV mount.

### 6.3.1 Solution Validation

To validate our computational model, it is important to develop a measure that can quantify the difference in detailed flow patterns between simulation and PIV results. Because the flow dynamics are extremely complex, it is difficult to do a point-to-point comparison of the flow fields. A natural way to compare is to use averaged fields over multiple cycles, but it is computationally costly. Another possible means to compare is to look at the steady flow cases and compare time-averaged

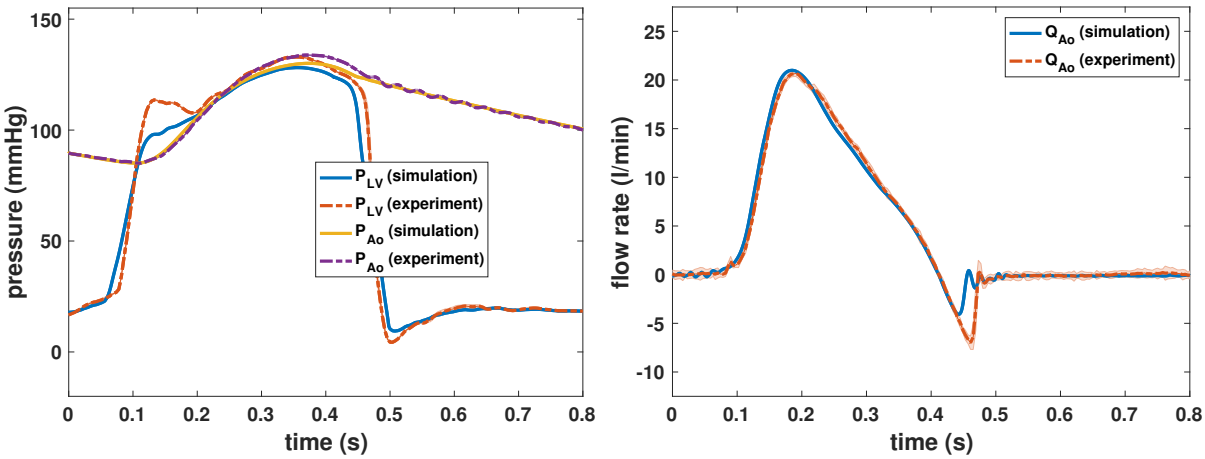


**(a)** Simulation vs. experiment for 60 bpm

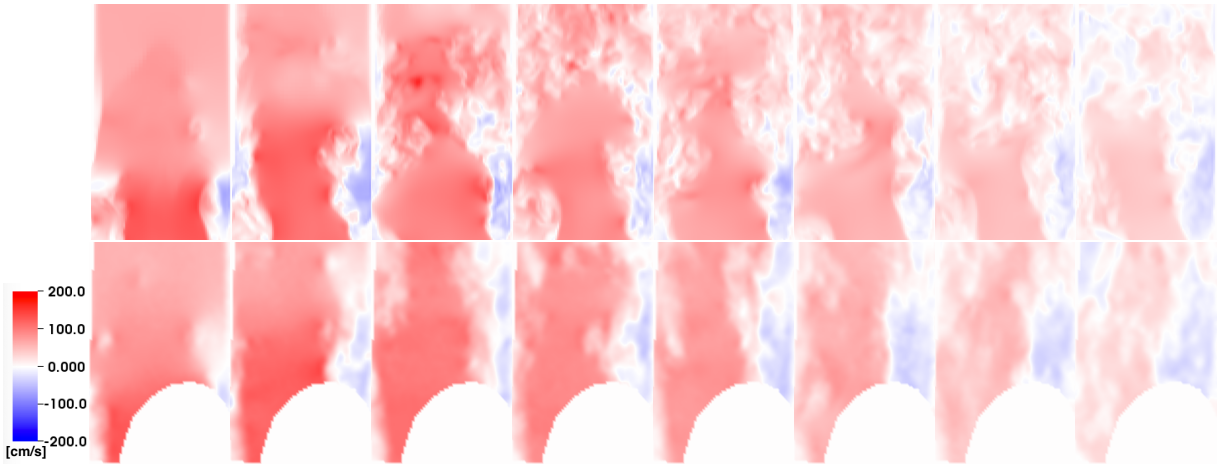


**(b)** Simulation (*top panels*) vs. PIV (*bottom panels*) for 60 bpm

**Figure 6.6:** (a) Comparisons between simulated and experimental pressure and flow rate waveforms at 60 bpm. The experimental waveforms shown are the average waveforms over 10 cycles of data with shaded regions showing where 95% of the data fall. (b) Comparisons in the cross-section view of simulated flow patterns between simulation (*top panels*) and PIV (*bottom panels*) at 60 bpm. The color shows the axial velocity through the aortic test section at the center plane, with red indicating forward flow and blue indicating reverse flow. $Re_{\text{peak}} = 6{,}167$. The time increment between frames is 30.0 ms, which corresponds to 33 fps.

velocity field or turbulence kinetic energy. Therefore, we perform validation studies using steady flow conditions by observe the time-averaged flow fieldsbetween the PIV and simulation results. We use the measured flow data at the flow source that drives the corresponding steady flow experiment to derive the driving condition using the reduced-order model shown in Figure 6.10. The upstream

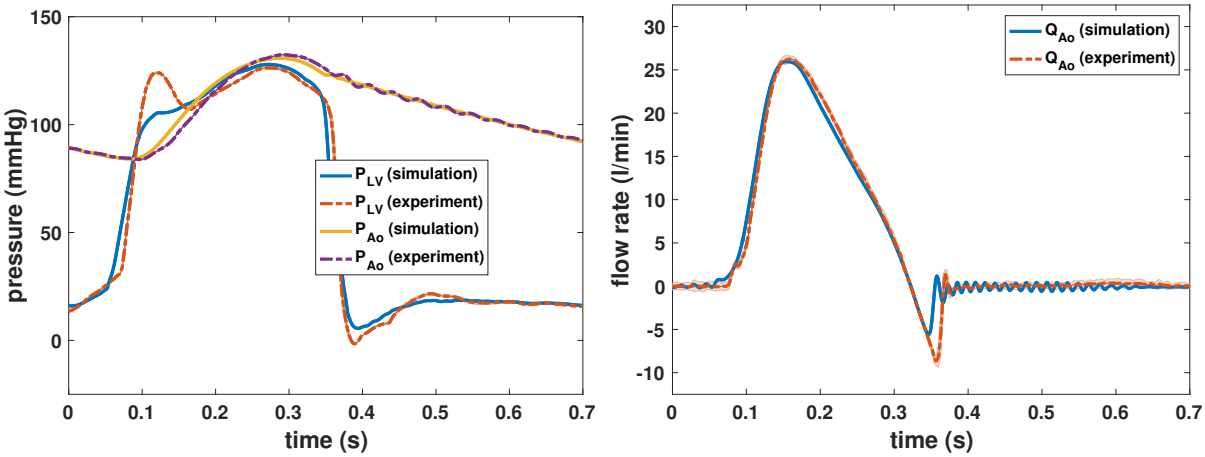


**(a)** Simulation vs. experiment for 80 bpm

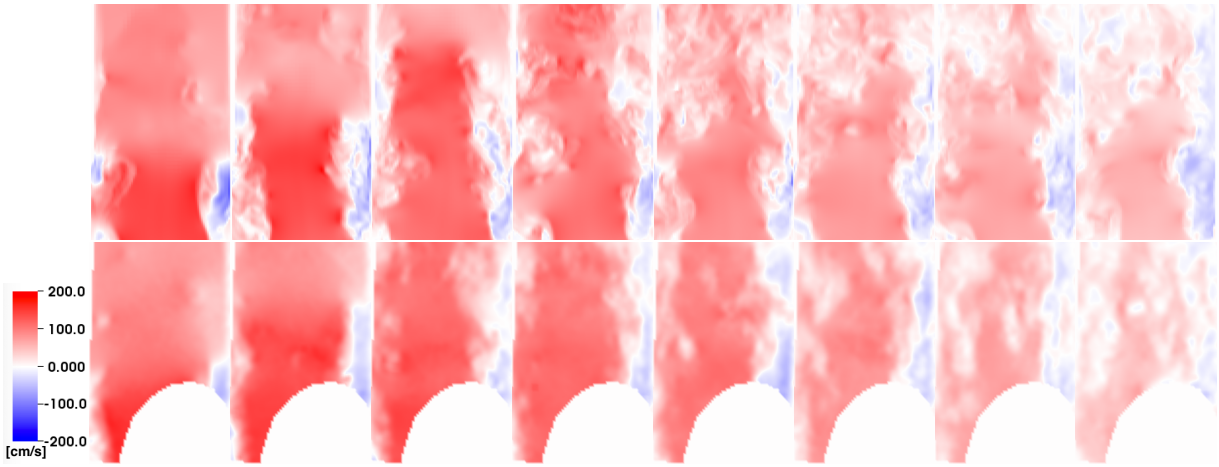


**(b)** Simulation (*top panels*) vs. PIV (*bottom panels*) for 80 bpm

**Figure 6.7:** (a) Comparisons between simulated and experimental pressure and flow rate waveforms at 80 bpm. The experimental waveforms shown are the average waveforms over 10 cycles of data with shaded regions showing where 95% of the data fall. (b) Comparisons in the cross-section view of simulated flow patterns between simulation (*top panels*) and PIV (*bottom panels*) at 80 bpm. The color shows the axial velocity through the aortic test section at the center plane, with red indicating forward flow and blue indicating reverse flow. $Re_{\text{peak}} = 6{,}167$. The time increment between frames is 20.0 ms, which corresponds to 50 fps.

pressure, $P_{\text{LV}}$, is determined by solving

$$C\frac{\mathrm{d}P_{\text{Wk}}}{\mathrm{d}t} = Q_{\text{LV}} - Q_{\text{src}} \tag{6.14}$$

$$P_{\text{LV}} = P_{\text{Wk}} + Q_{\text{LV}}R. \tag{6.15}$$

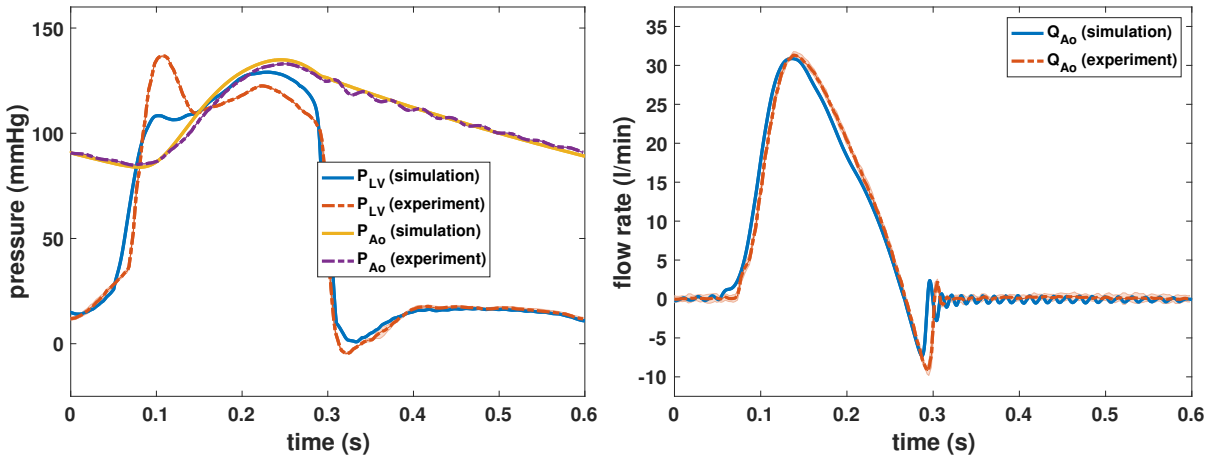


**(a)** Simulation vs. experiment for 100 bpm

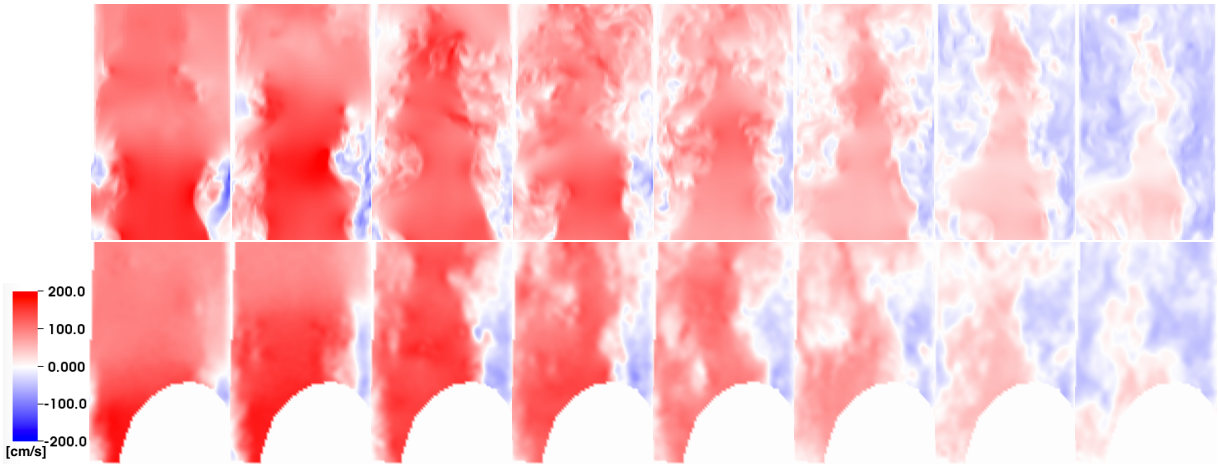


**(b)** Simulation (*top panels*) vs. PIV (*bottom panels*) for 100 bpm

**Figure 6.8:** (a) Comparisons between simulated and experimental pressure and flow rate waveforms at 100 bpm. The experimental waveforms shown are the average waveforms over 10 cycles of data with shaded regions showing where 95% of the data fall. (b) Comparisons in the cross-section view of simulated flow patterns between simulation (*top panels*) and PIV (*bottom panels*) at 100 bpm. The color shows the axial velocity through the aortic test section at the center plane, with red indicating forward flow and blue indicating reverse flow. $Re_{\text{peak}} = 6{,}167$. The time increment between frames is 20.0 ms, which corresponds to 50 fps.

We use zero normal traction boundary condition downstream. We use $R = 0.5$ mmHg mL$^{-1}$ s and $C = 0.01$ mmHg mL$^{-1}$, which are determined empirically. The mean flow is determined via Eq. (5.20) from Section 5.3.1.

PIV reconstruction of the flow fields involve averaging positions of the particles in the out-of-plane direction, which is about $\pm 1$ mm, so we discretely average the velocity fields through the aortic test section at different planes within the averaging window of $\pm 1$ mm as well. Figure 6.11 shows the

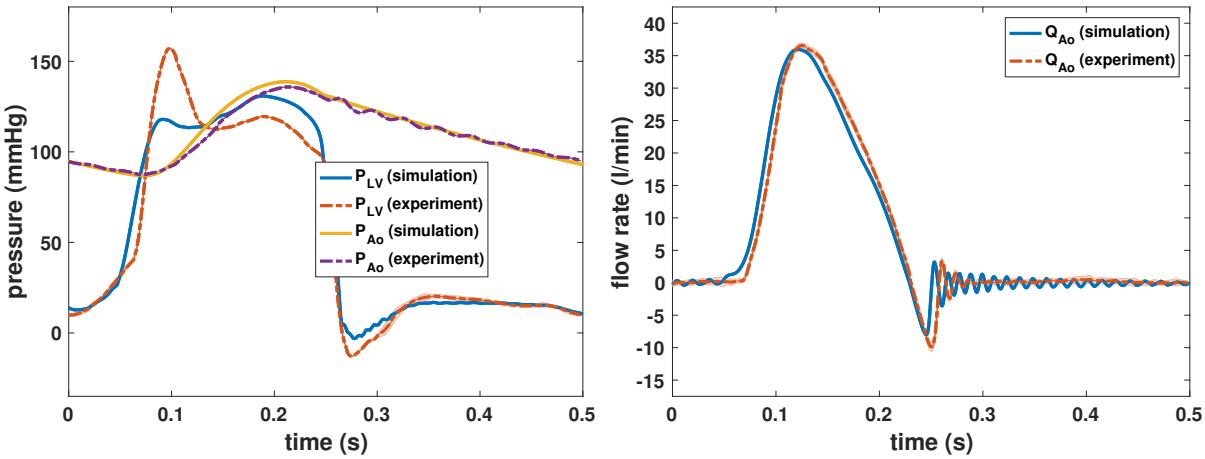


**(a)** Simulation vs. experiment for 120 bpm

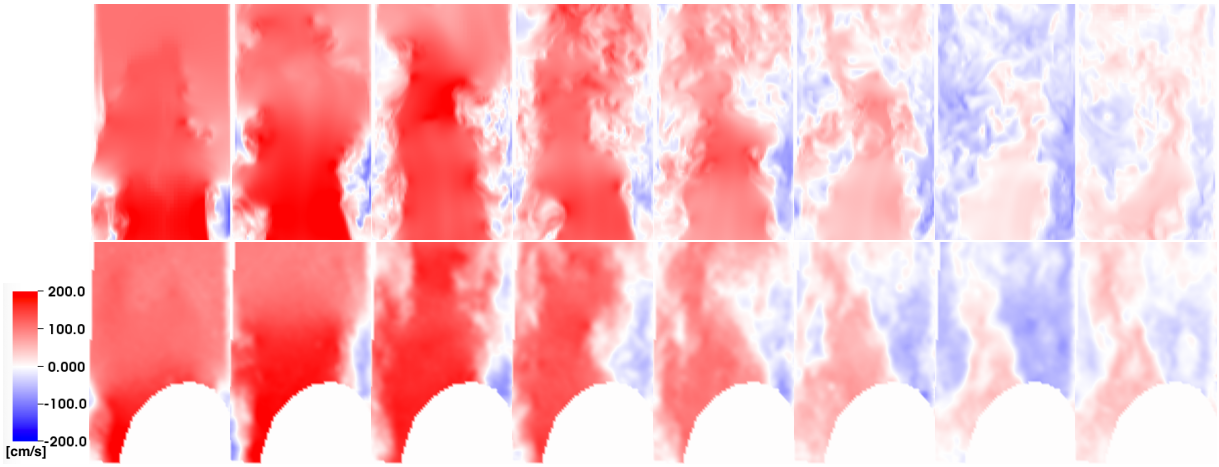


**(b)** Simulation (*top panels*) vs. PIV (*bottom panels*) for 120 bpm

**Figure 6.9:** (a) Comparisons between simulated and experimental pressure and flow rate waveforms at 120 bpm. The experimental waveforms shown are the average waveforms over 10 cycles of data with shaded regions showing where 95% of the data fall. (b) Comparisons in the cross-section view of simulated flow patterns between simulation (*top panels*) and PIV (*bottom panels*) at 120 bpm. The color shows the axial velocity through the aortic test section at the center plane, with red indicating forward flow and blue indicating reverse flow. $Re_{\text{peak}} = 6{,}167$. The time increment between frames is 20.0 ms, which corresponds to 50 fps.

time-averaged flow fields for PIV and simulation. Because the flow is complex, we do not expect to see symmetric flow field for each sinus, so we look at three different cross-section views by rotating the position of the sinuses into identical configurations. We then measure the variation of flow fields that result from which sinus we observe as shown in Figure 6.11b. The comparison in Figure 6.11 shows good agreement between PIV and simulation results.


**Figure 6.10:** The reduced-order model that provide steady driving condition. $P_{\mathrm{LV}}$ is derived from flow data from the flow source that drives the corresponding steady flow experiment. We use $R = 0.5$ mmHg mL$^{-1}$ s and $C = 0.01$ mmHg mL$^{-1}$, which are determined empirically.

## 6.4 Discussion

This study leverages a previously developed FSI model of bovine pericardial BHV in an experimental pulse duplicator [19] (Chapter 5), with an addition of particle image velocimetry technique to compare detailed flow dynamics downstream of the BHV. The boundary models are again calibrated independently from the detailed FSI model.

The numerical results in Figures 6.6a, 6.7a, 6.8a, and 6.9a show excellent agreement in flow rates for the most part except during valve closure. This is somewhat expected because we use idealized valve leaflet geometry that is similar but not exactly the same as the real leaflet geometry. This may result in difference in closing leaflet dynamics, in which the elasticity of the leaflets are important. The results during systole are expected to be in excellent agreement because the small discrepancy in the leaflet dynamics does not make significant amount of difference in the large scale flow. We also observe excellent agreement in pressure waveforms for 60 and 80 bpm cases, but not for 100 and 120 bpm cases. This may be due to less accurate fits for the upstream model (Figure 6.4) for these cases. We notice in the experimental upstream pressure data that we see larger "bumps" as the pulse

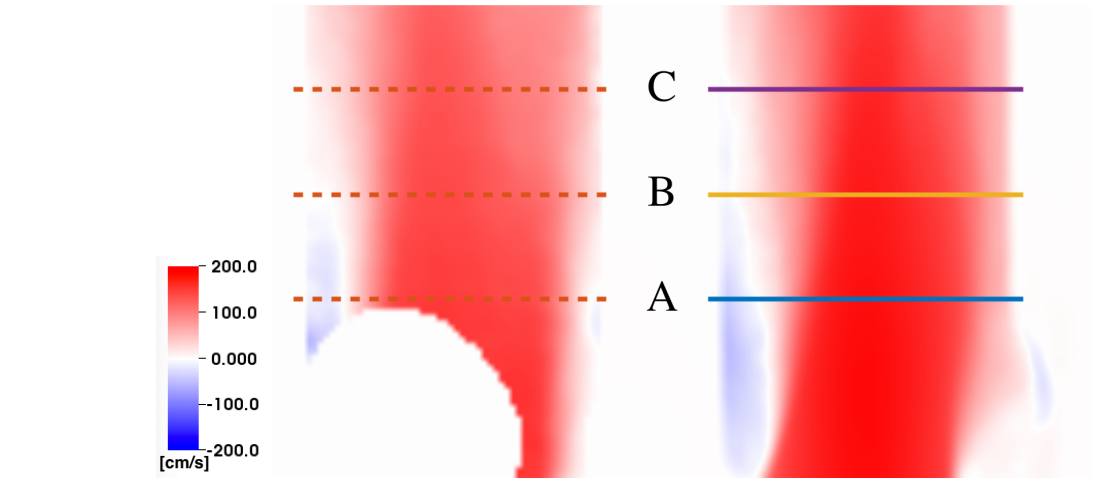


**(a)** PIV (left) vs. simulation (right)

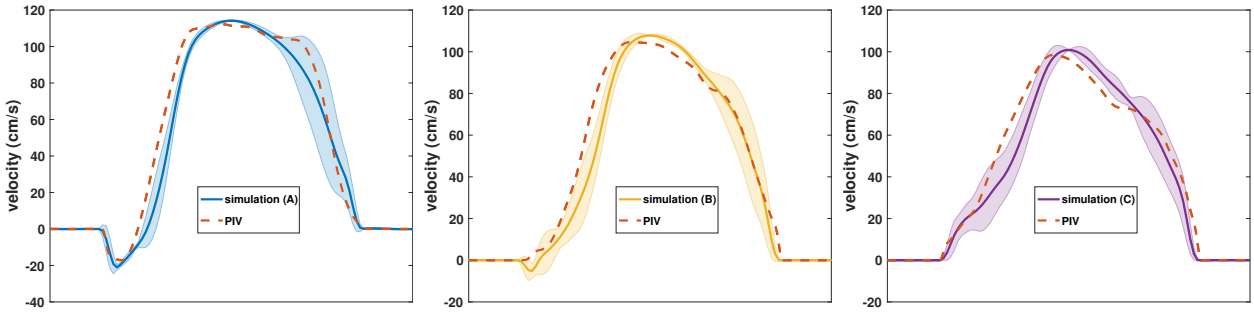


**(b)**

**Figure 6.11:** (a) Cross-section view of time-averaged flow fields under steady driving conditions. (b) Flow profiles at different locations downstream of the valve for the bovine pericardial valve model. We use steady flow at the maximum flow rate. In panel (a), the color shows the time-averaged axial velocity through the aortic test section at the center plane, with red indicating forward flow and blue indicating reverse flow. Lines show where the profiles shown in panel (b) are obtained, and the colors correspond to the colors of the profiles in panel (b). Red dashed lines show the profiles from the PIV data. In panel (b), shaded regions show the variations in the profiles for three different cross-sections based on the orientations of the valve leaflets, and the solid lines are the average of those profiles.

rate increases, which limits the upstream models to fit against. One possible explanation is that as the pulse rate increases in the pulse duplicator, the fluid builds up before the resistor, which is part of the compliance chamber that does not include the tube and separate air chamber. When this part fills, it may lead to pressure build-up, as we observe that it blows off the viewing window and sprays fluid on the cameras. Figures 6.6b, 6.7b, 6.8b, and 6.9b show reasonable agreements in detailed flow patterns between simulation and PIV reconstruction. Although it is hard to quantify the comparison for such complex flow fields at near turbulent regime, we see qualitatively that they

are in reasonable agreement. Simulation results are able to capture the recirculation zones that we observe in PIV results.

A limitation of the study is that the valve geometry in our simulations is highly idealized, assuming all three leaflets being identical. We plan to use the actual geometry that we can obtain from micro-CT reconstruction to account for the role of asymmetry in the valve geometry. We also do not have a detailed model of the stent wire and the external frame that wraps around the valve. The validation that we perform is for a steady flow case, so our immediate goal is to compare averaged fields over multiple cycles for the dynamic cases. We have made significant improvements in performance of our simulations, and we expect to be able to make such comparisons in the near future.

Despite its limitations, this study still shows promising results, which is a step towards developing an experimentally validated high-fidelity FSI platform. This platform may be used in various settings to assess medical device performance. For example, this validated methodology may allow use to assess TAVR devices with intra- and paravalvular leak, reduced leaflet motility, subclinical valve thrombosis, and pannus formation [103].

CHAPTER 7

# BIOPROSTHETIC AORTIC VALVE DIAMETER AND THICKNESS ARE DIRECTLY RELATED TO LEAFLET FLUTTERING

**Material in this section is adapted from a paper currently in review.**

## 7.1 Background

Bioprosthetic heart valves (BHVs) are widely used in valve replacement procedures to treat stenosis or regurgitation because they generate hemodynamics similar to native valves. In contrast to mechanical heart valves, which require patients to receive sustained anticoagulation, BHVs reduce or eliminate the need for anticoagulation. In the majority of cases, patients who receive BHVs are prescribed antiplatelet therapy, but the bleeding risk with antiplatelet therapy is less than that for anticoagulation [121]. The chemically fixated tissues used to construct BHVs deteriorate over time, however, and surgical valves are known to have a durable lifetime of only 10–15 years [122, 123]. With the addition of transcatheter aortic valve replacement (TAVR), BHV use continues to increase, including in younger and lower-risk patients, because of improvements in patient outcomes, progress in valve design, and the growing availability of valve-in-valve TAVR if these valves fail [124–126]. Advancing our understanding of the mechanisms that determine BHV durability remains crucial in improving patient care.

Bioprosthetic valves can flutter [127–130], and it is well known that fluttering is associated with premature fatigue and failure in thin flexible plates [131]. The impact of fluttering on durability has been studied in diverse systems, including basilar membranes in the cochlea [132, 133] and flapping flags [134, 135], but the role of fluttering in BHV durability has not been clearly established. Further, prior studies on the impact of valve geometry on leaflet kinematics are lacking, and our understanding of the determinants of BHV flutter is rudimentary. This study aims to begin to link our more theoretical understanding of the impact of fluttering in the durability of natural and manufactured systems to potential avenues to improve the durability of BHVs by systematically characterizing the roles of device diameter and leaflet thickness in leaflet kinematics.

Leaflet fluttering is challenging to study in vivo. Consequently, this work uses a well characterized experimental pulse duplicator platform [77–79] and a computational fluid-structure interaction model of this system [19] to study the effects of valve geometry on leaflet dynamics. Pulse duplicators are widely used to assess prosthetic valve performance [77–79]. Computational models complement experiments by enabling the assessment of device performance under a broader range of conditions [3]. Further, operating conditions are tightly controlled and trivially reproducible in a computer model, allowing for the elimination of variations both within a given experiment and between different experiments.

The key finding of this study is that, at least in this experimental platform, smaller diameter BHVs show markedly higher fluttering frequencies than larger valves, both under consistent operating conditions (flow rates and pressures) and also under consistent flow conditions (characterized by the Reynolds number). Although the impact of BHV size on mortality after aortic valve replacement is unknown [136, 137], it is known that smaller-diameter bioprosthetic aortic valves fail earlier than larger valves [124, 138–140]. Understanding both the determinants and impacts of fluttering could ultimately influence patient-specific surgical planning and device selection as well as the design of novel devices, such as polymeric valves [141, 142].

## 7.2 Methods

### 7.2.1 Experimental setup

Experimental studies used a customized pulse duplicator based on the ViVitro Pulse Duplicator System (ViVitro Labs, Inc., Victoria, BC, Canada) (Figure 5.1a), which is used and accepted by regulatory agencies, including the U.S. Food and Drug Administration [77–79]. The customized pulse duplicator has a prototype electro-optical subsystem [76] to assess projected dynamic valve area (PDVA) [143]. We used Labcor DKA valves (Labcor Laboratórios Ltda., Belo Horizonte, Brazil) with diameters 21 mm (DKA015849), 25 mm (DKA015141), and 27 mm (DKA015562), which have bovine pericardial leaflets that are externally wrapped around their frames. Flow and pressure signals are filtered at 100 Hz, and PDVA signals are not filtered. We use 10 consecutive cycles of experimental pressure, flow rate, and PDVA signals for each device. We report average experimental measurements and cycle-to-cycle variations using confidence intervals. The experimental test fluid was saline, which is accepted under the ISO 5840-3 standard [78] and widely used to assess BHV

performance [77–79] because it provides best optical clarity when freshly mixed and a consistent and well characterized density and viscosity. We perform experiments using a pulse rate of 70 beats per minute (BPM). Additional pressure and flow waveforms were obtained using a glycerin-based blood analogue in a commercial ViVitro Pulse Duplicator at 60 BPM.

### 7.2.2 Computational model of BHV dynamics

Computer simulations used a fluid-structure interaction model of the aortic valve test section of the experimental pulse duplicator described previously [19]. Briefly, interactions between the test fluid and the thin flexible BHV leaflets in the aortic test section (length 10.1 cm and diameter 28 mm) are simulated using an immersed finite element method [34], implemented by the IBAMR software [48, 49]. Identical leaflet biomechanics models (see Section 5.2.2 and Appendix C) are used in all simulations, eliminating this potential source of variability. Test fluids are described by the incompressible Navier-Stokes equations. We use both saline and glycerin in the computer simulations, with densities $\rho = 1.0$ and 1.17 g cm$^{-3}$ and dynamic viscosities $\mu = 1.0$ and 3.60 cP, respectively. Reduced-order models characterize upstream and downstream system components. We construct a model bovine pericardial BHV with variable diameter, leaflet thickness, and leaflet curvature. See Figure 6.3. We perform simulations using pulse rates of 70 BPM for saline cases and 60 BPM for glycerin cases, in accordance with the corresponding experiments.

### 7.2.3 Parameter fitting for the reduced-order models

We use reduced-order models previously described by Lee et al. [19], and also described in Chapters 5 and 6 of this thesis, are used to provide the driving and loading conditions for the three-dimensional FSI models. Pulse duplicator system components upstream of the aortic test section, including the resistance and compliance of the pump, the viscoelastic impedance adapter (VIA) subsystem, and the left ventricular chamber of the pulse duplicator, are described by reduced-order models. A three-element Windkessel model [62] is used for the upstream model for the saline case (Figure 5.3a), and a more detailed upstream model is used for the glycerin-based blood analogue case (Figure 5.3b). The main difference is the pump flow rate data available for the blood analogue case, which allows us to modify to match the Reynolds numbers and prescribe consistent flow conditions between different valve diameter cases. These calibrations, which are done for each experimental condition, are performed independently from the fluid-structure interaction (FSI) model of the valve (Figure 7.1). Tables 7.1 and 7.2 report all of the calibrated parameters used for the saline and blood

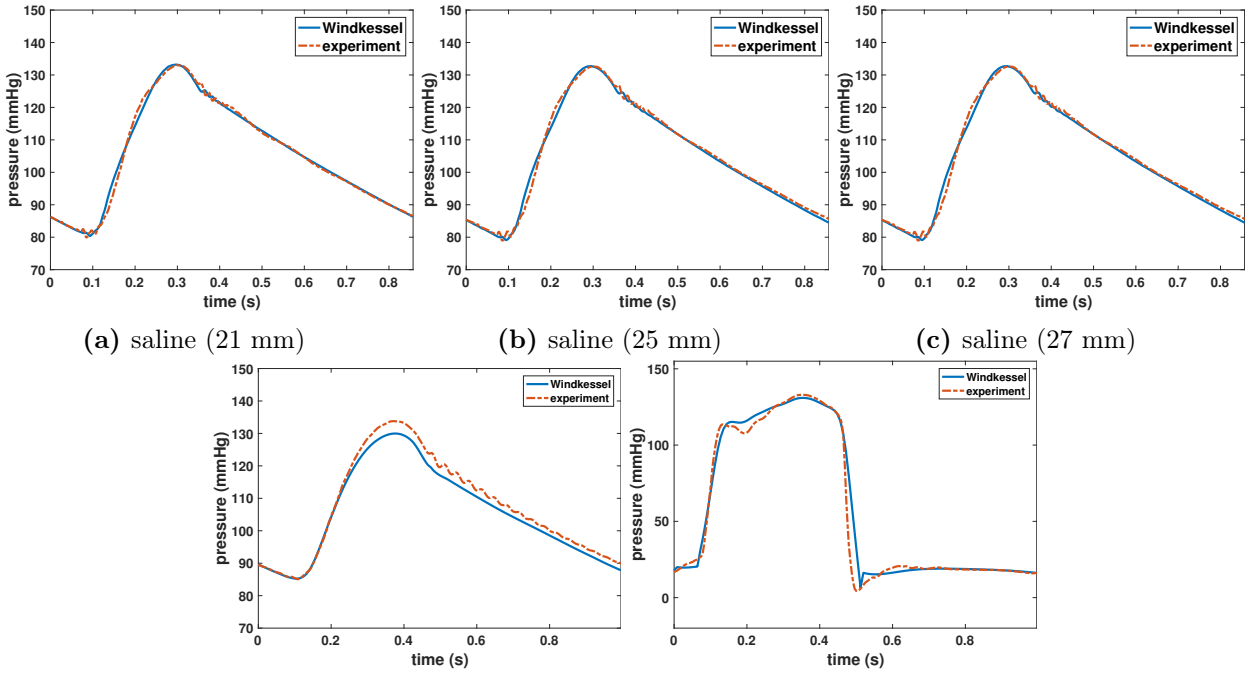


**(a)** saline (21 mm) **(b)** saline (25 mm) **(c)** saline (27 mm)

**(d)** blood analogue **(e)** blood analogue

**Figure 7.1:** Reduced-order model fits of the experimental pressure data for the saline and glycerin-based analogue cases. (a)-(d) show the fits of the experimental downstream pressure data for both saline and glycerin-based blood analogue cases. These fits are obtained using the nonlinear optimization tool fmincon in MATLAB by comparing experimental values of downstream pressure to the computed downstream pressure from the reduced-order model with experimental values of downstream flow rate as inputs to the model. (e) shows the experimental upstream pressure data for glycerin-based blood analogue case. The fit is obtained by comparing experimental values of upstream pressure to the computed upstream pressure from the reduced-order model with experimental values of left atrial pressure and pump flow rate as inputs to the model.

analogue case, respectively.

### 7.2.4 Flow characterization

To normalize flow conditions between different devices, it is convenient to use the peak Reynolds number,

$$Re_{\text{peak}} = \frac{\rho Q_{\text{peak}} D}{\mu A}, \tag{7.1}$$

which is a ratio of inertial and viscous fluid forces, in which $Q_{\text{peak}}$ is the peak volumetric flow rate and $D$ and $A$ are the geometrical diameter and cross-sectional area of the valve. Low (<2,000), intermediate (2,000–4,000), and high (>4,000) Reynolds numbers are associated with laminar, transitional, and turbulent flow regimes, respectively [144]. Physiological Reynolds numbers in

**Table 7.1:** Calibrated parameters for the reduced-order model for saline case.*

| | $R_c$ [mmHg ml$^{-1}$ s] | $R_p$ [mmHg ml$^{-1}$ s] | $C$ [mmHg ml$^{-1}$] | $R_1$ [mmHg ml$^{-1}$ s] | $R_2$ [mmHg ml$^{-1}$ s] | $C_{VIA}$ [mmHg ml$^{-1}$] |
|---|---|---|---|---|---|---|
| 21 mm (DKA015849) | 0.0184 | 1.2382 | 1.0360 | 0.3 | 0.15 | 0.1 |
| 25 mm (DKA015141) | 0.0246 | 1.1983 | 1.1241 | 0.3 | 0.15 | 0.1 |
| 27 mm (DKA015562) | 0.0255 | 1.1978 | 1.1243 | 0.3 | 0.15 | 0.1 |

* Parameters reduced-order model similar to the model in Figure 5.3a that characterize the pulse-duplicator system components both upstream and downstream of the aortic test section, including the resistance and compliance of the pump, the viscoelastic impedance adapter (VIA) subsystem, and the left ventricular chamber for saline case. The parameters are calibrated using experimental pressure and flow data obtained from the pulse duplicator. These calibrations, which are done for each experimental condition, are performed independently from the fluid-structure interaction model of the valve.

**Table 7.2:** Calibrated parameters for the reduced-order model for blood analogue case.*

| $R_c$ [mmHg ml$^{-1}$ s] | $R_p$ [mmHg ml$^{-1}$ s] | $C$ [mmHg ml$^{-1}$] | $R_{MV}$ [mmHg ml$^{-1}$ s] | $R_{out}$ [mmHg ml$^{-1}$ s] | $R_{VIA}$ [mmHg ml$^{-1}$ s] | $C_{VIA_1}$ [mmHg ml$^{-1}$] | $C_{VIA_2}$ [mmHg ml$^{-1}$] |
|---|---|---|---|---|---|---|---|
| 0.0037 | 1.8365 | 0.9490 | 0.0116 | 0.1819 | 0.15 | 0.0010 | 0.1456 |

* Parameters for the reduced-order model similar to the model in Figure 5.3b that characterize the pulse-duplicator system components both upstream and downstream of the aortic test section, including the resistance and compliance of the pump, the viscoelastic impedance adapter (VIA) subsystem, and the left ventricular chamber, as well as mitral valve and left atrial chamber for blood analogue case. The parameters are calibrated using experimental pressure and flow data obtained from the pulse duplicator. These calibrations, which are done for each experimental condition, are performed independently from the fluid-structure interaction model of the valve.

the aortic root and ascending aorta range from 5,000 to 7,000. Reynolds numbers in the in vitro system when using saline as a test fluid range from 20,000 to 30,000. This means that we are in turbulent flow regime in all cases. Notice that maintaining a constant value of $Re_{peak}$ as the device size decreases requires decreasing the flow rate.

### 7.2.5 Frequency analysis

Fluttering frequencies are assessed from PDVA and leaflet tip position time series data. We use the MATLAB Signal Processing Toolbox (The MathWorks, Inc., Natick, MA, USA) to determine the power spectral density. Because the highest peak in the power spectral density corresponds to the zero-frequency content, we use the second highest peak to determine the dominant frequency that characterizes leaflet fluttering.

### 7.2.6 Statistical analysis

We perform simple linear regression to describe the linear relationship between the dominant fluttering frequency and valve diameter. To quantify goodness of fit, we use the coefficient of

determination, $R^2$,

$$R^2 = 1 - \frac{\sum_{i=1}^{n}(y_i - \hat{y}_i)^2}{\sum_{i=1}^{n}(y_i - \bar{y})^2}, \tag{7.2}$$

in which $y_i$ are the observed dominant fluttering frequency for each valve diameter, $\bar{y}$ is the mean of $y_i$, and $\hat{y}_i$ are the predicted dominant fluttering frequency from the linear fit for each $y_i$.

### 7.2.7 Stress analysis

Changes in leaflet dimensions may alter leaflet stress distributions, which can be quantified by the von Mises stress,

$$\sigma_{\mathrm{vM}} = \sqrt{\frac{1}{2}\left[(\sigma_{11} - \sigma_{22})^2 + (\sigma_{22} - \sigma_{33})^2 + (\sigma_{33} - \sigma_{11})^2 + 6(\sigma_{23}^2 + \sigma_{31}^2 + \sigma_{12}^2)\right]}, \tag{7.3}$$

in which $\sigma_{ij}$ are the components of Cauchy elastic stress [145]. von Mises stresses are used to characterize material failure.

## 7.3 Results

Because we aim to use the computer model to systematically examine the impact of variations in device geometry on leaflet dynamics under controlled operating conditions, we first establish correspondence of the experimental and computational models for the three BHV devices available for experimental analysis. PDVA measurements are available for both experimental and computational platforms, and tip displacement measurements are available in the computational model. The experimental operating conditions are similar for the different devices, and operating conditions for the computational models can be made to be consistent with the corresponding experiment in each case. Figure 7.2 compares the measurements for corresponding experimental and computational models. The simulated pressure and flow rates are in excellent agreement with the experimental data. The dominant fluttering frequencies from experimental and simulated PDVA signals and simulated tip displacement signals, respectively, are 70.97 ± 2.11 Hz, 59.63 Hz, and 59.26 Hz (21 mm); 32.74 ± 3.14 Hz, 38.62 Hz, and 32.88 Hz (25 mm); and 26.03 ± 1.04 Hz, 21.05 Hz, and 26.32 Hz (27 mm). This demonstrates excellent qualitative agreement and reasonable quantitative agreement in leaflet fluttering frequency for each device. Further, both experimental and computational results show that much higher fluttering frequencies occur with smaller valve diameters. Experimental and simulated PDVA signals and tip displacement signals show similar fluttering frequency responses, but it is clear

that the tip displacement waveforms more directly capture the fluttering dynamics. Consequently, we use tip displacement waveforms for all subsequent spectral analyses. Figure 7.3 compares leaflet kinematics for the different valve diameters. Each row shows the leaflet cross section along its midline at selected instants. These results provide an additional qualitative description of the differences in the kinematics of the different valves. Figure 7.4 shows that fluttering frequency is negatively related to BHV diameter, with proportionality coefficients for a linear fit of $-5.65$ Hz mm$^{-1}$ ($R^2 = 0.97934$) and $-7.79$ Hz mm$^{-1}$ ($R^2 = 0.96259$), respectively, for computational and experimental models.

A major advantage of the computational model is that it allows us to eliminate variations in operating conditions. Figure 7.5 compares PDVA and tip displacements obtained using the computational model for different valve diameters, as in Figure 7.2, but now using flow rates and driving and loading pressures that are consistent with the experimental conditions used with the 21 mm valve to eliminate variations in operating conditions. Dominant fluttering frequencies determined from tip displacement waveforms are 59.26 Hz (21 mm), 32.88 Hz (25 mm), and 26.32 Hz (27 mm), respectively, which are identical to the results obtained when matching the experimental operating conditions for each device. Because the frequencies are the same, this clearly demonstrates that variations in leaflet flutter are maintained when operating conditions are normalized across valve sizes.

We next use the computational model to consider the effect of leaflet thickness on device kinematics at a fixed device diameter of 25 mm. Figure 7.6 shows that valves with thicker leaflets open less, consistent with prior studies [32]. It also shows that valves with thicker leaflets flutter at higher frequencies than valves with thinner leaflets. The dominant fluttering frequencies are 27.40 Hz (0.2 mm), 32.88 Hz (0.4 mm), and 43.84 Hz (0.6 mm). Figure 7.7 shows cross-sectional views of each valve leaflet through its midline. The dynamics of the thicker leaflets are consistent with those of a valve of normal thickness and smaller diameter, whereas the thinner leaflets yield kinematics like a valve of normal thickness and larger diameter.

Experimental data characterizing the role of device geometry on leaflet kinematics are only available for cases that use saline as the test fluid. Consequently, we use our computer model to study leaflet fluttering using parameters consistent with a glycerin-based blood analogue, which provides a more physiological Reynolds number than saline. We perform computer simulations with 1) consistent operating conditions (flow rates and pressure differences) and 2) consistent peak

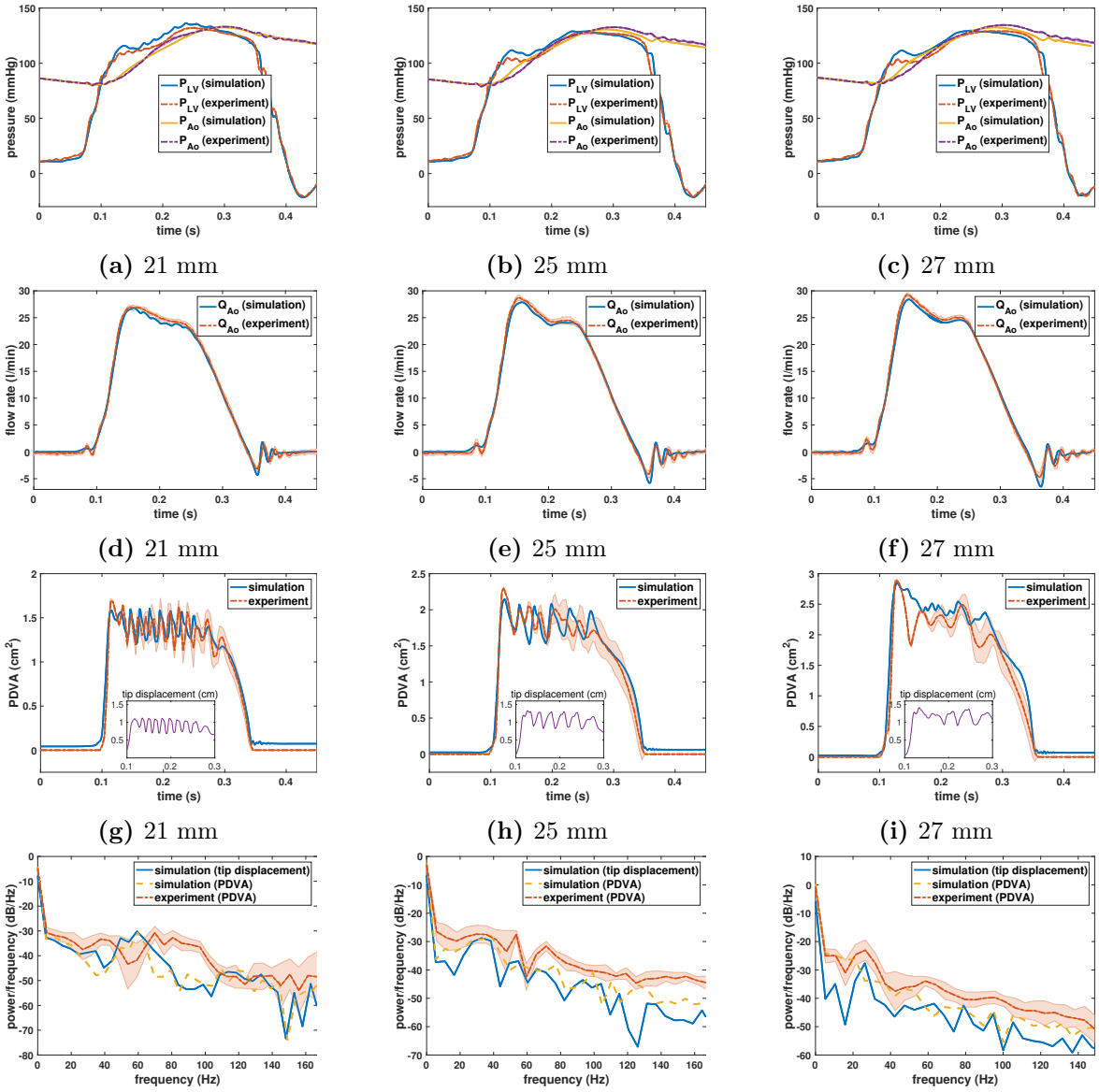


**(a)** 21 mm **(b)** 25 mm **(c)** 27 mm

**(d)** 21 mm **(e)** 25 mm **(f)** 27 mm

**(g)** 21 mm **(h)** 25 mm **(i)** 27 mm

**(j)** 21 mm **(k)** 25 mm **(l)** 27 mm

**Figure 7.2:** Comparison between in vitro and in silico (a)-(c) pressure, (d)-(f) volumetric flow rates, and projected dynamic valve area (PDVA). Experimental measurements show variations over 10 consecutive cycles, with shaded regions showing where 95% of the data fall. For each valve diameter, the computational model matches the experimental operating conditions, which are different for each valve. The inner plots in (g)-(i) show the simulated displacement of the leaflet tip from the center of the valve. Panels (j)-(l) show frequency analyses of leaflet fluttering to quantify the dominant fluttering frequencies from experimental and simulated PDVA signals and simulated tip displacement signals are, respectively: (j) 70.97 ± 2.11 Hz, 59.63 Hz, 59.26 Hz; (k) 32.74 ± 3.14 Hz, 38.62 Hz, 32.88 Hz; and (l) 26.03 ± 1.04 Hz, 21.05 Hz, 26.32 Hz. Smaller valves clearly show high fluttering frequencies, whereas larger valves show lower frequencies.

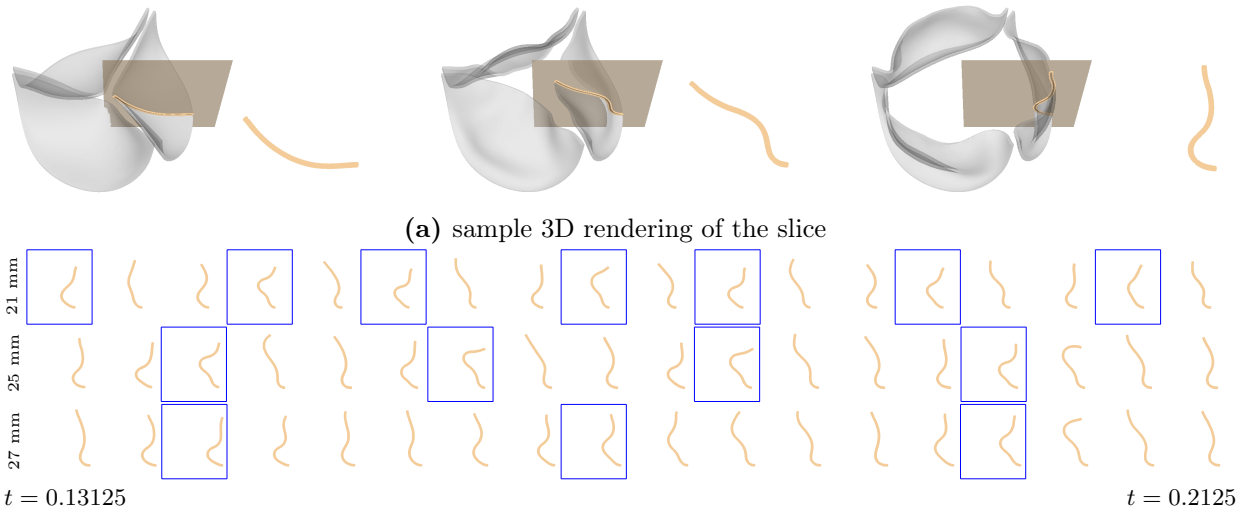


**(a)** sample 3D rendering of the slice

**(b)** sliced views

**Figure 7.3:** Detailed leaflet kinematics obtained from the computational model with different valve diameters. (a) Three-dimensional rendering of the valve leaflets. Leaflet kinematics are detailed on the highlighted cross-sections in (b). (b) Time series of leaflet cross sections for different valve diameters described in Figure 7.2. Blue boxes indicate the times when the peak tip displacement of the leaflet occurs. Note that complex flow patterns result in only quasi-periodic leaflet kinematics. The smaller-diameter valve (21 mm) shows more frequent leaflet bending than the larger-diameter valve (27 mm).

Reynolds numbers for a broad range of device sizes (19, 21, 23, 25, and 27 mm). In these computer experiments, the volumetric pump waveform that drives the flow is reduced by the ratio between the control (27 mm) to the valve diameter of interest. This reduces the peak flow rate by the same ratio, yielding constant values of $Re_{\text{peak}}$. Figure 7.8 shows that after matching the flow conditions for the 19, 21, 23, and 25 mm cases to the flow condition for the 27 mm case, the dominant fluttering frequencies are 47.86 Hz (19 mm), 35.82 Hz (21 mm), 31.75 Hz (23 mm), 25.24 Hz (25 mm), and 12.12 Hz (27 mm). If we instead match operating conditions, but not flow conditions, using the glycerin, the dominant fluttering frequencies are 59.70 Hz (19 mm), 46.75 Hz (21 mm), 32.00 Hz (23 mm), 25.32 Hz (25 mm), and 12.12 Hz (27 mm). Figure 7 compares linear regressions of fluttering frequency with respect to valve diameter for consistent operating and flow conditions. Frequency response is negatively related to valve diameter in both cases, with coefficients $-5.65$ Hz mm$^{-1}$ ($R^2 = 0.97934$) and $-5.83$ Hz mm$^{-1}$ ($R^2 = 0.96259$) for consistent operating and flow conditions, respectively. These results indicate that fluttering frequencies differ markedly with valve diameter, even under identical flow conditions. Importantly, the proportionality coefficients are essentially the

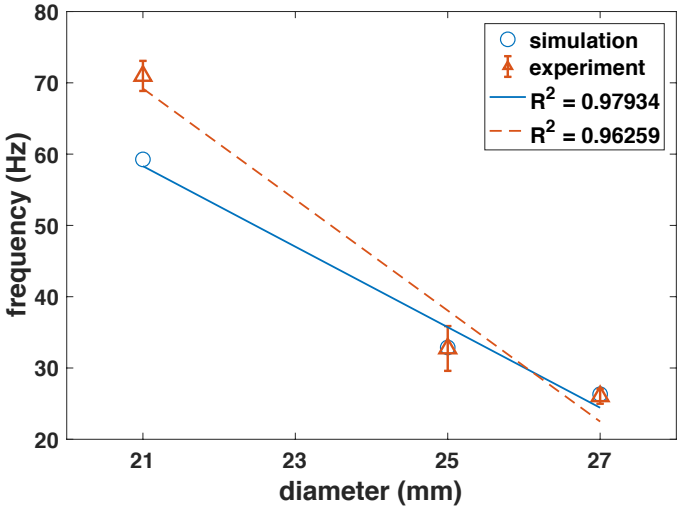


**Figure 7.4:** Comparison of linear regressions of fluttering frequency vs. valve diameter between simulations and experiments. Blue circles represent dominant fluttering frequency data from simulations that match the slightly different experimental operating conditions for each device. Red triangles represent dominant fluttering frequency data with respect to valve diameters obtained from experimental projected dynamic valve area measurements. Linear regression fits show that both results show negative relation between the frequency response and the valve diameter, with proportionality coefficients of $-5.65$ Hz mm$^{-1}$ and $-7.79$ Hz mm$^{-1}$, respectively, for simulation (blue solid) and experiment (red dashed).

same for glycerin ($-5.83$ and $-4.10$ Hz mm$^{-1}$) and for saline ($-5.65$ Hz mm$^{-1}$), which suggests that relative differences in fluttering frequencies are largely independent of flow conditions and are, instead, determined primarily by device geometry.

It is known that the largest stresses that the valves experience occur in diastole [146], and the valve leaflets experience largest stress and fatigue near its commissures [96, 146]. Our computational model correctly predicts the high stress region near the commissures, and this analysis allows us to quantify diastolic stress distributions using exactly the same BHV biomechanics models as used to quantify leaflet kinematics (Figure 7.10). In addition to locating the regions of large stresses, our model also recapitulates that at a fixed thickness, the larger diameter valve shows reduced stresses [147], particularly near the commissures. For a fixed diameter, the valve with thinner leaflets experiences much larger stresses than the valve with thicker leaflets as shown previously [32], although our dynamic results indicate that the valve with thinner leaflets produces systolic dynamics analogous to a larger-diameter valve. The stress analysis in Figure 7.10 clearly indicates that larger diameter valves have an advantage not only during systole because of reduced fluttering, but also

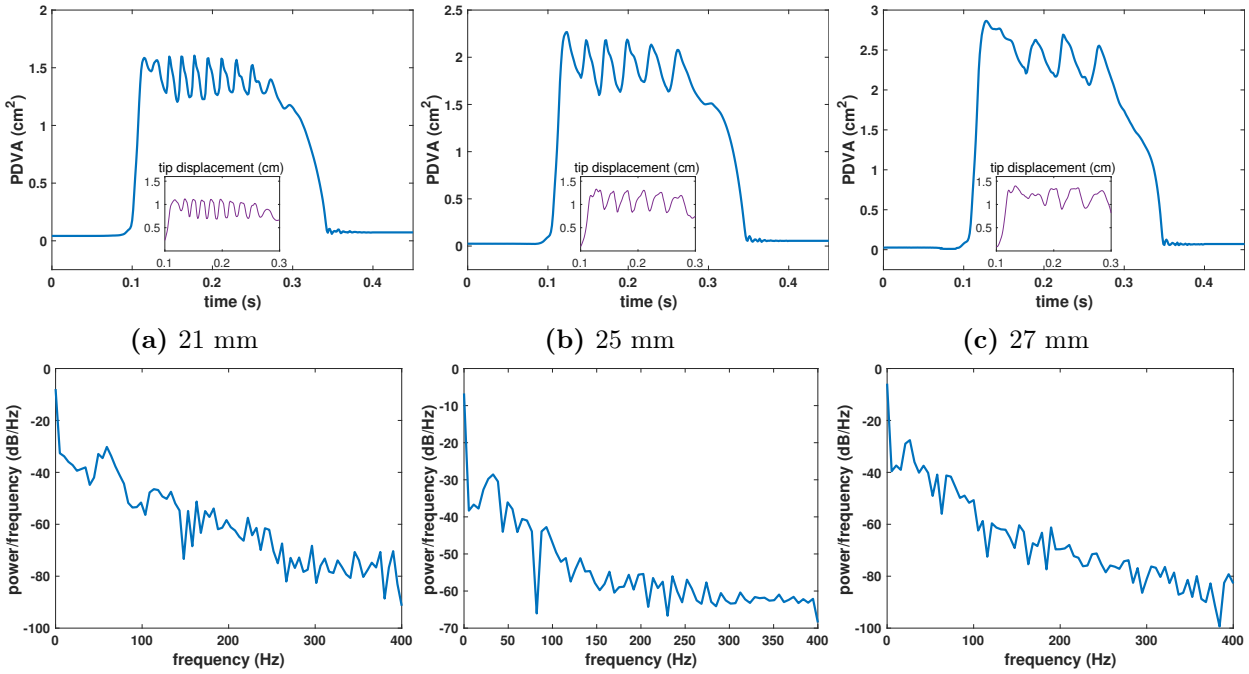


**(a)** 21 mm **(b)** 25 mm **(c)** 27 mm

**(d)** 21 mm **(e)** 25 mm **(f)** 27 mm

**Figure 7.5:** Analysis of simulated leaflet kinematics for valves with different diameters under consistent operating conditions. (a)-(c) PDVA and tip displacements are obtained from the computational models for each valve diameter using identical volumetric flow rates and pressure loads corresponding to the 21 mm valve in Figure 7.2g. (d)-(f) Frequency analyses to quantify the dominant fluttering frequencies: (d) 59.26 Hz; (e) 32.88 Hz; and (f) 26.32 Hz. These frequencies are identical to those reported in Figure 7.2.

during diastole through reduced leaflet stresses.

## 7.4 Discussion

To our knowledge, the only prior work to characterize the role of BHV geometry on fluttering dynamics is that of Avelar et al. [148], which used an experimental system to study fluttering in several sizes of bovine and porcine pericardial BHVs. That study did not control for variations in device diameter, leaflet thickness or biomechanics, or operating conditions, however, and it considered only steady flow conditions. In contrast, the experimental platform used in this study provides more physiological pulsatile operating conditions, and the computational platform provides precise control over device properties and operating conditions, enabling a more comprehensive assessment of the impacts of device geometry on leaflet dynamics.

Using both experimental and computational models, we consistently find that smaller-diameter pericardial aortic valves show substantially higher leaflet fluttering frequencies compared to larger

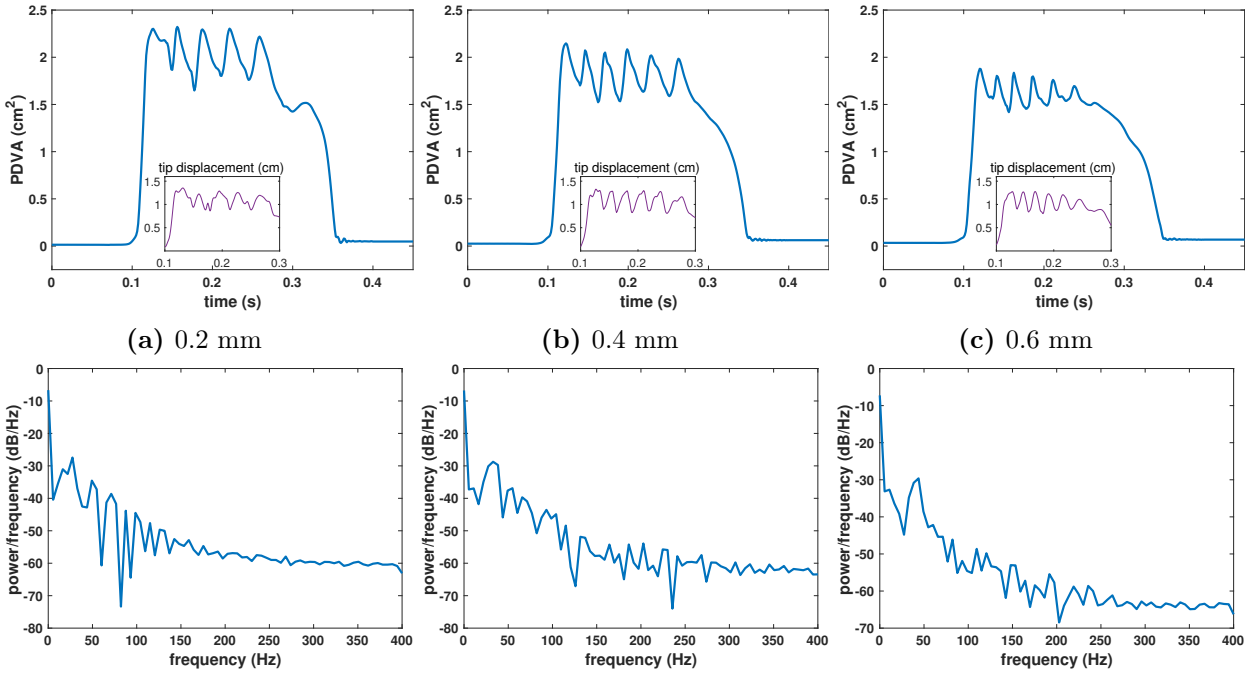


**(a)** 0.2 mm **(b)** 0.4 mm **(c)** 0.6 mm

**(d)** 0.2 mm **(e)** 0.4 mm **(f)** 0.6 mm

**Figure 7.6:** Analysis of simulated leaflet kinematics for valves with different leaflet thicknesses under consistent operating condition. (a)-(c) PDVA and tip displacements are obtained from the computational models using the operating condition for the 25 mm valve but with varying leaflet thicknesses. (d)-(f) Frequency analyses to quantify the dominant fluttering frequencies: (d) 27.40 Hz; (e) 32.88 Hz; and (f) 43.84 Hz. These results suggest that at a fixed diameter, valves with thinner leaflets flutter at lower frequencies.

valves. Further, our computer model predicts that at a fixed device diameter, thinner leaflets will yield smaller fluttering frequencies than thicker leaflets under consistent volumetric flow rates and pressure differences. Differences in operating or flow conditions can impact fluttering dynamics, but we confirm that under similar operating conditions, both saline and glycerin cases show that the fluttering frequency negatively related to the valve diameter, with proportionality coefficients from a linear regression of $-5.65$ Hz mm$^{-1}$ ($R^2 = 0.97934$) and $-5.83$ Hz mm$^{-1}$ ($R^2 = 0.98918$), respectively, for saline and glycerin. Differences in BHV fluttering have been ascribed to variations in pressures and flow rates in the clinical literature [130, 149]. Our tests using a pulse duplicator, however, clearly indicate that fluttering frequencies differ with valve geometry, even under identical operating or flow conditions.

Taken together with studies on the impact of flutter on the durability of thin structures in other biological and manufactured systems [131, 133, 135], the results of this study suggest that the

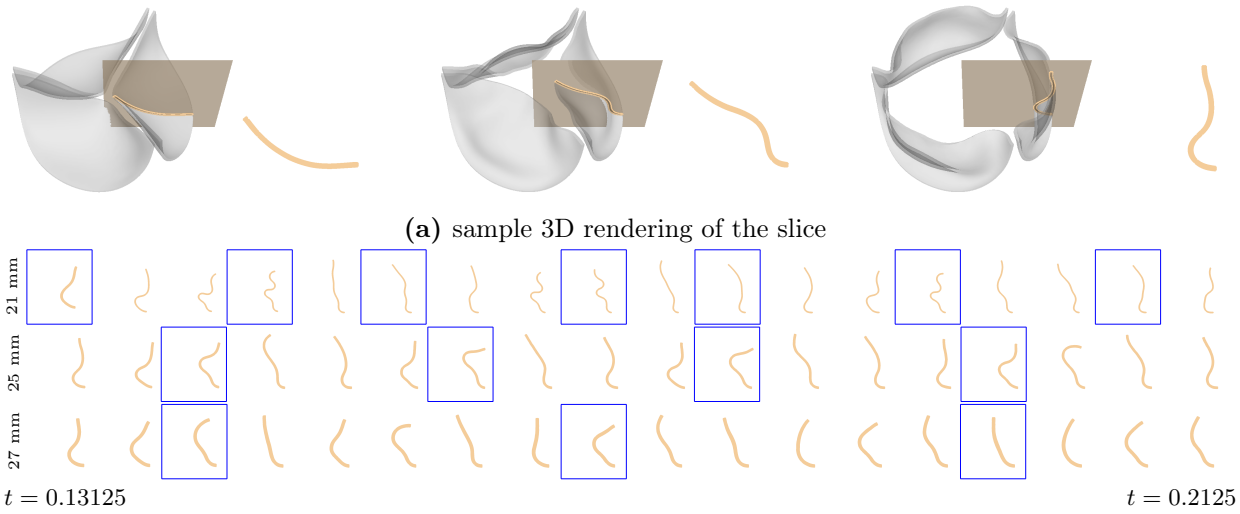


**(a)** sample 3D rendering of the slice

**(b)** sliced views

**Figure 7.7:** Detailed leaflet kinematics obtained from the computational model with different valve thicknesses. (a) Three-dimensional rendering of the valve leaflets. Leaflet kinematics are detailed on the highlighted cross-sections in (b). (b) Time series of leaflet cross sections for different valve thicknesses for a fixed valve diameter (25 mm) described in Figure 7.6. Blue boxes indicate the times when the peak tip displacement of the leaflet occurs. The thicker valve leaflet (0.6 mm) shows more frequent leaflet bending than the thinner valve leaflet (0.2 mm).

high frequency fluttering in smaller valves may provide a mechanistic explanation for prior clinical observations that aortic valve replacement using small BHVs leads to earlier device failure [138, 139]. Because our computer model suggests that for a fixed device diameter and pressure load, thicker leaflets show higher fluttering frequencies than thinner leaflets, an intriguing prediction of this study is that an approach to reducing leaflet flutter could be to use thinner biomaterials. However, as shown in Figure 7.10, thinner leaflets experience larger stresses in diastole, especially near the commissures, which may also cause fatigue [95, 146, 150]. The stress analysis in Figure 7.10 clearly shows that larger diameter valves have an advantage not only during systole because of reduced fluttering, but also during diastole through reduced leaflet stresses. Although there are limits in terms of what can be done with fixated tissues, one possibility is to use different fixation pressures to achieve different stiffnesses, or different fiber distributions can be designed [151]. Additional experimental, computational, and in vivo studies are clearly needed, but taken together with prior results [96, 146] that indicate that diastolic leaflet stresses are minimized in larger-diameter devices with thicker leaflets, our results suggest the hypothesis that durability will be maximized by choosing

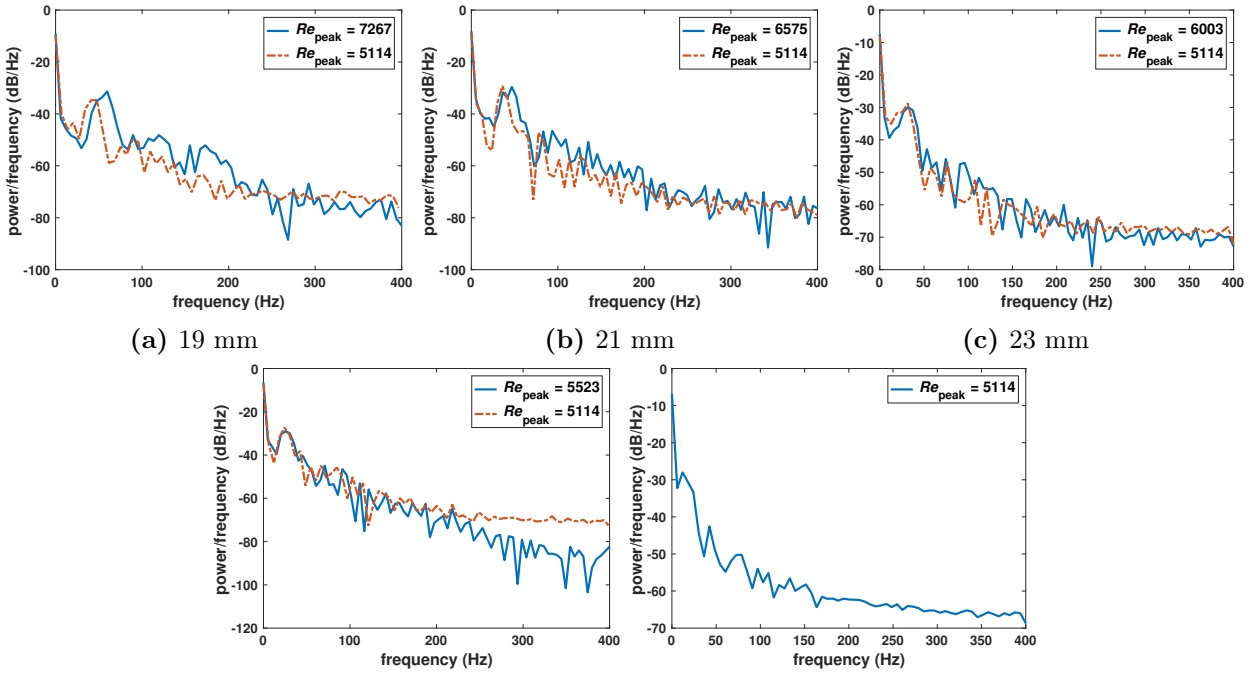


**(a)** 19 mm **(b)** 21 mm **(c)** 23 mm

**(d)** 25 mm **(e)** 27 mm

**Figure 7.8:** Analysis of simulated leaflet kinematics for valves with different diameters at physiological Reynolds numbers with consistent operating and flow conditions. (a)-(c) Frequency analyses of leaflet fluttering obtained using a glycerin-based blood analogue. Blue solid lines represent the simulation results obtained for a fixed operating condition but varying flow conditions (quantified by Reynolds number, $Re_{\text{peak}}$). Red dashed lines represent results for which the driving condition is modified to match $Re_{\text{peak}}$. The dominant fluttering frequencies for different Reynolds number cases: (a) 59.70 and 47.86 Hz; (b) 46.75 and 35.82 Hz; (c) 32.00 and 31.75 Hz; (d) 25.32 and 25.24 Hz; and (e) 12.12 Hz. Smaller-diameter valves show higher frequency leaflet fluttering; see also Figure 7.9.

the largest possible BHV diameter along with a leaflet thickness that is optimized for both systolic and diastolic conditions.

A limitation of this study is that our experimental studies analyze the performance of only Labcor bovine pericardial BHVs, which are not FDA approved and is not used in the U.S. We use Labcor DKA bovine pericardial valves because they were available to use in a variety of sizes and without any restriction on publication. We have also looked at samples of Edward PERIMOUNT (Edwards Lifesciences, Irvine, CA, USA) valves of size 25 mm, although they are tested in different operating conditions (Figure 7.11). We do not include the Edwards valve data in our full study because we do not have other sizes to study the relationship between leaflet kinematics and valve diameters. However, our computational model uses a generic pericardial BHV leaflet biomechanics

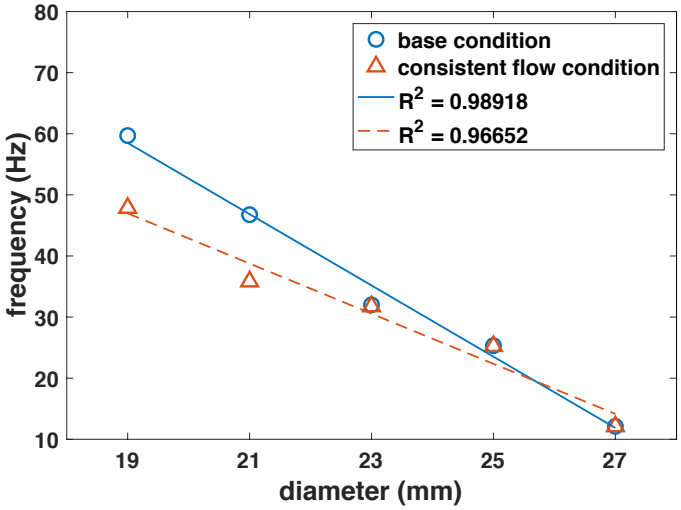


**Figure 7.9:** Linear regression of fluttering frequency vs. valve diameter at physiological Reynolds numbers with consistent operating and flow conditions. Blue circles represent dominant fluttering frequency data with respect to valve diameters obtained for a fixed operating condition but varying flow conditions (quantified by Reynolds number). Red triangles represent dominant fluttering frequency data with respect to valve diameters in which the driving condition is modified to match Reynolds number. Linear regression fits show negative relation between the frequency response and the valve diameter, with proportionality coefficients of $-5.83$ Hz mm$^{-1}$ (blue solid) and $-4.10$ Hz mm$^{-1}$ (red dashed) for consistent operating conditions and flow conditions, respectively.

model that was not tuned in any way to match the properties of the Labcor BHVs. Consequently, our key findings may generalize to devices produced by other manufacturers. we can see in Figure (Figure 7.11) that the dominant fluttering frequencies are similar: 32.74 $\pm$ 3.14 Hz for Labcor valve and 29.62 $\pm$ 4.7 Hz for Edwards valve. Our previous work [19] in Section 5 has also shown that our leaflet mechanics models of valves based on experimental biaxial tensile test data are able to capture the leaflet kinematics of different types of surgical bioprosthetic valves (porcine aortic valve and Edwards PERIMOUNT bovine pericardial valve). Another limitation is that we use a rigid aortic root model, which could influence fluttering frequencies. In future work, we plan to consider flexible aortic valve test sections within both the experimental ViVitro Pulse Duplicator system and our computer model of this experimental system, as well as to study leaflet kinematics in cryopreserved aortic root grafts. We also note that although some studies report fluttering in native aortic valves [152–154], this study does not address native valves, which possess different material properties than pericardial BHVs. Further, native valve leaflets are living tissue that may not suffer from fluttering in the same way as chemically fixated tissues.

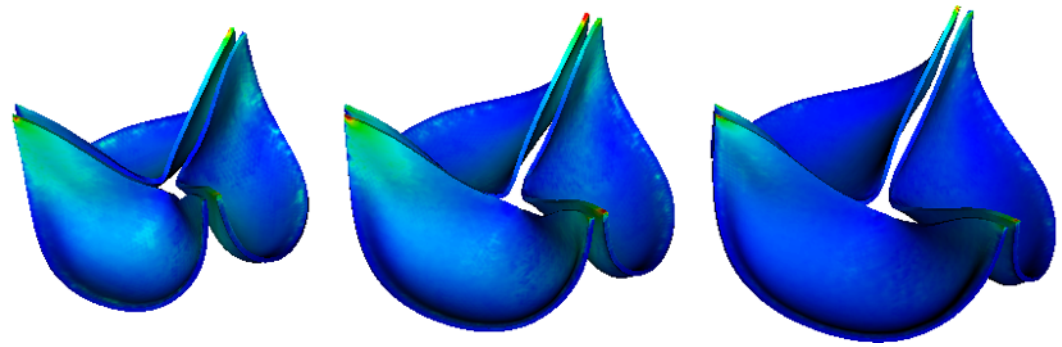

**(a)** variations in diameter: 21 mm, 25 mm, 27 mm

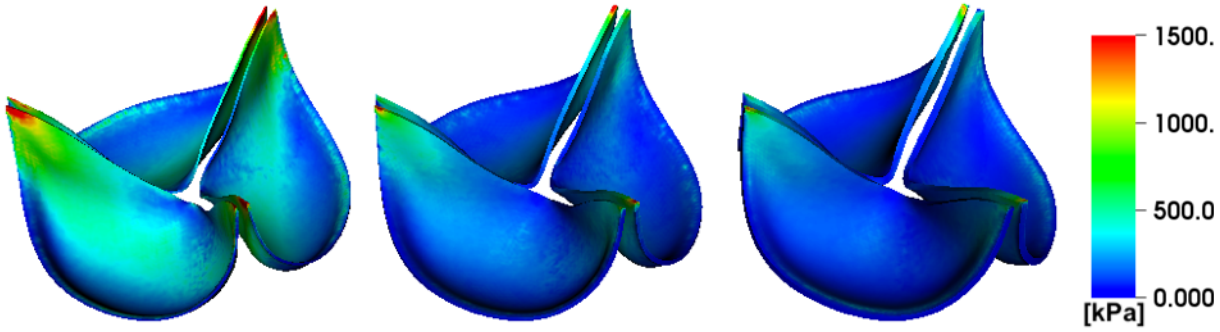


**(b)** variations in thickness: 0.2 mm, 0.4 mm, 0.6 mm

**Figure 7.10:** Stress analyses for 25mm valves with different leaflet thicknesses. (a) Comparison of von Mises stress between valves with a fixed thickness (0.4 mm) and different diameters (21 mm, 25 mm, 27 mm). (b) Comparison of von Mises stress between valves with a fixed diameter (25 mm) and different thicknesses (0.2 mm, 0.4 mm, 0.6 mm). The results in panel (a) indicate that for a fixed thickness, the larger valve experiences smaller stress on the leaflets during diastole. This suggests that larger diameter valves may have an advantage in durability both during systole and diastole. The results in panel (b) indicate that for a fixed diameter, the thinner valve leaflets experience higher stress loads.

Ultimately, our goal is to optimize BHV design by understanding the geometrical and mechanical factors that govern BHV leaflet fluttering and its impact on leaflet durability. Although the present study is unable to reveal the underlying mechanisms that determine leaflet durability, understanding the effects of device geometry on leaflet kinematics may help to improve guidelines for BHV selection. This is potentially highly relevant for both surgical and transcatheter valve replacement. In surgical valve replacement, for instance, our results suggest that there may be a role for aortic root enlargement in improving the BHV durability. Interestingly, several prior studies have reported on the effects of aortic root enlargement [155, 156] in improving hemodynamics and alleviating prosthesis–patient mismatch by using larger valves [124, 125, 140]. Similarly, this study has potential implications in

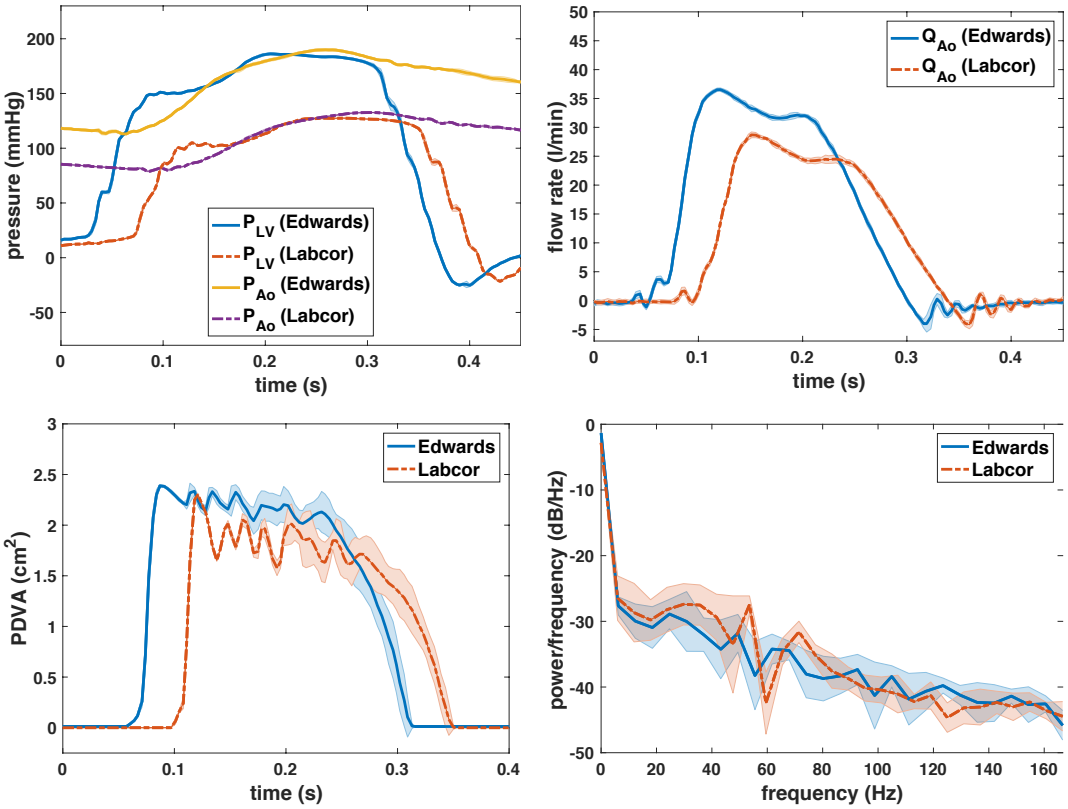


**Figure 7.11:** Comparison of leaflet kinematics of 25 mm Labcor DKA vs. Edwards PERIMOUNT valves. Experimental measurements show variations over 10 consecutive cycles, with shaded regions showing where 95% of the data fall for both valves. We quantify the dominant fluttering frequencies from the experimental projected dynamic valve area (PDVA) signals: 32.74 $\pm$ 3.14 Hz for the Labcor valve and 29.62 $\pm$ 4.7 Hz for the Edwards valve.

identifying factors that impact the durability of TAVR. Importantly, in TAVR valves, it is desirable to use thinner biomaterials to improve device deliverability. Our analysis suggests that these leaflets will flutter at a lower frequency than thicker valve leaflets at the same deployed device diameter, potentially reducing flutter-related fatigue, although thinner biomaterials will also be subject to additional stress during diastole. These predictions have yet to be verified either experimentally or computationally, however, and further work is clearly needed to determine whether the current findings apply to TAVR valves. It is possible to extend these platforms to study other geometrical variations in TAVR valves, including the effect of incompletely expanded TAVR valves that can demonstrate "pin-wheeling" of the leaflets [85]. Understanding the precise role of fluttering on device fatigue and failure requires further study, but device designs may ultimately aim to balance these two geometrical factors to optimize device durability.

APPENDIX A

# STABILIZATION METHOD FOR THE HYPERELASTIC IMMERSED BOUNDARY METHOD

**Data in this section are from a paper published in *Computer Methods in Applied Mechanics and Engineering* [42] and are provided by Ben Vadala-Roth.**

In the continuum equations of the IB framework, the Cauchy stress on the full domain can be seen to take the form

$$\boldsymbol{\sigma}(\mathbf{x},t) = \boldsymbol{\sigma}_{\mathrm{f}}(\mathbf{x},t) + \begin{cases} \mathbb{0}, & \mathbf{x} \in \Omega_t^{\mathrm{f}}, \\ \boldsymbol{\sigma}_{\mathrm{e}}(\mathbf{x},t), & \mathbf{x} \in \Omega_t^{\mathrm{s}}, \end{cases} \tag{A.1}$$

which can also be written as

$$\boldsymbol{\sigma}(\mathbf{x},t) = \mathrm{dev}[\boldsymbol{\sigma}_{\mathrm{v}}(\mathbf{x},t)] - p(\mathbf{x},t)\mathbb{I} + \begin{cases} \mathbb{0}, & \mathbf{x} \in \Omega_t^{\mathrm{f}}, \\ \boldsymbol{\sigma}_{\mathrm{e}}(\mathbf{x},t), & \mathbf{x} \in \Omega_t^{\mathrm{s}}, \end{cases} \tag{A.2}$$

in which $\boldsymbol{\sigma}_{\mathrm{e}} = \frac{1}{J}\mathbb{P}\mathbb{F}^T$, $\boldsymbol{\sigma}_{\mathrm{v}} = \mu(\nabla\mathbf{u} + \nabla\mathbf{u}^T)$ is the viscous stress, the pressure $p$ is a Lagrange multiplier that imposes the incompressibility constraint for both the fluid and structure, and $\mathrm{dev}[\boldsymbol{\sigma}_{\mathrm{v}}] = \boldsymbol{\sigma}_{\mathrm{v}} - \frac{\mathrm{tr}(\boldsymbol{\sigma}_{\mathrm{v}})}{3}\mathbb{I}$ is the deviatoric part of $\boldsymbol{\sigma}_{\mathrm{v}}$. Although the continuous IB equations model the structure as exactly incompressible, the present numerical method is not guaranteed to preserve the divergence of the Eulerian velocity field when that field is evaluated on the Lagrangian finite element mesh. Consequently, the method only approximately accounts for the incompressibility of the immersed structure, although the accuracy of this approximation improves under grid refinement. Vadala-Roth et al. [42] introduced a volumetric energy in the solid region to stabilize and improve the accuracy of the numerical scheme substantially,

$$\boldsymbol{\sigma}(\mathbf{x},t) = \mathrm{dev}[\boldsymbol{\sigma}_{\mathrm{v}}(\mathbf{x},t)] - p(\mathbf{x},t)\mathbb{I} + \begin{cases} \mathbb{0}, & \mathbf{x} \in \Omega_t^{\mathrm{f}}, \\ \mathrm{dev}[\boldsymbol{\sigma}_{\mathrm{e}}(\mathbf{x},t)] - p_{\mathrm{stab}}(\mathbf{x},t)\mathbb{I}, & \mathbf{x} \in \Omega_t^{\mathrm{s}}, \end{cases} \tag{A.3}$$

in which the stabilization term $p_{\mathrm{stab}} = -\partial U/\partial J$ acts as a pressure that reinforces incompressibility in the solid region in the numerical method. We refer to this as a stabilization method because its effect vanishes under grid refinement. Specifically, in the continuum limit, the structure is automatically

incompressible in the IB framework, and so $J \equiv 1$ and $p_{\text{stab}} \equiv 0$. This stabilization method has been tested using standard quasi-static solid mechanics benchmark problems. Sections A.1 and A.2 show two benchmark examples from Vadala-Roth et al. [42] that demonstrate the effect of this stabilization method. These results are compared to and show excellent agreement with the results from a stabilized incompressible finite element solid mechanics formulation. Additional details are provided by Vadala-Roth et al. [42].

## A.1 Compression benchmark

This benchmark involves a rectangular block with a downward traction of 200 dyn cm$^{-2}$ applied at the center of the top side along with zero horizontal displacement. Zero vertical displacement is imposed at the bottom side of the block, and zero traction is applied at all sides other than the top side [157], as shown in Figure A.1a. The block is a neo-Hookean material,

$$\Psi = \frac{c_1}{2}(\bar{I}_1 - 3) + \frac{\kappa_{\text{stab}}}{2}(\ln J)^2, \tag{A.4}$$

in which $\bar{I}_1 = \text{tr}(\overline{\mathbb{C}})$ is the first invariant of the modified right Cauchy-Green strain tensor $\overline{\mathbb{C}} = \overline{\mathbb{F}}^T\overline{\mathbb{F}} = J^{-2/3}\mathbb{F}^T\mathbb{F}$. Here, $c_1$ is the shear modulus, and $\kappa_{\text{stab}}$ is the numerical bulk modulus controlled by the shear modulus and the numerical Poisson ratio, $\nu_{\text{stab}}$, via

$$\kappa_{\text{stab}} = \frac{2\mu_{\text{s}}(1+\nu_{\text{stab}})}{3(1-2\nu_{\text{stab}})}, \tag{A.5}$$

in which $\mu_{\text{s}}$ is the linearized ($\mathbb{F} = \mathbb{I}$) shear modulus. For the neo-Hookean model, $\mu_{\text{s}} = c_1$. This test uses $c_1 = 80.194$ dyn cm$^{-2}$ and $\nu_{\text{stab}} = 0.4$. The density and viscosity are $\rho = 1.0$ g cm$^{-3}$ and $\mu = 0.01$ dyn s cm$^{-2}$, respectively. We again emphasize that the numerical bulk modulus, $\kappa_{\text{stab}}$, and the numerical Poisson ratio, $\nu_{\text{stab}}$, act as stabilization parameters, and not as physical parameters of the model, and that their effects vanish under grid refinement. This test shows that using the stabilization method yields superior volume conservation and smooth deformations for the mesh elements (Figures A.1b and A.1d).

## A.2 Torsion benchmark

This benchmark involves applying torsion to an elastic beam [158] as shown in Figure A.2a. Torsion is applied to the top face of the beam while zero displacement is imposed at the opposite

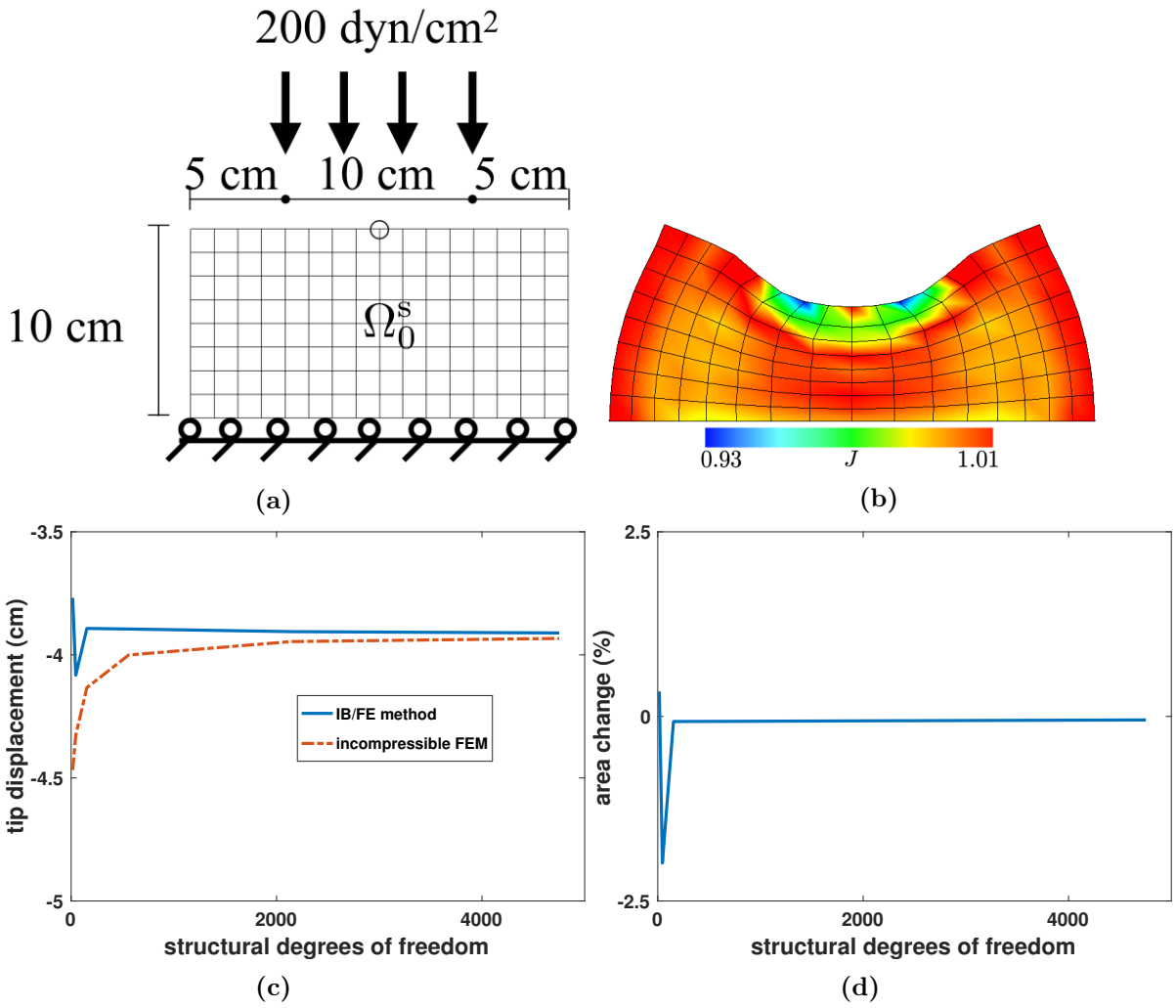


**Figure A.1:** (a) Schematic of the compressed block benchmark from Vadala-Roth et al. [42]. A downward traction applied at the center of the top side along with zero horizontal displacement. Zero vertical displacement is imposed at the bottom side of the block, and zero traction is applied at all sides other than the top side, as used by Reese et al. [157]. (b) Deformation of the compressed block for a neo-Hookean material model. The stabilization method results in smooth element deformation as well as excellent volume (area) conservation. The color shows the magnitude of $J = \det(\mathbb{F})$. (c) Displacement of the circled location in panel a compared to result from using standard incompressible structural mechanics formulation. (d) Percent change in total area; see also panel (b).

face. Zero traction boundary conditions were used on all the other faces. The elastic beam is a Mooney-Rivlin material,

$$\Psi = c_1(\bar{I}_1 - 3) + c_2(\bar{I}_2 - 3) + \frac{\kappa_{\text{stab}}}{2}(\ln J)^2, \tag{A.6}$$

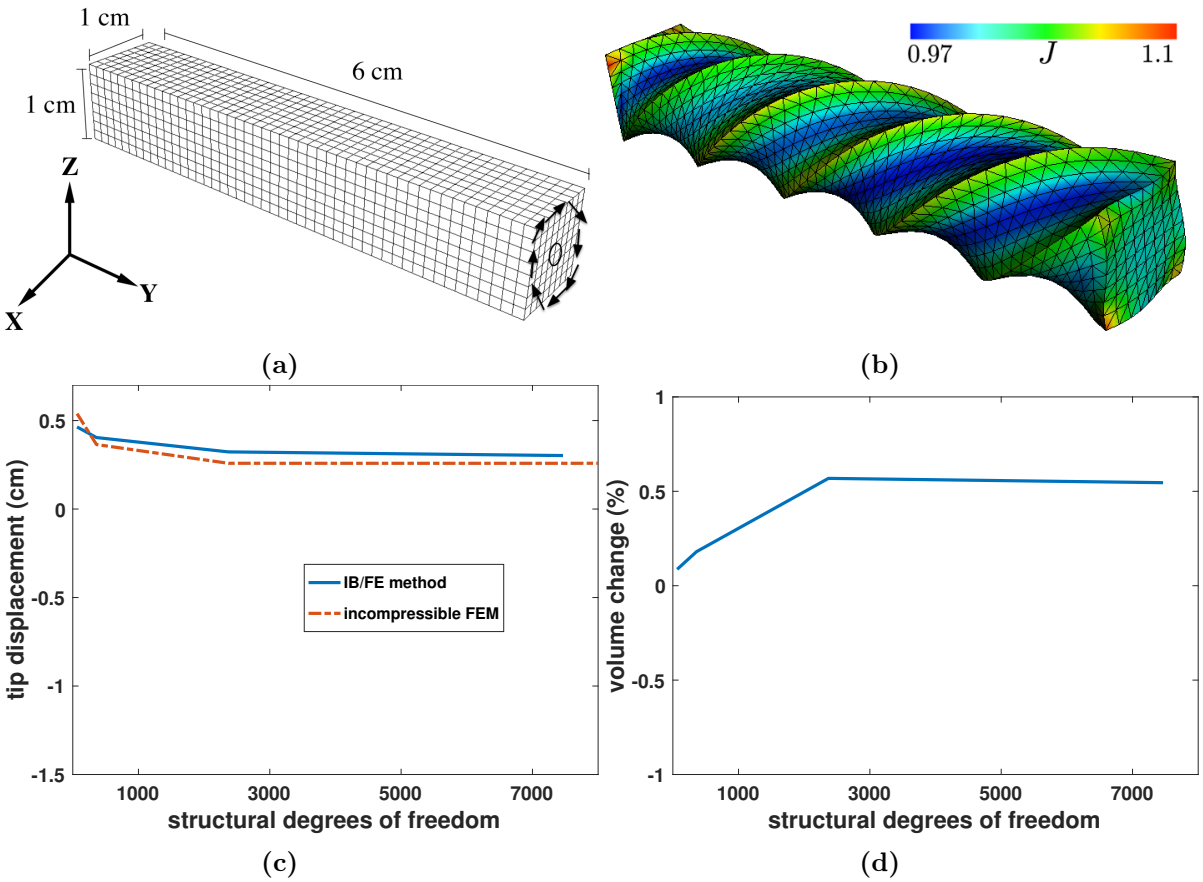


**Figure A.2:** (a) Schematic of the torsion benchmark from Vadala-Roth et al. [42]. A Mooney-Rivlin material model is used, and torsion is applied to the top face of the beam while zero displacement is imposed at the opposite face. Zero traction boundary conditions were used on all the other faces, as in Bonet et al. [158]. (b) Deformation of the torsion test for a Mooney-Rivlin material model. The stabilization method results in smooth element deformation as well as excellent volume conservation. The color shows the magnitude of $J = \det(\mathbb{F})$. (c) Displacement of the tip position (the circled location in panel a) on the beam in the axial (Y) direction compared to result from using standard incompressible structural mechanics formulation. (d) Percent change in total volume; see also panel (b).

in which $\bar{I}_2 = (\bar{I}_1^2 - \mathrm{tr}(\overline{\mathbb{C}}^2))/2$ is the second invariant of $\overline{\mathbb{C}}$. For the Mooney-Rivlin model, $\mu_s = 2(c_1 + c_2)$. This test uses material parameters $c_1 = 9000$ dyn cm$^{-2}$, $c_2 = 9000$ dyn cm$^{-2}$, and $\nu_{\text{stab}} = 0.4$. The density and viscosity are $\rho = 1.0$ g cm$^{-3}$ and $\mu = 0.04$ dyn s cm$^{-2}$, respectively. This test also shows that the stabilization method gives reasonable deformation (Figure A.2c) as well as yielding superior volume conservation (Figures A.2b and A.2d).

APPENDIX B

# TUREK-HRON BENCHMARK RESULTS FOR VARIOUS CHOICES OF KERNEL FUNCTION

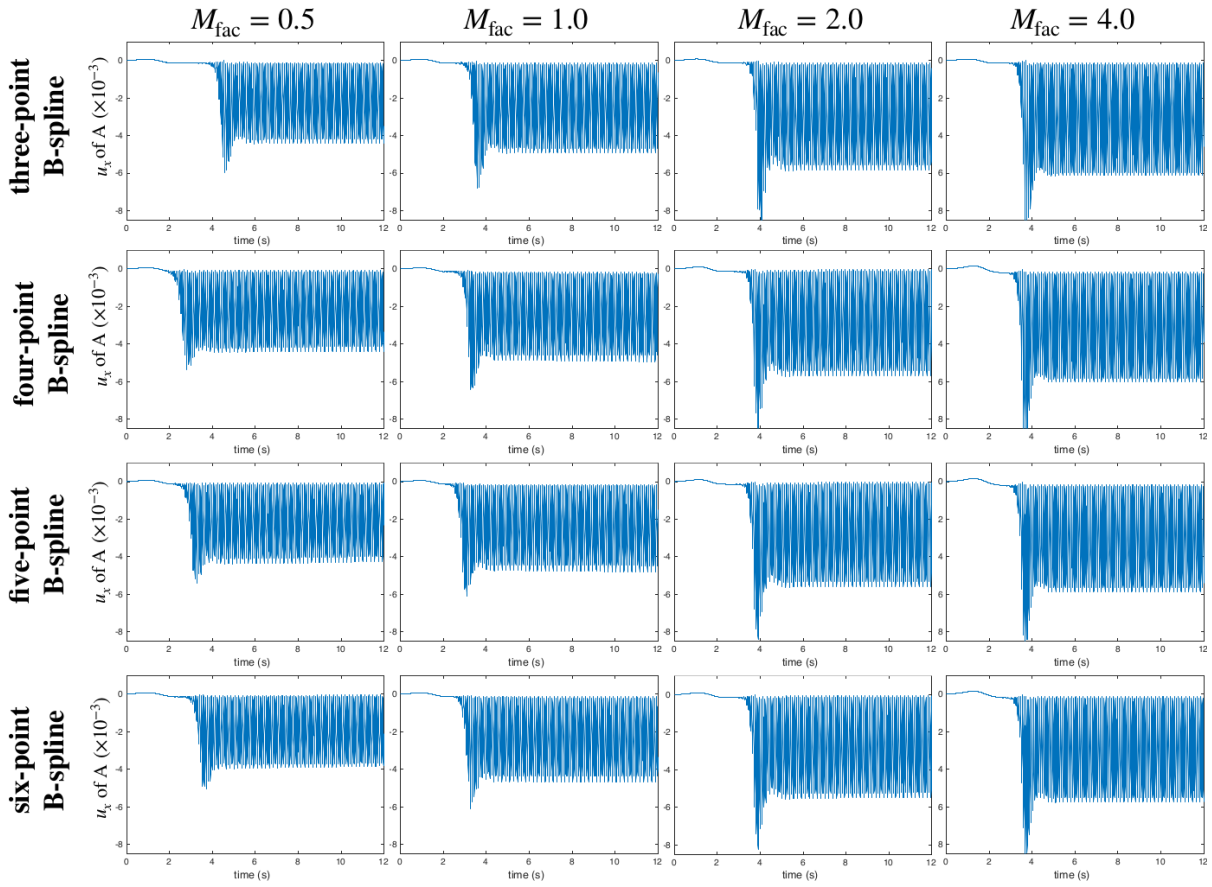


**Figure B.1:** $x$-displacement ($u_x$) of the point $A$ for different values of $M_{\text{fac}}$ for the neo-Hookean model using different B-spline kernels.

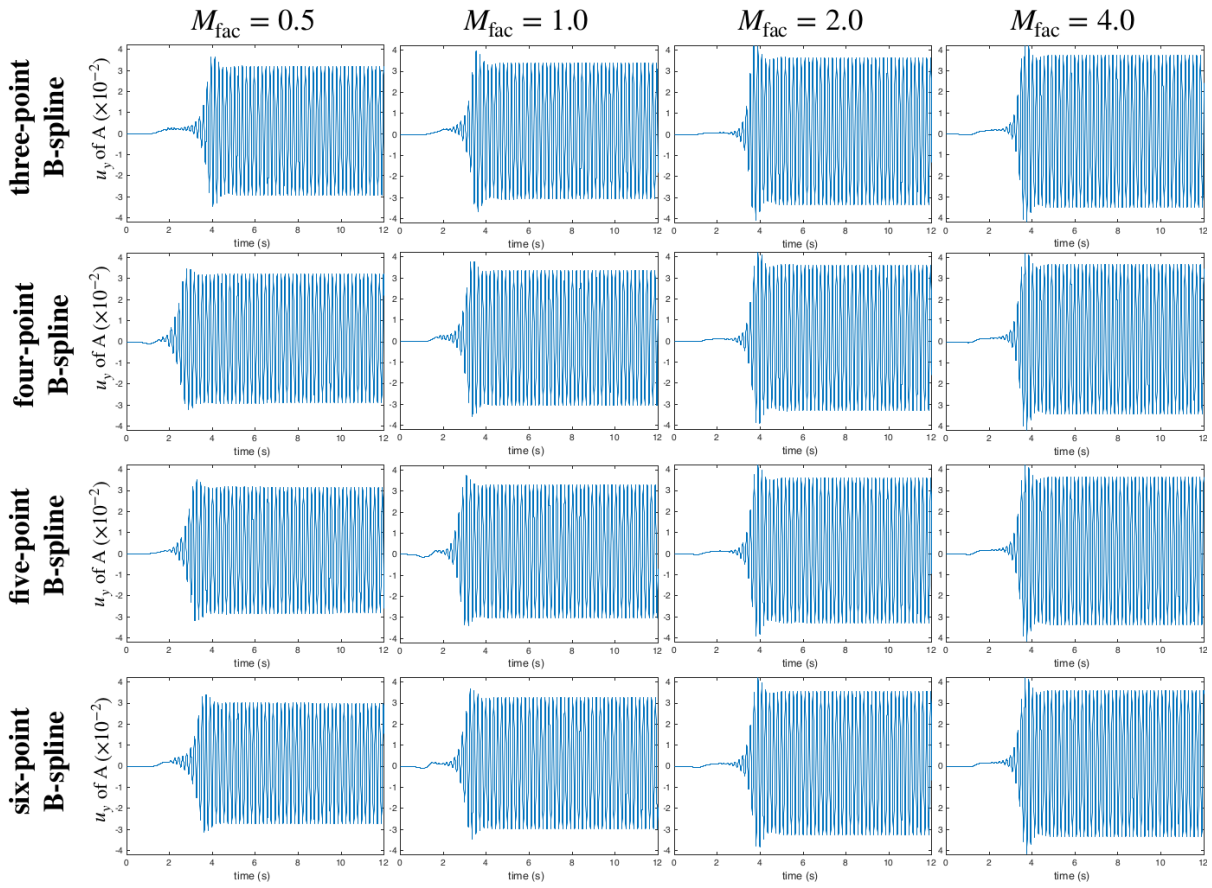


**Figure B.2:** $y$-displacement ($u_y$) of the point $A$ for different values of $M_{\text{fac}}$ for the neo-Hookean model using different B-spline kernels.

| | $M_{\text{fac}}$ | $u_x(A)$ ($\times 10^{-3}$) | $u_y(A)$ ($\times 10^{-3}$) | $St_x$ | $St_y$ |
|---|---|---|---|---|---|
| B-spline (3-point) | 0.5 | -2.31 ± 2.17 | 1.47 ± 30.6 | 10.93 | 5.46 |
| | 1.0 | -2.65 ± 2.47 | 1.67 ± 32.4 | 10.94 | 5.47 |
| | 2.0 | -2.89 ± 2.84 | 1.56 ± 34.9 | 10.93 | 5.46 |
| | 4.0 | -3.16 ± 3.00 | 1.24 ± 36.1 | 11.25 | 5.52 |
| B-spline (4-point) | 0.5 | -2.24 ± 2.18 | 1.51 ± 30.6 | 10.90 | 5.45 |
| | 1.0 | -2.56 ± 2.38 | 1.56 ± 32.1 | 10.95 | 5.47 |
| | 2.0 | -2.86 ± 2.82 | 1.54 ± 34.7 | 10.93 | 5.47 |
| | 4.0 | -3.08 ± 2.93 | 1.31 ± 35.5 | 11.27 | 5.64 |
| B-spline (5-point) | 0.5 | -2.20 ± 2.14 | 1.58 ± 30.0 | 10.89 | 5.44 |
| | 1.0 | -2.49 ± 2.33 | 1.49 ± 31.7 | 10.92 | 5.46 |
| | 2.0 | -2.81 ± 2.78 | 1.53 ± 34.3 | 10.93 | 5.47 |
| | 4.0 | -3.00 ± 2.85 | 1.36 ± 35.1 | 11.29 | 5.64 |
| B-spline (6-point) | 0.5 | -1.98 ± 1.94 | 1.38 ± 28.6 | 10.91 | 5.45 |
| | 1.0 | -2.42 ± 2.28 | 1.46 ± 31.3 | 10.88 | 5.44 |
| | 2.0 | -2.77 ± 2.74 | 1.53 ± 34.0 | 10.93 | 5.46 |
| | 4.0 | -2.94 ± 2.81 | 1.37 ± 34.6 | 11.30 | 5.65 |
| **Turek and Hron [58]** | | -2.69 ± 2.53 | 1.48 ± 34.4 | 10.9 | 5.3 |

**Table B.1:** Results for the neo-Hookean model using different B-spline kernels with various values of $M_{\text{fac}}$. $N = 32$ is the number of grid cells on coarsest grid level, $u_x(A)$ and $u_y(A)$ are $x$-, $y$-displacements of the point $A$, and $St_x$ and $St_y$ are Strouhal numbers for the oscillations of $u_x(A)$ and $u_y(A)$.

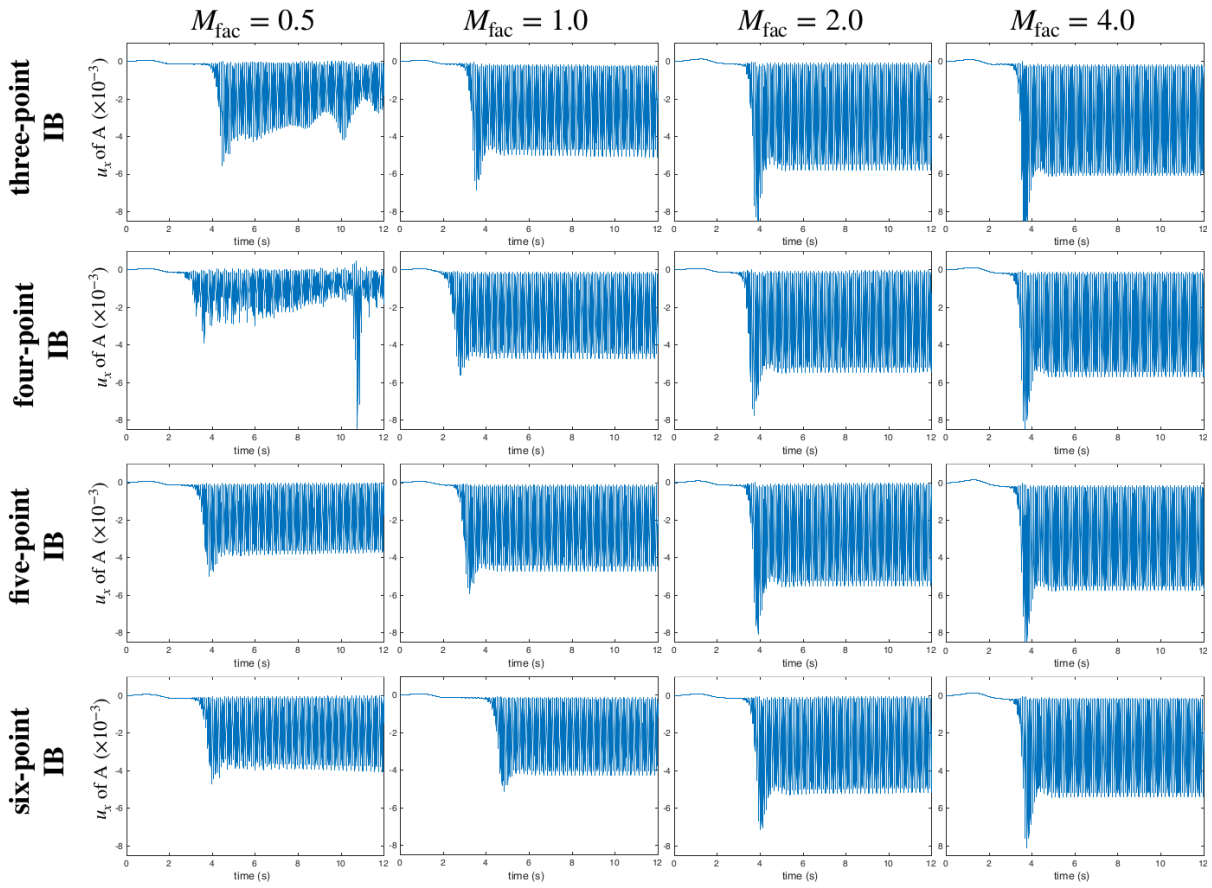


**Figure B.3:** $x$-displacement ($u_x$) of the point $A$ for different values of $M_{\text{fac}}$ for the neo-Hookean model using different IB kernels.

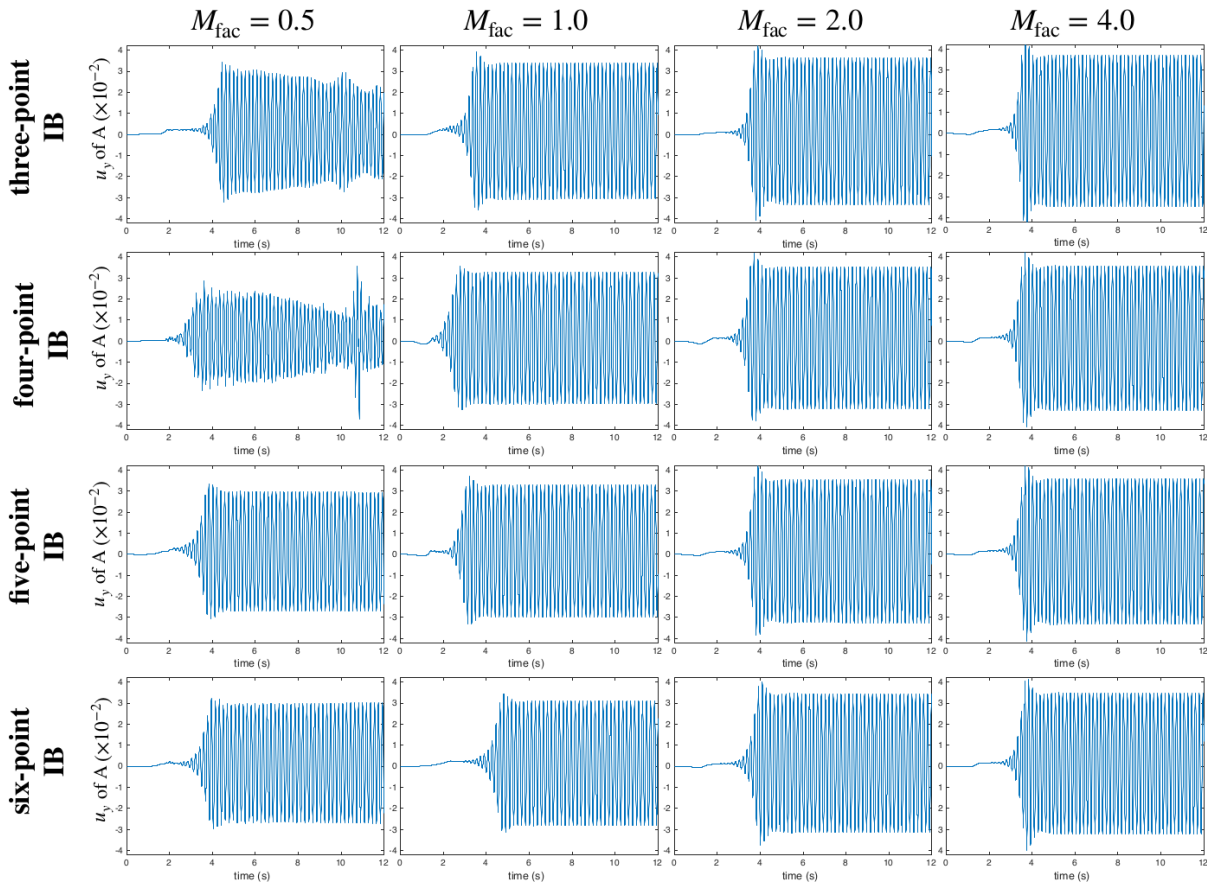


**Figure B.4:** $y$-displacement ($u_y$) of the point $A$ for different values of $M_{\text{fac}}$ for the neo-Hookean model using different IB kernels.

| | $M_{\text{fac}}$ | $u_x(A)$ ($\times 10^{-3}$) | $u_y(A)$ ($\times 10^{-3}$) | $St_x$ | $St_y$ |
|---|---|---|---|---|---|
| IB (3-point) | 0.5 | -2.09 ± 2.11 | 1.01 ± 28.4 | 11.18 | 5.57 |
| | 1.0 | -2.64 ± 2.45 | 1.58 ± 32.3 | 10.94 | 5.47 |
| | 2.0 | -2.93 ± 2.84 | 1.56 ± 34.9 | 10.93 | 5.47 |
| | 4.0 | -3.12 ± 2.96 | 1.22 ± 35.9 | 11.25 | 5.63 |
| IB (4-point) | 0.5 | -3.98 ± 4.48 | -0.68 ± 36.2 | 20.27 | 6.15 |
| | 1.0 | -2.42 ± 2.30 | 1.45 ± 31.3 | 10.85 | 5.43 |
| | 2.0 | -2.74 ± 2.70 | 1.52 ± 33.8 | 10.92 | 5.46 |
| | 4.0 | -2.90 ± 2.77 | 1.41 ± 34.4 | 11.31 | 5.65 |
| IB (5-point) | 0.5 | -1.90 ± 1.90 | 1.34 ± 28.3 | 10.90 | 5.45 |
| | 1.0 | -2.43 ± 2.31 | 1.45 ± 31.4 | 10.87 | 5.43 |
| | 2.0 | -2.76 ± 2.73 | 1.53 ± 34.0 | 10.93 | 5.47 |
| | 4.0 | -2.94 ± 2.80 | 1.38 ± 34.6 | 11.30 | 5.65 |
| IB (6-point) | 0.5 | -2.04 ± 2.02 | 1.61 ± 28.8 | 10.80 | 5.40 |
| | 1.0 | -2.21 ± 2.08 | 1.42 ± 29.7 | 10.82 | 5.41 |
| | 2.0 | -2.62 ± 2.59 | 1.50 ± 32.0 | 10.91 | 5.45 |
| | 4.0 | -2.76 ± 2.64 | 1.42 ± 33.4 | 11.33 | 5.66 |
| **Turek and Hron [58]** | | -2.69 ± 2.53 | 1.48 ± 34.4 | 10.9 | 5.3 |

**Table B.2:** Results for the neo-Hookean model using different IB kernels with various values of $M_{\text{fac}}$. $N = 32$ is the number of grid cells on coarsest grid level, $u_x(A)$ and $u_y(A)$ are $x$-, $y$-displacements of the point $A$, and $St_x$ and $St_y$ are Strouhal numbers for the oscillations of $u_x(A)$ and $u_y(A)$.

APPENDIX C

# PARAMETER FITTING FOR THE VALVE MATERIAL MODELS

We perform model fits for the constitutive model of the valves detailed in Section 5.2.2 in the main text using experimental data from Billiar and Sacks [73,74] for the porcine tissue BHV and from Kim et al. [75] for the bovine pericardial BHV. In the biaxial tests of Billiar and Sacks, the specimens were mounted onto the testing device so that the radial and circumferential directions were aligned with the direction of the applied forces, as shown in Figure C.1a. Kim et al. used a stress-control biaxial testing method on a gluteraldehyde-treated bovine pericardial tissue sample. As shown in Figure C.1c, the specimen was aligned at 45° to the direction of the applied forces, mimicking the fiber alignment of the pericardial valve leaflets. To determine constitutive model parameters, we assume that the solid is incompressible, compute the second Piola-Kirchhoff stress ($\mathbb{S}$), and compare it to the experimental values for given values of the Green-Lagrange strain $\mathbb{E} = \frac{1}{2}(\mathbb{C} - \mathbb{I})$. The stress is computed by

$$\mathbb{S} = \mathbb{S}^{\text{dev}} - p\mathbb{C}^{-1}, \tag{C.1}$$

$$\mathbb{S}^{\text{dev}} = 2\frac{\partial W}{\partial \mathbb{C}}, \tag{C.2}$$

$$p = \frac{\mathbb{S}^{\text{dev}}_{33}}{(\mathbb{C}^{-1})_{33}}, \tag{C.3}$$

in which $W = W_{\text{iso}} + W_{\text{aniso}}$ is the Holzapfel-Gasser-Ogden model described by (5.2) and (5.3) in Section 5.2.2 of the main text, $\mathbb{S}^{\text{dev}}$ is the deviatoric part of the second Piola-Kirchhoff stress, $\mathbb{C} = \mathbb{F}^T\mathbb{F}$ is the Cauchy-Green strain, $\mathbb{F}$ is the deformation gradient tensor, and $p$ is the pressure assuming that the specimen is acted on only by in-plane loads. We use lsqcurvefit in MATLAB (The MathWorks, Inc., Natick, MA, USA), a nonlinear least-squares solver, to determine the model parameters. Figures C.1b and C.1d show constitutive model fits obtained using this approach.

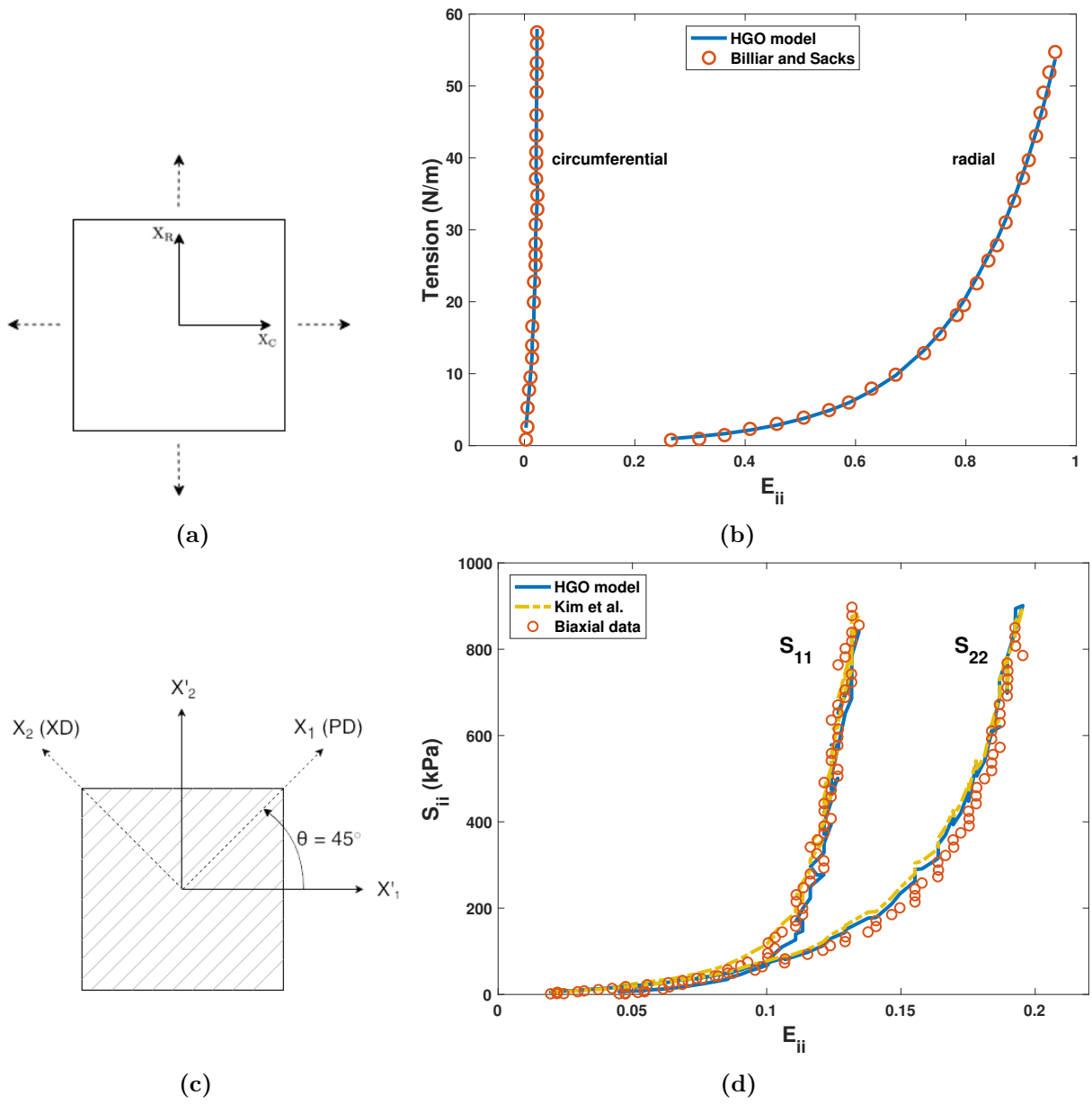


**Figure C.1:** (a) Schematic of the biaxial tensile test of Billiar and Sacks [73, 74] for porcine aortic valve tissue specimens to study their material response. $X_C$ is the circumferential axis and $X_R$ is the radial axis. The dashed lines are the directions in which forces were applied. (b) Parameter fitting for the porcine aortic valve using the experimental tensile test data from Billiar and Sacks [73, 74] for glutaraldehyde-fixed porcine aortic valves. (c) Schematic of the biaxial tensile tests of Kim et al. [75] for bovine pericardium tissue specimens to study their material response. $X_1$ is the preferred mean fiber direction (PD) also shown by gray lines, $X_2$ is the cross-preferred fiber direction (XD), and $X_1'$ and $X_2'$ are the directions in which forces were applied. (d) Parameter fitting for the bovine pericardial valve using the equibiaxial data from Kim et al. [75] compared to the plot using parameters determined by Kim et al. using a finite element model of the biaxial test.

## REFERENCES


[1] E. J. Benjamin, M. J. Blaha, S. E. Chiuve, M. Cushman, S. R. Das, R. Deo, S. D. de Ferranti, J. Floyd, M. Fornage, C. Gillespie, C. R. Isasi, M. C. Jiménez, L. C. Jordan, S. E. Judd, D. Lackland, J. H. Lichtman, L. Lisabeth, S. Liu, C. T. Longenecker, R. H. Mackey, K. Matsushita, D. Mozaffarian, M. E. Mussolino, K. Nasir, R. W. Neumar, L. Palaniappan, D. K. Pandey, R. R. Thiagarajan, M. J. Reeves, M. Ritchey, C. J. Rodriguez, G. A. Roth, W. D. Rosamond, C. Sasson, A. Towfighi, C. W. Tsai, M. B. Turner, S. S. Virani, J. H. Voeks, J. Z. Willey, J. T. Wilkins, J. H. Wu, H. M. Alger, S. S. Wong, and P. Muntner, "Heart Disease and Stroke Statistics-2017 Update: A Report From the American Heart Association," *Circulation*, vol. 135, no. 10, pp. e146–e603, 2017.

[2] "Noncommunicable diseases country profiles 2018," *World Health Organization*, 2018.

[3] T. M. Morrison, M. L. Dreher, S. Nagaraja, L. M. Angelone, and W. Kainz, "The role of computational modeling and simulation in the total product life cycle of peripheral vascular devices," *J Med Device*, vol. 11, no. 2, p. 024503, 2017.

[4] "Regulatory Science Priorities (FY2017)," tech. rep., U.S. Food and Drug Administration Center for Devices and Radiological Health, 2016.

[5] N. Duraiswamy, J. D. Weaver, Y. Ekrami, S. M. Retta, and C. Wu, "A parametric computational study of the impact of non-circular configurations on bioprosthetic heart valve leaflet deformations and stresses: possible implications for transcatheter heart valves," *Cardiovasc Eng Technol*, vol. 7, no. 2, pp. 126–138, 2016.

[6] A. P. Yoganathan, K. B. Chandran, and F. Sotiropoulos, "Flow in prosthetic heart valves: state-of-the-art and future directions," *Ann Biomed Eng*, vol. 33, no. 12, pp. 1689–1694, 2005.

[7] R. Zakerzadeh, M.-C. Hsu, and M. S. Sacks, "Computational methods for the aortic heart valve and its replacements," *Expert Rev Med Devices*, vol. 14, no. 11, pp. 849–866, 2017.

[8] A. M. Bavo, G. Rocatello, F. Iannaccone, J. Degroote, J. Vierendeels, and P. Segers, "Fluid–structure interaction simulation of prosthetic aortic valves: comparison between immersed boundary and arbitrary Lagrangian–Eulerian techniques for the mesh," *PLoS ONE*, vol. 11, no. 4, p. e0154517, 2016.

[9] J. H. Spühler, J. Jansson, N. Jansson, and J. Hoffman, "3D fluid-structure interaction simulation of aortic valves using a unified continuum ALE FEM model," *Front Physiol*, vol. 16, no. 9, p. 363, 2018.

[10] C. S. Peskin, "The immersed boundary method," *Acta Numer*, vol. 11, pp. 479–517, 2002.

[11] C. S. Peskin, "Flow patterns around heart valves: a numerical method," *J Comput Phys*, vol. 10, no. 2, pp. 252–271, 1972.

[12] C. S. Peskin, "Numerical analysis of blood flow in the heart," *J Comput Phys*, vol. 25, no. 3, pp. 220–252, 1977.

[13] B. E. Griffith and N. A. Patankar, "Immersed method for fluid–structure interaction," *Annu Rev Fluid Mech*, vol. 52, pp. 421–448, 2020.

[14] B. E. Griffith, X. Y. Luo, D. M. McQueen, and C. S. Peskin, "Simulating the fluid dynamics of natural and prosthetic heart valves using the immersed boundary method," *Int J Appl Mech*, vol. 1, no. 1, pp. 137–177, 2009.

[15] B. E. Griffith, "Immersed boundary model of physiological driving and loading conditions," *Int J Numer Methods Biomed Eng*, vol. 28, no. 3, pp. 317–345, 2012.

[16] I. Borazjani, "Fluid–structure interaction, immersed boundary-finite element method simulations of bio-prosthetic heart valves," *Comput Methods Appl Mech Eng*, vol. 257, no. 0, pp. 103–116, 2013.

[17] V. Flamini, A. DeAnda, and B. E. Griffith, "Immersed boundary-finite element model of fluid–structure interaction in the aortic root," *Theor Comput Fluid Dyn*, vol. 30, no. 1, pp. 139–164, 2016.

[18] A. Hasan, E. M. Kolahdouz, A. Enquobahrie, T. G. Caranasos, J. P. Vavalle, and B. E. Griffith, "Image-based immersed boundary model of the aortic root," *Med Eng Phys*, vol. 47, pp. 72–84, 2017.

[19] J. H. Lee, A. D. Rygg, E. M. Kolahdouz, S. Rossi, S. M. Retta, N. Duraiswamy, L. N. Scotten, B. A. Craven, and B. E. Griffith, "Fluid–structure interaction models of bioprosthetic heart valve dynamics in an experimental pulse duplicator," *Ann Biomed Eng*, vol. 48, no. 5, pp. 1475–1490, 2020.

[20] J. de Hart, G. W. M. Peters, P. J. G. Schreurs, and F. P. T. Baaijens, "A three dimensional computational analysis of fluid-structure interaction in the aortic valve," *J Biomech*, vol. 36, no. 1, pp. 102–112, 2003.

[21] J. de Hart, F. P. T. Baaijens, G. W. M. Peters, and P. J. G. Schreurs, "A computational fluid-structure interaction analysis of a fiber-reinforced stentless aortic valve," *J Biomech*, vol. 36, no. 5, pp. 699–712, 2003.

[22] J. de Hart, G. W. M. Peters, P. J. G. Schreurs, and F. P. T. Baaijens, "Collagen fibers reduce stresses and stabilize motion of aortic valve leaflets during systole," *J Biomech*, vol. 37, no. 3, pp. 303–311, 2004.

[23] M.-C. Hsu, D. Kamensky, Y. Bazilevs, M. S. Sacks, and T. J. R. Hughes, "Fluid-structure interaction analysis of bioprosthetic heart valves: significance of arterial wall deformation," *Comput Mech*, vol. 54, no. 4, pp. 1055–1071, 2014.

[24] M.-C. Hsu, D. Kamensky, F. Xu, J. Kiendl, C. Wang, M. C. H. Wu, J. Mineroff, A. Reali, Y. Bazilevs, and M. S. Sacks, "Dynamic and fluid-structure interaction simulations of bioprosthetic heart valves using parametric design with T-splines and Fung-type material models," *Comput Mech*, vol. 55, no. 6, pp. 1211–1225, 2015.

[25] D. Kamensky, M.-C. Hsu, D. Schillinger, J. A. Evans, A. Aggarwal, Y. Bazilevs, M. S. Sacks, and T. J. Hughes, "An immersogeometric variational framework for fluid–structure interaction: application to bioprosthetic heart valves," *Comput Methods Appl Mech Eng*, vol. 284, pp. 1005–1053, 2015.

[26] D. Kamensky, J. A. Evans, M.-C. Hsu, and Y. Bazilevs, "Projection-based stabilization of interface Lagrange multipliers in immersogeometric fluid–thin structure interaction analysis,

with application to heart valve modeling," *Comput Math Appl*, vol. 74, no. 9, pp. 2068–2088, 2017.

[27] F. Xu, S. Morganti, R. Zakerzadeh, D. Kamensky, F. Auricchio, A. Reali, T. J. R. Hughes, M. S. Sacks, and M.-C. Hsu, "A framework for designing patient-specific bioprosthetic heart valves using immersogeometric fluid–structure interaction analysis," *Int J Numer Method Biomed Eng*, vol. 34, no. 4, p. e2938, 2018.

[28] M. C. H. Wu, R. Zakerzadeh, D. Kamensky, J. Kiendl, M. S. Sacks, and M.-C. Hsu, "An anisotropic constitutive model for immersogeometric fluid–structure interaction analysis of bioprosthetic heart valves," *J Biomech*, vol. 74, pp. 23–31, 2018.

[29] W. Mao, K. Li, and W. Sun, "Fluid–structure interaction study of transcatheter aortic valve dynamics using smoothed particle hemodynamics," *Cardiovasc Eng Technol*, vol. 7, no. 4, pp. 374–388, 2016.

[30] H. S. Kandail, S. D. Trivedi, A. C. Shaikh, T. K. Bajwa, D. P. O'Hair, A. Jahangir, and J. F. LaDisa Jr., "Impact of annular and supra-annular CoreValve deployment locations on aortic and coronary artery hemodynamics," *J Mech Behav Biomed Mater*, vol. 86, pp. 131–142, 2018.

[31] Y. Chen and H. Luo, "A computational study of the three-dimensional fluid–structure interaction of aortic valve," *J Fluids Struct*, vol. 80, pp. 332–349, 2018.

[32] Y. Chen and H. Luo, "Pressure distribution over the leaflets and effect of bending stiffness on fluid–structure interaction of the aortic valve," *J Fluid Mech*, vol. 883, no. A52, pp. 1–29, 2020.

[33] ASME V&V 40-2018, *Assessing Credibility of Computational Modeling Through Verification and Validation: Application to Medical Devices*, 2018.

[34] B. E. Griffith and X. Y. Luo, "Hybrid finite difference/finite element immersed boundary method," *Int J Numer Methods Biomed Eng*, vol. 33, no. 11, p. e2888, 2017.

[35] G. A. Holzapfel, *Nonlinear Solid Mechanics: A Continuum Approach for Engineering*. Wiley, 1 ed., 2000.

[36] J. Bonet and R. D. Wood, *Nonlinear Continuum Mechanics for Finite Element Analysis*. The Edinburgh Building, Cambridge CB2 8RU, UK: Cambridge University Press, 2 ed., 2008.

[37] L. Zhang, A. Gerstenberger, X. Wang, and W. K. Liu, "Immersed finite element method," *Comput Methods Appl Mech Engrg*, vol. 193, no. 21–22, pp. 2051–2067, 2004.

[38] W. K. Liu, Y. Liu, D. Farrell, L. Zhang, X. S. Wang, Y. Fukui, N. Patankar, Y. Zhang, C. Bajaj, J. Lee, *et al.*, "Immersed finite element method and its applications to biological systems," *Comput Methods Appl Mech Engrg*, vol. 195, no. 13–16, pp. 1722–1749, 2006.

[39] L. T. Zhang and M. Gay, "Immersed finite element method for fluid-structure interactions," *J Fluids Struct*, vol. 23, no. 6, pp. 839–857, 2007.

[40] X. Wang and L. T. Zhang, "Interpolation functions in the immersed boundary and finite element methods," *Comput Methods Appl Mech Engrg*, vol. 45, no. 4, pp. 321–334, 2010.

[41] X. Wang, C. Wang, and L. T. Zhang, "Semi-implicit formulation of the immersed finite element method," *Comput Methods Appl Mech Engrg*, vol. 49, no. 4, pp. 421–430, 2012.

[42] B. Vadala-Roth, S. Acharya, N. A. Patankar, S. Rossi, and B. E. Griffith, "Stabilization approaches for the hyperelastic immersed boundary method for problems of large-deformation incompressible elasticity," *Comput Methods Appl Mech Eng*, vol. 365, p. 112978, 2020.

[43] C. H. Liu, G. Hofstetter, and H. A. Mang, "3D finite element analysis of rubber-like materials at finite strains," *Eng Comput*, vol. 11, no. 2, pp. 111–128, 1994.

[44] B. E. Griffith, "An accurate and efficient method for the incompressible Navier–Stokes equations using the projection method as a preconditioner," *J Comput Phys*, vol. 228, no. 20, pp. 7565–7595, 2009.

[45] B. E. Griffith, "On the volume conservation of the immersed boundary method," *Commun Comput Phys*, vol. 12, no. 2, pp. 401–432, 2012.

[46] W. J. Rider, J. A. Greenough, and J. R. Kamm, "Accurate monotonicity- and extrema-preserving methods through adaptive nonlinear hybridizations," *J Comput Phys*, vol. 225, no. 2, pp. 1827–1848, 2007.

[47] P. Colella and P. R. Woodward, "The piecewise parabolic method (PPM) for gas-dynamical simulations," *J Comput Phys*, vol. 54, no. 1, pp. 174–201, 1984.

[48] B. E. Griffith, R. D. Hornung, D. M. McQueen, and C. S. Peskin, "An adaptive, formally second order accurate version of the immersed boundary method," *J Comput Phys*, vol. 223, no. 1, pp. 10–49, 2007.

[49] "IBAMR: Immersed Boundary Method Adaptive Mesh Refinement Software Infrastructure. https://ibamr.github.io/."

[50] R. D. Hornung and S. R. Kohn, "Managing application complexity in the SAMRAI object-oriented framework," *Concurr Comput Pract Exp*, vol. 14, pp. 347–368, 2002.

[51] B. S. Kirk, J. W. Peterson, R. H. Stogner, and G. F. Carey, "`libMesh`: a C++ library for parallel adaptive mesh refinement/coarsening simulations," *Eng Comput*, vol. 22, no. 3–4, pp. 237–254, 2006.

[52] S. Balay, S. Abhyankar, M. F. Adams, J. Brown, P. Brune, K. Buschelman, L. Dalcin, A. Dener, V. Eijkhout, W. D. Gropp, D. Kaushik, M. G. Knepley, D. A. May, L. C. McInnes, R. T. Mills, T. Munson, K. Rupp, P. Sanan, B. F. Smith, S. Zampini, H. Zhang, and H. Zhang, "PETSc Users Manual," Tech. Rep. ANL-95/11 - Revision 3.10, Argonne National Laboratory, 2018.

[53] A. M. Roma, C. S. Peskin, and M. J. Berger, "An adaptive version of the immersed boundary method," *J Comput Phys*, vol. 153, no. 2, pp. 509–534, 1999.

[54] Y. Bao, J. Kaye, and C. S. Peskin, "A Gaussian-like immersed-boundary kernel with three continuous derivativs and improved translational invariance," *J Comput Phys*, vol. 316, pp. 139–144, 2016.

[55] Y. Bao, A. Donev, B. E. Griffith, D. M. McQueen, and C. S. Peskin, "An immersed boundary method with divergence-free velocity interpolation and force spreading," *J Comput Phys*, vol. 347, pp. 183–206, 2017.

[56] M. Unser, A. Aldroubi, and M. Eden, "On the asymptotic convergence of B-spline wavelets to Gabor functions," *IEEE Trans Inf Theory*, vol. 38, no. 2, pp. 864–872, 1992.

[57] K. Taira and T. Colonius, "The immersed boundary method: a projection approach," *J Comput Phys*, vol. 225, no. 2, pp. 2118–2137, 2007.

[58] S. Turek and J. Hron, "Proposal for numerical benchmarking of fluid–structure interaction between an elastic object and laminar incompressible flow," in *Fluid–Structure Interaction* (H. J. Bungartz and M. Schäfer, eds.), vol. 53 of *Lecture Notes in Computational Science and Engineering*, pp. 371–385, Springer, Berlin, Heidelberg, 2006.

[59] S. Roy, L. Heltai, and F. Costanzo, "Benchmarking the immersed finite element method for fluid-structure interaction problems," *Comput Math Appl*, vol. 69, pp. 1167–1188, 2015.

[60] G. Pedrizzetti and F. Domenichini, "Left ventricular fluid dynamics: the long way from theoretical models to clinical applications," *Ann Biomed Eng*, vol. 43, no. 1, pp. 26–40, 2015.

[61] A. Santhanakrishnan and L. A. Miller, "Fluid dynamics of heart development," *Cell Biochem and Biophys*, vol. 61, pp. 1–22, 2011.

[62] N. Stergiopulos, B. E. Westerhof, and N. Westerhof, "Total arterial inertance as the fourth element of the windkessel model," *Am J Physiol Heart Circ Physiol*, vol. 276, no. 1, pp. H81–H88, 1999.

[63] T. Korakianitis and Y. Shi, "A concentrated parameter model for the human cardiovascular system including heart valve dynamics and atrioventricular interaction," *Med Eng Phys*, vol. 28, no. 7, pp. 613–628, 2006.

[64] E. M. Kolahdouz, A. P. S. Bhalla, B. A. Craven, and B. E. Griffith, "An immersed interface method for discrete surfaces," *J Comput Phys*, vol. 400, no. 108854, 2020.

[65] L. P. Dasi, H. A. Simon, P. Sucosky, and A. P. Yoganathan, "Fluid mechanics of artificial heart valves," *Clin Exp Pharmacol Physiol*, vol. 36, no. 2, pp. 225–237, 2009.

[66] T. Rodriguez-Gabella, P. Voisine, R. Puri, P. Pibarot, and J. Rodés-Cabau, "Aortic bioprosthetic valve durability: incidence, mechanisms, predictors, and management of surgical and transcatheter valve degeneration," *J Am Coll Cardiol*, vol. 70, no. 8, pp. 1013–1028, 2017.

[67] R. F. Siddiqui, J. R. Abraham, and J. Butany, "Bioprosthetic heart valves: modes of failure," *Histopathology*, vol. 55, no. 2, pp. 135–144, 2009.

[68] A. Gilmanov, H. Stolarski, and F. Sotiropoulos, "Flow–structure interaction simulations of the aortic heart valve at physiologic conditions: The role of tissue constitutive model," *J Biomech Eng*, vol. 140, no. 4, p. 041003, 2018.

[69] A. K. S. Iyengar, H. Sugimoto, D. B. Smith, and M. S. Sacks, "Dynamic in vitro quantification of bioprosthetic heart valve leaflet motion using structured light projection," *Ann Biomed Eng*, vol. 29, no. 11, pp. 963–973, 2001.

[70] W. Sun, A. Abad, and M. S. Sacks, "Simulated bioprosthetic heart valve deformation under quasi-static loading simulated bioprosthetic heart valve deformation under quasi-static loading," *J Biomech Eng*, vol. 127, pp. 905–914, 2005.

[71] A. M. Tango, J. Salmonsmith, A. Ducci, and G. Burriesci, "Validation and extension of a fluid–Structure interaction model of the healthy aortic valve," *Cardiovasc Eng Technol*, vol. 9, no. 4, pp. 739–751, 2018.

[72] J. Sigüenza, D. Pott, S. Mendez, S. J. Sonntag, T. A. S. Kaufmann, U. Steinseifer, and F. Nicoud, "Fluid–structure interaction of a pulsatile flow with an aortic valve model: a combined experimental and numerical study," *Int J Numer Method Biomed Eng*, vol. 34, no. 4, p. e2945, 2018.

[73] K. L. Billiar and M. S. Sacks, "Biaxial mechanical properties of the natural and glutaraldehyde treated aortic valve cusp. Part I: experimental results," *J Biomech Eng*, vol. 122, no. 1, pp. 23–30, 2000.

[74] K. L. Billiar and M. S. Sacks, "Biaxial mechanical properties of the native and glutaraldehyde-treated aortic valve cusp. Part II: a structural constitutive model," *J Biomech Eng*, vol. 122, no. 4, pp. 327–335, 2000.

[75] H. Kim, K. B. Chandran, M. S. Sacks, and J. Lu, "An experimentally derived stress resultant shell model for heart valve dynamic simulations," *Ann Biomed Eng*, vol. 35, no. 1, pp. 30–44, 2007.

[76] L. N. Scotten and R. Siegel, "Importance of shear in prosthetic valve closure dynamics," *J Heart Valve Dis*, vol. 20, pp. 664–672, 2011.

[77] S. M. Retta, J. Kepner, S. Marquez, B. A. Herman, M. C. S. Shu, and L. W. Grossman, "In-vitro pulsatile flow measurement in prosthetic heart valves: an inter-laboratory comparison," *J Heart Valve Dis*, vol. 26, no. 1, pp. 72–80, 2017.

[78] "Cardiovascular implants – Cardiac valve prostheses – Part 3: Heart valve substitutes implanted by transcatheter techniques," *ISO*, vol. 5840-3, p. 2013(E), 2013.

[79] C. Wu, N. Saikrishnan, A. J. Chalekian, R. Fraser, O. Ieropoli, S. M. Retta, R. Joseph, S. Lee, S. Marquez, D. Mester, N. Pan, S. Vatanpour, C. Weinberg, and U. Steinseifer, "In-vitro pulsatile flow testing of prosthetic heart valves: a round-robin study by the ISO Cardiac Valves Working Group," *Cardiovasc Eng Technol*, vol. 10, no. 3, pp. 397–422, 2019.

[80] N. J. B. Driessen, C. V. C. Bouten, and F. P. T. Baaijens, "A Structural Constitutive Model For Collagenous Cardiovascular Tissues Incorporating the Angular Fiber Distribution," *J Biomech Eng*, vol. 127, no. 3, pp. 494–503, 2005.

[81] K. Murdock, C. Martin, and W. Sun, "Characterization of mechanical properties of pericardium tissue using planar biaxial tension and flexural deformation," *J Mech Behav Biomed Mater*, vol. 77, pp. 148–156, jan 2018.

[82] T. C. Gasser, R. W. Ogden, and G. A. Holzapfel, "Hyperelastic modelling of arterial layers with distributed collagen fibre orientations," *J R Soc Interface*, vol. 3, pp. 15–35, Feb 2006.

[83] J. Wong and E. Kuhl, "Generating fibre orientation maps in human heart models using Poisson interpolation," *Comput Methods Biomech Biomed Eng*, vol. 17, no. 11, pp. 1217–1226, 2014.

[84] B. Kallemov, A. P. S. Bhalla, B. E. Griffith, and A. Donev, "An immersed boundary method for rigid bodies," *Commun App Math Comput Sci*, vol. 11, no. 1, pp. 79–141, 2016.

[85] C. Doose, M. Kütting, S. Egron, P. F. Ghalati, C. Schmitz, M. Utzenrath, A. Sedaghat, B. Fujita, T. Schimitz-Rode, S. Ensminger, and U. Steinseifer, "Valve-in-valve outcome: design impact of a pre-existing bioprosthesis on the hydrodynamics of an Edwards Sapien XT valve," *Eur J Cardiothorac Surg*, vol. 51, pp. 562–570, 2017.

[86] A. Rassoli, N. Faltouraee, and R. Guidoin, "Structural model of viscoelastic properties of pericardial bioprosthetic valves," *Artif Organs*, vol. 42, no. 6, pp. 630–639, 2018.

[87] J. A. Funder, M. W. Frost, P. Wierup, K. Klaaborg, V. Hjortdal, H. Nygaard, and J. M. Hasenkam, "Turbulence downstream of subcoronary stentless and stented aortic valves," *J Biomech*, vol. 44, pp. 2273–2278, 2011.

[88] P. Colella and M. D. Sekora, "A limiter for PPM that preserves accuracy at smooth extrema," *J Comput Phys*, vol. 227, no. 15, pp. 7069–7076, 2008.

[89] P. McCorquodale and P. Colella, "A high-order finite-volume method for conservation laws on locally refined grids," *Commun App Math Comput Sci*, vol. 6, no. 1, pp. 1–25, 2011.

[90] P. Sagaut, *Large Eddy Simulation for Incompressible Flows, an Introduction*. Berlin: Springer, 2014.

[91] L. C. Berselli, T. Iliescu, and W. J. Layton, *Mathematics of Large Eddy Simulation of Turbulent Flows*. Berlin: Springer, 2006.

[92] M. H. Aazami and M. Salehi, "The Arantius nodule: a 'stress-decreasing effect'," *J Heart Valve Dis*, vol. 14, no. 4, pp. 565–566, 2005.

[93] M. Arsalan and T. Walther, "Durability of prostheses for transcatheter aortic valve implantation," *Nat Rev Cardiol*, vol. 13, no. 6, pp. 360–367, 2016.

[94] T. Rodriguez-Gabella, P. Voisine, R. Puri, P. Pibarot, and J. Rodés-Cabau, "Aortic bioprosthetic valve durability: incidence, mechanisms, predictors, and management of surgical and transcatheter valve degeneration," *J Am Coll Cardiol*, vol. 70, no. 8, pp. 1013–1028, 2017.

[95] P. Singhal, A. Luk, and J. Butany, "Bioprosthetic heart valves: impact of implantation on biomaterials," *ISRN Biomater*, pp. 1–14, 2013.

[96] C. Martin and W. Sun, "Comparison of transcatheter aortic valve and surgical bioprosthetic valve durability: a fatigue simulation study," *J Biomech*, vol. 48, no. 12, pp. 3026–3034, 2015.

[97] R. M. Buchanan and M. S. Sacks, "Interlayer micromechanics of the aortic heart valve leaflet," *Biomech Model Mechanobiol*, vol. 13, pp. 813–826, 2014.

[98] B. V. Rego and M. S. Sacks, "A functionally graded material model for the transmural stress distribution of the aortic valve leaflet," *J Biomech*, vol. 54, pp. 88–95, 2017.

[99] H. Sugimoto and M. S. Sacks, "Effects of leaflet stiffness on dynamic bioprosthetic heart valve leaflet shape," *Cardiovasc Eng Technol*, vol. 4, no. 1, pp. 2–15, 2013.

[100] M. Rashtian, D. M. Stevenson, D. T. Allen, A. P. Yoganathan, E. C. Harrison, W. A. Edmiston, and S. H. Rahimtoola, "Flow characteristics of bioprosthetic heart valves," *Chest*, vol. 98, no. 2, pp. 365–375, 1990.

[101] S. C. Reimold, A. P. Yoganathan, H. W. Sung, L. H. Cohn, M. G. Sutton, and R. T. Lee, "Doppler echocardiographic study of porcine bioprosthetic heart valves in the aortic valve position in patients without evidence of cardiac dysfunction," *Am J Cardiol*, vol. 67, no. 7, pp. 611–615, 1991.

[102] S. Marquez, R. T. Hon, and A. P. Yoganathan, "Comparative hydrodynamic evaluation of bioprosthetic heart valves," *J Heart Valve Dis*, vol. 10, no. 6, pp. 802–811, 2001.

[103] E. De Marchena, J. Mesa, S. Pomenti, C. Marin Y Kall, X. Marincic, K. Yahagi, E. Ladich, R. Kutz, Y. Aga, M. Ragosta, A. Chawla, M. E. Ring, and R. Virmani, "Thrombus formation following transcatheter aortic valve replacement," *JACC Cardiovasc Interv*, vol. 8, no. 5, pp. 728–739, 2015.

[104] R. Toninato, J. Salmon, F. M. Susin, A. Ducci, and G. Burriesci, "Physiological vortices in the sinuses of Valsalva: an in vitro approach for bio-prosthetic valves," *J Biomech*, vol. 49, pp. 2635–2643, 2016.

[105] W. L. Lim, Y. T. Chew, T. C. Chew, and H. T. Low, "Steady flow dynamics of prosthetic aortic heart valves: a comparative evaluation with PIV techniques," *J Biomech*, vol. 31, pp. 411–421, 1998.

[106] W. L. Lim, Y. T. Chew, T. C. Chew, and H. T. Low, "Pulsatile flow studies of a porcine bioprosthetic aortic valve in vitro: PIV measurements and shear-induced blood damage," *J Biomech*, vol. 34, pp. 1417–1427, 2001.

[107] K. B. Manning, V. Kini, A. A. Fontaine, S. Deutsch, and J. M. Tarbell, "Regurgitant flow field characteristics of the St. Jude bileaflet mechanical heart valve under physiological pulsatile flow using particle image velocimetry," *Artif Organs*, vol. 27, no. 9, pp. 840–846, 2003.

[108] H. L. Leo, L. P. Dasi, J. Carberry, H. A. Simon, and A. P. Yoganathan, "Fluid dynamic assessment of three polymeric heart valves using particle image velocimetry," *Ann Biomed Eng*, vol. 34, no. 6, pp. 936–952, 2006.

[109] L. P. Dasi, L. Ge, H. A. Simon, F. Sotiropoulos, and A. P. Yoganathan, "Vorticity dynamics of a bileaflet mechanical heart valve in an axisymmetric aorta," *Phys Fluids*, vol. 19, p. 067105, 2007.

[110] N. Saikrishnan, C. Yap, N. C. Milligan, N. V. Vasilyev, and A. P. Yoganathan, "In vitro characterization of bicuspid aortic valve hemodynamics using particle image velocimetry," *Ann Biomed Eng*, vol. 40, no. 8, pp. 1760–1775, 2012.

[111] E. M. Groves, A. Falahatpisheh, J. L. Su, and A. Kheradvar, "The effects of positioning of transcatheter aortic valve on fluid dynamics of the aortic root," *Am Soc Artif Intern Organs J*, vol. 60, no. 5, pp. 545–552, 2014.

[112] A. Yousefi, A. Vaesken, A. Amri, L. P. Dasi, and F. Heim, "Heart valves from polyester fibers vs. biological tissue: comparative study in vitro," *Ann Biomed Eng*, vol. 45, no. 2, pp. 476–486, 2017.

[113] H. Hatoum, A. Yousefi, S. Lilly, P. Maureira, J. Crestanello, and L. P. Dasi, "An in vitro evaluation of turbulence after transcatheter aortic valve implantation," *J Thorac Cardiovasc Surg*, vol. 156, no. 5, pp. 1837–1848, 2018.

[114] H. Hatoum, J. Dollery, S. M. Lilly, J. Crestanello, and L. P. Dasi, "Impact of patient-specific morphologies on sinus flow stasis in transcatheter aortic valve replacement: an in vitro study," *J Thorac Cardiovasc Surg*, vol. 157, no. 2, pp. 540–549, 2019.

[115] M. Heitkemper, H. Hatoum, and L. P. Dasi, "In vitro hemodynamic assessment of a novel polymeric transcatheter aortic valve," *J Mech Behav Biomed Material*, vol. 98, pp. 163–171, 2019.

[116] W. A. Pruett, J. S. Clemmer, and R. L. Hester, "Physiological modeling and simulation – validation, credibility, and application," *Annu Rev Biomed Eng*, vol. 22, pp. 185–206, 2020.

[117] R. Cheng, Y. G. Lai, and K. B. Chandran, "Three–dimensional fluid–structure interaction simulation of bileaflet mechanical heart valve flow dynamics," *Ann Biomed Eng*, vol. 32, pp. 1471–1483, 2004.

[118] J. Stijnen, J. de Hart, P. Bovendeerd, and F. Van de Vosse, "Evaluation of a fictitious domain method for predicting dynamic response of mechanical heart valves," *J Fluids Struct*, vol. 19, pp. 835–850, 2004.

[119] L. Ge, H. Leo, F. Sotiropoulos, and A. P. Yoganathan, "Flow in a mechanical bileaflet heart valve at laminar and near-peak systole flow rates: CFD simulations and experiments," *J Biomech Eng*, vol. 127, pp. 782–797, 2005.

[120] L. Ge, L. P. Dasi, F. Sotiropoulos, and A. P. Yoganathan, "Characterization of hemodynamics forces induced by mechanical heart valves: Reynolds vs. viscous stresses," *Ann Biomed Eng*, vol. 36, pp. 276–297, 2008.

[121] R. A. Nishimura, C. M. Otto, R. O. Bonow, B. A. Carabello, J. P. Erwin III, R. A. Guyton, P. T. O'Gara, C. E. Ruiz, N. J. Skubas, P. Sorajja, T. M. Sundt III, J. D. Thomas, and ACC/AHA Task Force Members, "2014 AHA/ACC Guideline for the Management of Patients With Valvular Heart Disease: executive summary: a report of the American College of Cardiology/American Heart Association Task Force on Practice Guidelines," *Circulation*, vol. 129, no. 23, pp. 2440–2492, 2014.

[122] D. Dvir, T. Bourguignon, C. Otto, R. Hahn, R. Rosenhek, J. Webb, H. Treede, M. Sarano, T. Feldman, H. Wijeysundera, Y. Topilsky, M. Aupart, M. Reardon, G. Mackensen, W. Szeto, R. Kornowski, J. Grammie, A. Yoganathan, Y. Arbel, M. Borger, M. Simonato, M. Reisman, R. Makkar, A. Abizaid, J. McCabe, G. Dahle, G. Aldea, J. Leipsic, P. Pibarot, N. Moat, M. Mack, A. Kappetein, and M. Leon, "Standardized definition of structural valve degeneration for surgical and transcatheter bioprosthetic aortic valves," *Circulation*, vol. 137, no. 4, pp. 388–399, 2018.

[123] E. Salaun, M. Clavel, J. Rodés-Cabau, and P. Pibarot, "Bioprosthetic aortic valve durability in the era of transcatheter aortic valve implantation," *Heart*, vol. 104, pp. 1323–1332, 2018.

[124] R. Reul, M. Ramchandani, and M. Reardon, "Transcatheter aortic valve-in-valve procedure in patients with bioprosthetic structural valve deterioration," *Methodist Debakey Cardiovasc J*, vol. 13, no. 3, pp. 132–141, 2017.

[125] R. Rocha, C. Manlhiot, C. Feindel, T. Yau, B. Mueller, T. David, and M. Ouzounian, "Surgical enlargement of the aortic root does not increase the operative risk of aortic valve replacement," *Circulation*, vol. 137, no. 15, pp. 1585–1594, 2018.

[126] M. Mack, M. Leon, V. Thourani, R. Makkar, S. Kodali, M. Russo, S. Kapadia, S. Malaisrie, D. Cohen, P. Pibarot, J. Leipsic, R. Hahn, P. Blanke, M. Williams, J. McCabe, D. Brown, V. Babaliaros, S. Goldman, W. Szeto, P. Genereux, A. Pershad, S. Pocock, M. Alu, J. Webb,

and C. Smith, "Transcatheter aortic-valve replacement with a balloon-expandable valve in low-risk patients," *N Engl J Med*, vol. 380, no. 18, pp. 1695–1705, 2019.

[127] M. Alam, J. B. Lakier, and S. Goldstein, "Echocardiographic evaluation of porcine bioprosthetic valve degeneration," *Henry Ford Hosp Med J*, vol. 30, no. 3, pp. 124–127, 1982.

[128] J. A. Peacock, "An in vitro study of the onset of turbulence in the sinus of valsalva," *Circ Res*, vol. 67, pp. 448–460, 1990.

[129] A. Erasmi, H. Sievers, M. Scharfschwerdt, T. Eckel, and M. Misfeld, "In vitro hydrodynamics, cusp-bending deformation, and root distensibility for different types of aortic valve-sparing operations: remodeling, sinus prosthesis, and reimplantation," *J Thorac Cardiovasc Surg*, vol. 130, pp. 1044–1049, 2005.

[130] A. Aljalloud, M. Shoaib, S. Egron, J. Arias, L. Tewarie, H. Schnoering, S. Lotfi, A. Goetzenich, N. Hatam, D. Pott, Z. Zhong, U. Steinseifer, R. Zayat, and R. Autschbach, "The flutter-by effect: a comprehensive study of the fluttering cusps of the Perceval heart valve prosthesis," *Interact Cardiovasc Thorac Surg*, vol. 27, no. 5, pp. 664–670, 2018.

[131] M. P. Païdoussis, *Fluid–structure interactions: slender structures and axial flow*, vol. 2. London: Academic Press, 2016.

[132] M. Ruggero, S. Narayan, A. Temchin, and A. Recio, "Mechanical bases of frequency tuning and neural excitation at the base of the cochlea: comparison of basilar-membrane vibrations and auditory-nerve-fiber responses in chinchilla," *Proc Natl Acad Sci*, vol. 97, no. 22, pp. 11744–11750, 2000.

[133] P. Sun, J. Qin, and K. Campbell, "Fatigue modeling via mammalian auditory system for prediction of noise induced hearing loss," *Comput Math Methods Med*, vol. 2015, p. 753864, 2015.

[134] J. Sader, J. Cossé, D. Kim, B. Fan, and M. Gharib, "Large-amplitude flapping of an inverted flag in a uniform steady flow – a vortex-induced vibration," *J Fluid Mech*, vol. 793, pp. 524–555, 2016.

[135] M. Langthjem, "On the mechanism of flutter of a flag," *Acta Mech*, vol. 230, pp. 3759–3781, 2019.

[136] C. Blais, J. G. Dumesnil, R. Baillot, S. Simard, D. Doyle, and P. Pibarot, "Impact of valve prosthesis-patient mismatch on short-term mortality after aortic valve replacement," *Circulation*, vol. 108, no. 8, pp. 983–988, 2003.

[137] D. J. Lapar, G. Ailawadi, C. M. Bhamidipati, G. Stukenborg, I. K. Crosby, J. A. Kern, and I. L. Kron, "Small prosthesis size in aortic valve replacement does not affect mortality," *Ann Thorac Surg*, vol. 92, no. 3, pp. 880–888, 2011.

[138] J. Relland, P. Perier, and B. Lecointe, "The third generation Carpentier–Edwards bioprosthesis: early results," *J Am Coll Cardiol*, vol. 6, no. 5, pp. 1149–1154, 1985.

[139] H. B. Barner, A. J. Labovitz, and A. C. Fiore, "Prosthetic valves for the small aortic root," *J Card Surg*, vol. 9, no. s2, pp. 154–157, 1994.

[140] J. Rodés-Cabau, P. Pibarot, R. Suri, S. Kodali, V. Thourani, W. Szeto, L. Svensson, E. Dumont, K. Xu, R. Hahn, and M. Leon, "Impact of aortic annulus size on valve hemodynamics and clinical outcomes after transcatheter and surgical aortic valve replacement," *Circ Cardiovasc Interv*, vol. 7, no. 5, pp. 701–711, 2014.

[141] C. Kan, J. Wang, W. Chen, P. Lu, M. Chan, C. Lin, and W. Hsieh, "Applicability of handmade expanded polytetrafluoroethylene trileaflet-valved conduits for pulmonary valve reconstruction: an ex vivo and in vivo study," *J Thorac Cardiovasc Surg*, vol. 155, no. 2, pp. 765–774, 2018.

[142] F. Coulter, M. Schaffner, J. Faber, A. Rafsanjani, R. Smith, H. Appa, P. Zilla, D. Bezuidenhout, and A. Studart, "Bioinspired heart valve prosthesis made by silicone additive manufacturing," *Matter*, vol. 1, pp. 266–279, 2019.

[143] L. Scotten and D. Walker, "New laboratory technique measures projected dynamic area of prosthetic heart valves," *J Heart Valve Dis*, vol. 13, no. 1, pp. 120–132, 2004.

[144] P. J. LaNasa and E. L. Upp, *Fluid Flow Measurement: A Practical Guide to Accurate Flow Measurement*. Butterworth–Heinemann, 3 ed., 2014.

[145] K. Rajagopal, B. Griffith, and A. DeAnda Jr., "Reply: the stresses of cardiovascular mechanics," *J Thorac Cardiovasc Surg*, vol. 159, no. 3, pp. e158–e159, 2020.

[146] I. Vesely, "The evolution of bioprosthetic heart valve design and its impact on durability," *Cardiovasc Pathol*, vol. 12, no. 5, pp. 277–286, 2003.

[147] J. R. González-Juanatey, J. M. Garcia-Acuña, M. Vega Fernandez, A. Amaro Cendón, V. Castelo Fuentes, J. B. García-Bengoechea, and M. G. de la Peña, "Influence of the size of aortic valve prostheses on hemodynamics and change in left ventricular mass: implications for the surgical management of aortic stenosis," *J Thorac Cardiovasc Surg*, vol. 112, no. 2, pp. 273–280, 1996.

[148] A. Avelar, J. Canestri, C. Bim, M. Silva, R. Huebner, and M. Pinotti, "Quantification and analysis of leaflet flutter on biological prosthetic cardiac valves," *Artif Organs*, vol. 41, no. 9, pp. 835–844, 2017.

[149] J. Vacek, J. Phelix, and J. Rycyna, "The inaccuracy of aortic valve systolic flutter as a screening test for significant aortic stenosis," *Clin Cardiol*, vol. 7, pp. 229–232, 1984.

[150] J. Butany, V. Nair, S. Leong, G. Soor, and C. Feindel, "Carpentier-Edwards Perimount valves–morphological findings in surgical explants," *J Card Surg*, vol. 22, no. 1, pp. 7–12, 2007.

[151] J. S. Soares, K. R. Feaver, W. Zhang, D. Kamensky, A. Aggarwal, and M. S. Sacks, "Biomechanical behavior of bioprosthetic heart valve heterograft tissues: characterization, simulation, and performance," *Cardiovasc Eng Technol*, vol. 7, no. 4, pp. 309–351, 2016.

[152] P. A. Chandraratna, P. Samet, M. J. Robinson, and C. Byrd, "Echocardiography of the "floppy" aortic valve. Report of a case," *Circulation*, vol. 52, no. 5, pp. 959–962, 1975.

[153] E. R. Pinto, P. M. Damani, C. N. Sternberg, and A. J. Liedtke, "Fine flutterings of the aortic valve as demonstrated by aortic valve echocardiograms," *Am Heart J*, vol. 95, no. 6, pp. 807–808, 1978.

[154] V. Rameh and A. Kossaify, "A rare echocardiographic features: systolic fluttering of the noncoronary cusp of the aortic valve," *Int J Med Res Health Sci*, vol. 5, no. 1, pp. 113–114, 2016.

[155] K. Grubb, "Aortic root enlargement during aortic valve replacement: Nicks and Manouguian techniques," *Oper Tech Thorac Cardiovasc Surg*, vol. 20, no. 3, pp. 206–218, 2015.

[156] M. Roeser, "The Konno-Rastan procedure for anterior aortic annular enlargement," *Oper Tech Thorac Cardiovasc Surg*, vol. 20, no. 3, pp. 219–233, 2015.

[157] S. Reese, M. K. Ussner, and B. D. Reddy, "A new stabilization technique for finite elements in non-linear elasticity," *Int J Numer Meth Biomed Engng*, vol. 44, pp. 1617–1652, 1999.

[158] J. Bonet, A. J. Gil, and R. Ortigosa, "A computational framework for polyconvex large strain elasticity," *Comput Methods Appl Mech Engrg*, vol. 283, pp. 1061–1094, 2015.